High Sensitivity Nucleic Acid Detection using Electrocatalytic Metal Nanoparticles

Hazel McArdle BSc (Hons)

Thesis submitted for the award of PhD

School of Chemical Sciences

Dublin City University

Supervisor:

Prof. Robert J. Forster

June 2016

Declaration

I hereby certify that this material, which I now submit for assessment on the programme of study leading to the award of Doctor of Philosophy is entirely my own work, and that I have exercised reasonable care to ensure that the work is original, and does not to the best of my knowledge breach any law of copyright, and has not been taken from the work of others save and to the extent that such work has been cited and acknowledged within the text of my work.

Signed: _____ ID No.:_____ Date: _____

TABLE OF CONTENTS

LIST OF ABBREVIATIONS

A	adenine
AFM	atomic force spectroscopy
Ag	silver
Ag/AgCl	silver/silver chloride
$AgClO_4$	silver perchlorate
AgNC	silver nanoclusters
Au	gold
BSA	bovine serum albumin
C	Cytosine
CAD	computer aided design
CCD	charge coupled device
CO_2	carbon dioxide
COOH-C_{11}-SH	11-mercaptoundecanoic acid
CPE	constant phase elements
CV	cyclic voltammetry
DF	dissolvable film
DNA	deoxyribonucleic acid
DPBS	Dulbecco's phosphate buffer saline
DPV	differential pulse voltammetry
ds	double stranded
EA	electrochemical area,
EDX	energy dispersive X-ray spectroscopy
EIS	electrochemical impedance spectroscopy
ELISA	enzyme-linked immunosorbent assay
EtOH	ethanol
$[Fe(CN)_6]^{3-/4-}$	ferri/ferro cyanide

G	guanine
GC	glassy carbon
H_2O	water
H_2O_2	hydrogen peroxide
H_2SO_4	sulfuric acid
HNO_3	nitric acid
H_2PtCl_6	chloroplatinic acid hydrate
ITO	indium tin oxide
KCl	potassium chloride
LAMP	loop mediated isothermal amplification
$LiClO_4$	lithium perchlorate
LOD	limit of detection
LSPR	local surface plasmon resonance
miRNA	micro ribonucleic acid
MCH	mercaptohexanol
MWCNT	multi-walled carbon nanotube
N_2	nitrogen
NA	nucleic acid
NASBA	nucleic acid sequence based amplification
NIR	near infra-red
NP	nanoparticle
O_2	oxygen
PBS	phosphate buffer saline
PCR	polymerase chain reaction
PMMA	Poly(methyl methacrylate)
Pt	platinum
PSA	pressure-sensitive adhesive
PVA	poly-vinyl alcohol
PVP	Polyvinylpyrrolidone

RCA	rolling circle amplification
RF	roughness factor
RNA	ribonucleic acid
RT-PCR	reverse-transcriptase polymerase chain reaction
SAM	self-assembled monolayer
SCC	somatic cell count
SEM	scanning electron microscopy
SERS	surface enhanced raman spectroscopy
SR	surface roughness
ss	single stranded
T	thymine
TEM	transmission electron microscopy
THF	tetrahydrofuran
TSNP	triangular silver nanoplates
U	uracil
Z	impedance

Symbols:

A_G	geometrical area of the electrode (0.0314 cm^2),
aM	attomoles per litre
A_p	area under the peak, cm^2
C	charge, Coulombs
cm	centimetre
cm^{-1}	wavenumber
e-	electron
E_t	potential at time t
fM	femtomoles per litre
Hz	frequency, Hertz

i	current, Amps
I_t	current at time t
kg	kilograms
kV	kilovolts
L	litre
M	moles per litre
mA	milliamps
mL	millilitres
mM	millimoles per litre
ms	millisecond
mV	millivolts
nM	nanomoles per litre
nm	nanometres
Ω	resistance, Ohms
Φ	phase shift
pM	picomoles per litre
R_{ct}	charge transfer resistance
s	second
t	time
µA	microamps
µL	microlitre
µM	micromoles per litre
µm	micrometer
V	volts
ω	radial frequency

ABSTRACT

Hazel McArdle

High Sensitivity Nucleic Acid Detection using Electrocatalytic Metal Nanoparticles

The detection and quantitation of specific nucleic acid (NA) sequences continue to grow in importance. This is driven by the increasing need for the development of point of care devices, which can test levels of biomarkers in various samples, such as blood, serum, saliva, urine, etc.

Reported here are ways to detect specific NA sequences without the need for amplification. An electrochemical biosensor has been developed which amplifies the signal associated with a single NA binding event, rather than amplifying the target NA, which is the case in PCR or NASBA. This sensor involves a three step procedure; initially the capture NA strand is immobilised onto the electrode surface, this is then hybridised to the complementary target sequence, which is then followed by target hybridisation to a complementary probe strand which is labelled with a nanoparticle.

The ability to modify the size and structure of nanomaterials so as to control their properties has led to novel sensors and the enhanced performance of bioanalytical assays. By controlling the size and shape of nanoparticles, their properties can be finely tuned to suit the application required. A double potential step electrodeposition technique was used to control the deposition of platinum nanoparticles (PtNPs). This involved using a short nucleation pulse at a large overpotential, following by a longer growth pulse at a lower overpotential, to grow the platinum up from these nucleation sites. This method of platinum deposition was investigation on both planar gold and into the defect sites of a self-assembled monolayer (SAM). By using the SAM template, hemispherical nanoparticles are formed which can then be functionalised on one side with NA prior to desorption, allowing for the underside of the nanoparticle to be left clean.

PtNPs are widely known for their catalytic properties, including the reduction of hydrogen peroxide. The catalytic activity of these regioselectively functionalised, hemispherical PtNPs was assessed by monitoring the difference in current associated with the reduction of hydrogen peroxide in H_2SO_4 before and after the addition of the peroxide. Capture NA was bound to the underlying gold electrode, and

probe NA was bound to the PtNP; these then hybridise together with the complementary target strand that is uniquely associated to the pathogen Staphylococcus Aureus. This modified electrode allows detection of the target with high sensitivity and response time. Semi-log plots of the pathogen concentration vs. change in current were linear from 1 aM to 1 µM, with a wide dynamic range.

A microfluidic disc has been designed to detect NA biomarkers with high sensitivity, selectivity and discrimination. The disc is pre-loaded with miRNA strands and each hybridization step is completed inside the disc by triggering the tabs of chambers to burst to release the contents. When the hybridization is complete, the target miRNA specific to epilepsy, is detected based on the electrocatalytic reduction of hydrogen peroxide at the PtNPs which are functionalised to the probe miRNA strand. A linear response is achieved from 1 pM to 1 µM. Electrochemical Impedance Spectroscopy (EIS) was also performed on the modified electrode as another method of NA detection and a linear response is achieved with a standard deviation between 2 – 9 %.

Silver is also catalytically active to the reduction of hydrogen peroxide. Triangular Silver Nanoplates (TSNPs) functionalised with probe strand NA were immobilised onto a gold electrode surface via a target miRNA strand that is unique to Neuroblastoma. The change in current before and after the addition of hydrogen peroxide was monitored and the semi-log plots of the pathogen concentration vs change in current were linear from 100 fM to 1 µM. These TSNPs were immobilised within gold nanocavity arrays via RNA hybridisation of the target NA. When the TSNPs are immobilised in the cavities, they can also give a plasmonic enhancement by using different metals, excitation wavelengths and distances between the nanoplate and the surface of the cavity.

PUBLICATIONS AND PRESENTATIONS:

Spain, E., Brennan, E., McArdle, H., Keyes, T. E., Forster, R. J. High Sensitivity DNA Detection Based on Regioselectively Decorated Electrocatalytic Nanoparticles*. Anal. Chem.* **2012**, *84*, 6471−6476

Spain, E., McArdle, H., Keyes, T. E., Forster, R. J. Detection of Sub-Femtomolar DNA Based on Double Potential Step Electrodeposition of Regio-Selectively Modified Platinum Nanoparticles. *Analyst.* **2013**, *138,* 4340-4344

Aydemir, N., McArdle, H., Patel, S., Whitford, W., Evans, C. W., Travas-Sejdic, J., Williams, D. E. A Label-Free, Sensitive, Real-Time, Semiquantitative Electrochemical Measurement Method for DNA Polymerase Amplification (ePCR). *Anal. Chem.* **2015**, *87*, 5189-5197.

Conference Contributions and Poster Presentations:

Posters:

H. McArdle, E. Spain, T.E. Keyes, R.J. Forster, *"Ultra-Sensitive DNA Detection Based on Nanoparticle Functionalization and Electrocatalysis of Nanoparticle Release",* Smart Surfaces 2012, Solar and Biosensor Applications, March 2012, Dublin

H. McArdle, E. Spain, T.E. Keyes, R.J. Forster, *"Ultra-Sensitive DNA Detection Based on Nanoparticle Functionalization and Electrocatalysis of Nanoparticle Release",* 64th Irish Universities Chemistry Research Colloquium 2012, 14th – 15th June 2012, Limerick.

H. McArdle, E. Spain, N. Aydemir, J. Travas-Sejdic, D.E. Williams, T.E. Keyes, R.J. Forster. *"Real-Time Electrochemical Monitoring of the Polymerase Chain Reaction by Conducting Polymers and Ultra-Sensitive Direct Detection of DNA using Nanoparticles",* 13th Topical Meeting of the International Society of Electrochemistry, April 2013, Pretoria, South Africa

Oral Presentations:

"Real-Time Electrochemical Monitoring of the Polymerase Chain Reaction by Conducting Polymers", 8th Polymer Electronics Research Centre (PERC) symposium / 3rd Hybrid Polymers Symposium 2012, December 2012, Auckland, New Zealand

"Detection of Sub-Femtomolar DNA Based on Double Potential Electrodeposition of Electrocatalytic Platinum Nanoparticles", Electrochem 2013, September 2013, University of Southampton, UK.

CHAPTER 1

INTRODUCTION AND LITERATURE REVIEW

1.1 INTRODUCTION AND OVERALL OBJECTIVES

Specific sequences of nucleic acids can provide practical targets for the identification and diagnosis of disease since unique sequences can be associated with particular conditions, e.g., DNA in the case of genetic disorders or microRNA, miRNA, for conditions such as cancer and cardiovascular disease. A particular challenge is the sensitive and accurate detection of nucleic acid markers since this allows disease to be detected early, e.g., before clinical symptoms can be detected. One attractive strategy for low-cost, rapid and sensitive detection is the use of (bio)chemical sensors. The development of electrochemical sensors based on nanomaterials and new detection strategies is the major objective of this thesis.

Shown in Figure 1.1 is a schematic diagram of the concept that has been pursued in this work, i.e., a fully integrated, sample-to-answer microfluidic device that can detect nucleic acid strands that are associated with different diseases. The detection of target nucleic acids is achieved using a sandwich assay, where an electrocatalytic metal nanoparticle label is brought to the surface via complementary nucleic acid hybridisation, and can then be detected at extremely low concentrations using electrochemical methods. Many different target nucleic acid strands can be detected, by varying the capture strand to be complementary to the required target. In this work a biosensor is described for the detection of DNA from Staph aureus mastitis as well as miRNAs associated with neuroblastoma and epilepsy.

A biosensor is a sensing device that can detect a biological parameter, such as binding event or target concentration.[1] The minimum requirements needed for a biosensor are[2,3]:

- A molecular recognition layer that allows for a highly selective, preferably specific, biological interaction to take place between the surface and the target such as nucleic acids, enzymes, tissues, microorganisms, etc.

- A transducer that converts the recognition event into a measurable signal.
- A detector that can convert the measureable signal into a parameter that can be understood, such as optical, electrochemical, magnetic, etc.

An electrochemical biosensor uses a biological recognition element that is in contact with an electrochemical transduction element. The characteristics of an electrochemical biosensor include[4,5]:

- Have a biorecognition layer that enables selective detection of the analyte;
- Have a transducer that is able to convert the recognition event to an electrical signal;
- Have self-contained instrumentation, with easily controlled reaction conditions and minimal need for sample preparation, for possible use out a centralised laboratory;
- Be accurate and simple to use;
- Rapid analysis and output of results;
- Independent of physical parameters and surrounding, such as pH and temperature;

There are many electrochemical transduction approaches including impedance (changes in resistance and capacitance), conductivity,[6] potentiometry[7] (changes in potential) and amperometry (changes in current due to oxidation or reduction). Amperometric detection is attractive as small currents can be easily measured making it sensitive and it can have a wide dynamic range.[8]

Where the target is a nucleic acid, the molecular recognition and hence the selective response, is achieved by immobilising a nucleic acid biorecognition layer onto the electrode surface. This recognition layer comprises a capture strand that is complementary to a section of the target nucleic acid strand; this allows the target strand to be confined on the surface of the electrode through complementary hybridisation. The “sandwich” is completed by adding a second probe strand that is labelled, e.g., with a redox active molecule or nanoparticle, which is also complementary to a section of the target. Successful hybridisation, enabled by the presence of the target, can be

detected using amperometric methods by measuring the current response associated with the bound target.[9]

For many clinical applications, sensitivity is the main challenge. This is due to the target nucleic acid being present at a low concentration, pM or lower, especially before symptoms of the disease manifest. One approach for improving the sensitivity of these electrochemical nucleic acid biosensors is to use a nanomaterial[10], such as nanowires, nanoparticles or quantum dots[11], as the label so as to generate a large current in response to a small number of binding events.

In particular, metal nanoparticles are an attractive label to use in the sandwich assay, as the shape and composition can be varied and tailored to tune their optical and electrochemical properties so as to enhance the signal generated or for multiplexing.[12] This ability allows metal nanoparticles to be produced where the detection sensitivity rivals PCR, without the need for prior amplification. The main advantage of metal nanoparticles in electroanalysis is that the nanoparticles can achieve a massive increase in electrode area, and hence increase the electrochemical signal of the electrode.[13] To detect target nucleic acids at low concentrations, there are few hybridisation events on the electrode surface; by labelling these hybridisation events with a metal nanoparticle, there is an increased area available on the electrode, which therefore would give an increased response signal. The response generated correlates to the amount of nanoparticles present on the electrode, which are brought to the surface via complementary hybridisation to the target nucleic acid; therefore the response can be correlated to the concentration of the target nucleic acid.

In Chapter 1, various biosensors for the detection of nucleic acids are discussed, focusing particularly on metal nanoparticles as a method of increasing the signal to noise ratio and the overall sensitivity. The detection of specific nucleic acids using integrated microfluidic devices is also discussed.

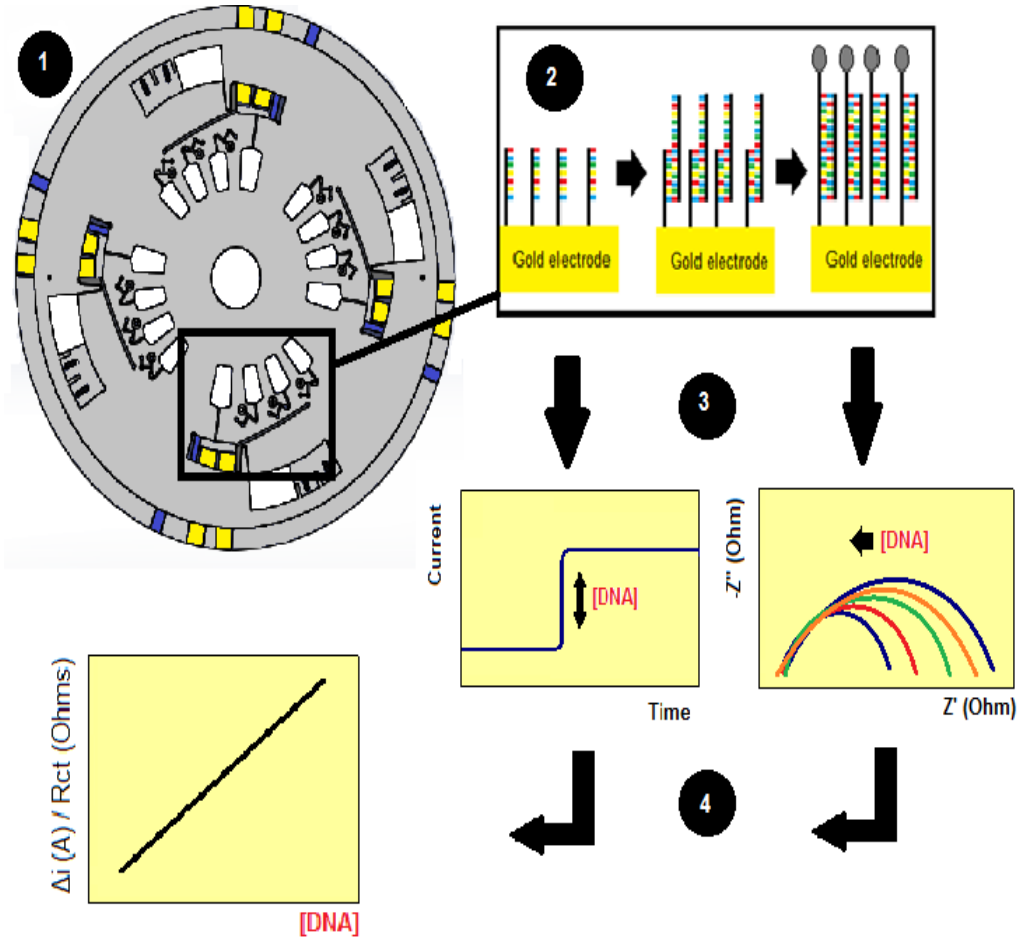

Figure 1.1: Schematic of the integrated microfluidic device described in this thesis. **1:** a centrifugal microfluidic device is made with electrodes included in the base that can be pre-loaded and triggered to release the contents of the chambers after a certain event. **2:** the electrode is functionalised with capture strand nucleic acid, the target nucleic acid, and the probe functionalised platinum nanoparticle, to make the sandwich assay inside the disc. **3:** the external parts of the electrode are attached to a potentiostat to detect the target nucleic acid concentration using amperometric detection and impedimetric detection. **4** By varying the target nucleic acid concentration, a calibration curve of the nucleic acid concentration vs the electrochemical response can be obtained.

1.2 NUCLEIC ACIDS

1.2.1 Nucleic Acid Structures

Nucleic acids are biological polymers and include DNA and RNA. DNA and RNA share many structural similarities, as they are both linear polymers made up of individual building blocks called nucleotides. RNA strands tend to be shorter, in the range of hundreds to thousands of bases, whereas DNA is longer and can be up to millions of nucleotides in length.

RNA and DNA are composed of five nucleotides that are displayed in Figure 1.2; Guanine (G) and Adenine (A), which contain a six membered ring fused to a five membered ring, and Thymine (T), Cytosine (C) and Uracil (U), which contain a five membered ring. A, G, and C are found in both DNA and RNA; T is found only in DNA and U is found only in RNA. These nucleotides are bound to a backbone; this is composed of a five carbon sugar that is phosphorylated at carbon 5, and has a hydroxyl group at carbon 3. This gives the single stranded nucleic acid directionality, and it is commonly read from the 5' end to the 3' end. DNA contains the sugar 2-deoxyribose.[14] RNA contains the sugar ribose which contains an extra hydroxyl group. A phosphodiester bond links the individual bases together from the 3' end of one base to the 5' end of another base.

Watson and Crick discovered in 1953 that DNA had a double helix structure, which was a major breakthrough for the understanding of the nature of DNA.[15] They determined that DNA is composed of two strands of nucleotides that bind together to form a double helix. Base pairing holds the two strands together; A is paired to T via two hydrogen bonds, G is paired to C by three hydrogen bonds. The strength of the double helix is achieved due to the secondary structure of the double stranded DNA, which included hydrophobic interactions, van der Waal forces and stacking.[16,17]

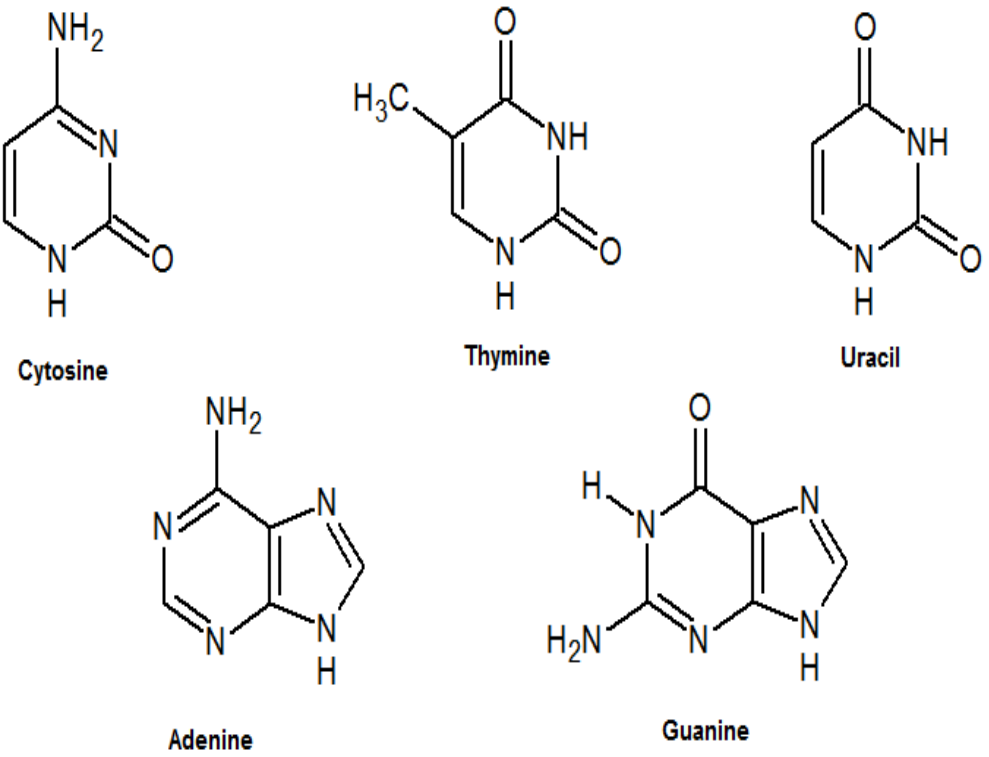

Figure 1.2: Structures of the five nucleotides.

1.2.2 DNA

DNA contains all of the information needed to build a cell, become tissues and form organs. DNA must be protected from damage to ensure the integrity of the information it holds for these purposes.[18] As DNA has a double helix structure, this infers that each cell has two copies of the information needed to operate that cell, and if one of the strands becomes damaged, this can be identified by its base paired strand, which allows the damaged cell to carry out programmed cell death to prevent the mutations from progressing to the rest of the organism[19].

The cells in the human body received tens of thousands of DNA lesions per day, which can block genome transcription.[20] If they are not repaired, or repaired incorrectly, they can lead to mutations or abnormalities that can threaten cell or organism viability. Some of these abnormalities arise through processes in the cell, such as mismatches occurring through DNA replication, reactions in the cell or by-products from environmental toxic agents. They can also occur from sites of inflammations or infection; these attack DNA which leads to compounds that prevent base pairing, block DNA processes or cause breaks in the strand.[21] If these occur in close proximity, the double-stranded DNA can break, which is very different to repair and can cause cell toxicity. These alterations can lead to cellular death, or degenerative changes and aging of multicellular organisms.[22]

To convey the information contained in DNA to the rest of the cell to carry out its function, the DNA is transcribed into RNA.

1.2.3 miRNA

MicroRNAs (miRNAs) are group of small, non-coding RNA molecules that are approximately 18 – 25 nucleotides long; their function is to regulate the protein

function in cells post-transcriptionally.[23] There are many different types of RNA that are transcribed in the nucleus of the cell and contribute to the cell function. They can be broken down into two main groups, protein coding and non-protein coding.[24,25] The main function of coding RNA is to transfer DNA to the ribosome of the cell. The majority of RNA in the cell is non-protein coding.

miRNAs are capable of switching between the upregulation and downregulation of proteins, which makes the measurements of miRNA an important indication of how the cell is functioning.[26] This allows for detection of cells that are potentially abnormal.

miRNAs circulating in blood are an attractive target for disease detection, which could lead to non-invasive screening processes for a range of different illnesses and infections.[27] However, the detection methods need to be able to detect ultralow concentrations of the miRNA, as these are the concentrations present in circulating blood samples at early stages of the disease. Point of care detection is ideal, however to achieve this objective, the device must be inexpensive, sensitive, rapid and simple.

1.3 NUCLEIC ACID BIOSENSORS

Nucleic acids are attractive disease biomarkers since they are easy to manipulate, purify, label and sequence, which makes them easy to detect. They have the ability to be amplified and therefore the sensitivity can be increased. They can also be detected with great selectivity due to the complementary base pairing of nucleotides which will be disrupted by even a small number of mismatches. Much of the typical nucleic acid analysis consists of a sample preparation, amplification of the nucleic acids, followed by nucleic acid detection.[28]

Rapid nucleic acid testing is required in many different fields, including disease diagnostics, forensics, genetic testing, environmental testing, etc. Amplification of the target, e.g., by PCR, can be challenging under these circumstances. Therefore, the development of an inexpensive, easy to use, fast sensor device is vital to carry out these tests. The main task in making an effective nucleic acid sensor is to be able to detect the hybridisation event efficiently, at a very low target concentration. Some methods for detection are not sensitive enough to detect ultralow concentrations of the target at early stages of disease detection, and therefore need amplification to obtain a large enough signal. Enzyme Linked Immunoassays (ELISA)[29], loop-mediated isothermal amplification (LAMP),[30] rolling circle amplification (RCA)[31], and, most commonly, polymerase chain reaction (PCR)[32-35] are all common amplification methods of target nucleic acid strands.

There are many different methods for detecting nucleic acids, including fluorescence[36], chemiluminescence[37], and gravimetric[38] biosensors. Electrochemical detection has the advantages of being cheap, user-friendly, sensitive and selective[39,40]. It also has the advantage of the ability to be combined with different labels to improve sensitivity, such as organic dyes[41], metal complexes[42], enzymes[43] and metal nanoparticles[44].

1.3.1 Nanoparticle Based Biosensor

As mentioned previously, one of the main advantages of incorporating nanoparticles into electrochemical sensing is the massive increase in surface area that is achieved by using nanoparticles, as this can then increase the electrochemical signal.

There are many types of nanoparticles that can be used in electrochemical sensors, such as metal nanoparticles, oxide nanoparticles,[45,46] or composite nanoparticles.[47,48] Even though each nanoparticle can act differently depending on the circumstances, there are some functions that most nanoparticles perform:[49]

- Immobilization of the biomolecules;
- Catalysis of electrochemical reactions;
- Enhancement of electron transfer;
- Labelling of the biomolecules;
- Acting as a reactant.

The functions of metal nanoparticles can be both the carriers of the biological molecules for the recognition events, and as tags for the electrochemical signal response, amplification and output.[50] The ability to modify functional groups onto the metal nanoparticle surface allows the capability of loading single or multiple species of biological species onto the surface.

Nobel metal nanoparticles, specifically platinum, gold and silver are interesting for biosensing applications due to their size and shape dependent optic and electrochemical properties.[51] These metal nanoparticles are attractive due to their ease of synthesis, characterisation and surface functionalisation.

By incorporating gold nanoparticles into their electrochemical DNA sensor, Hu et al used nano-porous gold electrodes in a sandwich assay to detect target DNA strand. The gold nanoparticles were bound with a Ruthenium complex and a limit of detection of 28 aM for the target DNA was achieved using chronocoulometry, with high sensitivity, selectivity and stability.[52] Yu et al used

a sandwich assay by hybridising the target DNA strand on magnetic beads that were functionalised with capture DNA strand. Gold nanoparticles and marker-loaded apoferritin were hybridised to the target DNA strand via complementary strand on the gold nanoparticle. The marker was released into acidic buffer and subsequent electrochemical stripping analysis of the electroactive markers released from apoferritin NPs provided a means to quantify the concentration of target DNA. A linear range from 2.0×10^{-16} to 1.0×10^{-14} M, with a limit of detection of 50 aM was achieved.[53] Kawde et al used gold nanoparticles embedded in polymeric beads.[54] The gold nanoparticles amplified the signal to detect target DNA strands using electrochemical stripping as the detection method, with a detection limit of 300 aM. Wang et al[55] used silver coated gold nanoparticles for detection of the target strand corresponding to a breast cancer DNA target. The gold nanoparticle tags and a subsequent electrochemical stripping detection of the dissolved silver enhances the response, giving detection limits of 32 pM, which could be even further improved by increasing the hybridisation time.

These show just a fraction of the possibilities of using metal for electrochemical nucleic acid detection at ultralow concentrations. The ability to tailor the size, shape and surface of different metal nanoparticles improves the performance of the biosensors in all aspects, such as sensitivity and specificity. Electrocatalytic metal nanoparticles were used in this PhD project and will therefore be discussed further.

1.3.1.1 Electrocatalytic Biosensor

Nobel metal nanoparticles can also be used in nucleic acid electrochemical biosensors by detecting the electrocatalysis of the reaction when hydrogen peroxide is added to the sensor. As this reduction of peroxide can be monitored and the signal produced is proportional to the amount of nanoparticles present in the reaction, the nanoparticles can be labelled with a nucleic acid or an aptamer that is complementary to the target; therefore the signal produced is proportional to the amount of target present. Metal nanoparticles such as gold, platinum and silver are catalytically active, and hence can enhance the reduction of hydrogen peroxide. In a comprehensive review by Chen et al,[56] the electrochemical sensing properties of hydrogen peroxide by metal nanoparticles were reported. It reported on many different types of metal nanoparticles, showing the wide range of properties that metal nanoparticles have in hydrogen peroxide sensing.

Dong et al[57] have reported a simple, sensitive, label-free electrochemical biosensing strategy for detecting miRNA, using oligonucleotide encapsulated silver nanoclusters (Ag-NCs) as an electrocatalytic label. Here, a molecular beacon probe (MB) in the form of a hairpin miRNA probe is immobilised onto a gold electrode. When the target miRNA and functional probe encapsulated in the Ag-NCs hybridise to the molecular beacon, it opens out and brings the Ag-NCs to the electrode surface. This is described in Figure 1.3. The Ag-NCs are synthesised using ssDNA to achieve the required size. They are then characterised using AFM, TEM, UV-vis and EDS. The high catalytic activity of these Ag-NCs towards H_2O_2 reduction results in a sensitive electrochemical miRNA biosensor, while the selectivity of the MB probe allows high discrimination against base mismatches. Figure 1.4 show the differential pulse voltammetry (DPV) results of the current response when different concentrations of target miRNA are used. Inset in Figure 1.4 is the calibration curve between target miRNA concentration and the current response, which show microamp reproducibility. As the concentration lowers, so does the current response, as there are less Ag-NCs present on the electrode surface.

The limit of detection was determined to be 67 fM target concentration. This biosensing method is highly selective, as the current response for a single base mismatch was almost 4 times lower than that of the complementary target strand.

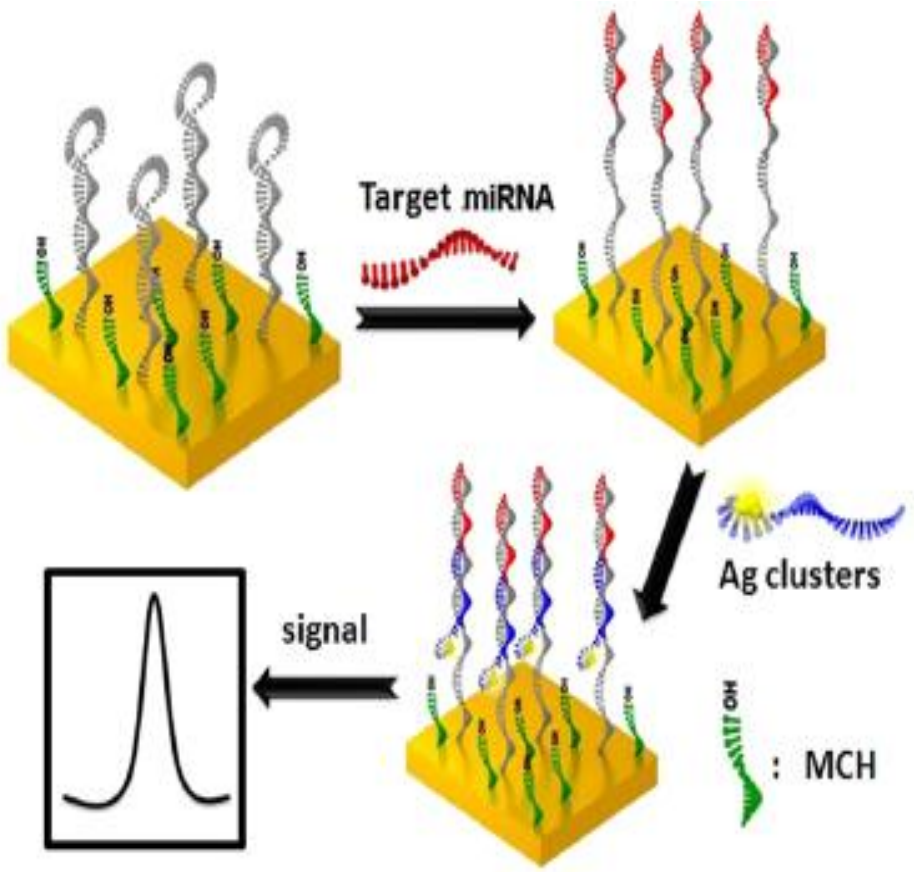

Figure 1.3: Schematic diagram of the electrochemical detection of miRNA using oligonucleotide encapsulated silver-nanoclusters. . *[Reproduced from ref 57:* Dong, H.; Jin, S.; Ju, H.; Hao, K.; Xu, L.; Lu, H.; Zhang, X. *Anal. Chem.* **2012***, 84*, 8670-8674.*]*

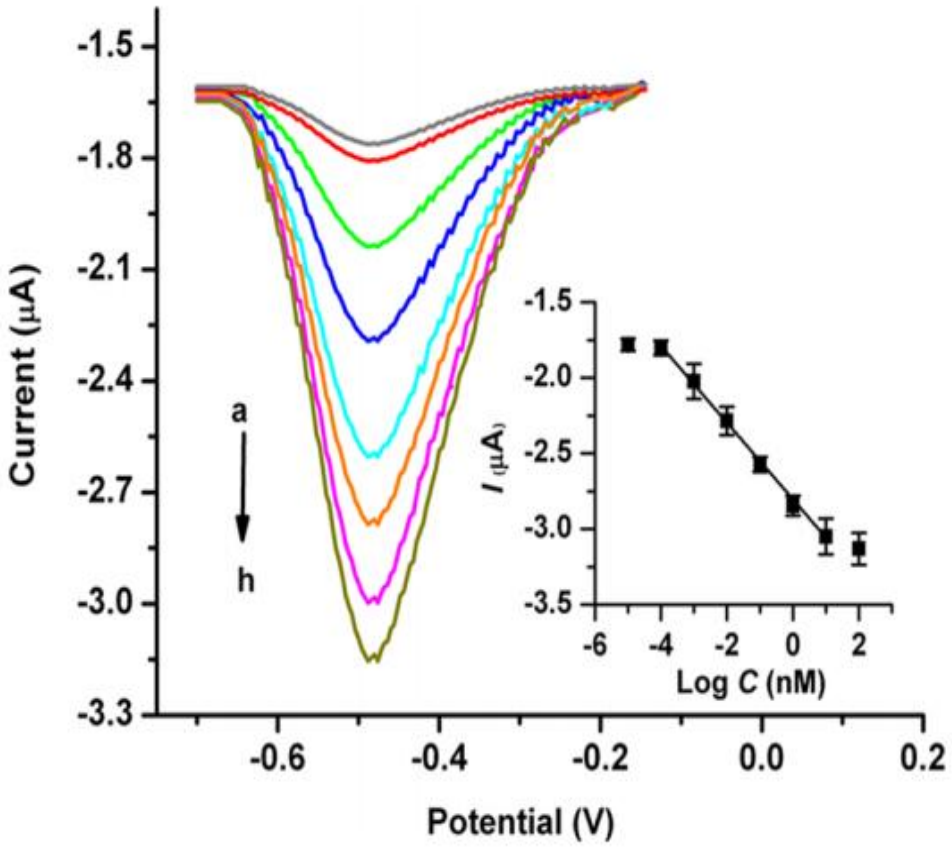

Figure 1.4: DPV curves of silver-nanoclusters modified Au electrodes in N_2-saturated PBS (100 mM, pH 7.0) containing H_2O_2 (3 mM) at 10 fM, 100 fM, 1 pM, 10 pM, 100 pM, 1 nM, 10 nM, and 100 nM target miRNA (from a to h). Inset: plot of the peak current versus the logarithm of target concentration. *[Reproduced from ref 57:* Dong, H.; Jin, S.; Ju, H.; Hao, K.; Xu, L.; Lu, H.; Zhang, X. *Anal. Chem.* **2012***, 84*, 8670-8674*.]*

Shahdost-fard et al[58] have recently described an aptasensor for the detection of adenosine using platinum nanoparticles as an electrocatalytic label. Adenosine plays a fundamental role in many biological processes, for example energy generation and protein metabolism. There is also promising investigations into the possibility of using it as a biomarker for cancer detection. In this study, platinum nanoparticles are functionalised with aptamers capture strands, and immobilised onto multi-walled carbon nanotubes (MWCNT) composites. The catalytic response of the platinum nanoparticles to the reduction of H_2O_2 was monitored. When adenosine was present in the solution, the peak reduction decreased, as the aptamer on the platinum nanoparticles release from the capture probe, and forms a complex between the aptamer functionalised platinum nanoparticles and the adenosine. Shown in Figure 1.5 are the voltammogram responses of the different concentrations of adenosine in the presence of 150 mM H_2O_2. As the concentration of adenosine increases, the current response of the reduction peak decreases. The limit of detection is determined to be 1 nM concentration of adenosine, which is reported to be an improvement on other detection methods. They have shown also that this is a reproducible and stable for storage. The selectivity is shown to be excellent; when uridine, cytidine and guanosine were used instead of adenosine, there was no recognisable decrease in the electrocatalytic reduction signal of H_2O_2. This adenosine detection method was also used to determine the concentration of adenosine in human blood serum and pharmaceutical formulations, and gave results in the expected ranges. This approach therefore is successful in determination of the concentration of adenosine and could be expanded to detect other small molecules by changing the aptamer to the complementary for the target molecule.

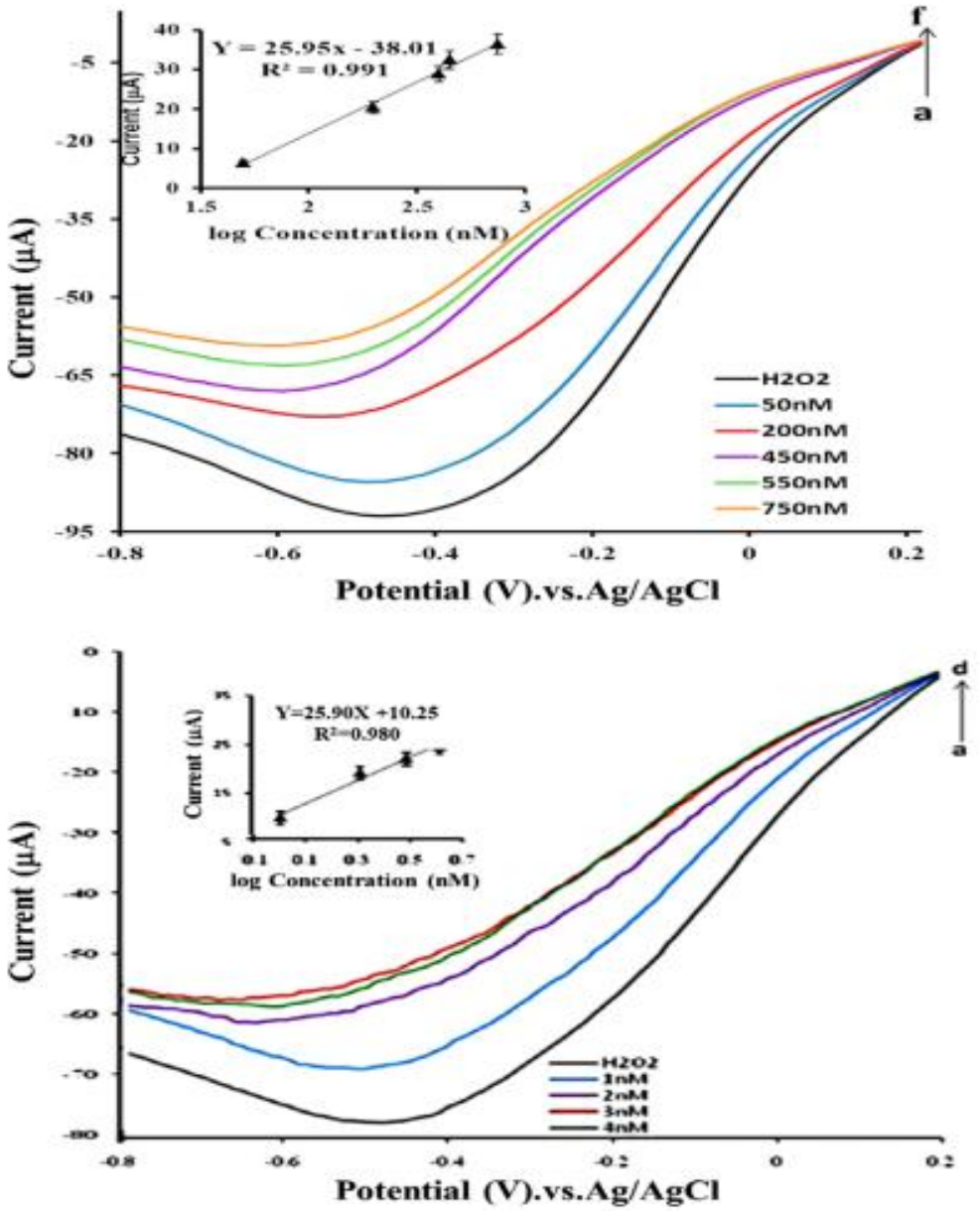

Figure 1.5: Voltammograms of Pt-NPdsDNA-modified GC electrode after dropping of different concentration of adenosine in 0.1 M PBS (pH 7.4) containing 150 mM of H_2O_2 at a scan rate of 10 mV/s. Insets: plots of reduction peak current vs log $C_{adenosine}$ (nM). *[Reproduced from ref 58:* Shahdost-fard, F.; Salimi, A.; Khezrian, S. *Biosens. Bioelectron.* **2014***, 53*, 355-362*.]*

Polsky et al[59] used catalytic platinum nanoparticles as catalytic labels for the amplified detection of DNA hybridisation and aptamer/protein recognition. Figure 1.6 shows the two schemes used for these detection methods. Platinum nanoparticles were functionalised with a thiol end group probe strand on DNA for the DNA detection. A thiol end group DNA strand was immobilised on the surface of a gold slide electrode; this DNA strand is complementary to the target analyte. The platinum nanoparticles were then confined on the surface of a gold slide electrode by complementary hybridisation to the target DNA strand. Platinum nanoparticles were also functionalised for thrombin detection. An aptamer modified surface was immobilised on the gold electrode for capture on thrombin, and then the platinum nanoparticles were brought to the surface of the electrode for detection, as shown in Figure 1.6.

The results of these detection methods are shown in Figure 1.7. Figure 1.7A shows the amperometric responses for the DNA target analyte of different concentrations. This investigation demonstrated that there is a catalytic response of the platinum nanoparticle catalytic label, and the limit of detection was determined to be 10 pM. Figure 1.7B shows the amperometric response of the reduction of hydrogen peroxide for the thrombin detection method, and a limit of detection for this study was determined to be at least 1 nM of thrombin. No catalytic current was determined when there was no thrombin present, or when a control of BSA was used in replacement of thrombin. The sensitivity of thrombin detection is improved 100-fold to present thrombin detection methods. The analysis of DNA is comparable to available procedures at that time, but by using other nanoparticles or substrates could improve the sensitivity of this method greatly. While the responses generated here are impressive and they are the first to demonstrate the use of electrocatalytic nanoparticles for amplifying the response in biosensing, the concentration range used isn't very wide, as only 4 concentrations are reported for each study. Also, there is an absence of error bars in Figure 1.7 and the reproducibility of the biosensor is not discussed in the publication. This could prove to be an issue, as reproducibility is a huge factor in biosensing.

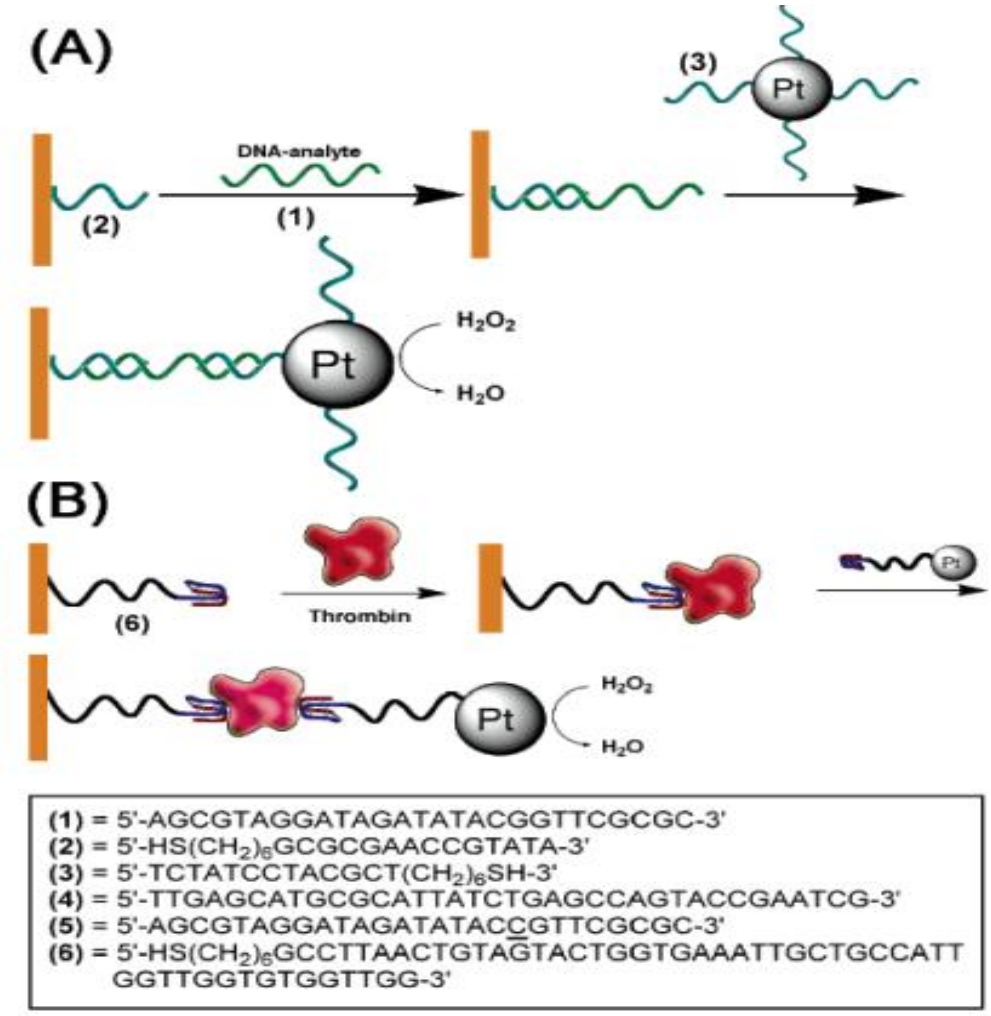

Figure 1.6: Scheme depicting the analytical procedure for using the Pt-NPs in the analysis of (A) DNA and (B) thrombin. *[Reproduced from ref 59:* Polsky, R.; Gill, R.; Kaganovsky, L.; Willner, I. *Anal. Chem.* **2006***, 78*, 2268-2271.*]*

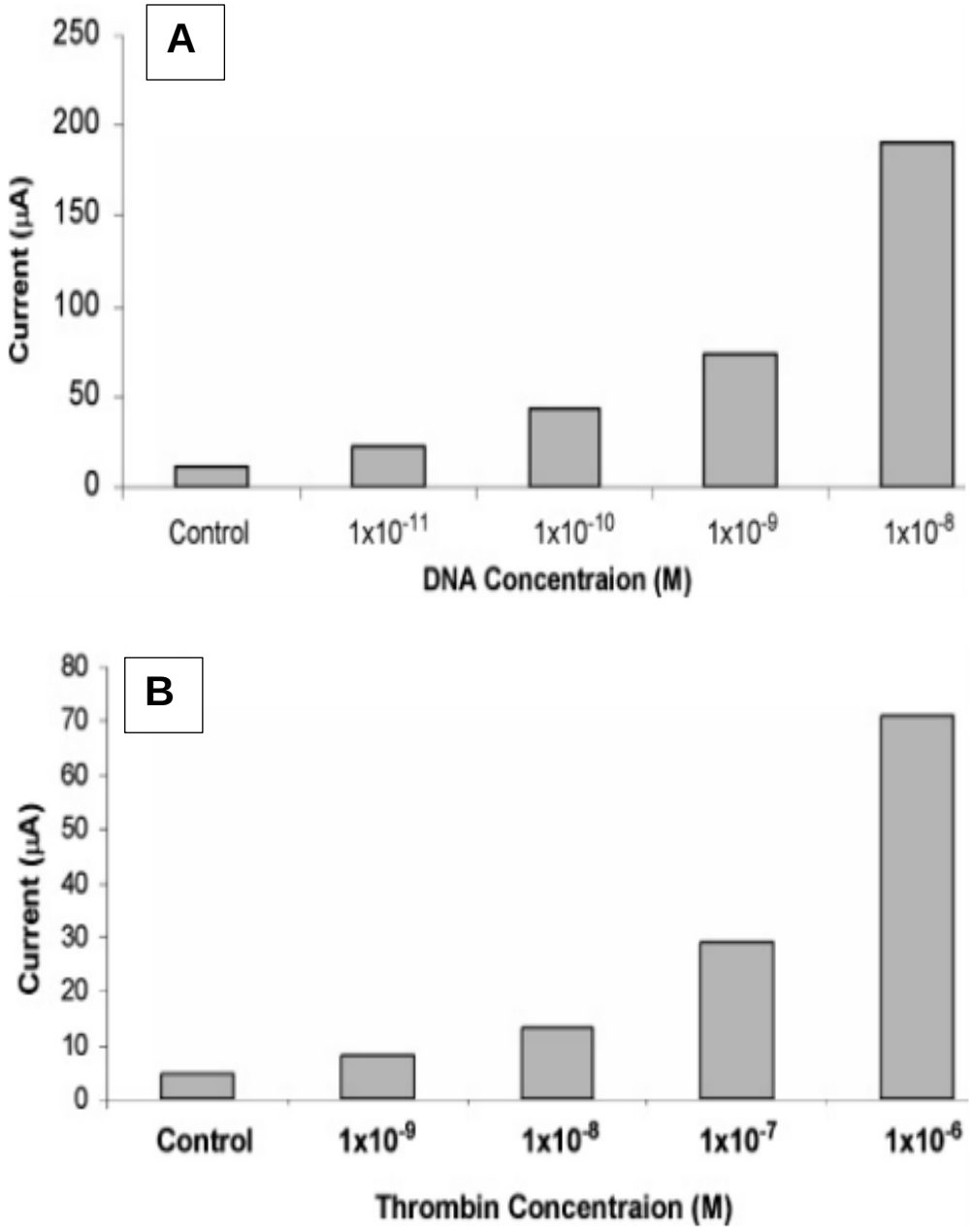

Figure 1.7: Chronoamperometric results for different concentrations of (A) DNA, and (B) thrombin in 0.1 M phosphate buffer that included 2 mM H_2O_2 for (A) and 10 mM H_2O_2 for (B) *[Reproduced from ref 59:* Polsky, R.; Gill, R.; Kaganovsky, L.; Willner, I. *Anal. Chem.* **2006***, 78*, 2268-2271.*]*

1.3.2 Impedimetric Based Biosensor

1.3.2.1 Electrochemical Impendence Spectroscopy Background

Electrochemical impedance spectroscopy is a sensitive electrochemical technique for investigating a wide range of bulk and interfacial electrical properties of electrode systems.[60] By modifying the surface of the electrode, for example with a biorecognition event, the interfacial properties change in accordance with how it was modified and what properties are associated with the new, modified surface.

EIS is the measurement of impedance (Z) over a wide range of frequencies. Impedance is a measure of the ability of a circuit to resist the flow of an electrical current.

As depicted in Figure 1.8, impedance measurements consist of applying a small sinusoidal ac potential excitation to an electrochemical cell and measuring the current and phase difference of the electrical current that develops across it. The excitation voltage can be expressed as:

$$E_t = E_o \sin(\omega t) \qquad \text{Equation 1.1}$$

where E_t is the potential at time t, E_o is the amplitude of the signal, and ω is the radial frequency and t is time. The sinusoidal current response signal therefore has a phase shift that is expressed as:

$$I_t = I_O \sin(\omega t + \Phi) \qquad \text{Equation 1.2}$$

where I_t is the current at time t, I_o is the current amplitude and Φ is the phase shift. Impedance can then be calculated in an expression analogous to Ohm's Law as follows:

$$Z = \frac{E}{I} = \frac{Eo \sin(\omega t)}{Io \sin(\omega t + \Phi)} = Zo \frac{Eo \sin(\omega t)}{Io \sin(\omega t + \Phi)}$$

Equation 1.3

There are two common methods of displaying impedance data; Nyquist plots and Bode plots. Nyquist plots shows the real data (Z') versus the imaginary data (Z''). Nyquist plots usually include a semi-circle lying on the x-axis followed by a straight line. At a higher frequency, the semi-circle portion corresponds to the electron transfer limited process and at a lower frequency, the straight line corresponds to the diffusion limited process. In fast electron transfer processes, only the linear process is observed while in very slow electrode transfer processes, a large semi-circular region is shown. The diameter of the semi-circle is equal to the electron transfer resistance.

The primary disadvantage of the Nyquist plot is that the frequency isn't shown. However, the Bode plot shows the phase and amplitude over the frequency range analysed. The bode plot is the logarithm of the absolute value of the impedance and the logarithm of the phase, plotted against the logarithm of the frequency.

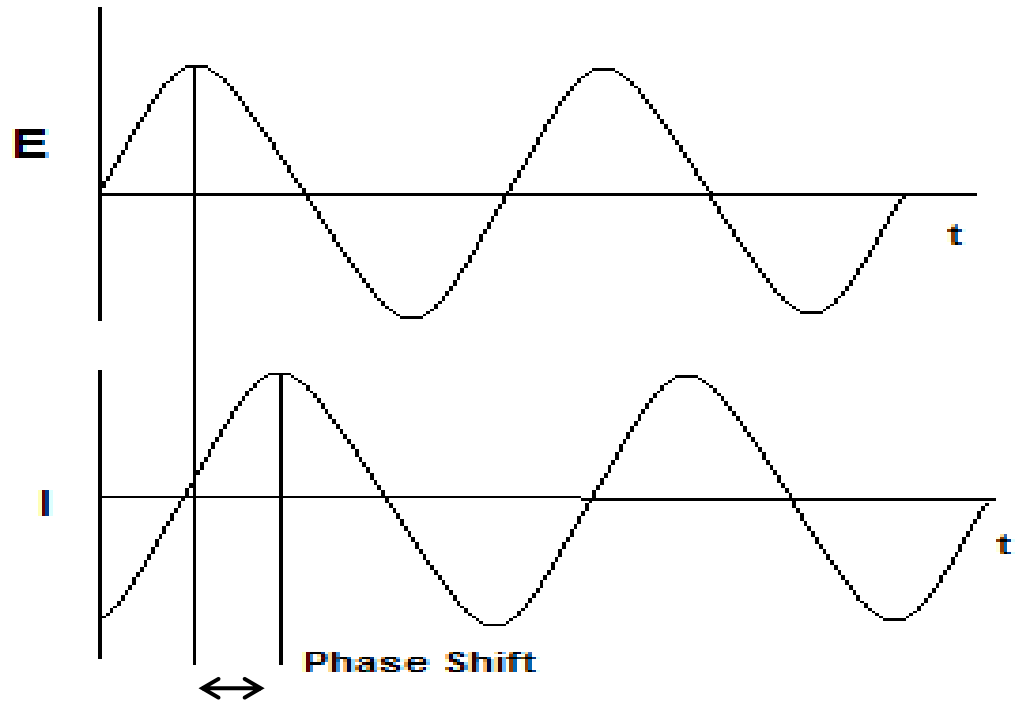

Figure 1.8: Schematic of sinusoidal applied potential and the current response as a function of time, displaying the phase shift.

1.3.2.2 EIS in Biosensing

Various strategies are used to design impedimetric biosensors, such as forming functional groups on the surface of the electrode, physical entrapment of the biomolecules, and layer by layer assembly; these methods are all used in various different impedimetric biosensors.

Impedimetric biosensors can be divided into four main groups based on the biorecognition / immobilization process. The main groups would be antibody-antigen based biosensors,[61-63] aptamer based biosensors,[64-66] cell-based biosensors,[67-69] and enzyme based biosensors.[70,71]

As previously mentioned, electrochemical nucleic acid biosensors can provide sensitive and inexpensive detection for complex samples. In impedimetric nucleic acid sensors, changes in current, resistance or impedance following the binding of a target sequences, conformational changes or DNA damages can be monitored.

Zhang et al[72] have recently described a label-free impedimetric biosensor for detection of DNA sequence and used an adjunct probe to amplify the EIS signal. Figure 1.9 shows a schematic diagram of the biosensor. The adjunct probe is a thiol terminated DNA strand with 14 bases that functions as a fixer to immobilise the dissociative element of the reporter probe to form loop structure. When the target sequence is exposed to this surface, the target DNA displaces the reporter probe; the adjunct probe can then immobilise this element of the reporter probe, bending the reporter probe so it collides with the electrode surface and effectively blocks the charge transfer. An increase in R_{ct} was observed in the presence of the adjunct probe that was more than ten times that of the R_{ct} without the adjunct probe due to the increased steric hindrance on the electrode and blocking of the charge transfer. Displayed in Figure 1.10 are the overlaid Nyquist plots of varying concentrations of the target DNA strand, showing how the R_{ct} values depend on the concentration of target. The inset shows a dynamic range from 0.1 nM to 0.5 M with an R^2 of 0.9972. The limit of detection was determined to be 6.3 pM. This biosensor

was shown also to be selective and could discriminate against interferences. It could also be used for different DNA or RNA target strand sequences, by using complementary adjunct and reporter probe sequences.

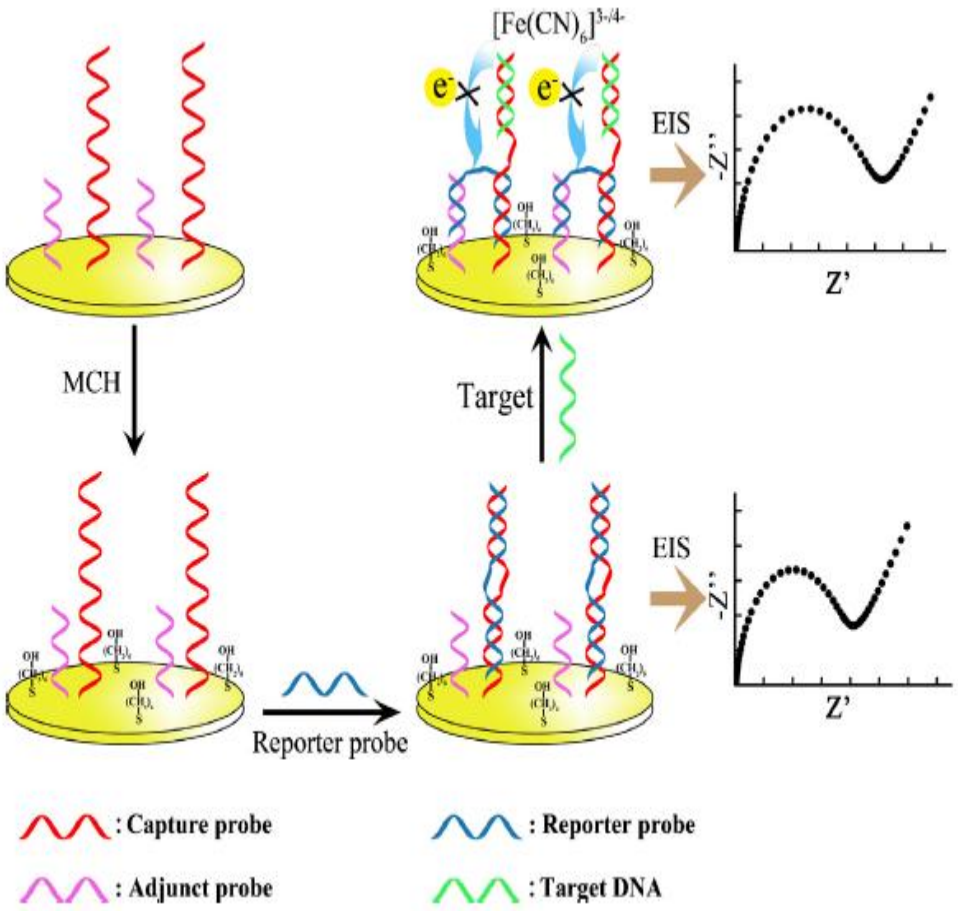

Figure 1.9: A schematic illustration of using an adjunct probe for sensitive and label-free electrochemical impedance spectroscopy detection of DNA sequence. *[Reproduced from ref 72:* Zhang, X. Y.; Zhou, L. Y.; Luo, H. Q.; Li, N. B. *Anal. Chim. Acta* **2013***, 776*, 11-16.*]*

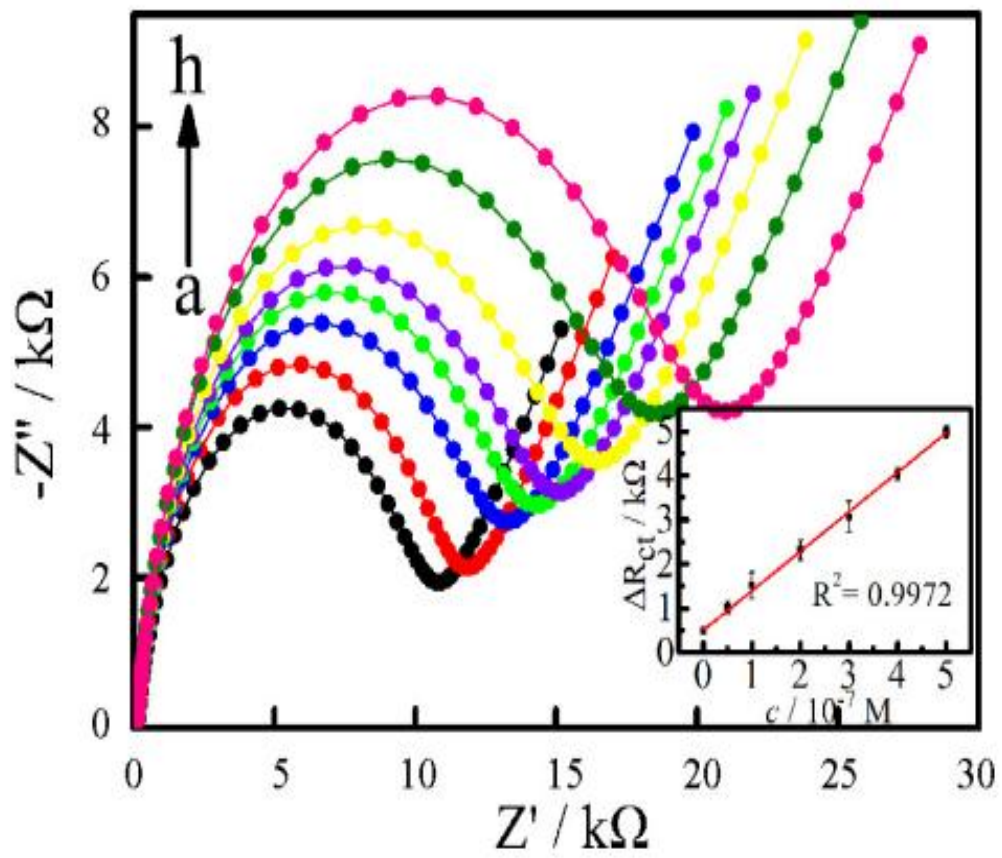

Figure 1.10: Nyquist diagrams for the sensor incubated with different concentrations of target DNA (a–h): (a) blank (0 nM target), (b) 0.1 nM, (c) 50 nM, (d) 0.1 M, (e) 0.2 M, (f) 0.3 M, (g) 0.4 M, and (h) 0.5 M. Inset: the resulting calibration curve of c vs. Rct for the target DNA over the range of 0.1 nM–0.5 M. Error bars represent the standard deviation of three replicates. *[Reproduced from ref 72:* Zhang, X. Y.; Zhou, L. Y.; Luo, H. Q.; Li, N. B. *Anal. Chim. Acta* **2013***, 776*, 11-16.*]*

Wang et al[73] have developed a sequence-specific and ultrasensitive sandwich impedimetric DNA sensor. Gold nanoparticles are used as a signal enhancer in this instance, along with a hairpin DNA probe. The hairpin probe is self-assembled onto the electrode; when it is exposed to the target strand, the hairpin opens. The remaining stem of this hairpin is then labelled with the reporter DNA / gold nanoparticles, forming the sandwich system. The reporter DNA – gold nanoparticle conjugates were used as the seeds for their catalytic enlargement in a growth solution containing a negatively charged surfactant. The electrode surface became more negatively charged after this, and therefore more significant amplification was achieved due to the surface exerting an electrostatic repulsive force against the redox probe in the electrolyte. Displayed in Figure 1.11 are Nyquist plots, showing the increase R_{ct} response to increasing target DNA concentrations. The detection limit for this system was determined to be 30 aM. The system is also selective to base mismatches and non-complementary targets, showing how this is also a promising biosensor for impedimetric nucleic acid detection.

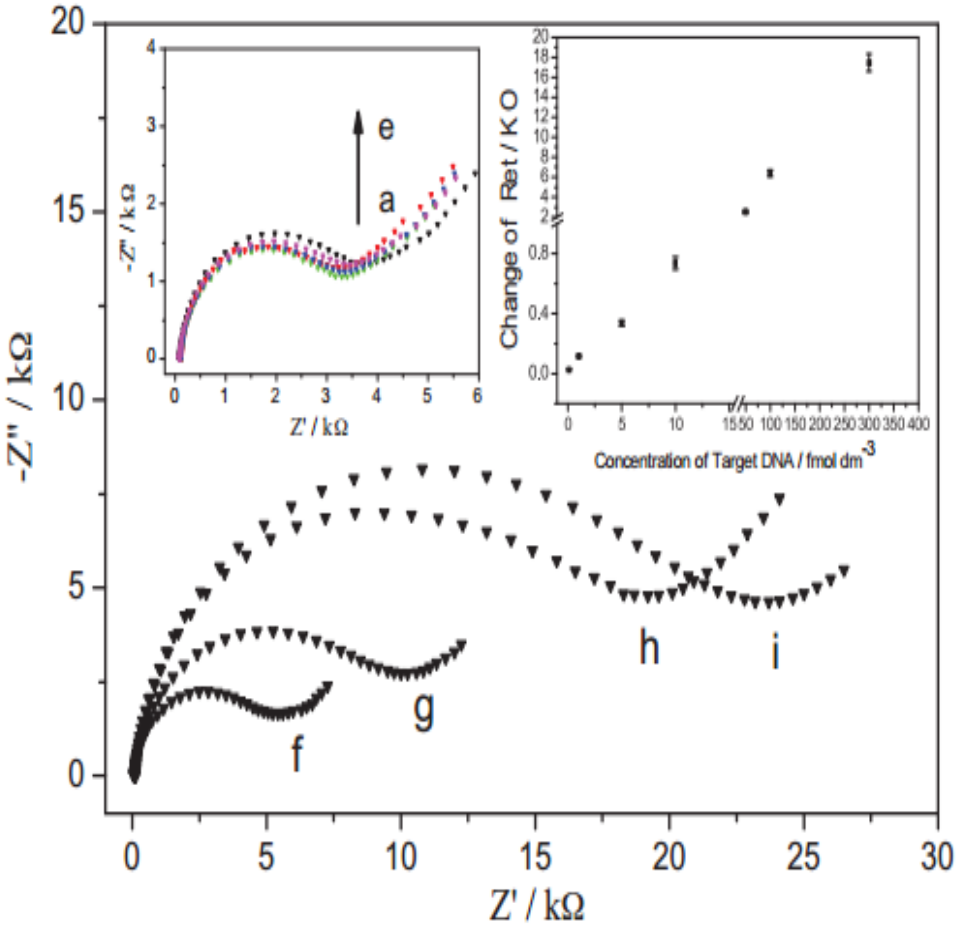

Figure 1.11: Nyquist plots of the impedance spectra obtained by the DNA sensor after incubation in different concentrations of complementary target DNA and signal amplification. (a) 0 fM; (b) 0.1 fM; (c) 1 fM; (d) 5 fM; (e) 10 fM; (f) 50 fM; (g) 100 fM; (h) 300 fM and (i) 500 fM. *[Reproduced from ref 73:* Wang, W.; Yuan, X.; Zhang, W.; Gao, Q.; Qi, H.; Zhang, C. *Electrochim. Acta* **2012**, *78*, 377-383.*]*

1.4 MICROFLUIDIC BIOSENSORS

Standard methods of biomarker detection involve often time consuming, laborious methods that require specific training, such as cell culture, nucleic acid amplification and enzyme linked immunoassays. The number of deaths attributed to preventable or treatable causes could be severely reduced by improving diagnosis to allow for a rapid and accurate diagnosis, so treatment can begin sooner.[74]

Microfluidic-based diagnosis devices are on-chip sensing platforms that require only a small amount of bodily fluid and can be used for diagnosis and real-time monitoring of biomarkers.[75] Microfluidic devices have the ability to analyse a diverse range of clinical samples, such as blood, urine and saliva.

There are many different types of microfluidic biosensors, usually categorised according to the way the fluid is transported inside the device.[76] These can primarily be divided into two categories; passive flow approaches and active flow approaches. Passive flow approaches require little instrumentation to function and for this reason they can easily be made inexpensive and portable. Examples of passive flow approaches include osmotic flow,[77] surface tension[78] and capillary force.[79] Active flow approaches reply on fluid handling forces such as pressure driven flow,[80] electrical force[81] and centrifugal force.[82]

A huge advantage of microfluidic devices for detection is that many different biomarkers can be detected. These types of biomarkers vary and include bacteria,[83] viruses,[80,84] proteins,[85] cells[86,87] and nucleic acids. As the main focus of this work is on the detection of nucleic acids, this will primarily be explored here.

1.4.1 Nucleic Acid Detection in Microfluidic Device

There are many advantages to carrying out nucleic acid amplification in microfluidic devices such as faster reaction times, disposability, compactness, smaller sample and reagent sizes, and the ability to integrate with other devices or instrumentation for analysis.[88] There are numerous microfluidic devices that demonstrate the nucleic acid amplification step inside the device. Common amplification methods used in a microfluidic device include PCR,[89] NASBA,[90] LAMP[91] and RCA.[92]

PCR is an enzyme-driven, non-isothermal nucleic acid amplification technique that involves three different reactions during the amplification process; denaturing, annealing and extension. These steps are easily controlled through thermal cycling, as each step occurs at a different temperature. Reverse-Transcriptase PCR (RT-PCR) is a variation of the PCR technique that is more suitable for target RNA detection.[88] This involved isolating the target RNA from the sample, and then reverse transcriptase is used to produce complementary DNA. The target is then amplified via PCR.

The microfluidics work in this thesis is based on centrifugal force as the fluid transportation method. Centrifugal microfluidics is a suitable technique for fully integrated devices due to having simple interfaces and only requiring a single actuator. They also have the potential for complete point-of-care systems, by allowing prestorage of the reagents. Recently, Stumpf et al[93] have presented a complete sample-to-answer nucleic acid based detection LabDisk for detection of influenza A H3N2. This is the first demonstration of a fully automated sample-to-answer centrifugal microfluidic disc, comprising of the pre-storage of all of the required reagents. The layout of the disc is displayed and explained in Figure 1.12.

Supply of the sample into the LabDisk is the only manual handling step. Included in the disc is RNA extraction via chemical lysis and a bind-wash-elute protocol, based on transport of silica coated magnetic particles. The eluate is pumped to the structure via centrifuge-dynamic inward pumping. RT-PCR is

then performed on the extracted RNA. All of the required reagents are pre-stored, either as dry reagents or as liquid reagents using miniature stick-packs. The processing of the LabDisk was conducted on a LabDisk player that includes the PCR-thermocycling, fluorescence detection and controls the rotational frequencies. This processing device is suitable for operation at the point-of-care due to its small size (15 cm x 18 cm x 28 cm) and light weight (2 kg).

The detection method for this device is optical fluorescence. Shown in Figure 1.13 are the normalized fluorescence signals for the three different concentrations investigated. The concentration detected in this study is approximately four-fold lower than the range of clinical relevance described in literature; therefore sufficient sensitivity is achieved. The total turnaround time for complete analysis is reported to be less than 3.5 hours.

While this work is very impressive and is a huge step forward in point-of-care diagnostics, only three different concentrations were tested. In order to improve this detection method further, more concentrations should be tested to obtain a full assay with a range of concentrations for influenza A H3N2. While the concentrations tested here are lower than the range of clinical relevance for this virus, having a lower LOD for this device could mean earlier detection, which is something to consider in future work on this device. However, this system is extremely relevant in the detection of pathogens, as it is quick, portable, and requires minimal, user-friendly steps, as the only manual handling is the initial sample injection.

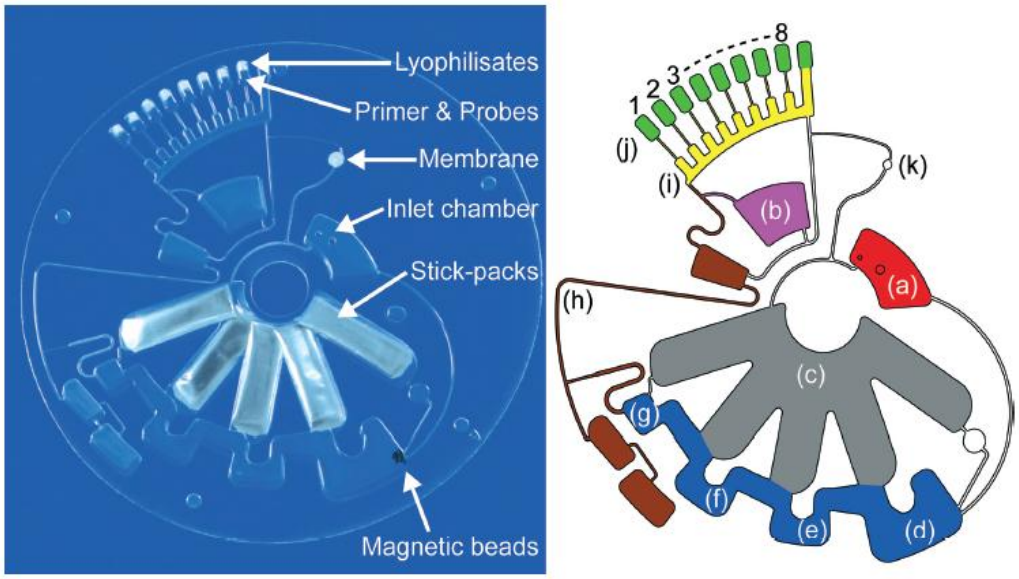

Figure 1.12: Photograph (left) of the LabDisk for sample-to-answer nucleic acid based detection of respiratory pathogens with complete reagents prestorage and a CAD drawing (right) of the microfluidic structure. The sample is supplied into the inlet chamber (a) while liquid reagents are prestored in stick packs and placed therein into the overlapping stick-pack chambers (c) which are connected to the Teflon coated nucleic acid extraction structure (d-g) consisting of the lysis and binding chamber (d) wherein the magnetic beads are prestored, the washing chamber (e) and 2 (f) and the eluate chamber (g). The microfluidic channels and pneumatic chambers in the area of (h) are used for inward pumping of the eluate into the aliquoting structure (i) and transferred subsequently to the reaction cavities (j). Primers and fluorescence probes are prestored in the reaction cavities as well as the RT-PCR lyophilisates. For optional reagent addition during the development phase of the LabDisk, chamber (b) was implemented. It can be used e.g. for loading a liquid RT-PCR mastermix instead of lyophilisates. The air vent (k) is covered by a hydrophobic membrane prohibiting contamination by aerosol dissemination. *[Reproduced from ref 93:* Stumpf, F.; Schwemmer, F.; Hutzenlaub, T.; Baumann, D.; Strohmeier, O.; Dingemanns, G.; Simons, G.; Sager, C.; Plobner, L.; von Stetten, F.; Zengerle, R.; Mark, D. *Lab Chip* **2016***, 16*, 199-207.*]*

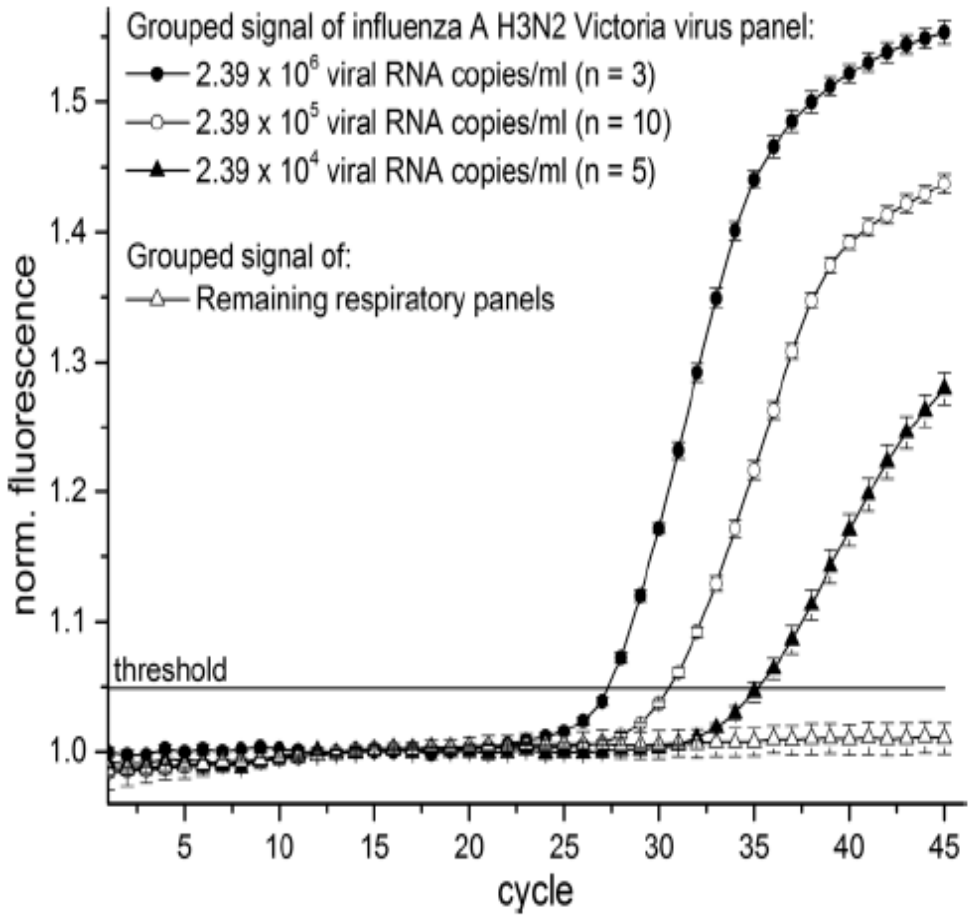

Figure 1.13: Combined fluorescence signals of 18 individual LabDisk experiments with different influenza A H3N2 virus concentrations. *[Reproduced from ref 93:* Stumpf, F.; Schwemmer, F.; Hutzenlaub, T.; Baumann, D.; Strohmeier, O.; Dingemanns, G.; Simons, G.; Sager, C.; Plobner, L.; von Stetten, F.; Zengerle, R.; Mark, D. *Lab Chip* **2016***, 16*, 199-207.*]*

There have also been reports of detecting nucleic acids inside microfluidic devices, without using an amplification process prior to detection, although these are less common.[94-97] This could be due to the fact that often the target nucleic acid is being detected is in such a low concentration in the sample and the detection method is not sensitive enough to pick up the low concentrations. Therefore, an amplification method is necessary.

Goral et al reported an electrochemical microfluidic biosensor that detected DNA associated with Dengue virus.[97] Used in this study were interdigitated ultramicroelectrode arrays with a PDMS microfluidic device. The sequences are detected via hybridisation to two DNA oligonucleotides, one of which is immobilised on a superparamagnetic bead captured on a magnet; the other is labelled with a liposome that has entrapped potassium ferro/ferricyanide. Therefore, the concentration of DNA molecules present is directly proportional to the number of liposomes captured. The liposomes are then lysed so the electrochemical markers are released and can therefore be detected at the interdigitated ultramicroelectrode arrays that are downstream in the device.

Shown in Figure 1.14 is the response curve of varying concentrations of DNA vs the area of the current peak associated with that concentration. The limit of detection was determined to be 1 fmol of DNA, with a dynamic range between 1 fmol and 50 fmol of DNA per assay. A simplified two electrode system is used, which requires only a simple potentiostat for signal detection which could easily be miniaturised into a hand-held unit for potential point-of-care diagnostics. The overall assay was completed in 6 minutes, with an extra 15-20 minutes of pre-incubation, which is another advantage for diagnostics, as it gives a rapid response.

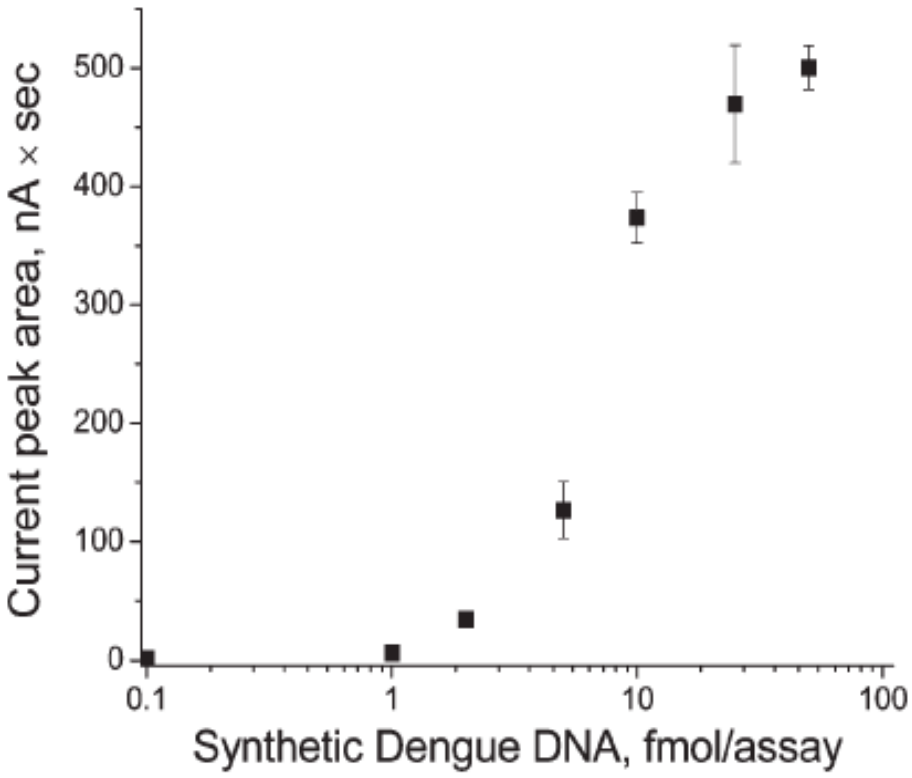

Figure 1.14: Dose response curve for synthetic Dengue virus DNA. Analyses were done in triplicate and the peak area is reported. *[Reproduced from ref 97:* Goral, V.; Zaytseva, N.; Baeumner, A. *Lab Chip* **2006***, 6*, 414-421*.]*

1.5 METAL NANOPARTICLES

1.5.1 Platinum Nanoparticles

As discussed in previous sections, platinum is electrocatalytic and can catalyse the reduction of peroxide, resulting in an amplified current. This can be used in biosensing applications as demonstrated above, by immobilizing a biomarker onto the nanoparticle and measuring the catalytic current; as the signal generated is proportional to the amount of nanoparticles present, and the amount of nanoparticles present is proportional to the amount of target analyte. In this way, a calibration curve can be achieved.[98-100]

There are many methods of preparing metal nanoparticles.[101] This work focusses on electrodeposition. Electrodeposition is the process whereby a potential difference is applied to an electrode at an electrolyte interface resulting in electron transfer between the electrode and the electrolyte, therefore causing the deposition of atoms in the electrolyte onto the electrode surface. There are many advantages of electrodeposition over other methods such as[102]:

- High rate of deposition;
- High shape stability;
- Low cost;
- Clean method;
- Can deposit onto a broad range of materials;
- Can be performed at room temperature.

1.5.1.1 Control of Platinum Nanoparticle Deposition

In order to produce an optimized electrocatalytic surfaces, the nanoparticles must be produced in a controlled manner, so that the size and surface coverage of the particles can be accurately controlled. By separating the nucleation and growth steps of the electrodeposition process, it has been demonstrated that it is possible to control the size of the nanoparticles formed.[101,103-105] Penner et al have developed this method by applying different potentiostatic pulses for the nucleation and growth steps, for different lengths of time.[106-109] This method involves applying a high overpotential nucleation pulse for a very short period, followed by the growth pulse at a lower overpotential for a longer period. This allows the surface of the electrode to become seeded with the nuclei of the nanoparticles, and then it is these nuclei that are subsequently grown during the growth pulse.

An example of Penner's work is shown in Figure 1.15; here silver nanoparticles are deposited onto highly orientated pyrolytic graphite, using a silver plating solution containing 1mM $AgClO_4$ with a supporting electrolyte of 0.1 M $LiClO_4$ in acetonitrile.[106] The double pulse method is used to grow the silver nanoparticles. Firstly, a nucleation pulse potential was applied for 5 ms followed by a -70 mV deposition potential ranging from 500 ms to 120 s. What is clear from these images is the difference in size and density of the nanoparticles. In comparison to silver nanoparticles grown at just -400 mV or -500 mV for 150 ms, the nanoparticles grown using the double pulse method are more narrowly dispersed in diameter, and also the density is 1 – 3 orders of magnitude lower. The smallest particles grown here were 240 nm in diameter, but by shortening the growth time down to 50 ms, smaller particles were obtained, down to 42 nm in diameter. Penner's group have also had great success in using this method to grow nanoparticles of different metals, such as molybdenum dioxide, cadmium, copper, nickel, gold and platinum.[107]

The purpose of separating the nucleation and growth phases of the electrodeposition is to eliminate progressive nucleation. Progressive nucleation means that there is continuous nucleation onto the surface that the nanoparticles are created throughout the entire deposition process; this

therefore means that the nanoparticles are grown at different rates, to different sizes, causing size polydispersity.

Progressive nucleation can be caused also by diffusion zone coupling. Surrounding each nucleus after deposition is a depletion layer; this is an area where the volume of the electrolyte has a lower concentration of metal ions than in the bulk electrolyte, due to the deposition. When diffusion zone coupling occurs, the depletion layers of two or more nuclei join together and therefore the supply of metal ions to these nuclei will be slower in comparison to uncoupled nuclei, resulting in size polydispersity. Elimination of the diffusion zone coupling should improve size monodispersity. The expansion of the depletion zone is a function of the rate of particle growth; the faster the growth time, the faster the uptake of metal ions by the nucleus and hence, the faster the expansion of the depletion zone. Therefore, by using a shorter growth time, along with a lower overpotential, there is less expansion of the depletion zone and therefore less diffusion zone coupling. This means that there is less polydispersity and a greater uniformity in the size of the deposited nanoparticles.[108]

What Penner has also reported from these results is that the fraction of the nucleated silver nanoparticles that grow further into larger silver nanoparticles depends on the growth potential used. Even when large growth potentials were used, still only 1 in 10 of the nucleated nanoparticles grew to larger particles. This has also been observed and explained by Plieth et al.[110,111] It occurs due to gas evolution at large over potentials, along with the stability of the nanoparticles deposited. Only the larger particles deposited are stable enough to survive the growth step when some potentials are used.

Hence, it is clear that many parameters are involved in the deposition of metal nanoparticles. Both the deposition time and potential(s) are intrinsically involved in the size, shape and density of the deposited nanoparticles, and need to be carefully considered prior to growing the nanoparticles. However, this means that the nanoparticles can be tailored to the size and density that is required for further application, by just changing the deposition times, potentials for the nucleation or the growth pulses.

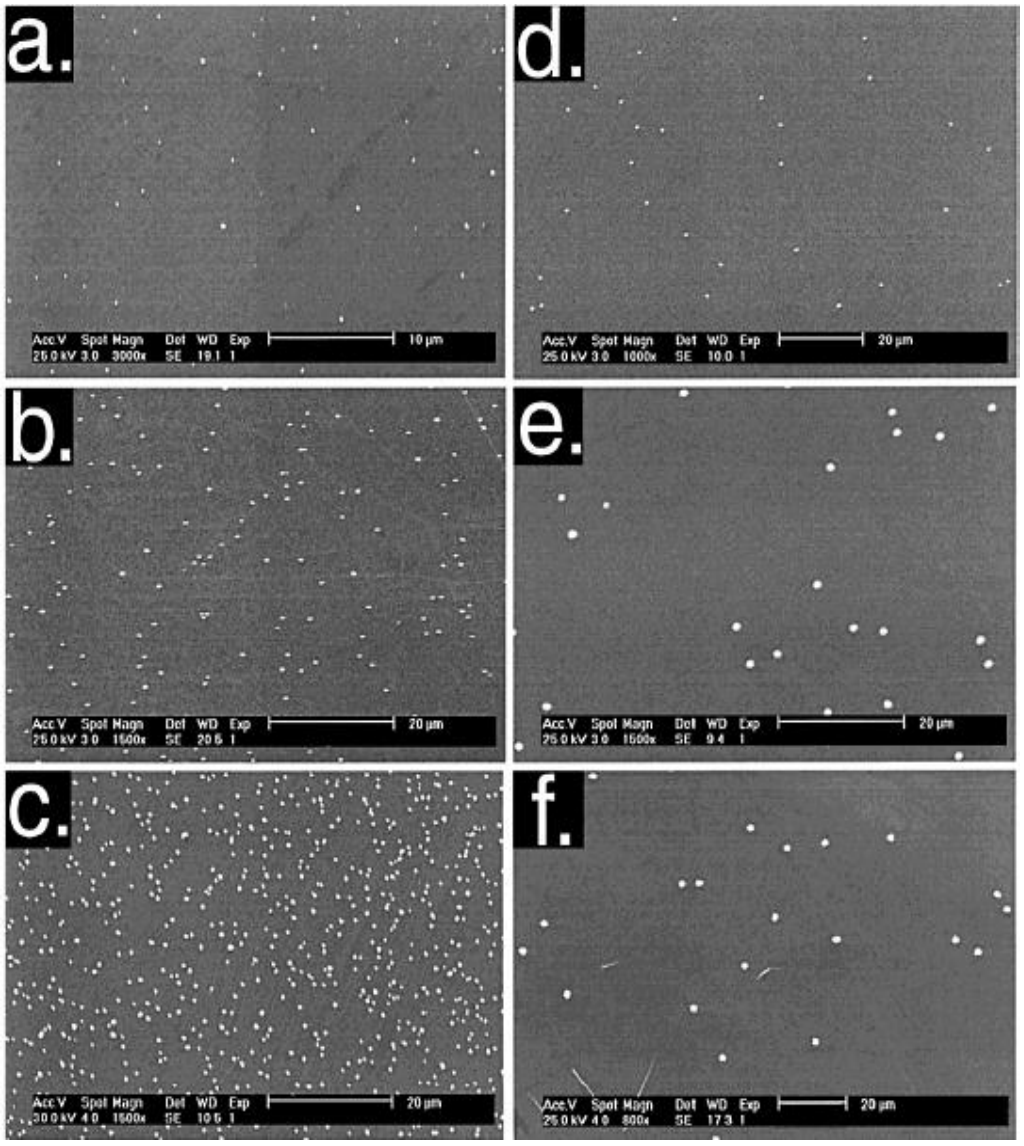

Figure 1.15: Scanning electron micrographs of silver particles deposited onto highly orientated pyrolytic graphite using a plating solution of 1 mM $AgClO_4$ in 0.1 M $LiClO_4$ in ACN. A nucleation pulse was applied for 5 ms at -500 mV, followed by a deposition potential of -70 mV applied for durations of (a) 500 ms, (b) 1 s, (c) 5 s, (d) 10 s, (e) 30 s and (f) 120 s. *[Reproduced from ref 106:* Liu, H.; Penner, R. *J Phys Chem B* **2000***, 104*, 9131-9139*.]*

1.5.2 Silver Nanoparticles

Silver is another noble metal that is electrocatalytic towards the reduction of hydrogen peroxide.[112-114] Silver nanoparticles can be used in a similar way as mentioned above, for biosensing applications to detect target analytes.

Silver also has the advantage of its optical properties. Silver is SERS (Surface Enhanced Raman Spectroscopy) active.[115,116] SERS is a technique that provides great enhancement of the Raman signal for Raman-active analytes that have been immobilised onto nanostructured metal surfaces. In some instances, the Raman signal has been increased with an enhancement factor up to 10^{14}.[117] The importance of SERS is that it is both surface selective and highly sensitive, whereas Raman spectroscopy is not. SERS is selective to the surface signal, and not that of the bulk material; it can selectively enhance the signal of the analyte on the surface, making it more sensitive to Raman spectroscopy, where the signal from the bulk material can overwhelm the signal coming from the surface analyte. This means that SERS active nanoparticles can be used in biosensing applications also.[118,119]

1.5.2.1 Tuneable Silver Nanoparticle Shapes

By controlling the shape of the silver nanoparticles, the properties of the nanoparticle can be controlled. There are many ways to synthesis triangular silver nanoparticles, such as photoinduced method,[120] seed-mediated approach[121] and nanosphere lithography.[122]

The SERS properties of triangular silver nanoparticles have been utilized for sensing and imaging of lung cancer cells.[123] Potara et al have coated triangular silver nanoplates with chitosan, which are then labelled with para-aminothiophenol (p-ATP). The triangular silver nanoplates are used in this instance as Raman scattering enhancers, which yield a reproducible and

strong SERS signal. A strong, distinct SERS signal was produced under a wide range of excitation wavelengths, which overcomes the limited range possible with spherical nanoparticles.[124] They also have low toxicity to the cells and don't interfere with cell proliferation. These results are promising and open up more functions for triangular silver nanoplates, such as for cell imaging and as an imaging probe for the integration of a therapeutic agent.

Another advantage of using triangular shaped silver nanoparticles is that they have unique optical properties that can be tailored to many different biosensing opportunities.[125,126] In SERS, "hotspots" are created between the nanoparticles to produce intense electromagnetic fields that increase the Raman intensity of the molecules located in these regions. When triangular silver nanoplates are used, these hotspots occur at the edges or at the tips of the triangles, and therefore they can operate individually as a highly sensitive SERS substrate. These hotspots can be utilised by controlling the distance between nanoparticles, or between the nanoparticle and surface to overlap these electromagnetic fields in order to obtain the greatest enhancement.[127,128]

1.6 CONCLUSION AND THESIS OUTLINE

As detailed above, the robust, low cost detection and quantitation of nucleic acid sequences or specific mutations requires highly sensitive and specific detection strategies in order to detect the diseases before any clinical symptoms appear, for increased treatment and prognosis. Nucleic acid (DNA and RNA) strands are simple molecules that can be important biomarkers of diseases and can be found in all body fluids. An increased emphasis is now being placed on point-of-care diagnostics, which can determine the concentration of these biomarkers in real world samples, e.g., plasma or even whole blood. These point-of-care devices need to be inexpensive, simple to use by an untrained person, quick, and with limited instrumentation.

In this review, various biosensors that detect nucleic acids have been described. Metal nanoparticles are used as a method of increasing the signal and therefore the sensitivity of the biosensors. Nobel metal nanoparticles are electrocatalytic towards the reduction of hydrogen peroxide; therefore if they are brought to the electrode surface via target nucleic acid hybridisation, the signal achieved from the electrocatalysis would correlate to the amount of nanoparticles present on the surface, and hence, the concentration of target analyte. Another advantage of using nanoparticles is to increase the surface area, which gives a high local concentration of binding sites and also gives more surface area for the electrocatalytic activity to occur.

In Chapter 3, the synthesis of regioselectively functionalised nanoparticles is reported. A double pulse potential electrodeposition method is used in order to control the growth of these nanoparticles to achieve size monodispersity. The platinum nanoparticles are templated also, in order to regioselectively functionalise them with nucleic acid strands prior to desorption. This allows the underside of the nanoparticle to remain clean, unmodified and available for efficient electrocatalysis.

The application of these nanoparticles in a DNA assay is described in Chapter 4, using electrocatalysis as the detection method. A range of concentrations of

target DNA was immobilised onto a gold electrode via capture strand hybridisation; the platinum nanoparticles were brought to the surface of the electrode via complementary probe strand hybridisation and the catalytic activity was measured after the injection of hydrogen peroxide.

Chapter 5 furthers this electrocatalytic assay, by incorporating the detection into a microfluidic disc. The nucleic acid strands are pre-loaded into the device and each chamber is triggered to release after a certain event, to allow each hybridisation step to occur sequentially.

The electrocatalytic activity of silver nanoparticles is reported in Chapter 6. As silver nanoparticles have unique optical properties, the nanoparticles are also immobilised in gold microcavities, via nucleic acid hybridisation, to investigate the plasmonic properties.

A major overall objective of this work is to achieve ultrasensitive detection of nucleic acid sequences that are associated with different diseases. This is achieved by using electrocatalytic metal nanoparticles to amplify the signal and sensitivity of the detection methods, allowing low concentrations to be determined leading to earlier diagnosis. This approach also negates the need for target analyte amplification and therefore requires less time for a diagnosis.

1.7 REFERENCES

1. Chen, J.; Miao, Y.; He, N.; Wu, X.; Li, S. Nanotechnology and biosensors. *Biotechnol. Adv.* **2004***, 22*, 505-518.

2. Wang, J. Electrochemical nucleic acid biosensors. *Anal. Chim. Acta* **2002***, 469*, 63-71.

3. Drummond, T.; Hill, M.; Barton, J. Electrochemical DNA sensors. *Nat. Biotechnol.* **2003***, 21*, 1192-1199.

4. Odenthal, K. J.; Gooding, J. J. An introduction to electrochemical DNA biosensors. *Analyst* **2007***, 132*, 603-610.

5. Pohanka, M.; Skladai, P. Electrochemical biosensors - principles and applications. *J. Appl. Biomed.* **2008***, 6*, 57-64.

6. Wei, D.; Bailey, M. J. A.; Andrew, P.; Ryhaenen, T. Electrochemical biosensors at the nanoscale. *Lab Chip* **2009***, 9*, 2123-2131.

7. Wang, J. Electrochemical biosensors: Towards point-of-care cancer diagnostics. *Biosens. Bioelectron.* **2006***, 21*, 1887-1892.

8. Wang, J. Amperometric biosensors for clinical and therapeutic drug monitoring: a review. *J. Pharm. Biomed. Anal.* **1999***, 19*, 47-53.

9. Gooding, J. Electrochemical DNA Hybridization Biosensors. *Electroanalysis* **2002***, 14*, 1149-1156.

10. Wang, J. Nanomaterial-based electrochemical biosensors. *Analyst* **2005***, 130*, 421-426.

11. Dolatabadi, J. E. N.; Mashinchian, O.; Ayoubi, B.; Jamali, A. A.; Mobed, A.; Losic, D.; Omidi, Y.; de la Guardia, M. Optical and electrochemical DNA nanobiosensors. *Trac-Trends Anal. Chem.* **2011***, 30*, 459-472.

12. Alivisatos, P. The use of nanocrystals in biological detection. *Nat. Biotechnol.* **2004***, 22*, 47-52.

13. Wang, J. Nanoparticle-based electrochemical DNA detection. *Anal. Chim. Acta* **2003***, 500*, 247-257.

14. Ghosh, A.; Bansal, M. A glossary of DNA structures from A to Z. *Acta Crystallogr. Sect. D-Biol. Crystallogr.* **2003***, 59*, 620-626.

15. Watson, J.; Crick, F. Molecular Structure of Nucleic Acids - a Structure for Deoxyribose Nucleic Acid. *Nature* **1953***, 171*, 737-738.

16. Yakovchuk, P.; Protozanova, E.; Frank-Kamenetskii, M. Base-stacking and base-pairing contributions into thermal stability of the DNA double helix. *Nucleic Acids Res.* **2006***, 34*, 564-574.

17. McMurray, C. DNA secondary structure: A common and causative factor for expansion in human disease. *Proc. Natl. Acad. Sci. U. S. A.* **1999***, 96*, 1823-1825.

18. Shiloh, Y. ATM and related protein kinases: Safeguarding genome integrity. *Nat. Rev. Cancer* **2003***, 3*, 155-168.

19. Khanna, K.; Jackson, S. DNA double-strand breaks: signaling, repair and the cancer connection. *Nat. Genet.* **2001***, 27*, 247-254.

20. Jackson, S. P.; Bartek, J. The DNA-damage response in human biology and disease. *Nature* **2009***, 461*, 1071-1078.

21. Lindahl, T. Instability and Decay of the Primary Structure of Dna. *Nature* **1993***, 362*, 709-715.

22. Sancar, A.; Lindsey-Boltz, L.; Unsal-Kacmaz, K.; Linn, S. Molecular mechanisms of mammalian DNA repair and the DNA damage checkpoints. *Annu. Rev. Biochem.* **2004***, 73*, 39-85.

23. Etheridge, A.; Lee, I.; Hood, L.; Galas, D.; Wang, K. Extracellular microRNA: A new source of biomarkers. *Mutat. Res. -Fundam. Mol. Mech. Mutag.* **2011***, 717*, 85-90.

24. Nirenber. M.; Leder, P.; Bernfiel. M.; Brimacom, R.; Trupin, J.; Rottman, F.; ONeal, C. Rna Codewords and Protein Synthesis .7. on General Nature of Rna Code. *Proc. Natl. Acad. Sci. U. S. A.* **1965***, 53*, 1161-&.

25. Guttman, M.; Amit, I.; Garber, M.; French, C.; Lin, M. F.; Feldser, D.; Huarte, M.; Zuk, O.; Carey, B. W.; Cassady, J. P.; Cabili, M. N.; Jaenisch, R.; Mikkelsen, T. S.; Jacks, T.; Hacohen, N.; Bernstein, B. E.; Kellis, M.; Regev, A.; Rinn, J. L.; Lander, E. S. Chromatin signature reveals over a thousand highly conserved large non-coding RNAs in mammals. *Nature* **2009***, 458*, 223-227.

26. Mitchell, P. S.; Parkin, R. K.; Kroh, E. M.; Fritz, B. R.; Wyman, S. K.; Pogosova-Agadjanyan, E. L.; Peterson, A.; Noteboom, J.; O'Briant, K. C.; Allen, A.; Lin, D. W.; Urban, N.; Drescher, C. W.; Knudsen, B. S.; Stirewalt, D. L.; Gentleman, R.; Vessella, R. L.; Nelson, P. S.; Martin, D. B.; Tewari, M. Circulating microRNAs as stable blood-based markers for cancer detection. *Proc. Natl. Acad. Sci. U. S. A.* **2008***, 105*, 10513-10518.

27. Vaca, L. Point-of-care Diagnostic Tools to Detect Circulating MicroRNAS as Biomarkers of Disease. *Sensors* **2014***, 14*, 9117-9131.

28. Gorkin, R.; Park, J.; Siegrist, J.; Amasia, M.; Lee, B. S.; Park, J.; Kim, J.; Kim, H.; Madou, M.; Cho, Y. Centrifugal microfluidics for biomedical applications. *Lab Chip* **2010***, 10*, 1758-1773.

29. Voller, A.; Bidwell, D.; Bartlett, A. Enzyme Immunoassays in Diagnostic Medicine - Theory and Practice. *Bull. World Health Organ.* **1976***, 53*, 55-65.

30. Notomi, T.; Mori, Y.; Tomita, N.; Kanda, H. Loop-mediated isothermal amplification (LAMP): principle, features, and future prospects. *J. Microbiol.* **2015***, 53*, 1-5.

31. Song, W.; Zhang, Q.; Sun, W. Ultrasensitive detection of nucleic acids by template enhanced hybridization followed by rolling circle amplification and catalytic hairpin assembly. *Chem. Commun.* **2015***, 51*, 2392-2395.

32. Peter, C.; Meusel, M.; Grawe, F.; Katerkamp, A.; Cammann, K.; Borchers, T. Optical DNA-sensor chip for real-time detection of hybridization events. *Fresenius J. Anal. Chem.* **2001***, 371*, 120-127.

33. Wang, J.; Cai, X.; Rivas, G.; Shiraishi, H.; Farias, P.; Dontha, N. DNA electrochemical biosensor for the detection of short DNA sequences related to the human immunodeficiency virus. *Anal. Chem.* **1996***, 68*, 2629-2634.

34. Palecek, E.; Billova, S.; Havran, L.; Kizek, R.; Miculkova, A.; Jelen, F. DNA hybridization at microbeads with cathodic stripping voltammetric detection. *Talanta* **2002***, 56*, 919-930.

35. Palecek, E.; Kizek, R.; Havran, L.; Billova, S.; Fojta, M. Electrochemical enzyme-linked immunoassay in a DNA hybridization sensor. *Anal. Chim. Acta* **2002***, 469*, 73-83.

36. Kushon, S.; Ley, K.; Bradford, K.; Jones, R.; McBranch, D.; Whitten, D. Detection of DNA hybridization via fluorescent polymer superquenching. *Langmuir* **2002***, 18*, 7245-7249.

37. Beck, S.; OKeeffe, T.; Coull, J.; Koster, H. Chemi-Luminescent Detection of Dna - Application for Dna Sequencing and Hybridization. *Nucleic Acids Res.* **1989***, 17*, 5115-5123.

38. Gabl, R.; Feucht, H.; Zeininger, H.; Eckstein, G.; Schreiter, M.; Primig, R.; Pitzer, D.; Wersing, W. First results on label-free detection of DNA and protein molecules using a novel integrated sensor technology based on gravimetric detection principles. *Biosens. Bioelectron.* **2004***, 19*, 615-620.

39. Nam, J.; Stoeva, S.; Mirkin, C. Bio-bar-code-based DNA detection with PCR-like sensitivity. *J. Am. Chem. Soc.* **2004***, 126*, 5932-5933.

40. Cai, H.; Cao, X.; Jiang, Y.; He, P.; Fang, Y. Carbon nanotube-enhanced electrochemical DNA biosensor for DNA hybridization detection. *Anal. Bioanal. Chem.* **2003***, 375*, 287-293.

41. Napier, M.; Loomis, C.; Sistare, M.; Kim, J.; Eckhardt, A.; Thorp, H. Probing biomolecule recognition with electron transfer: Electrochemical sensors for DNA hybridization. *Bioconjug. Chem.* **1997***, 8*, 906-913.

42. Campbell, C.; Gal, D.; Cristler, N.; Banditrat, C.; Heller, A. Enzyme-amplified amperometric sandwich test for RNA and DNA. *Anal. Chem.* **2002***, 74*, 158-162.

43. Cai, H.; Wang, Y.; He, P.; Fang, Y. Electrochemical detection of DNA hybridization based on silver-enhanced gold nanoparticle label. *Anal. Chim. Acta* **2002***, 469*, 165-172.

44. Kerman, K.; Kobayashi, M.; Tamiya, E. Recent trends in electrochemical DNA biosensor technology. *Meas Sci Technol* **2004***, 15*, R1-R11.

45. Kim, M. I.; Park, K. S.; Park, H. G. Ultrafast colorimetric detection of nucleic acids based on the inhibition of the oxidase activity of cerium oxide nanoparticles. *Chem. Commun.* **2014***, 50*, 9577-9580.

46. Pandey, C. M.; Sharma, A.; Sumana, G.; Tiwari, I.; Malhotra, B. D. Cationic poly(lactic-co-glycolic acid) iron oxide microspheres for nucleic acid detection. *Nanoscale* **2013***, 5*, 3800-3807.

47. Jin, R.; Cao, Y.; Thaxton, C.; Mirkin, C. Glass-bead-based parallel detection of DNA using composite Raman labels. *Small* **2006***, 2*, 375-380.

48. Xu, X.; Georganopoulou, D. G.; Hill, H. D.; Mirkin, C. A. Homogeneous detection of nucleic acids based upon the light scattering properties of silver-coated nanoparticle probes. *Anal. Chem.* **2007***, 79*, 6650-6654.

49. Luo, X.; Morrin, A.; Killard, A.; Smyth, M. Application of nanoparticles in electrochemical sensors and biosensors. *Electroanalysis* **2006***, 18*, 319-326.

50. Wang, J. Electrochemical biosensing based on noble metal nanoparticles. *Microchim. Acta* **2012***, 177*, 245-270.

51. Chen, A.; Chatterjee, S. Nanomaterials based electrochemical sensors for biomedical applications. *Chem. Soc. Rev.* **2013***, 42*, 5425-5438.

52. Hu, K.; Lan, D.; Li, X.; Zhang, S. Electrochemical DNA Biosensor Based on Nanoporous Gold Electrode and Multifunctional Encoded DNA-Au Bio Bar Codes. *Anal. Chem.* **2008***, 80*, 9124-9130.

53. Yu, F.; Li, G.; Qu, B.; Cao, W. Electrochemical detection of DNA hybridization based on signal DNA probe modified with Au and apoferritin nanoparticles. *Biosens. Bioelectron.* **2010***, 26*, 1114-1117.

54. Kawde, A.; Wang, J. Amplified electrical transduction of DNA hybridization based on polymeric beads loaded with multiple gold nanoparticle tags. *Electroanalysis* **2004***, 16*, 101-107.

55. Wang, J.; Polsky, R.; Xu, D. K. Silver-enhanced colloidal gold electrochemical stripping detection of DNA hybridization. *Langmuir* **2001***, 17*, 5739-5741.

56. Chen, S.; Yuan, R.; Chai, Y.; Hu, F. Electrochemical sensing of hydrogen peroxide using metal nanoparticles: a review. *Microchimica Acta* **2013***, 180*, 15-32.

57. Dong, H.; Jin, S.; Ju, H.; Hao, K.; Xu, L.; Lu, H.; Zhang, X. Trace and Label-Free MicroRNA Detection Using Oligonucleotide Encapsulated Silver Nanoclusters as Probes. *Anal. Chem.* **2012***, 84*, 8670-8674.

58. Shahdost-fard, F.; Salimi, A.; Khezrian, S. Highly selective and sensitive adenosine aptasensor based on platinum nanoparticles as catalytical label

for amplified detection of biorecognition events through H2O2 reduction. *Biosens. Bioelectron.* **2014***, 53*, 355-362.

59. Polsky, R.; Gill, R.; Kaganovsky, L.; Willner, I. Nucleic acid-functionalized Pt nanoparticles: Catalytic labels for the amplified electrochemical detection of biomolecules. *Anal. Chem.* **2006***, 78*, 2268-2271.

60. Bahadir, E. B.; Sezginturk, M. K. A review on impedimetric biosensors. *Artif. Cell. Nanomed. Biotechnol.* **2016***, 44*, 248-262.

61. Hou, L.; Gao, Z.; Xu, M.; Cao, X.; Wu, X.; Chen, G.; Tang, D. DNAzyme-functionalized gold-palladium hybrid nanostructures for triple signal amplification of impedimetric immunosensor. *Biosens. Bioelectron.* **2014***, 54*, 365-371.

62. Luna, D. M. N.; Avelino, K. Y. P. S.; Cordeiro, M. T.; Andrade, C. A. S.; Oliveira, M. D. L. Electrochemical immunosensor for dengue virus serotypes based on 4-mercaptobenzoic acid modified gold nanoparticles on self-assembled cysteine monolayers. *Sensors and Actuators B-Chemical* **2015***, 220*, 565-572.

63. Spain, E.; Gilgunn, S.; Sharma, S.; Adamson, K.; Carthy, E.; O'Kennedy, R.; Forster, R. J. Detection of prostate specific antigen based on electrocatalytic platinum nanoparticles conjugated to a recombinant scFv antibody. *Biosens. Bioelectron.* **2016***, 77*, 759-766.

64. Bonanni, A.; Esplandiu, M. J.; del Valle, M. Impedimetric genosensors employing COOH-modified carbon nanotube screen-printed electrodes. *Biosens. Bioelectron.* **2009***, 24*, 2885-2891.

65. Gupta, V. K.; Yola, M. L.; Qureshi, M. S.; Solak, A. O.; Atar, N.; Ustundag, Z. A novel impedimetric biosensor based on graphene oxide/gold nanoplatform for detection of DNA arrays. *Sensors and Actuators B-Chemical* **2013***, 188*, 1201-1211.

66. Xu, H.; Gorgy, K.; Gondran, C.; Le Goff, A.; Spinelli, N.; Lopez, C.; Defrancq, E.; Cosnier, S. Label-free impedimetric thrombin sensor based on poly(pyrrole-nitrilotriacetic acid)-aptamer film. *Biosens. Bioelectron.* **2013***, 41*, 90-95.

67. Venkatanarayanan, A.; Keyes, T. E.; Forster, R. J. Label-Free Impedance Detection of Cancer Cells. *Anal. Chem.* **2013***, 85*, 2216-2222.

68. Qi, P.; Wan, Y.; Zhang, D. Impedimetric biosensor based on cell-mediated bioimprinted films for bacterial detection. *Biosens. Bioelectron.* **2013***, 39*, 282-288.

69. Guo, X.; Kulkarni, A.; Doepke, A.; Halsall, H. B.; Iyer, S.; Heineman, W. R. Carbohydrate-Based Label-Free Detection of Escherichia coli ORN 178 Using Electrochemical Impedance Spectroscopy. *Anal. Chem.* **2012***, 84*, 241-246.

70. Rushworth, J. V.; Ahmed, A.; Griffiths, H. H.; Pollock, N. M.; Hooper, N. M.; Millner, P. A. A label-free electrical impedimetric biosensor for the specific detection of Alzheimer's amyloid-beta oligomers. *Biosens. Bioelectron.* **2014***, 56*, 83-90.

71. Cortina, M.; Esplandiu, M. J.; Alegret, S.; del Valle, M.; Sensors & Biosensors Group Urea impedimetric biosensor based on polymer degradation onto interdigitated electrodes. *Sensors and Actuators B-Chemical* **2006***, 118*, 84-89.

72. Zhang, X. Y.; Zhou, L. Y.; Luo, H. Q.; Li, N. B. A sensitive and label-free impedimetric biosensor based on an adjunct probe. *Anal. Chim. Acta* **2013***, 776*, 11-16.

73. Wang, W.; Yuan, X.; Zhang, W.; Gao, Q.; Qi, H.; Zhang, C. Cascade signal amplification for ultra-sensitive impedimetric detection of DNA hybridization using a hairpin DNA as probe. *Electrochim. Acta* **2012***, 78*, 377-383.

74. Yager, P.; Domingo, G. J.; Gerdes, J. Point-of-care diagnostics for global health. *Annu. Rev. Biomed. Eng.* **2008***, 10*, 107-144.

75. El-Ali, J.; Sorger, P. K.; Jensen, K. F. Cells on chips. *Nature* **2006***, 442*, 403-411.

76. Su, W.; Gao, X.; Jiang, L.; Qin, J. Microfluidic platform towards point-of-care diagnostics in infectious diseases. *J. Chromatogr. A* **2015***, 1377*, 13-26.

77. Park, J. Y.; Yoo, S. J.; Hwang, C. M.; Lee, S. Simultaneous generation of chemical concentration and mechanical shear stress gradients using microfluidic osmotic flow comparable to interstitial flow. *Lab Chip* **2009***, 9*, 2194-2202.

78. Meyvantsson, I.; Warrick, J. W.; Hayes, S.; Skoien, A.; Beebe, D. J. Automated cell culture in high density tubeless microfluidic device arrays. *Lab Chip* **2008***, 8*, 717-724.

79. Blazkova, M.; Javurkova, B.; Fukal, L.; Rauch, P. Immunochromatographic strip test for detection of genus Cronobacter. *Biosens. Bioelectron.* **2011***, 26*, 2828-2834.

80. Yang, S.; Lien, K.; Huang, K.; Lei, H.; Lee, G. Micro flow cytometry utilizing a magnetic bead-based immunoassay for rapid virus detection. *Biosens. Bioelectron.* **2008***, 24*, 855-862.

81. Gao, Y.; Hu, G.; Lin, F.; Sherman, P.; Li, D. An electrokinetically-controlled immunoassay for simultaneous detection of multiple microbial antigens. *Biomed. Microdevices* **2005***, 7*, 301-312.

82. Nwankire, C. E.; Donohoe, G. G.; Zhang, X.; Siegrist, J.; Somers, M.; Kurzbuch, D.; Monaghan, R.; Kitsara, M.; Burger, R.; Hearty, S.; Murrell, J.; Martin, C.; Rook, M.; Barrett, L.; Daniels, S.; McDonagh, C.; O'Kennedy, R.; Ducree, J. At-line bioprocess monitoring by immunoassay

with rotationally controlled serial siphoning and integrated supercritical angle fluorescence optics. *Anal. Chim. Acta* **2013***, 781*, 54-62.

83. Walter, A.; Maerz, A.; Schumacher, W.; Roesch, P.; Popp, J. Towards a fast, high specific and reliable discrimination of bacteria on strain level by means of SERS in a microfluidic device. *Lab Chip* **2011***, 11*, 1013-1021.

84. Zhang, H.; Xu, T.; Li, C.; Yang, M. A microfluidic device with microbead array for sensitive virus detection and genotyping using quantum dots as fluorescence labels. *Biosens. Bioelectron.* **2010***, 25*, 2402-2407.

85. Sang, C.; Chou, S.; Pan, F. M.; Sheu, J. Fluorescence enhancement and multiple protein detection in ZnO nanostructure microfluidic devices. *Biosens. Bioelectron.* **2016***, 75*, 285-292.

86. Xu, Y.; Phillips, J. A.; Yan, J.; Li, Q.; Fan, Z. H.; Tan, W. Aptamer-Based Microfluidic Device for Enrichment, Sorting, and Detection of Multiple Cancer Cells. *Anal. Chem.* **2009***, 81*, 7436-7442.

87. Nwankire, C. E.; Venkatanarayanan, A.; Glennon, T.; Keyes, T. E.; Forster, R. J.; Ducree, J. Label-free impedance detection of cancer cells from whole blood on an integrated centrifugal microfluidic platform. *Biosens. Bioelectron.* **2015***, 68*, 382-389.

88. Chang, C.; Chang, W.; Wang, C.; Wang, J.; Mai, J. D.; Lee, G. Nucleic acid amplification using microfluidic systems. *Lab Chip* **2013***, 13*, 1225-1242.

89. Miao, B.; Peng, N.; Li, L.; Li, Z.; Hu, F.; Zhang, Z.; Wang, C. Centrifugal Microfluidic System for Nucleic Acid Amplification and Detection. *Sensors* **2015***, 15*, 27954-27968.

90. Nugen, S. R.; Asiello, P. J.; Connelly, J. T.; Baeumner, A. J. PMMA biosensor for nucleic acids with integrated mixer and electrochemical detection. *Biosens. Bioelectron.* **2009***, 24*, 2428-2433.

91. Myers, F. B.; Henrikson, R. H.; Bone, J.; Lee, L. P. A Handheld Point-of-Care Genomic Diagnostic System. *PLoS One* **2013***, 8*, e70266.

92. Lin, X.; Chen, Q.; Liu, W.; Li, H.; Lin, J. A portable microchip for ultrasensitive and high-throughput assay of thrombin by rolling circle amplification and hemin/G-quadruplex system. *Biosens. Bioelectron.* **2014***, 56*, 71-76.

93. Stumpf, F.; Schwemmer, F.; Hutzenlaub, T.; Baumann, D.; Strohmeier, O.; Dingemanns, G.; Simons, G.; Sager, C.; Plobner, L.; von Stetten, F.; Zengerle, R.; Mark, D. LabDisk with complete reagent prestorage for sample-to-answer nucleic acid based detection of respiratory pathogens verified with influenza A H3N2 virus. *Lab Chip* **2016***, 16*, 199-207.

94. Kim, J.; Elsnab, J.; Gehrke, C.; Li, J.; Gale, B. K. Microfluidic integrated multi-walled carbon nanotube (MWCNT) sensor for electrochemical nucleic acid concentration measurement. *Sens. Actuator B-Chem.* **2013***, 185*, 370-376.

95. Kwakye, S.; Baeumner, A. A microfluidic biosensor based on nucleic acid sequence recognition. *Anal. Bioanal. Chem.* **2003***, 376*, 1062-1068.

96. Kwakye, S.; Goral, V.; Baeumner, A. Electrochemical microfluidic biosensor for nucleic acid detection with integrated minipotentiostat. *Biosens. Bioelectron.* **2006***, 21*, 2217-2223.

97. Goral, V.; Zaytseva, N.; Baeumner, A. Electrochemical microfluidic biosensor for the detection of nucleic acid sequences. *Lab Chip* **2006***, 6*, 414-421.

98. Dong, H.; Jin, S.; Ju, H.; Hao, K.; Xu, L.; Lu, H.; Zhang, X. Trace and Label-Free MicroRNA Detection Using Oligonucleotide Encapsulated Silver Nanoclusters as Probes. *Anal. Chem.* **2012***, 84*, 8670-8674.

99. Polsky, R.; Gill, R.; Kaganovsky, L.; Willner, I. Nucleic acid-functionalized Pt nanoparticles: Catalytic labels for the amplified electrochemical detection of biomolecules. *Anal. Chem.* **2006***, 78*, 2268-2271.

100. Shahdost-fard, F.; Salimi, A.; Khezrian, S. Highly selective and sensitive adenosine aptasensor based on platinum nanoparticles as catalytical label for amplified detection of biorecognition events through H2O2 reduction. *Biosens. Bioelectron.* **2014***, 53*, 355-362.

101. Peng, Z.; Yang, H. Designer platinum nanoparticles: Control of shape, composition in alloy, nanostructure and electrocatalytic property. *Nano Today* **2009***, 4*, 143-164.

102. Ruythooren, W.; Attenborough, K.; Beerten, S.; Merken, P.; Fransaer, J.; Beyne, E.; Van Hoof, C.; De Boeck, J.; Celis, J. Electrodeposition for the synthesis of microsystems. *J Micromech Microengineering* **2000***, 10*, 101-107.

103. Duarte, M.; Pilla, A.; Sieben, J.; Mayer, C. Platinum particles electrodeposition on carbon substrates. *Electrochem. Commun.* **2006***, 8*, 159-164.

104. Sheridan, E.; Hjelm, J.; Forster, R. J. Electrodeposition of gold nanoparticles on fluorine-doped tin oxide: Control of particle density and size distribution. *J Electroanal Chem* **2007***, 608*, 1-7.

105. Niu, L.; Li, Q.; Wei, F.; Wu, S.; Liu, P.; Cao, X. Electrocatalytic behavior of Pt-modified polyaniline electrode for methanol oxidation: Effect of Pt deposition modes. *J Electroanal Chem* **2005***, 578*, 331-337.

106. Liu, H.; Penner, R. Size-selective electrodeposition of mesoscale metal particles in the uncoupled limit. *J Phys Chem B* **2000***, 104*, 9131-9139.

107. Liu, H.; Favier, F.; Ng, K.; Zach, M.; Penner, R. Size-selective electrodeposition of meso-scale metal particles: a general method. *Electrochim. Acta* **2001***, 47*, 671-677.

108. Penner, R. Brownian dynamics simulations of the growth of metal nanocrystal ensembles on electrode surfaces in solution: 2. The effect of deposition rate on particle size dispersion. *J Phys Chem B* **2001***, 105*, 8672-8678.

109. Penner, R. Mesoscopic metal particles and wires by electrodeposition. *J Phys Chem B* **2002***, 106*, 3339-3353.

110. Ueda, M.; Dietz, H.; Anders, A.; Kneppe, H.; Meixner, A.; Plieth, W. Double-pulse technique as an electrochemical tool for controlling the preparation of metallic nanoparticles. *Electrochim. Acta* **2002***, 48*, 377-386.

111. Sandmann, G.; Dietz, H.; Plieth, W. Preparation of silver nanoparticles on ITO surfaces by a double-pulse method. *J Electroanal Chem* **2000***, 491*, 78-86.

112. Bui, M. N.; Pham, X.; Nan, K. N.; Li, C. A.; Kim, Y. S.; Seong, G. H. Electrocatalytic reduction of hydrogen peroxide by silver particles patterned on single-walled carbon nanotubes. *Sens. Actuator B-Chem.* **2010***, 150*, 436-441.

113. Wang, Q.; Zheng, J. Electrodeposition of silver nanoparticles on a zinc oxide film: improvement of amperometric sensing sensitivity and stability for hydrogen peroxide determination. *Microchim. Acta* **2010***, 169*, 361-365.

114. Wu, S.; Zhao, H.; Ju, H.; Shi, C.; Zhao, J. Electrodeposition of silver-DNA hybrid nanoparticles for electrochemical sensing of hydrogen peroxide and glucose. *Electrochem. Commun.* **2006***, 8*, 1197-1203.

115. Futamata, M.; Maruyama, Y.; Ishikawa, M. Microscopic morphology and SERS activity of Ag colloidal particles. *Vib. Spectrosc.* **2002***, 30*, 17-23.

116. Xu, H.; Bjerneld, E.; Kall, M.; Borjesson, L. Spectroscopy of single hemoglobin molecules by surface enhanced Raman scattering. *Phys. Rev. Lett.* **1999***, 83*, 4357-4360.

117. Kneipp, K.; Wang, Y.; Kneipp, H.; Perelman, L.; Itzkan, I.; Dasari, R.; Feld, M. Single molecule detection using surface-enhanced Raman scattering (SERS). *Phys. Rev. Lett.* **1997***, 78*, 1667-1670.

118. Wu, X.; Fu, P.; Ma, W.; Xu, L.; Kuang, H.; Xu, C. SERS-active silver nanoparticle trimers for sub-attomolar detection of alpha fetoprotein. *RSC Adv.* **2015***, 5*, 73395-73398.

119. Xu, L.; Yan, W.; Ma, W.; Kuang, H.; Wu, X.; Liu, L.; Zhao, Y.; Wang, L.; Xu, C. SERS Encoded Silver Pyramids for Attomolar Detection of Multiplexed Disease Biomarkers. *Adv Mater* **2015***, 27*, 1706-+.

120. Jin, R.; Cao, Y.; Hao, E.; Metraux, G.; Schatz, G.; Mirkin, C. Controlling anisotropic nanoparticle growth through plasmon excitation. *Nature* **2003***, 425*, 487-490.

121. Aherne, D.; Ledwith, D. M.; Gara, M.; Kelly, J. M. Optical properties and growth aspects of silver nanoprisms produced by a highly reproducible and rapid synthesis at room temperature. *Adv. Funct. Mater.* **2008***, 18*, 2005-2016.

122. Haynes, C.; Van Duyne, R. Nanosphere lithography: A versatile nanofabrication tool for studies of size-dependent nanoparticle optics. *J Phys Chem B* **2001***, 105*, 5599-5611.

123. Potara, M.; Boca, S.; Licarete, E.; Damert, A.; Alupei, M.; Chiriac, M. T.; Popescu, O.; Schmidt, U.; Astilean, S. Chitosan-coated triangular silver nanoparticles as a novel class of biocompatible, highly sensitive plasmonic platforms for intracellular SERS sensing and imaging. *Nanoscale* **2013***, 5*, 6013-6022.

124. Potara, M.; Baia, M.; Farcau, C.; Astilean, S. Chitosan-coated anisotropic silver nanoparticles as a SERS substrate for single-molecule detection. *Nanotechnology* **2012***, 23*, 055501.

125. Haes, A.; Van Duyne, R. A nanoscale optical blosensor: Sensitivity and selectivity of an approach based on the localized surface plasmon resonance spectroscopy of triangular silver nanoparticles. *J. Am. Chem. Soc.* **2002***, 124*, 10596-10604.

126. Zhang, J.; Sun, Y.; Zhang, H.; Xu, B.; Zhang, H.; Song, D. Preparation and application of triangular silver nanoplates/chitosan composite in surface plasmon resonance biosensing. *Anal. Chim. Acta* **2013***, 769*, 114-120.

127. Braun, G.; Lee, S. J.; Dante, M.; Nguyen, T.; Moskovits, M.; Reich, N. Surface-enhanced Raman spectroscopy for DNA detection by nanoparticle assembly onto smooth metal films. *J. Am. Chem. Soc.* **2007***, 129*, 6378-+.

128. Wang, H.; Dhawan, A.; Du, Y.; Batchelor, D.; Leonard, D. N.; Misra, V.; Tuan Vo-Dinh Molecular sentinel-on-chip for SERS-based biosensing. *Phys. Chem. Chem. Phys.* **2013***, 15*, 6008-6015.

CHAPTER 2

EXPERIMENTAL PROCEDURES

2.1 MATERIALS & CHEMICALS

Ethanol (99.5 %), sulphuric acid (H_2SO_4, 95-98 %), nitric acid (HNO_3), tetrahydrofuran (THF), Dulbecco's phosphate buffer saline (DPBS), chloroplatinic acid hydrate (H_2PtCl_6, ≥ 99.9 %), and hydrogen peroxide (H_2O_2, 30 % (w/w) in H_2O) were all supplied by Sigma-Aldrich. Denhardt's hybridization solution was obtained from Sigma Aldrich and consists of 1% Bovine Serum Albumin (BSA), 1 % Ficoll, and 1 % Polyvinylpyrrolidone (PVP) in water, at a pH of 7.

The electrodes were polished using alpha alumina with a particle size ranging from 1 µm to 0.05 µm (Buehler, USA). Gold on glass slides were supplied by Tyndall National Institute, and were cut into 1 cm x 1 cm squares using a diamond pen. The gold slides were cleaned with ethanol and then with deionised water prior to use.

1 mM dodecanethiol (C_{12}, 98 %) and 11-mercaptoundecanoic acid (COOH-C_{11}-SH, 95%) were both obtained from Sigma Aldrich and made up in ethanol (99.5 %).

The uniform platinum nanoparticles used in Chapter 4 were purchased from Particular GmbH. These platinum nanoparticles were 63±5 nm in size, citrate stabilized, and suspended in H_2O. The uniform platinum nanoparticles used in Chapter 5 were purchases from Strem Chemicals. They were 50-70 nm in diameter and suspended in acetone. Triangular silver nanoplates (base length: 100±20 nm, height: 150±20 nm) and gold-edged triangular silver nanoplates (base length: 200±50 nm; height: 300±50 nm) were obtained from Silvonics Technologies Ltd.

The gold coated silicon wafers used as electrodes were purchases from Amsbio. Poly(methyl methacrylate) (PMMA) and polyvinyl alcohol (PVA) was supplied by Radionics, Ireland. Pressure sensitive adhesive (PSA) was supplied by Adhesives Research, Ireland.

A 10% w/v solution of 5.43±0.14 μM polystyrene microspheres was obtained from Bangs Laboratories. The gold salt solution was supplied by Technic Inc, UK.

All of the aqueous solutions were prepared using Milli-Q water (Millipore Core, 18 $M\Omega cm^{-1}$).

2.1.1 Nucleic Acids

The oligonucleotides were purchased from Eurogentec ©^{TM} (98 %), Belgium. The base sequences for each strand are as follows.

2.1.1.1 DNA

Capture: 5'-CGG-CAG-TGT-TTA-TCA-3'-SH

Target (Staphylococcus Aureus - Mastitis): 5'-TGA-TAA-ACA-CTG-CCG-TTT-GAA-GTC-TGT-TTA-GAA-GAA-ACT-TA-3'

Probe: SH-5'-AT-AGT-TTC-TTC-TAA-ACA-GAC-3'

2.1.1.2 miRNA

Neuroblastoma target – miR-132-3p:

Capture: 5' – U-AGA-CUG-UUA-3'-SH-C3

Target (Neuroblastoma): 5' -UAA-CAG-UCU-ACA-GCC-AUG-GUC-G-3'

Probe: SH-C3-5'-C-GAC-CAU-GGC-U-3'

Epilepsy target – miR-134:

Capture: 5' – ACC-AGU-CAC-A-3'-SH-C3

Target (epilepsy, miR-132): 5' – UGU-GAC-UGG-UUG-ACC-AGA-GGG-G-3'

Probe: SH-C3 -5'-CCC-CUC-UGG-U - 3'

2.2 INSTRUMENTATION

2.2.1 Microscopic instrumentation

2.2.1.1 SEM

SEM images were taken using a Hitachi S300N scanning electron microscope at an accelerating voltage of 5 - 20 kV and a probe current of 25 – 35 mA. The samples were mounted on a high purity aluminium stub using conductive carbon tape.

2.2.1.2 FESEM

Field Emission Scanning Electron Microscopy (FESEM) was performed using a Carl Zeiss Supra Ultra plus microscope. The accelerating voltage was 5 – 20 kV and the probe current was 35 mA.

2.2.2 Spectroscopic Measurements

2.2.2.1 Raman

Raman measurements were carried out using a Peltier cooled (−70 °C) charge coupled device (CCD) camera (255×1024 pixels) attached to a HORIBA Jobin-Yvon Labram HR 1000 spectrometer coupled to a Digital Instruments Bioscope

II with an inverted microscope. Samples were excited with a 633 nm laser source. The spectrometer was equipped with diffraction gratings of 600 grooves / mm and the slit allowed the spectral resolution of 2 cm^{-1}.

The area of the laser spot on the samples was 1 µm in diameter. Data acquisition times used in the Raman experiments was 30 s. The Raman band of a silicon wafer at 520 cm^{-1} was used to calibrate the spectrometer. The spectral data acquired were analysed using LabSpec software.

2.2.2.2 UV

UV-Vis spectra were recorded on a Varian Cary 50 spectrophotometer. Samples were analysed in a quartz cuvette with a pathlength of 1 cm with a spectral range of 200-1000 nm unless otherwise stated. The background was corrected for blank solvent absorbance prior to every measurement and was performed at room temperature.

2.2.2.3 EDX

EDX measurements were performed using an Oxford INCA microanalysis system using an X-Max detection system. The accelerating voltage was 10 – 20kV and the probe current was 35 mA.

2.3 EXPERIMENTAL PROCEDURES

2.3.1 Electrode Fabrication and Cleaning

A three electrode electrochemical cell was used at room temperature 20 ± 3 ^{o}C for all electrochemical measurements including cyclic voltammetry. Unless stated otherwise, the working electrode was a 2 mm planar gold disc, the counter electrode was a large area coiled platinum wire and a silver/silver chloride (Ag/AgCl in 3 M KCl) was a reference electrode. All electrochemical measurements were carried out using a CH Instruments 760D and 760B.

Prior to use, the gold disc working electrode was polished with 0.3 µM alumina paste on a felt bed, followed by polishing with 0.05 µM alumina paste on a felt bed for at least 10 min. It was then thoroughly washed with Milli-Q water and ethanol before sonication in Milli-Q water for 5 min. All solutions were deoxygenated using a stream of nitrogen gas prior to use.

Voltammetry was used to determine the microscopic area and surface roughness factor (microscopic to geometric areas) by scanning the electrode in 0.1 M H_2SO_4 between 0 V and 1.5 V at a scan rate of 0.1 V/s, as shown in Figure 2.1. The gold oxide reduction peak, typically found ta 0.8 V is used. This peak is used to calculate the electrochemical area and the surface roughness factor.[1] These calculations are given below in Equations 2.1 – 2.3, where A_G is the geometrical area of the electrode (0.0314 cm^2), EA is the electrochemical area, A_p is the area under the peak and R.F. is the surface roughness factor.

$$A_G = \pi r^2 \qquad \text{Equation 2.1}$$

$$EA = \frac{A_p}{390\mu C cm^{-2}} \qquad \text{Equation 2.2}$$

$$R.F. = \frac{A_G}{EA} \qquad \text{Equation 2.3}$$

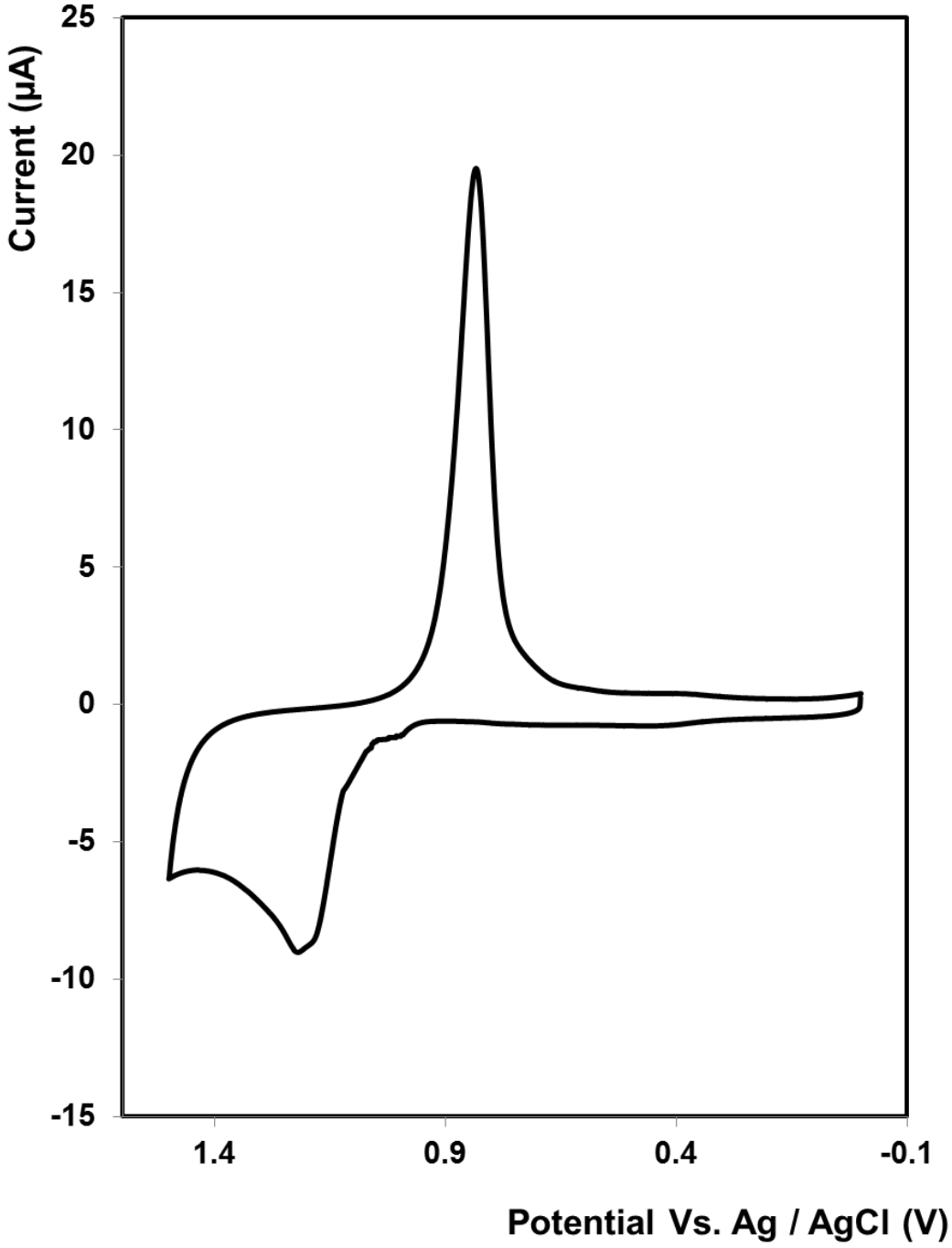

Figure 2.1: Cyclic voltammogram of a 2 mm gold disc electrode cycled in 0.1 M H_2SO_4 with a scan rate of 0.1 V/s. The counter electrode was a platinum wire; the reference electrode was Ag/AgCl in KCl. The sixth scan in presented.

2.3.2 Self-Assembled Monolayers

The available surface area of clean and polished gold electrodes was determined using the method described in Section 2.3.1. The modification of the gold surface involved the formation of alkanethiol self-assembled monolayers (SAMs) by placing the freshly polished electrodes into 150 µL of 1 mM dodecanethiol in ethanol. The vials were sealed using parafilm, to prevent solvent evaporation. The surface modification time had been previously optimised to be 7 hours.[2] A scheme of the steps involved for the whole process is shown in Figure 2.2. By modifying the surface of the gold electrode, PtNPs can be formed using defects within a dodecanethiol monolayer as a template.

2.3.3 Platinum Deposition

Platinum electrodeposition experiments were carried out with 0.5 M H_2SO_4 as the supporting electrolyte. A 1 mM platinum salt solution was made from chloroplatinic acid hydrate. The double-pulse potential method was used to deposit the metal. The two pulse method was carried out in two stages; firstly a short, large overpotential nucleation pulse was applied for 20 ms, followed by a longer, smaller overpotential growth pulse, lasting up to 90 s. A series of potentials for both the nucleation and growth step were investigated, ranging from -1000 mV to -1800 mV for the nucleation pulse, and 0 mV to -600 mV for the growth pulse. Electrodeposition was carried out on bare gold disc electrodes that were previously cleaned as shown in Section 2.3.1 and also on dodecanethiol, self-assembled monolayer modified gold disc electrodes, as explained in Section 2.3.2.

The electrochemical area associated with the deposited platinum nanoparticles was calculated as explained in Equations 2.1 – 2.3 for the surface area of gold, with the charge associated with the reduction of platinum as 210 µCcm^{-2}.

2.3.4 Nanoparticle Functionalisation

2.3.4.1 Regioselectively Functionalised Nanoparticles

Once the platinum nanoparticles were deposited into the monolayer defects, the upper, clean surface of the nanoparticles were functionalized with probe oligo (5' thiolate). The probe DNA strand was immobilized on the PtNP surface by immersing the nanoparticle functionalized electrode in 150 µL of a 1 µM solution of the probe DNA strand, dissolved in Denhardt's buffer for 3 h. The tube was sealed with parafilm to ensure no dust particles etc. entered the solution. After hybridization, the electrode surface was rinsed thoroughly with deionised water to remove any loosely attached strands. The DNA functionalised PtNPs were then desorbed as explained below in Section 2.3.5.

2.3.4.2 Uniformly Functionalised Nanoparticles

Nanoparticles in solution were uniformly functionalised across their entire surface with probe strand nucleic acids. The 1 µM probe nucleic acid strand in Denhardt's buffer solution was combined with the nanoparticles solution to form a nucleic acid layer with a density of approximately 1×10^{-10} mol.cm^2. For the spherical platinum nanoparticles, this involved adding 1 ml of the platinum nanoparticle suspension to 3.39 ml of the 1 µM probe miRNA solution and leaving overnight to functionalise.

This is calculated depending on the size of the nanoparticles that are used, and the available surface area of the nanoparticle. This method was used for both the uniformly functionalised platinum nanoparticles and the triangular silver nanoplates.

2.3.5 DNA hybridization

The following steps were carried out to create and regioselectively functionalise the nanoparticles and implement the DNA sandwich assay:

Step 1A: As described in Section 2.3.3, the PtNPs are grown on a gold disc electrode that has been functionalized with a self-assembled alkane thiol monolayer containing templating defects.

Step 1B: As described in Section 2.3.4.1, the upper surface of the PtNPs is then functionalized with probe oligo strands.

Step 1C: The probe-functionalised PtNPs were then desorbed as explained below in Section 2.3.5.

Step 2A: On a separate, freshly polished and cleaned gold disc electrode, a monolayer of the capture oligo (3' thiolate) was deposited by immersing the working electrode in a 1 µM solution of the thiolated oligo prepared in Denhardt's buffer. The tube was sealed with parafilm. After five hours, the electrode was thoroughly rinsed with deionised water to remove any loosely bound strands.

Step 2B: Concentrations of target oligo from 1 µM to 1 aM were hybridized to the immobilized capture oligo strand, by immersing the capture oligo functionalized electrode in 150 µL of the target strand dissolved in Denhardt's buffer for 3 hours. Following hybridization, the modified electrode was rinsed with deionised water.

Step 2C: The electrode modified with the capture and target strands were allowed to hybridize to the probe oligos immobilised on the upper surface of the PtNPs for 5 hours. Finally, it was rinsed thoroughly with deionised water and dried under a nitrogen stream.

2.3.6 Platinum Nanoparticle Desorption

To desorb the PtNPs that were deposited as described in Section 2.3.3, a current of 0.01 A was applied for 180 s to the working electrode, into an electrolyte of 0.05 M H_2SO_4, that had been previously deoxygenated with nitrogen for 15 min.

The key purpose in the desorption of the PtNPs is to have asymmetrically functionalized, electrocatalytic nanoparticles. By applying a large current jump, the inter-connection between the electrode and the nanoparticle is broken giving a suspension of PtNPs that are functionalized with DNA only on one hemispherical surface.

2.3.7 Electrochemical Detection of DNA

The hybridized target DNA can be detected by monitoring the reduction of hydrogen peroxide (H_2O_2) at the surface of the captured PtNPs, as shown in Equation 2.4. For the assays measuring the target DNA, a "full electrode" of DNA was used, such as the one shown in Figure 2.2; i.e. present on the electrode was capture DNA, target DNA and probe DNA, the probe DNA containing the desorbed hemispherical PtNPs that were suspended in solution, and hybridized onto the electrode, as explained in Section 2.3.4. The PtNPs / DNA modified electrode, was placed in 0.1 M H_2SO_4 and the current was measured at -0.25 V until it reached an equilibrium after approximately five min. Then, 2 mL of H_2O_2 was added and the reduction current was measured after approximately thirty min at -0.25 V, when an equilibrium had been reached once again. The difference in current, Δi, is taken as the response of the peroxide reduction at the bound PtNPs.

$$H_2O_2 \rightarrow O_2 + 2H^+ + 2e^-$$

$$H_2O_2 + 2H^+ + 2e^- \rightarrow 2H_2O \qquad \text{Equation 2.4}$$

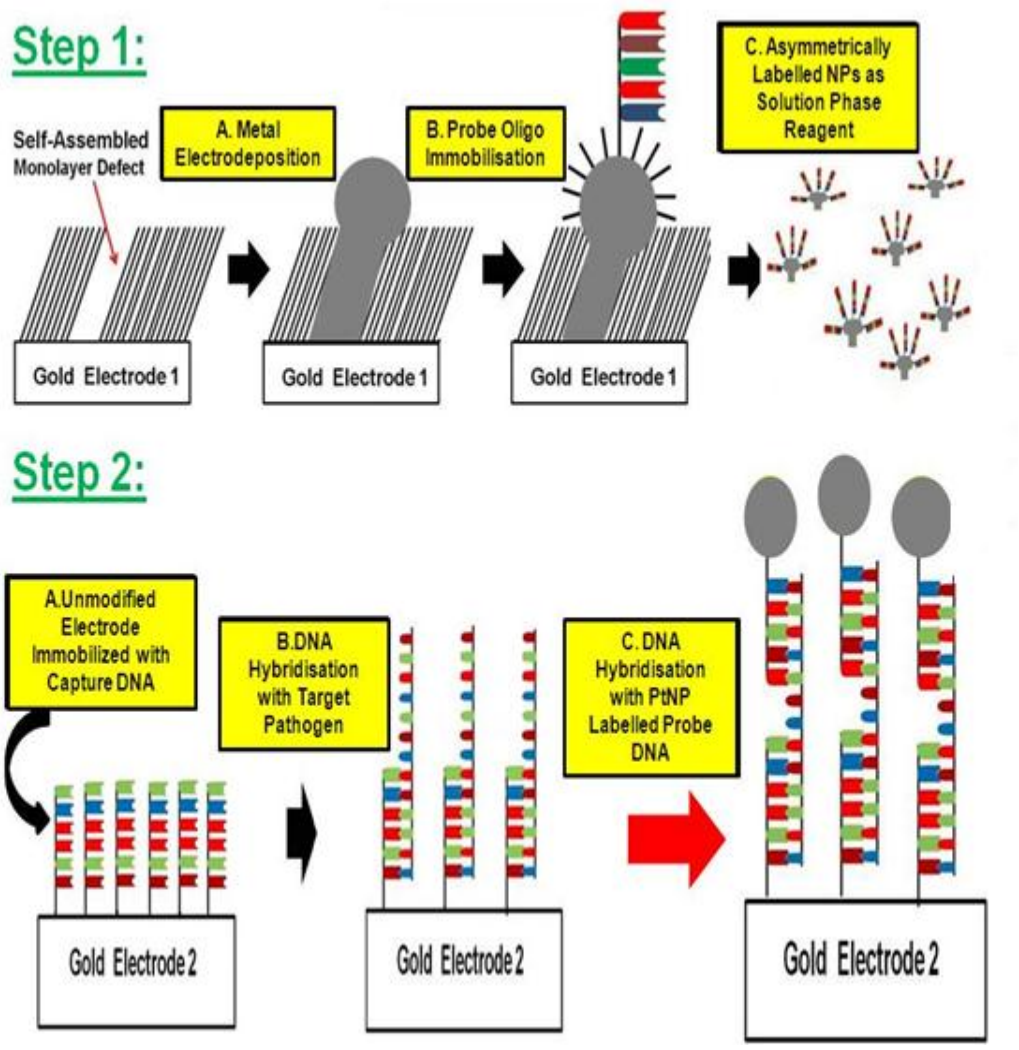

Figure 2.2: Schematic representation of the steps involved in this process. *Step 1:* Dodecanethiol monolayers are formed initially (Section 2.3.2); PtNPs are formed in the monolayer defects (Section 2.3.3); the regioselective PtNPs are functionalised on one side with probe DNA (Section 2.3.4); a large current jump was applied to desorb the functionalized PtNPs (Section 2.3.5). *Step 2:* on a different electrode, capture and target DNA sequences for staphylococcus aureus were hybridized and then functionalized with the suspended probe DNA / PtNPs (Section 2.3.4).

2.3.8 Nanocavity Array Synthesis

The nanocavities were synthesized as previously published.[3] The gold wafers were cut to the required size using a diamond pen and were washed, first with ethanol, then with deionised water. A 1/70 dilution of the 10% w/v stock polystyrene solution was made with water. 150 µL of this solution was dropcast onto the gold slide to give a uniform coverage. The samples were left to dry overnight.

Electrochemical deposition through this polystyrene sphere template was then achieved using the gold salt solution at a potential of -1 V. Deposition continued until a charge of 2.8 C had been passed through, which created a 3 µm thick film. The gold was washed with deionised water when finished to remove any salts.

2.3.9 Silver Nanoplate Synthesis

2.3.9.1 TSNP Electrocatalytic Array

The detection of DNA was carried out using Triangular Silver Nanoplates, TSNPs, as the label rather than the regioselectively or uniformly modified platinum nanoparticles as described in Section 2.3.4 and Section 2.3.6.

A gold disc electrode was prepared as described in Section 2.3.1. A monolayer of the capture miRNA was formed by immersing the electrode in 150 µL of a 1 µM solution of the thiolated strand in Denhardt's buffer at 37 ^{o}C for 5 h. The tube was sealed with parafilm. The miRNA modified electrode was then rinsed with deionised water. The target miRNA was hybridized to the immobilized capture strand by immersion in 150 µL of the target oligo solution for 3 hours at 37 ^{o}C. Varying concentrations of target miRNA were used, from

1 µM to 1 aM. Following hybridization, the electrode was rinsed thoroughly with deionised water. The TSNP-labelled probe miRNA that was made as described in Section 2.3.4.2 were then hybridized to the complementary section of the target miRNA by immersion in 150 µL of the NP-probe solution for five hours at 37 ^{o}C. The electrode was once again rinsed with deionised water to remove loosely bound strands.

The electrocatalytic assay was performed as described in Section 2.3.7. The only difference was the final concentration of hydrogen peroxide in the solution was 200 µM. This is because not as large a volume of peroxide was required for catalysis in this case.

2.3.9.2 TSNP Bio-Raman Nanoarray

The triangular silver nanoplates (TSNPs) were immobilised in the gold nanocavity array described in Section 2.3.5 (nanoparticle in microcavity architecture) to analyse via Raman spectroscopy, as shown in Figure 2.3.

Once the gold cavity array was electrodeposited as in Section 2.3.8, a monolayer of 11-mercaptoundecanoic acid was allowed to form on the top surface with the templating spheres in place, by immersing the nanocavity array in 1 mM of the monolayer in ethanol for 12 hours. This was to block any binding of the capture miRNA to the top surface of the nanocavity array. The polystyrene spheres were then removed by sonication in THF.

The capture miRNA was immobilized in the cavity by immersing the array in 150 µL of 1 µM of the capture miRNA dissolved in Denhardt's solutions for 5 hours at 37 ^{o}C. Hybridization of the target miRNA strand (1 µM concentration) to the capture strand was performed at 37 ^{o}C for 3 h. The probe-functionalized TSNPs (Section 2.3.4.2) were hybridized with the complementary section of the target not used for binding to the capture strand for 5 h at 37 ^{o}C, resulting in the structure in Figure 2.3. This was then used for Raman analysis.

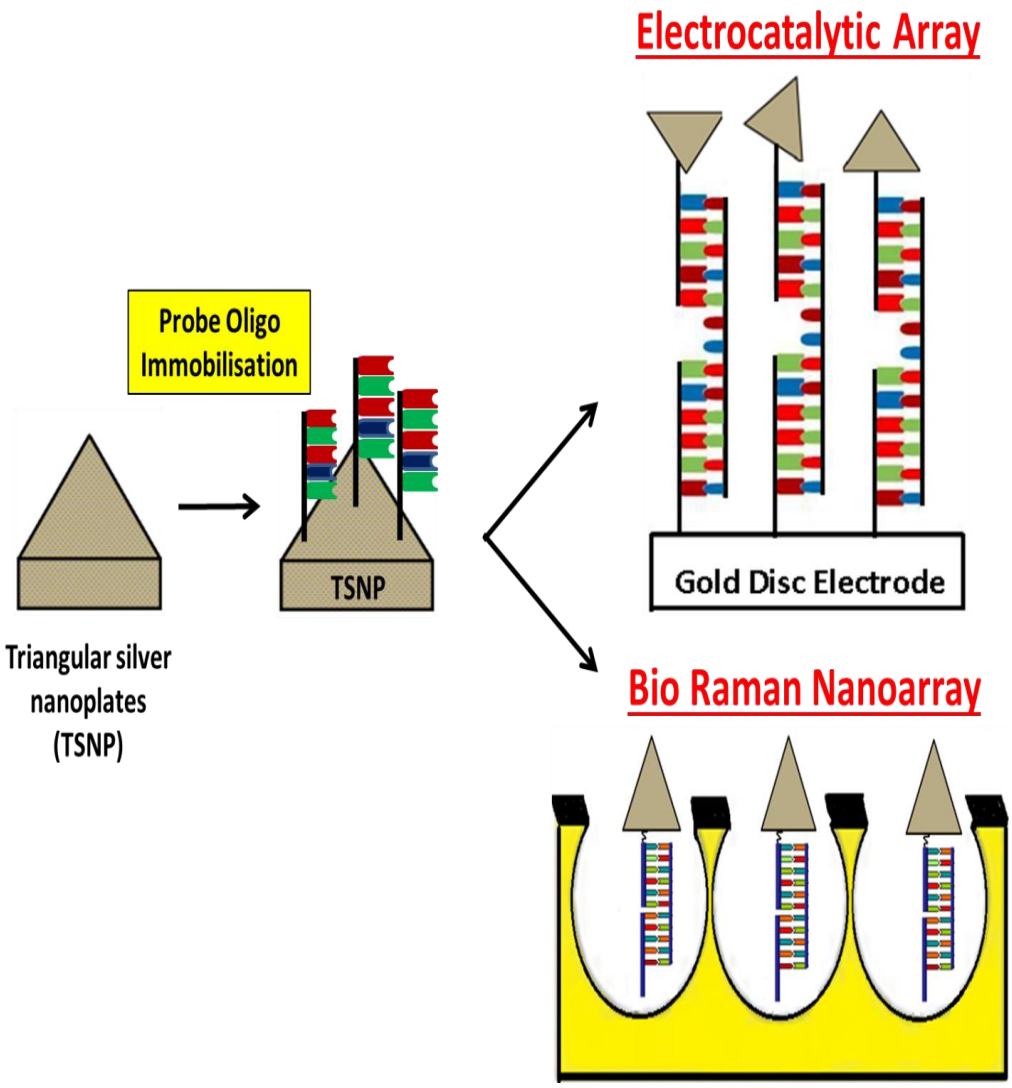

Figure 2.3: Scheme of how the Triangular Silver Nanoplates (TSNPs) are used in two arrays. The TSNPs are first functionalized with probe strand miRNA (Section 2.4.8.1). These are then used in an electrocatalytic assay (Section 2.4.8.2), and also in a Bio Raman Nanoarray (Section 2.4.8.3).

2.3.10 Microfluidic Disc Fabrication

The microfluidic disc is made up of 9 layers in total, consisting of four layer of PMMA and 5 layers of PSA. Computer-Aided Design (CAD) software package Pro/Engineer (PTC, USA) was used to design each layer of the disc. The larger voids such as reservoirs and vents were machined in PMMA using a CO_2 laser, Epilog Zing 16 laser (Epilog, USA). The PMMA layers used were 0.5 mm, 1.5 mm and 2 mm thick. Small features such as the microchannels and lower channels were cut from PSA using a knife cutter, Graphtec CE6000-40 (Graphtec, USA). Prior to assembly, each layer was cleaned with isopropanol. The disc was aligned using an assembly jig; between each step the discs were rolled using a temperature-controlled lamination press (Hot Roll Laminator, Chemsultant Int. US).

Dissolvable film (DF) tabs were made by attaching PVA to double-sided PSA to create sticky tabs. Circular and slot-shaped DF tabs were used in different areas of the disc to allow for systematic triggering of the disc to allow the hybridisation to occur fully inside the disc. The volume of the reservoir chambers and the sample chamber is 200 µL each. More detail on the working of the disc is described in Chapter 5.

2.3.10.1 Experimental Spin Stand

The discs were spun on an experimental spin stand[4] at varying frequencies from 1 – 35 Hz. They were spun using a computer controlled spindle motor (Faulhaber Minimotor SA, Switzerland). A stroboscopic light source (Drelloscop 3244, Drello, Germany), a short exposure-time camera (Pixelfly, PCO, Germany) and the motor are all synchronised using custom electronics to visualise the hydrodynamics on the rotating disc. Images are acquired as single files at a rate of ~6 Hz. Each image is imprinted with a time stamp accurate to 1 s.

2.3.11 Nucleic Acid Detection in Microfluidic Disc

2.3.11.1 Impedimetric Detection of Nucleic Acids in Microfluidic Disc

Electrochemical Impedance Spectroscopy (EIS) was carried out using a CH Instruments 760 E workstation. A three-electrode electrochemical cell was used, inside the microfluidic disc, at a temperature of 20 ± 3 ^{o}C. The working electrode was functionalised a gold electrode functionalised as explained above; the counter electrode was a gold slide; and an ITO slide acted as the reference electrode. The disc was placed inside a Faraday cage for analysis. EIS measurements were carried out at the open circuit potential in the frequency range of 0.01 – 100,000 Hz, with a 25 mV ac amplitude. A dilute electrolyte of 1 mM DPBS was used. The measured data was fit to an equivalent circuit model using Z-view software.

2.3.11.2 Electrocatalytic Detection of Nucleic Acids in Microfluidic Disc

The electrocatalytic detection of the nucleic acids immobilised on the electrode inside the microfluidic disc is performed as explained previously in Section 3.2.6, with a few differences. The electrolyte in this instance is DPBS, and the final concentration of H_2O_2 added is 20 µM.

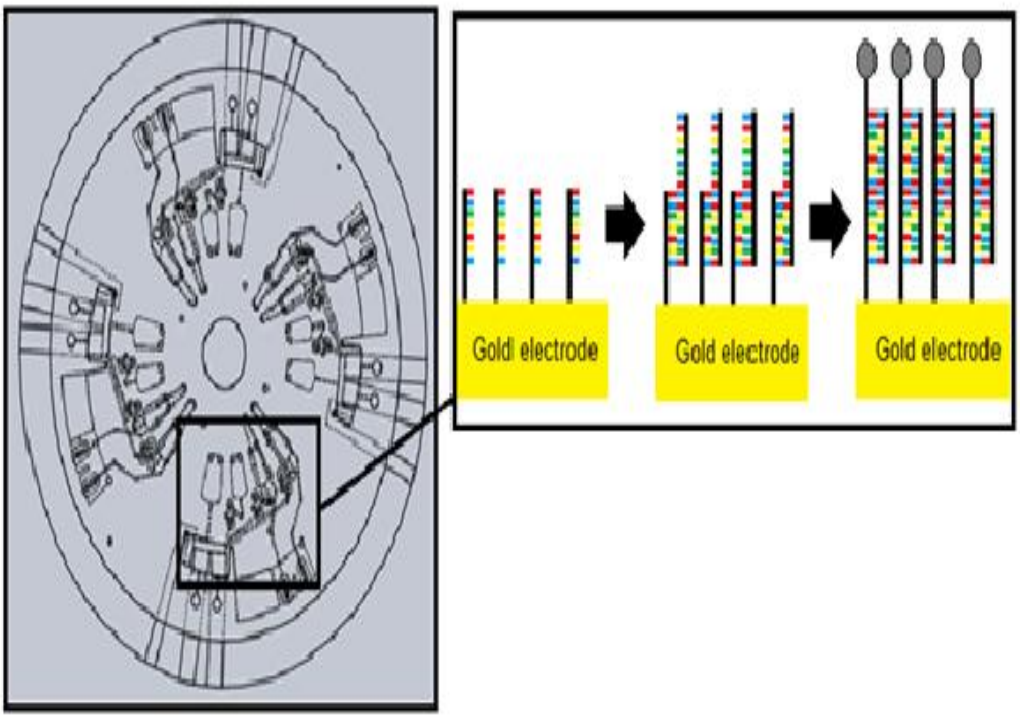

Figure 2.4: Microfluidic disc pre-loaded with target miRNA, miRNA functionalised PtNPs and DPBS. Each chamber is triggered to release after a certain event to functionalise the electrode with complementary miRNA strands.

2.4 CONCLUSION

In this chapter, the materials, instruments and chemicals used throughout the thesis are described. The experimental procedures are outlined, showing the preparation of the biosensor and substrates, using metal nanoparticles. This chapter also details the fabrication and cleaning processes for all materials used in the working chapters of this thesis.

2.5 REFERENCES

1. TRASATTI, S.; PETRII, O. Real Surface-Area Measurements in Electrochemistry. *Pure Appl. Chem.* **1991***, 63*, 711-734.

2. Spain, E.; Miner, B.; Keyes, T. E.; Forster, R. J. Regio selective functionalisation of gold nanoparticles with DNA. *Chemical Communications* **2012***, 48*, 838-840.

3. Mallon, C. T.; Spain, E.; Keyes, T. E.; Forster, R. J. DNA mediated immobilisation of electrocatalytic platinum nanoparticles in gold nanocavity arrays. *Chemical Communications* **2013***, 49*, 1380-1382.

4. Kinahan, D. J.; Kearney, S. M.; Dimov, N.; Glynn, M. T.; Ducree, J. Event-triggered logical flow control for comprehensive process integration of multi-step assays on centrifugal microfluidic platforms. *Lab Chip* **2014***, 14*, 2249-2258.

CHAPTER 3

FABRICATION OF PLATINUM NANOPARTICLES USING DOUBLE POTENTIAL STEP ELECTRODEPOSITION

3.1 INTRODUCTION

Metal nanoparticles are an area of continuing interest due to their wide array of potential applications. Noble metal nanoparticles, e.g. platinum, can electrocatalytically reduce hydrogen peroxide, and therefore have been used extensively in sensing applications, such as in nucleic acid and aptamer biosensors, and hydrogen peroxide sensors.[1-4] This reaction is fundamental in fuel cells[5-7], metal air batteries[8] and electrochemical sensors.[4,9,10]

However, in order to produce optimised electrocatalytic surfaces, it must be possible to produce nanoparticles in a controlled manner, such that the size and surface coverage of the particles can be accurately controlled. Many ways of preparing metal nanoparticles including sputter coating[11-13], chemical synthesis[14,15] and irradiation methods[16,17] have been developed. This work focused on electrodeposition due to the following advantages:

- Speed; it is a very quick method.
- Stability; produces stable nanoparticles that do not have any intentional surfactant stabiliser
- Ability to form single particles, instead of clusters.
- Ability to control the deposition process, and therefore the size of the particle.[18,19]

We have previously made regioselectively functionalised nanoparticles that were functionalised on one side with DNA, and the other side was left clean and therefore catalytically active.[20] The hemi-spherical gold nanoparticles were obtained by applying a self-assembled monolayer, with nanoscale defect sites, onto the surface of the gold electrode prior to electrodeposition. These particles were capable of detecting target DNA at picomolar concentrations in a DNA hybridisation assay. However, an issue with this approach is that when the target DNA concentration is in extremely low concentrations very few electrocatalytic nanoparticles are bound to the electrode surface. As the electrocatalytic current is proportional to the nanoparticle surface area, capturing a small number of randomly sized particles from a size *polydisperse*

population, will lead to significant variation of the electrocatalytic current for a given DNA target concentration. Therefore, a method of deposition size monodisperse nanoparticles is required in order to detect DNA at ultralow concentrations.

This chapter reports an approach to the fabrication of high density, size monodisperse platinum nanoparticles. The size and density of the platinum nanoparticles can be controlled by careful choice of deposition potentials, and also the duration of the potential. In the literature review, it was explained how electrodeposition is achieved by a nucleation and growth mechanism. By exploring different potentials, it is possible to tune the size and density of the nanoparticles. Another method used for controlling the size and density is to modify the surface of the gold disc electrode prior to deposition, using an alkanethiol self-assembled monolayer with nanoscale defect sites, and depositing the platinum into these defects. This allows the platinum to grow through the defect sites, and over the edge of the monolayer, in “mushroom” shapes, which means that the particles are hemispherical and therefore be regioselectively functionalised for further applications.

The particles are characterised by cyclic voltammetry to determine the electrochemical area of platinum deposited onto the electrode. The particles are also characterised by scanning electron microscopy in order to determine the shape and density of the particles and the efficiency of the desorption from the electrode.

The application of these platinum nanoparticles will be reported in later chapters of this thesis.

3.2 RESULTS AND DISCUSSION

3.2.1 Nucleation of Platinum on Non-Templated Gold Disc Electrodes

First, the optimization of single and double potential step waveforms to create size monodisperse platinum nanoparticles is reported. In order to characterise the nucleation process and obtain information about the reduction potential of the platinum salt, and the potentials at which the platinum metal can be electrodeposited, cyclic voltammetry was carried out on gold electrodes. The platinum salt chosen for these investigations was 1mM chloroplatinic acid hydrate (H_2PtCl_6) in 0.5 M H_2SO_4.

3.2.1.1 Voltammetric Characterisation of Nucleation of Platinum on Non-Templated Electrodes

An overpotential is the potential beyond the standard reduction potential that is needed to drive the reaction at a certain rate. This is based on Bulter-Volmer kinetics which shows that rate of the reaction increases at the overpotential increases. The standard reduction potential for platinum is at approximately 0.3 V. Therefore, the potential applied to deposit platinum needs to be negative of this. As this deposition potential becomes more negative (greater overpotential), the reaction proceeds quicker.

The nucleation step requires an overpotential that is extremely negative of the standard potential of platinum (0.3 V) to drive the instantaneous nucleation. The overpotential is then made more positive, to grow these particles and lower diffusion zone coupling. The key is finding a balance between the two; in

order to do this, many different potentials were investigated in different combinations.

The nucleation potentials investigated here were a pulse of -1.0 V to -1.8 V. A CV of the gold disc electrode after the nucleation of platinum electrodeposition is shown in Figure 3.1, showing how the electrode is affected by only the nucleation pulse for 20ms. The gold oxide reduction peak is visible at 0.8 V. This peak decreases and there is a large increase in the water reduction peak at -0.4 V for the platinum deposition; this shows that although there isn't enough platinum for the platinum oxide reduction peak to be completely visible at approximately 0.3 V, there is still platinum present in these nucleation sites, as it is platinum that catalyses this water reduction.

Table 3.1 shows the values of the electrochemical area and surface roughness of the gold oxide reduction peak and the platinum oxide reduction peak before and after nucleation. Equations 2.1 – 2.3 are used to calculate the electrochemical area and surface roughness, using 390 μCcm^{-2} for the charge under the gold oxide reduction peak and 210 μCcm^{-2} for the charge under the platinum oxide reduction peak. . By zooming into the CV around the point where the platinum oxide reduction peak should occur, it is possible to see the peak at 0.3 V that is not visible when the CV is in full view. The SEM image shown in Figure 3.2 confirms that nanoparticles are present. The electrochemical area of gold decreases in each case; this shows that the available surface area on the gold electrode is decreasing as platinum nanoparticles are deposited onto the surface. The average percentage decrease varies for each nucleation potential used, from approximately 39 % to 58 %. However, the error bars are small indicating that the percentage decrease is reproducible.

3.2.1.2 SEM Characterisation of Nucleation of Platinum on Non-Templated Electrodes

To characterise the nature of the platinum deposits, SEM images were taken after the nucleation pulse at each different potential was applied. An example of an image following a 20 ms pulse at a -1.6 V potential is shown in Figure 3.4.

As shown by the voltammetric characterisation of the nucleation step, the electrochemical area of platinum is minimal after only applying the nucleation potential of 1 V to -1.8 V for 20 ms. The amount deposited increases slightly as the over potential is decreased, as shown in Table 3.1; however, the available electrochemical area of platinum deposited is also very similar after each potential, especially for the potentials -1.0, -1.2 and -1.4 V, with a slightly larger E.A. for the -1.6 V pulse. These SEM images correlate with the voltammetric characterisation, and for this reason, the SEM image of the -1.6 V potential deposition is shown here. What can be seen in this image, are the tiny white dots of platinum that are starting to form, some of which are highlighted in a red circle for clarity; these are the nucleation sites, and it is on these that the platinum will be grown from when the growth pulse is applied. Using ImageJ software, the density of the nucleation particles was determined to be approximately 35 x 10^8 particles per cm^2. The size of the particles are between 50 – 100 nm.

These nucleation pulses will be discussed further on in this chapter, when they are combined with the growth pulses, to determine the best ones for the nanoparticles required here.

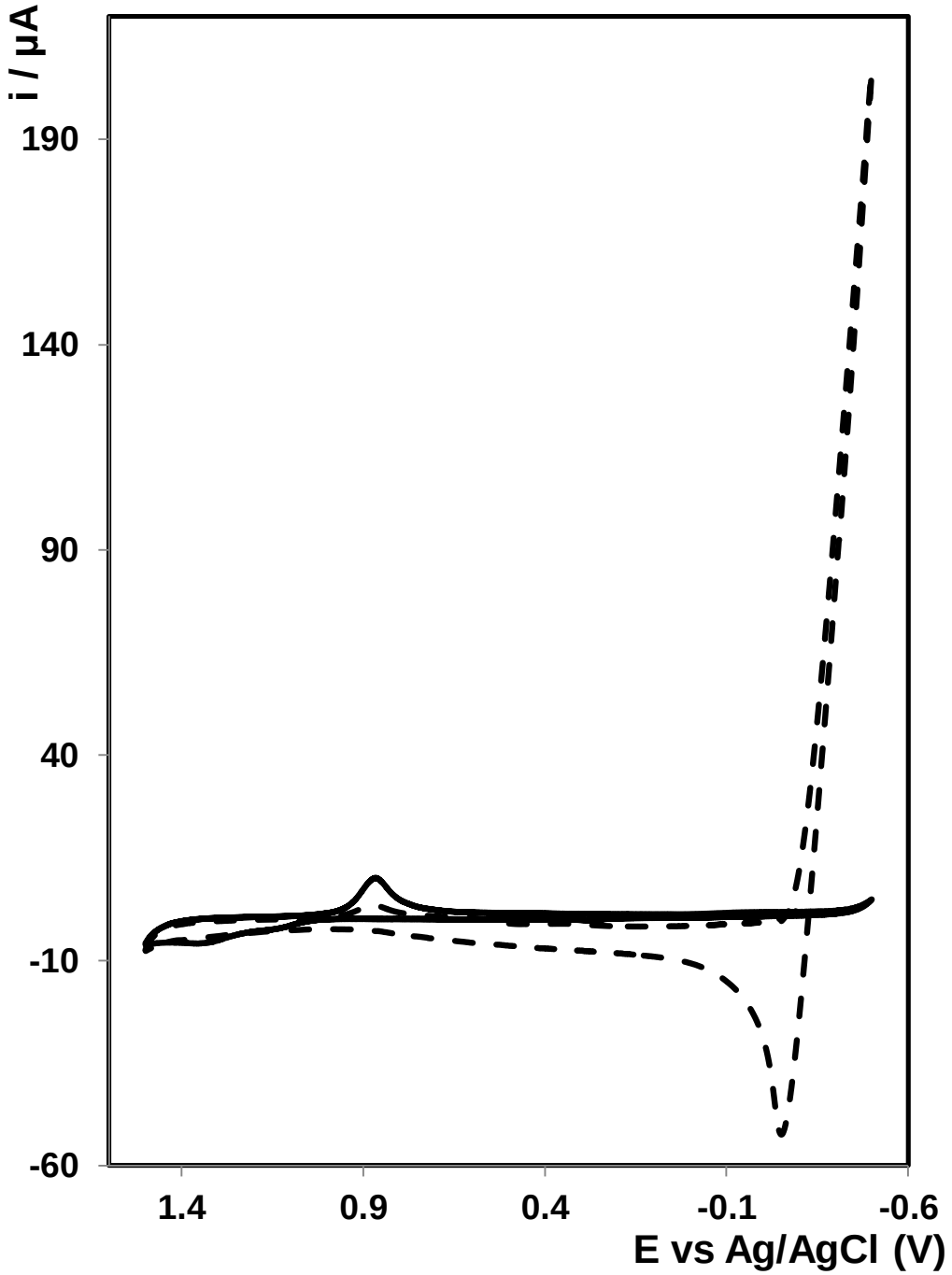

Figure 3.1: Cyclic voltammogram of a 2 mm diameter gold disc electrode in 0.1 M H_2SO_4 (solid line) and after deposition of platinum from a 1 mM Pt in 0.5 M H_2SO_4 solution at an applied potential of -1.6 V for 20 ms.

Table 3.1: Comparison of the average electrochemical area (E.A.) and average surface roughness (S.R.) factor values of the gold oxide and platinum oxide peaks of a gold disc electrode before and after a nucleation pulse is applied for 20 ms in 1 mM chloroplatinic acid hydrate in 0.5 M H_2SO_4. The average values are based on n = 3.

		Au Peak:				Pt Peak:		
Applied Potential		**Av. Ap**	**Av. E.A.**	**Av. S.R.**	**Av.% decrease**	**Av. Ap**	**Av. E.A.**	**Av S.R.**
-1.0	**Bare Elec.**	1.74×10^{-5}	4.46×10^{-2}	1.42	**47.503 ±1.791**	0	0	0
	After Nuc.	9.13×10^{-6}	2.34×10^{-2}	0.75		3.41×10^{-6}	1.63×10^{-2}	0.52
-1.2	**Bare Elec.**	1.54×10^{-5}	3.96×10^{-2}	1.26	**51.760 ±1.204**	0	0	0
	After Nuc.	7.44×10^{-6}	1.91×10^{-2}	0.61		3.42×10^{-6}	1.63×10^{-2}	0.52
-1.4	**Bare Elec.**	1.70×10^{-5}	4.35×10^{-2}	1.39	**56.108 ±0.320**	0	0	0
	After Nuc.	7.45×10^{-6}	1.91×10^{-2}	0.61		3.88×10^{-6}	1.85×10^{-2}	0.59
-1.6	**Bare Elec.**	1.64×10^{-5}	4.20×10^{-2}	1.34	**58.145 ±0.271**	0	0	0
	After Nuc.	6.85×10^{-6}	1.76×10^{-2}	0.56		8.24×10^{-6}	3.93×10^{-2}	1.25
-1.8	**Bare Elec.**	1.73×10^{-5}	4.44×10^{-2}	1.41	**39.082 ±2.698**	0	0	0
	After Nuc.	1.05×10^{-5}	2.70×10^{-2}	1.21		2.08×10^{-6}	9.89×10^{-3}	0.32

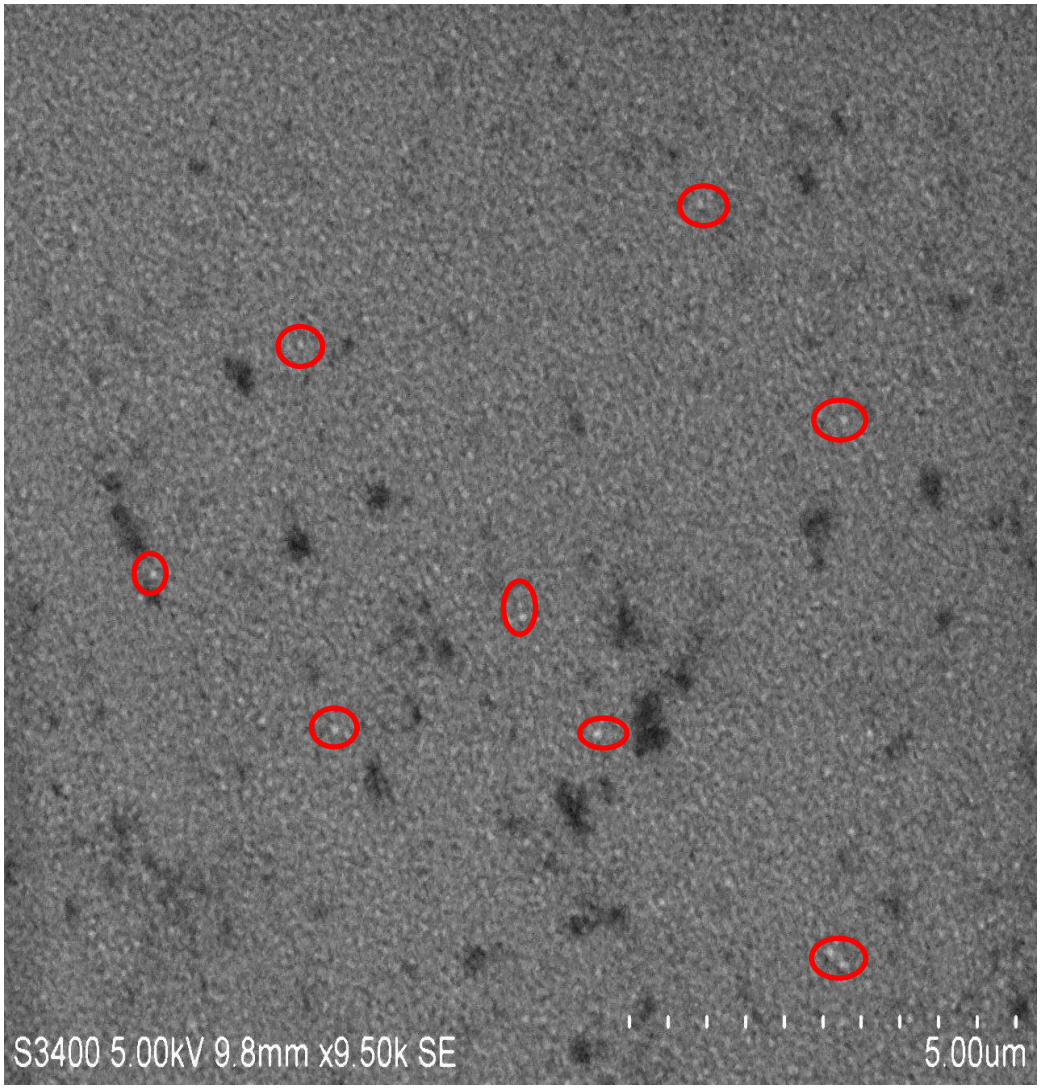

Figure 3.2: SEM images of a gold electrode after a potential of -1.6 V was applied for 20 ms in a 1 mM chloroplatinic acid hydrate in 0.5 M H_2SO_4 solution.

3.2.2 Nucleation of Platinum on Self-Assembled Monolayer Templated Gold Disc Electrodes

A self-assembled dodecanethiol monolayer (SAM) was formed on the surface of the gold disc electrode, using the method described in Section 2.3.2. These SAMs have defect sites, in which the platinum will be deposited after the nucleation pulse. The aim of using these SAMs and defect sites is to obtain platinum nano-scale particles that are size monodisperse and that can be grown out of the defect sites, to form hemispherical shaped particles. The influence of the nucleation step is reported here.

3.2.2.1 Voltammetric Characterisation of Nucleation of Platinum on Self-Assembled Monolayer Templated Electrodes

A CV comparing a gold electrode that is modified with the SAM with defect sites before and after the deposition of platinum using a -1.6 V nucleation pulse is shown in Figure 3.3. As in the previous section, the electrochemical area of the gold oxide reduction peak at 0.8 V decreases and the water reduction peak appears at -0.4 V once again after the platinum deposition.

Table 3.2 shows the average electrochemical area, surface roughness factor and average percentage decrease for the gold oxide reduction peak at 0.8 V after the -1.6 V pulse in 1 mM chloroplatinic acid hydrate. As the CV shows, there is no platinum oxide reduction peak to calculate the electrochemical area from. This could be attributed to the presence of the monolayer; as there is less gold available for the deposition of platinum, it takes a longer time to deposit into the defect sites at a large enough scale for the corresponding platinum oxide reduction peak to be clearly seen in cyclic voltammetry. However, as the electrochemical area of the gold oxide reduction peak has an average percentage decrease of 5 – 29 %, platinum is deposited.

By comparing the percentage decrease of the electrochemical area of the gold oxide peak both with and without the monolayer (Table 3.1), it can be seen that there is a bigger decrease without the monolayer on the gold surface, due to less gold availability initially in the defect sites of the SAM. This is indicative of less platinum deposited due to the presence of the SAM, which corresponds to no platinum oxide reduction peak present; however this will be investigated further, when the growth step has been incorporated into the deposition process.

3.2.2.2 SEM Characterisation of Nucleation of Platinum on Self-Assembled Monolayer Templated Electrodes

As reported previously in Section 3.2.1.2, SEM images were obtained for each of the potentials, after the pulse was applied to an alkanethiol modified electrode. However, no platinum deposits could be observed by cyclic voltammetry after a 20 ms nucleation pulse; therefore only one image is shown in Figure 3.4, after a -1.6 V nucleation pulse, and it is compared to an SEM image of just the self-assembled monolayer.

By comparing image A to B, it can be seen that there are platinum deposits present. The platinum can be seen by the small while dots on the surface, some of which are circled in red to highlight them. As expected on the basis of the voltammetric response, the density of the platinum particles deposited on the SAM modified electrode is less than when it is deposited onto the unmodified electrode. This is confirmed by analysis of the surface using ImageJ, as the density is approximately 27 x 10^8 particles /cm^2. This lower platinum coverage would also account for the smaller percentage decrease in the gold oxide reduction peak after the nucleation pulse. This will be further considered later, along with changes in the growth pulse, to determine the best potentials for these platinum nanoparticles to be deposited.

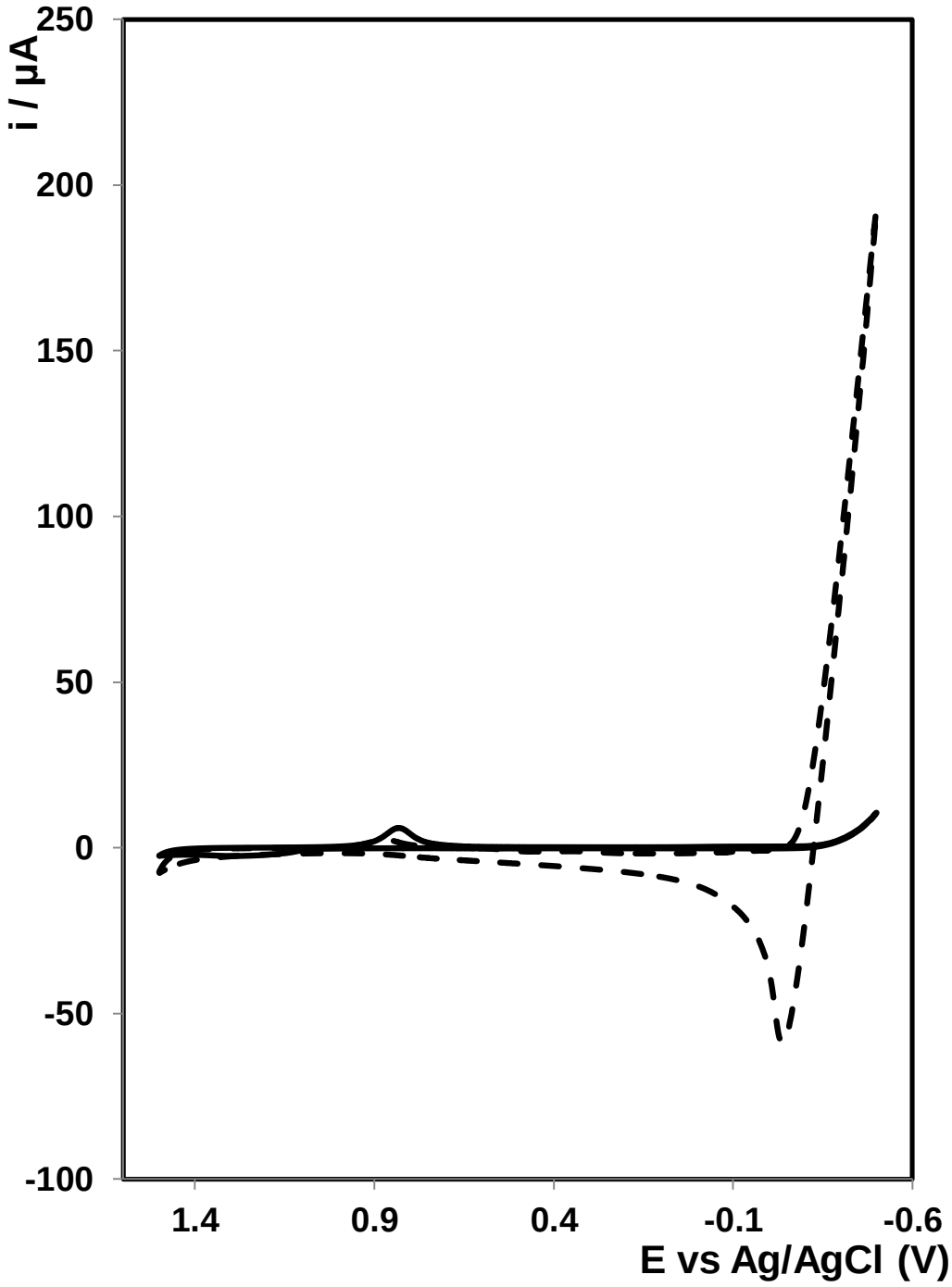

Figure 3.3: Cyclic voltammogram of a dodecanethiol modified 2 mm diameter gold disc electrode in 0.1 M H_2SO_4 (solid line) and after modification with platinum from a 1mM chloroplatinic acid hydrate in 0.5 M H_2SO_4 at an applied potential of -1.6 V for 20 ms.

Table 3.2: Comparison of the electrochemical area (E.A.) and surface roughness (S.R.) values based on the gold oxide peaks of a gold disc electrode with a self-assembled monolayer, before and after a nucleation pulse is applied for 20 ms in 1 mM chloroplatinic acid hydrate in 0.5 M H_2SO_4. The average values are based on n = 3.

Au Peak					
Applied potentials		**Av. Ap**	**Av. E.A.**	**Av S.R.**	**Average % decrease**
-1.0 V	Modified Elec	1.19×10^{-5}	3.05×10^{-2}	0.971	8.222 ± 1.475
	After Nuc	1.09×10^{-5}	2.80×10^{-2}	0.891	
-1.2 V	Modified Elec	1.52×10^{-5}	3.89×10^{-2}	1.238	13.627 ± 1.048
	After Nuc	1.31×10^{-5}	3.36×10^{-2}	1.069	
-1.4 V	Modified Elec	1.50×10^{-5}	3.84×10^{-2}	1.224	22.420 ± 0.777
	After Nuc	1.16×10^{-5}	2.98×10^{-2}	0.949	
-1.6 V	Modified Elec	1.37×10^{-5}	3.51×10^{-2}	1.119	29.636 ± 0.507
	After Nuc	9.64×10^{-6}	2.47×10^{-2}	0.787	
-1.8 V	Modified Elec	1.25×10^{-5}	3.20×10^{-2}	1.018	4.986 ± 0.582
	After Nuc	1.18×10^{-5}	3.04×10^{-2}	0.967	

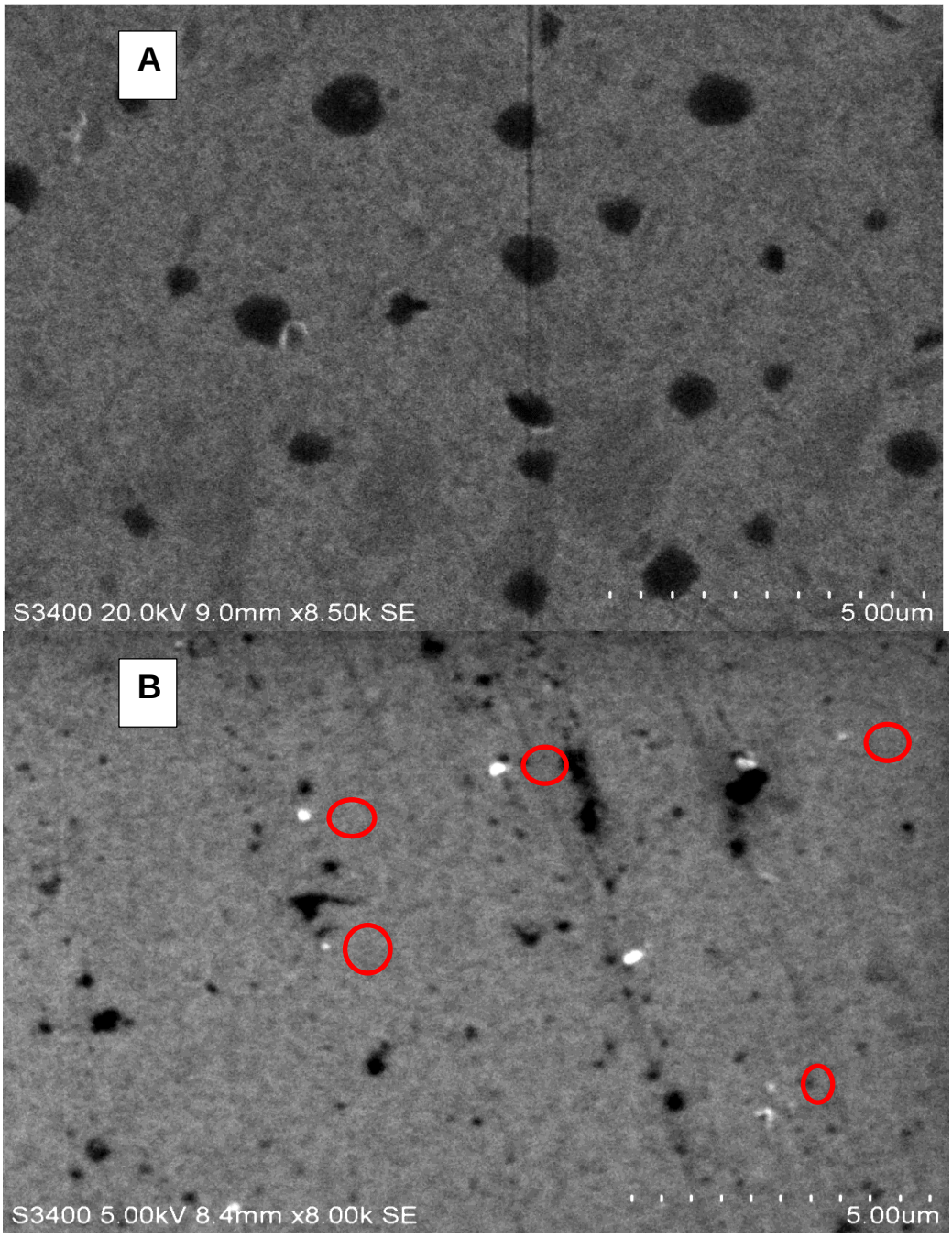

Figure 3.4: A: SEM image of an alkanethiol self-assembled monolayer grown for 7 h onto gold electrode. **B:** SEM image the SAM-modified gold electrode after a potential of -1.6 V was applied for 20 ms in a 1 mM chloroplatinic hydrate in 0.5 M H_2SO_4 solution.

.

3.2.3 Control of Nucleation and Growth using Double-Pulse Method

Previous work has been carried out using a single-pulse electrodeposition method, which has shown that it is an effective method in depositing platinum nanoparticles. However, in order to achieve instantaneous nucleation and to control the uniformity and size of the electrodeposited nanoparticles, it is necessary to separate the nucleation and growth steps.

This was first demonstrated by Penner as a method of controlling particle size distribution[21-23] and has been used by many others for this purpose.[24-27] By using this double pulse method, high nucleation densities can be achieved, while minimizing diffusion zone coupling and achieving better control over nanoparticle size. As shown schematically in Figure 3.5, a large overpotential that is more negative than the standard reduction potential is used first in order to achieve instantaneous nucleation to seed the surface with nuclei. Then, the potential is changed so that the growth of the particles occurs from the nuclei on the surface at the desired rate. This gives greater control over the size of nanoparticles, as they can be effectively tuned to the size and density that is required.

Initially the experiments were carried out on non-templated gold disc electrodes, to see if the defect containing monolayer deposition step could be omitted. First, the deposition of platinum nanoparticles onto pristine electrodes without a monolayer is discussed and then platinum deposition on monolayer functionalised gold disc electrodes is considered.

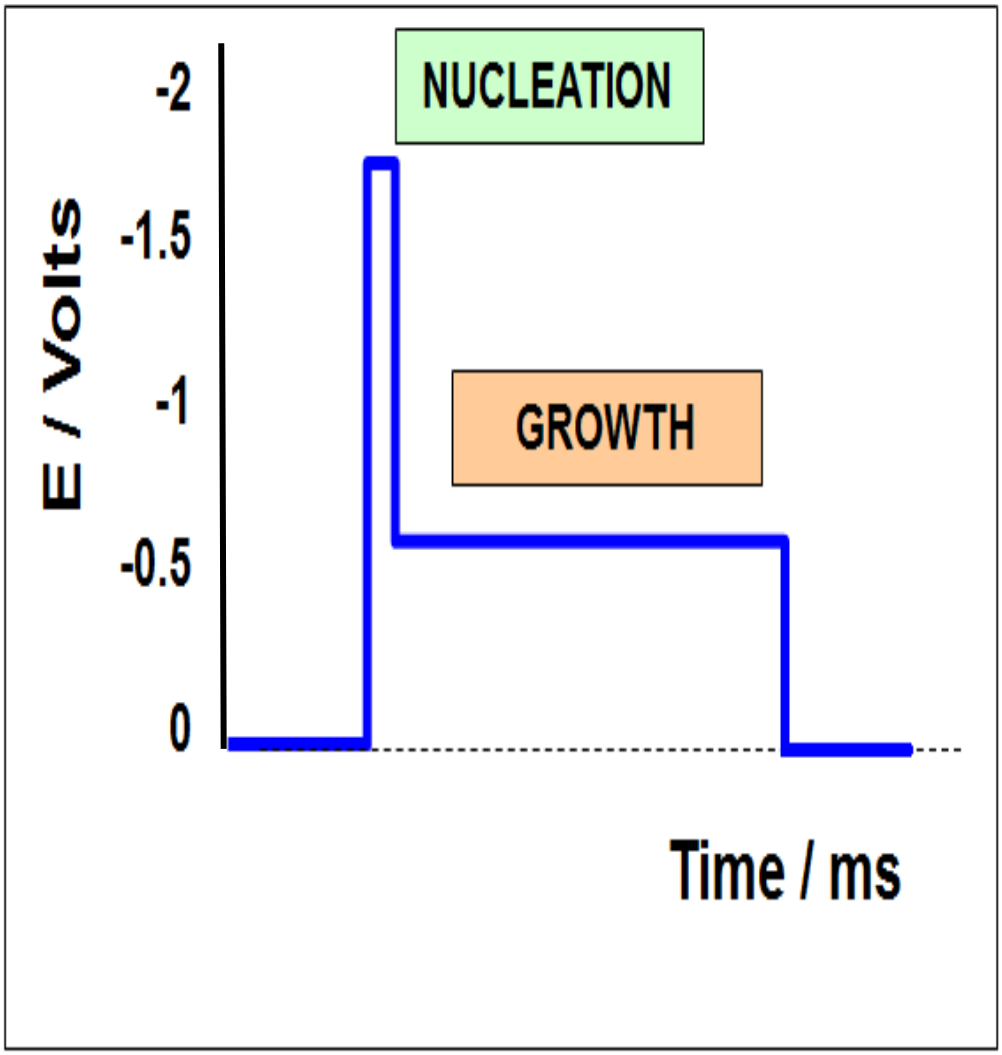

Figure 3.5: Schematic representation of the Double Pulse Potential electrodeposition method used in this chapter. Both the nucleation and growth potentials and the time applied can be varied.

3.2.3.1 Control of Nucleation and Growth using Double-Pulse Method on Non-Templated Gold Disc Electrodes

3.2.3.1.1 Voltammetric Characterisation of Platinum Deposition on Non-Templated Gold Disc Electrodes.

The growth potentials were investigated from 0 mV to -600 mV, in 100 mV increments. As the nucleation pulse should be at a more negative overpotential than the growth pulse, the potentials investigated were from -1000 mV to -1800 mV in 100 mV increments. The nucleation pulse was applied for 20 ms. The growth pulse was applied for both 30 s and 60 s, at each potential. For each potential looked at, a CV was obtained for the bare gold disc electrode, the electrode after platinum nanoparticle deposition, and once again after removing the platinum nanoparticles, in order to compare the gold and platinum oxide reduction peaks for each step. These are shown in Figure 3.6 for one growth cycle of platinum. Figure 3.6A is the bare electrode; the gold oxide reduction peak is present at 0.8 V. Figure 3.6B is after the deposition of platinum; the gold oxide reduction peak decreases and the platinum oxide reduction peak forms at 0.3 V. The large peak at -0.4 V is water reduction. Figure 3.6C is when the platinum deposits have been removed from the electrode. The gold oxide reduction peak increases and the platinum oxide reduction peak decreases significantly, showing that most of the platinum has been desorbed from the surface of the electrode. The electrochemical area and surface roughness factor were calculated for each step of the process using the gold oxide reduction peak and the platinum oxide reduction peak and compared in order to look at the area of platinum deposited and how it varied between each potential applied. These figures are shown in Table 3.3 for the corresponding CV in Figure 3.6. Only one value is shown here; deposition at each potential was performed, and these values are shown in the appendix.

By analysing the electrochemical area of the gold and platinum, before and after deposition and stripping, the best parameters for platinum deposition and desorption can be deduced. Optimum results would be achieving platinum nanoparticles that are size monodisperse and high density that retain their properties when desorbed from the electrode into suspension after deposition.

Table 3.3 shows the optimum parameters for platinum deposition. A nucleation pulse is applied for 20 ms at -1600 mV and a growth pulse is applied at -200 mV for both 30 s and 60 s. The electrochemical area of the deposited platinum is 0.119 cm^2 when it is grown for 30 s at a -200 mV potential, and 0.238 cm^2 when it is grown for 60 s at the same potential. The platinum deposits are then removed using a current jump, as explained in Section 2.3.5. After the platinum is removed, the electrochemical area of platinum decreases for both growth times, showing much of the platinum is removed from the surface of the electrodes. It would be expected that as the electrochemical area of platinum increased, the electrochemical area of the gold oxide reduction peak would decrease a substantial amount also, however this is found not to be the case. The electrochemical area of the gold oxide peak does decrease from 0.051 cm^2 to 0.043 cm^2 for the 30 s deposition time and from 0.049 cm^2 to 0.038 cm^2 for the 60 s deposition time. Although it is impossible to say for definite at this stage why this is the case, it is possible that the reason for this is due to the platinum growing in “cluster”-like shapes, so therefore there is a large electrochemical area for platinum present, but as it is growing on top of each other, there is still a significant amount of underlying gold left bare. This will be explored more thoroughly using SEM.

From analysing the electrochemical areas and surface roughness values for all of the potentials and times investigated, a trend is observed. The electrochemical area of platinum deposited increases as the nucleation pulse increases, up to -1600 mV but for -1800 mV it decreases again. This is thought to be because gas bubble formation impedes deposition or strips some of the platinum off the surface.

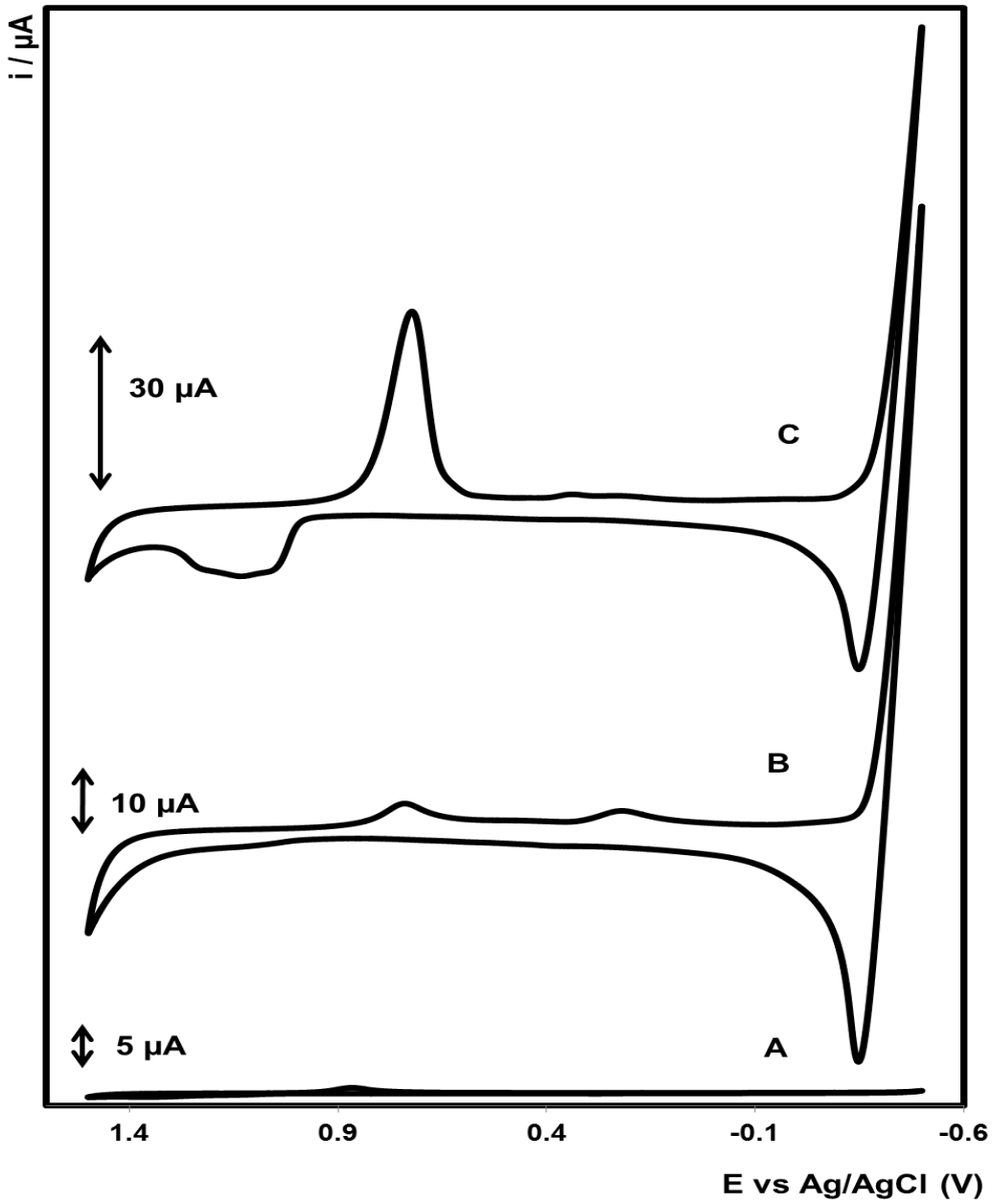

Figure 3.6: Cyclic voltammograms of: **(A)** 2 mm unmodified gold electrode, **(B)** after electrodeposition of platinum nanoparticles onto the gold surface **(C)** after the platinum nanoparticles have been desorbed. In all cases the supporting electrolyte was 0.1 M H_2SO_4. The voltammograms have been displaced vertically for clarity of presentation.

Table 3.3: Comparison of the electrochemical area (E.A.) and surface roughness factor (S.R.). values of the gold oxide reduction and platinum oxide reduction peaks of a bare gold disc electrode, before and after platinum deposition of a 1mM chloroplatinic acid hydrate solution in 0.5 M H_2SO_4 using the double step potential method, and after desorption of the platinum nanoparticles, using a current jump. A nucleation potential of **-1600 mV** is applied for **20 ms** and a **600 mV** growth pulse for **30 s** and **60 s**.

Exp conditions	-1600 mV nuc pulse for 20 ms; -200 mV growth pulse for **30 s**				-1600 mV nuc pulse for 20 ms; -200 mV growth pulse for **60 s**			
	Au Oxide Reduction Peak		**Pt Oxide Reduction Peak**		**Au Oxide Reduction Peak**		**Pt Oxide Reduction Peak**	
	E.A.	**S.R.**	**E.A.**	**S.R.**	**E.A.**	**S.R.**	**E.A.**	**S.R.**
Bare Gold Electrode	0.051	1.62	0.000	0.00	0.049	1.57	0.000	0.00
After Pt Deposition	0.043	1.38	0.119	3.79	0.038	1.21	0.238	7.59
After Pt Desorption	0.037	1.18	0.052	1.67	0.062	1.98	0.004	0.12

3.2.3.1.2 SEM Characterisation of Platinum Deposition on Non-Templated Gold Disc Electrodes

Figure 3.7 shows SEM images of platinum deposited onto gold using a -1600 mV nucleation pulse for 20 ms, along with a -200 mV growth pulse applied for 30 s and 60 s, in image A and B respectively. These electrodeposition parameters were chosen in order to compare with the voltammetric characterisation in the previous section. As can be seen from the images, the platinum isn't deposited in uniformly shaped nanoparticles; it is grown in clusters. This confirms the suggestion in the previous section that the platinum grows in clusters, as opposed to nanoparticles. It also confirms why the gold oxide reduction peak in the CV doesn't decrease as much as anticipated when the platinum is deposited. From the SEM image, it is clear that there is still a large amount of gold left bare, as the platinum is in large deposits.

For the 60 s growth time, there are more platinum deposits on the surface due to the longer growth time. This correlates with the voltammetric analysis, showing that there is a larger surface area of platinum present with a longer growth time, at 0.238 cm^2 for the 60 s growth time compared to 0.119 cm^2 for the 30 s growth time. The density of particles for the 30 s growth time is approximately 9 x 10^8 particles per cm^2, and 4 x 10^8 particles per cm^2 for the 60 s growth time. This correlates with the voltammetric characterisation and the SEM images, as even though the electrochemical area of platinum is larger for the 60 s growth time, the deposits clump together into large growths, which therefore means that there are less particles present.

From the analysis of this and the other potentials investigated (shown in the appendix), the parameters for the deposition of platinum that give the largest electrochemical areas can be obtained. All of the results to this point show that the amount of platinum deposited increases as nucleation potential decreases, down to -1800 mV. At -1800 mV the amount of platinum decreases, due to the platinum being knocked off the electrode as the over potential is too low and also due to the evolution of gas that will knock the deposits off the surface. The amount of platinum deposited increases as the growth potential is made more negative also, down to -200 / -300 mV growth

potential; after this, the amount of platinum decreases once again. However, despite a large surface area of platinum being deposited at these potentials, when the SEM images are examined, there is an issue with them for the application required here, i.e., large deposits with a variable size. For this reason, templated platinum nanoparticles were investigated also, and each type will be tested for the DNA detection.

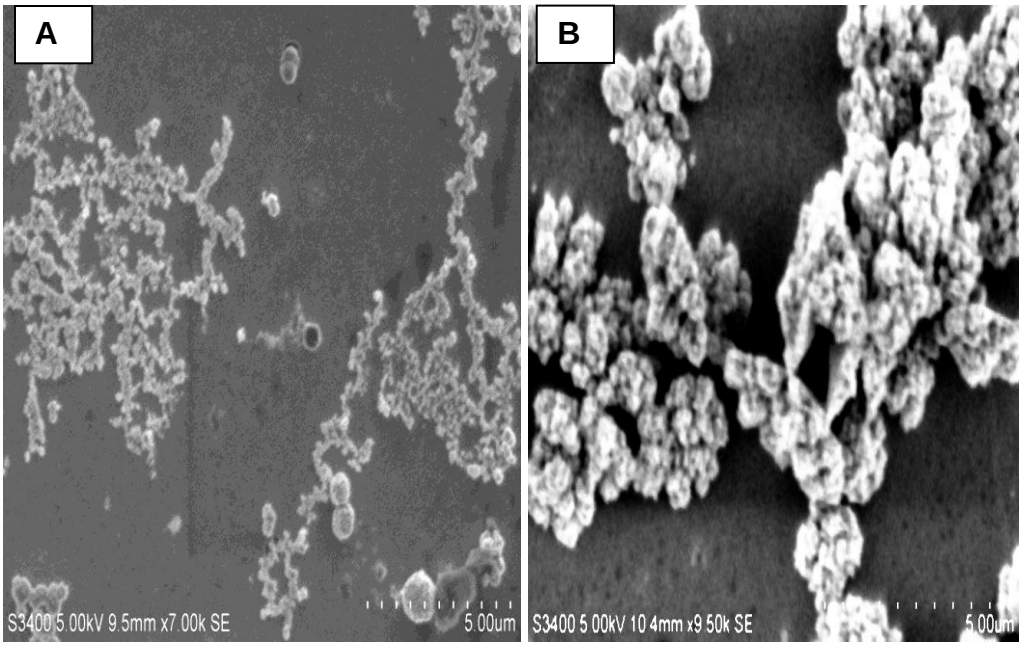

Figure 3.7: Scanning electron micrograph (SEM) images of gold electrodes after electrochemical deposition of platinum using the double pulse potential method. Platinum had been deposited onto **unmodified** gold electrode with a nucleation potential of -1600 mV for 20 ms and a growth potential of -200 mV for 30s **(A)**, and a nucleation pulse of -1600 mV for 20 ms and a growth potential of -200 mV for 60 s **(B)**.

3.2.3.2 Control of Nucleation and Growth using Double-Pulse Method on Self-Assembled Monolayer Modified Gold Disc Electrodes

As growing platinum on bare gold electrodes did not give the optimum platinum nanoparticles required, i.e., size monodisperse and highly electrocatalytic, platinum was then deposited onto electrodes that had been modified with a self-assembled monolayer, as described in Section 2.3.2. These monolayers had defect sites into which the platinum was nucleated and when the growth pulse was applied, the platinum should grow from the nucleation sites, through the defects of the monolayer, and over the top of the monolayer into a hemispherical shape. The exact same potentials were used here as were used to deposit onto the non-templated electrode. Shown in this section are the results from depositing the platinum using a nucleation pulse of -1600 mV for 20 ms and a growth pulse of -200 mV for 30 and 60 s. This was chosen as a direct comparison to the template free data presented above. Also as these were the parameters determined to be optimum for general platinum deposition; this will be discussed further in this section. The results of the other parameters investigated are included in the appendix.

3.2.3.2.1 Voltammetric Characterisation of Platinum Deposition on Self-Assembled Monolayer Modified Gold Disc Electrodes

Figure 3.10 shows a CV of each step for the -1600 mV nucleation potential, with the -200 mV growth potential for both 30 s and 60 s growth times; this relates to the surface roughness factors and electrochemical areas shown in Table 3.3.

The templated response shows features that are similar to those observed for pristine electrodes. The amount of platinum deposited increases as the nucleation potential becomes more negative, down to -1600 mV. The -1800

mV nucleation potential gives very irregular electrochemical areas for each of the growth potentials and times. Once again, this is attributed to gas bubbles being formed during the deposition process, causing the platinum to come away from the electrode. However, compared to the previous experiments with the non-templated electrodes, the electrochemical area of deposited platinum is less, as shown in Table 3.4. A reason for this is most likely due to the dramatically lower gold area.

Similarly once again to the study on bare planar gold, the potentials that give the most platinum deposition are the -1600 mV nucleation pulses, along with the -200 / -300 mV growth pulses, for both the 30 s and 60 s growth times. By looking at Figure 3.8, it is shown that when the self-assembled monolayer is added, the gold oxide reduction peak at 0.8 V decreases as there is much less gold available on the surface, only in the defect sites of the monolayer. Figure 3.8C shows that when the platinum is deposited the gold oxide reduction peak decreases and nearly disappears, as the gold available in the monolayer defect sites is now mainly covered with platinum nanoparticles. The platinum oxide reduction peak appears at 0.3 V, and the water reduction peak at -0.4 V is present when platinum is on the surface also. This correlates to the corresponding electrochemical area values of the gold available on the electrode and of the platinum deposited shown in Table 3.4. For the 60 s growth time, after platinum deposition, the electrochemical area of the gold oxide reduction peak decreases from 0.040 cm^2 with the monolayer, to 0.004 cm^2 with the platinum nanoparticles deposited. This shows that the gold is almost completely covered by both the monolayer and the platinum nanoparticles and there is minimal gold left bare. Figure 3.8D shows a CV when the platinum is desorbed using a current jump. Following desorption the electrochemical surface area of gold calculated from the gold oxide reduction peak increases, showing that the platinum has mostly been desorbed from the surface of the electrode. The gold oxide reduction peak is larger after desorption; the electrochemical area after desorption is 0.055 cm^2 compared to 0.040 cm^2 before platinum deposition. This is due to the large current jump that is applied during the desorption process, which leads to an increase the surface roughness of the electrode surface.

Looking at the platinum oxide reduction peaks in Figure 3.8 and the electrochemical areas in Table 3.4, the increase in platinum deposition correlates to the decrease in gold available. When the platinum was deposited, the platinum oxide reduction peak could be observed in sulphuric acid, and the electrochemical are is 0.236 cm^2 when it was grown for 60 s, as the electrochemical area of the gold oxide reduction peak decreased to 0.004 cm^2. When the platinum is then stripped off, the electrochemical area decreases to 0.003 cm^2, and in Figure 3.8D shows that on the CV that the platinum oxide reduction peak has greatly decreased in comparison to when it was deposited. The minor platinum oxide reduction peak still visible after desorption is most likely due to the platinum nanowire remains in the SAM defect sites.

As the shape, size, and monodispersity of the nanoparticles are vital, SEM images are investigated in the following section to ensure that this is the case.

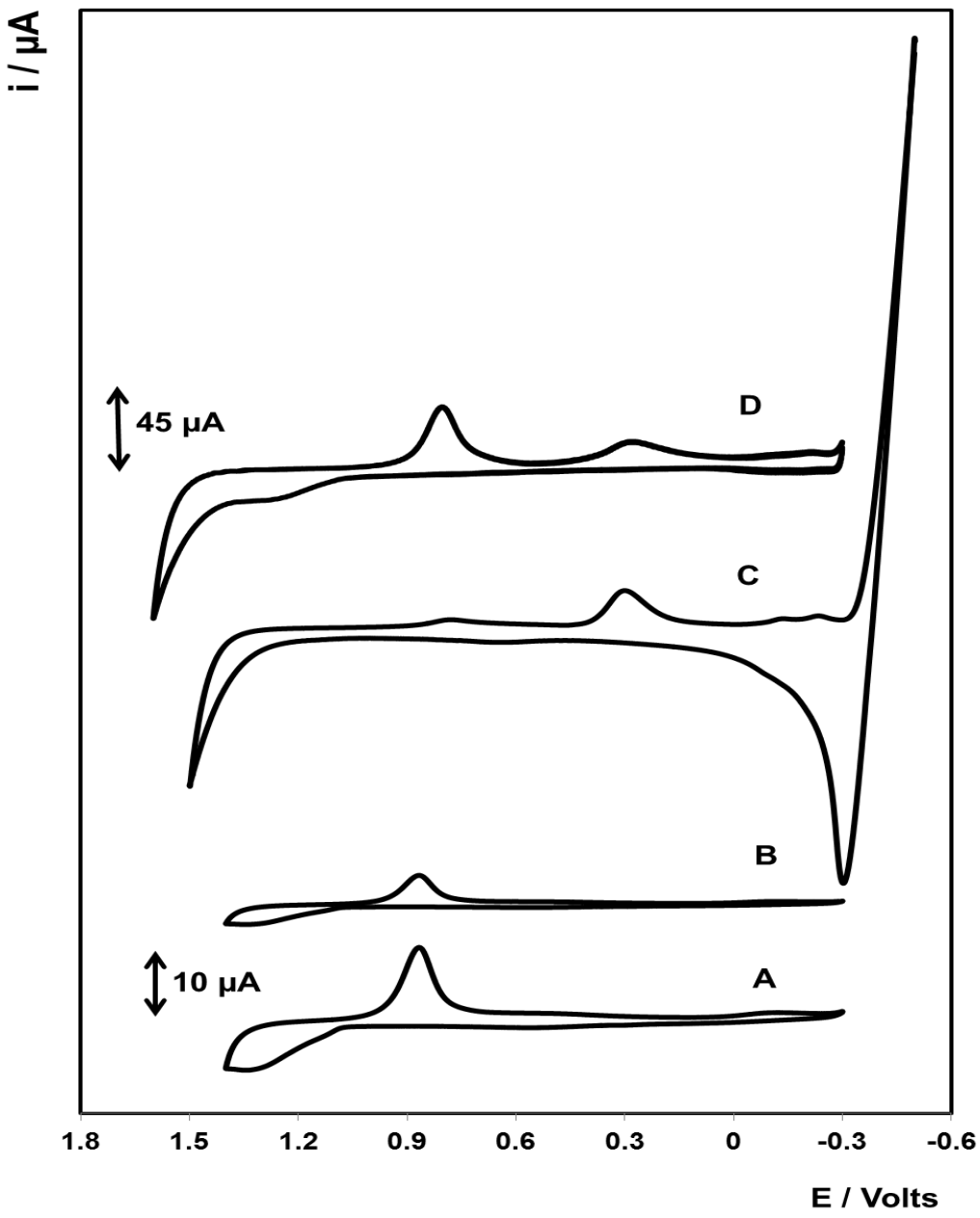

Figure 3.8: Cyclic voltammograms of: **(A)** 2 mm unmodified gold electrode, **(B)** after deposition of a defective monolayer, **(C)** after electrodeposition of platinum into the monolayer defects **(D)** after the platinum nanoparticles have been desorbed. In all cases the supporting electrolyte was 0.1 M H_2SO_4. The voltammograms have been displaced vertically for clarity of presentation.

Table 3.4: Comparison of the electrochemical area (E.A.) and surface roughness factor (S.R.). values of the gold oxide and platinum oxide peaks of a self-assembled monolayer modified gold disc electrode, before and after platinum deposition of a 1mM chloroplatinic acid hydrate solution in 0.5 M H_2SO_4 into the defect sites of the monolayer using the double step potential method, and after desorption of the platinum nanoparticles, using a current jump. A nucleation potential of **-1600 mV** is applied for **20 ms** and a **600 mV** growth pulse for **30 s** and **60 s**.

Exp conditions	-1600 mV nuc pulse for 20 ms; -200 mV growth pulse for **30 s**				-1600 mV nuc pulse for 20 ms; -200 mV growth pulse for **60 s**			
	Au Oxide Reduction Peak		**Pt Oxide Reduction Peak**		**Au Oxide Reduction Peak**		**Pt Oxide Reduction Peak**	
	E.A.	**S.R.**	**E.A.**	**S.R.**	**E.A.**	**S.R.**	**E.A.**	**S.R.**
SAM modified gold electrode	0.035	1.10	0.000	0.00	0.040	1.27	0.000	0.00
After Pt Deposition	0.014	0.46	0.109	3.46	0.004	0.12	0.236	7.51
After Pt Desorption	0.061	1.95	0.003	0.09	0.055	1.75	0.003	0.11

3.2.3.2.2 SEM Characterisation of Platinum Deposition on Self-Assembled Monolayer Modified Gold Disc Electrodes

The platinum nanoparticles were grown onto gold slides, with the same method that was used to deposit onto the gold disc electrodes, in order to view the particles by SEM. Shown in Figure 3.9 are the images for the -1600 mV nucleation pulse for 20 ms and the -200 mV growth pulse for both 30 s (Figure 3.9A) and for 60 s (Figure 3.9B). These parameters were chosen to be presented here as they were determined to be the optimum parameters for platinum deposition, for the type of nanoparticles that are required for the DNA assay.

Once again, the SEM images correlate with the voltammetric characterisation. From the images it can be seen that the amount of exposed underlying gold decreases greatly for the 30 s growth time, and decreases even further for the 60 s growth time and there is a large density of platinum nanoparticles present on the surface. The density of particles deposited using the 30 s growth time was determined to be 4×10^8 particles per cm^2; for the 60 s growth time, the density was 20×10^8 particles per cm^2. This correlates with the electrochemical area of platinum, as it is larger than the gold after deposition. This is important as it shows that the platinum is growing upwards in a mushroom shape, allowing for a larger area available. SEM images for the comprehensive set of conditions investigated are reported in the appendix. In summary, the platinum deposition followed the same trend indicated by the voltammetry; the electrochemical area of platinum increases as the over potential increased, from -1000 mV up – 1800 mV, where it then decreased. For the growth potentials, the electrochemical area of the platinum deposited increases as the overpotential increases again, up to approximately -200 mV.

By looking at the SEM images of all of the different parameters reported in the appendix, it is clear that for a single nucleation potential, as each growth overpotential is increased, the size of the nanoparticles produced does not necessarily increase as expected. Surprisingly, it is the density of the nanoparticles that changes, i.e., additional nanoparticles nucleate even at the

growth potential. This allows great control when growing these particles, and the size and density can both be tuned to what is required of the nanoparticles. This has been reported in literature previously also, and is due to gas evolution and the stability of the nanoparticles when deposited.[26,28] Only the larger particles that are deposited are stable enough to survive some of the growth potentials used.

For the DNA assay size monodisperse nanoparticles are desirable. In the next section, the impact of desorption on the on the nanoparticles' shape, size and monodispersity is reported.

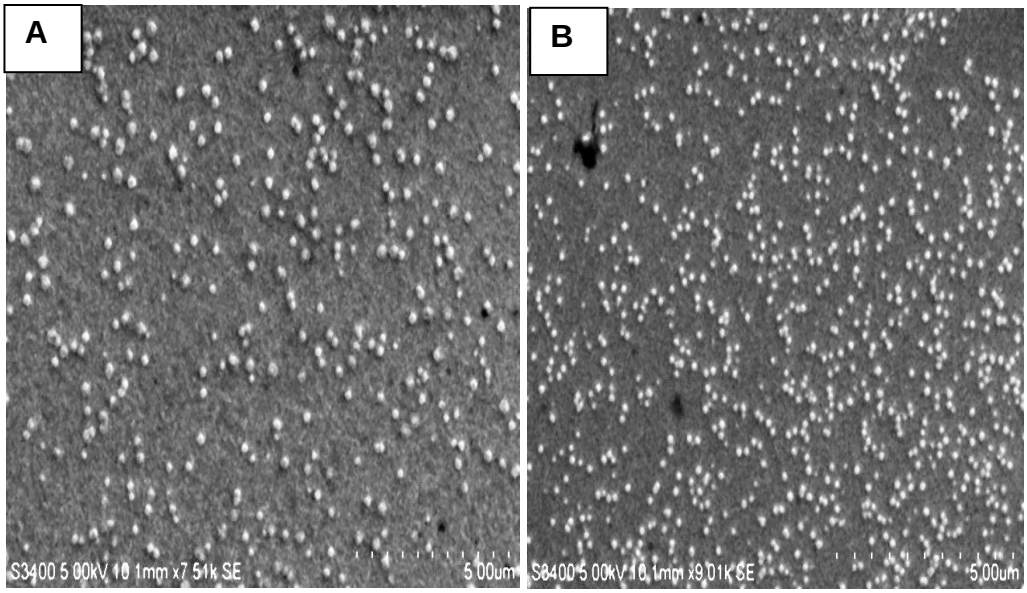

Figure 3.9: Scanning electron micrograph (SEM) images of a gold electrode after electrochemical deposition of platinum using the double pulse potential method. Platinum had been deposited onto a self-assembled monolayer modified gold electrode with a nucleation potential of -1600 mV for 20 ms and a growth potential of -200 mV for 30s (A), and a nucleation pulse of -1600 mV for 20 ms and a growth potential of -200 mV for 60 s (B).

3.2.4 Characterisation of the Desorbed Platinum Nanoparticles

Although the best parameters for the deposition of platinum is a very important factor in this study, what is of even more importance in this case is the structure/properties of the desorbed nanoparticles in solution. This is because these nanoparticles have a dual function, i.e., electrocatalysis and molecular recognition. On the exposed part of the particle when it is deposited, the probe DNA is immobilised (Section 2.3.4.1). Then when desorbed, the particle needs to retain its shape to then hybridise with the target DNA that is bound to the capture strand immobilized on the electrode so as to allow electrocatalysis from the clean underside from where it was desorbed. The desorption process is explained in Section 2.3.5, and the nanoparticles are desorbed into 0.05 M H_2SO_4. A low concentration of H_2SO_4 is used, with the intention of making the solution as close to water as possible, while keeping the acidity to allow ease of desorption of the particles.

3.2.4.1 Characterisation of the platinum nanoparticles desorbed from non-templated gold

3.2.4.1.1 Voltammetric characterisation of platinum nanoparticles desorbed from non-templated gold

A freshly cleaned bare gold disc electrode was cycled in the suspended platinum deposit solution to obtain a CV. Once again, the desorbed platinum deposits from each nucleation and growth potential used in the sections above were investigated.

Shown in Figure 3.10 are the results obtained when the platinum has been deposited using the -1600 mV nucleation pulse for 20 ms and the -200 mV growth pulse for 60 s.

The platinum oxide reduction peak isn't present when the gold electrode is cycled in the suspension due to many complex processes occurring and therefore not achieving a large enough current. It isn't possible to directly compare the deposits that are seen on the surface of the electrode to those that are seen in suspension by cyclic voltammetry, as many factors have an effect. It is likely that the deposits in suspension approach the surface, undergo partial oxidation and leave, with no guarantee that they arrive at the surface for a long enough period for complete oxide formation. Along with this, it is not known exactly how many of the deposits are desorbed. As shown in Figure 3.6, there is still some residual platinum left on the surface after the deposits are removed. It is thought that this could be due to the stripping process; as the platinum deposits are very polydisperse in both size, shape and density, this means that they could break up during this process, as the binding to the underlying gold electrode is strong. This also explains the larger gold oxide reduction peak in Figure 3.6; as the surface of gold electrode is roughened when the deposits are being desorbed.

This could indicate that the desorbed platinum deposits could be even more polydisperse in shape and density when removed. However in the following section, SEM imaging will be used to investigate this further.

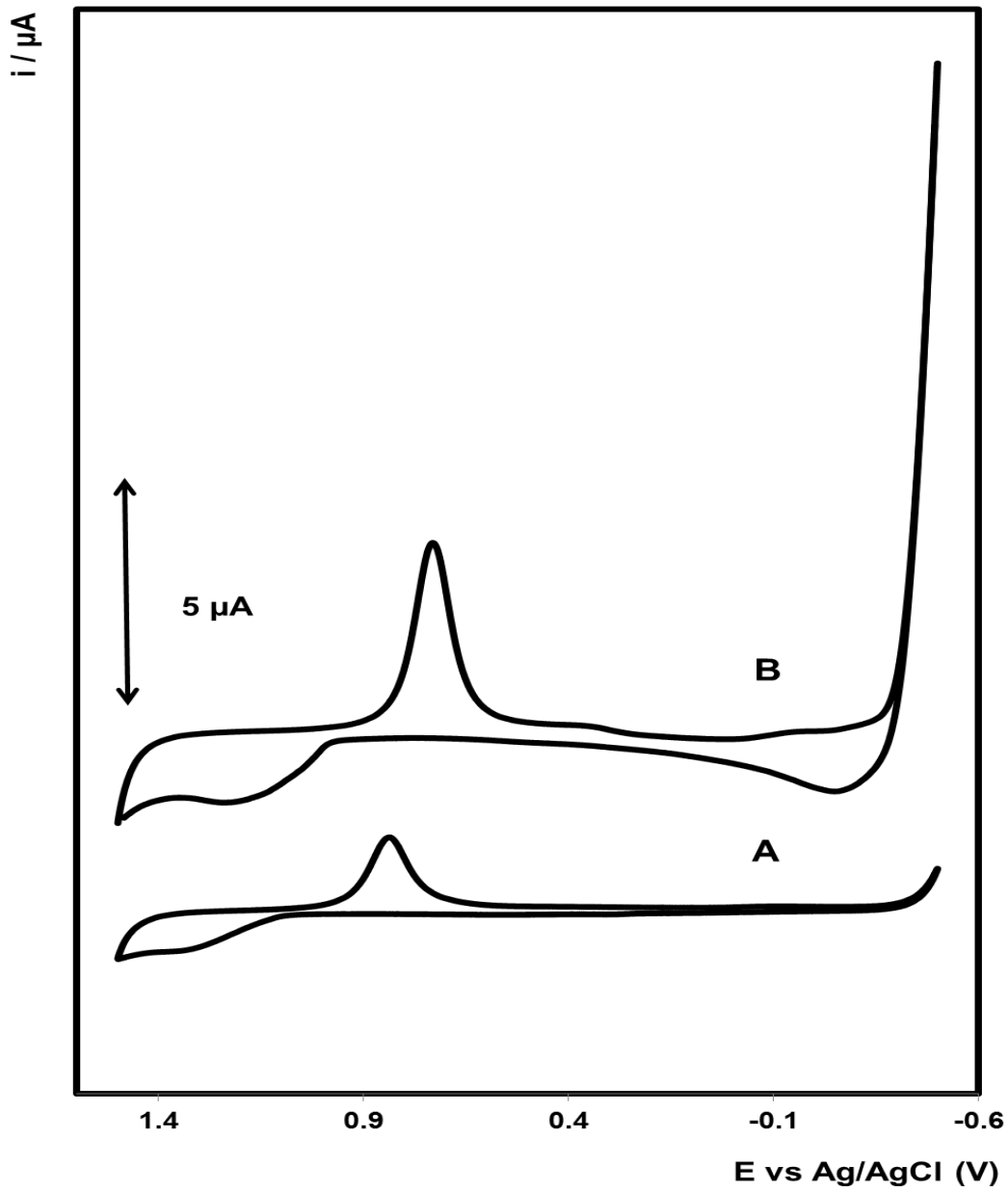

Figure 3.10: As Cyclic voltammograms of: **(A)** 2 mm unmodified gold electrode, **(B)** bare gold electrode cycled in the desorbed PtNP solution in 0.05 M H_2SO_4. The PtNPs were initially deposited onto an unmodified gold disc electrode using a nucleation pulse of -1600 mV for 20 ms, and a growth pulse of -200 mV for 60 s, and were desorbed using a current jump. The voltammograms have been displaced vertically for clarity of presentation.

3.2.4.1.2 SEM Characterisation of Platinum Nanoparticles Desorbed from non-templated gold

Figure 3.11 A and B show the SEM images of the desorbed platinum that was deposited for 30 s and 60 s, respectively. Initially the platinum was deposited onto unmodified gold disc electrodes and then desorbed into suspension. This suspension was centrifuged and then dropcast onto the surface of the clean gold electrodes and allowed to dry. These were then imaged to determine if desorption causes any change in the physical structure of the deposits.

These platinum deposits can be directly compared to those in Figure 3.7, as they were the deposits when initially deposited. What is clear is that the deposits appear similar when desorbed. While the density of these desorbed nanoparticle cannot accurately be compared to the density of the deposited nanoparticles, the size and shape can be, as it is important that this is retained after desorption. By comparing the images before and after desorption, the platinum deposits appear to break apart due to strong binding to the gold surface and therefore don't retain their shape.

The particles are still very size polydisperse, large and irregularly shaped. This trend is observed for platinum deposits created using the wide variety of potentials and different deposition times and these results are included in the appendix. This again is most likely due to the platinum deposits having strong binding to the surface of the gold electrode, due to the large surface area of the platinum on the gold. This therefore makes it harder to break this bond during the stripping process, and hence breaks the deposits into suspension.

The types of particles presented here aren't useful for the detection of DNA strands when they are made in this way. This is as they are irregular in shape, which would in turn make the functionalisation of DNA irregular also. This could inhibit the hybridisation of target DNA strands, if the particle is irregular, as DNA may stick into cracks etc. on the surface and the target strand may not be able to reach it fully and therefore can't hybridise, or the DNA may not be able to assemble onto the particle appropriately. Hence, the size and shape of these particles aren't suitable for this purpose. Nanoparticles desorbed from a SAM template are discussed in the next section.

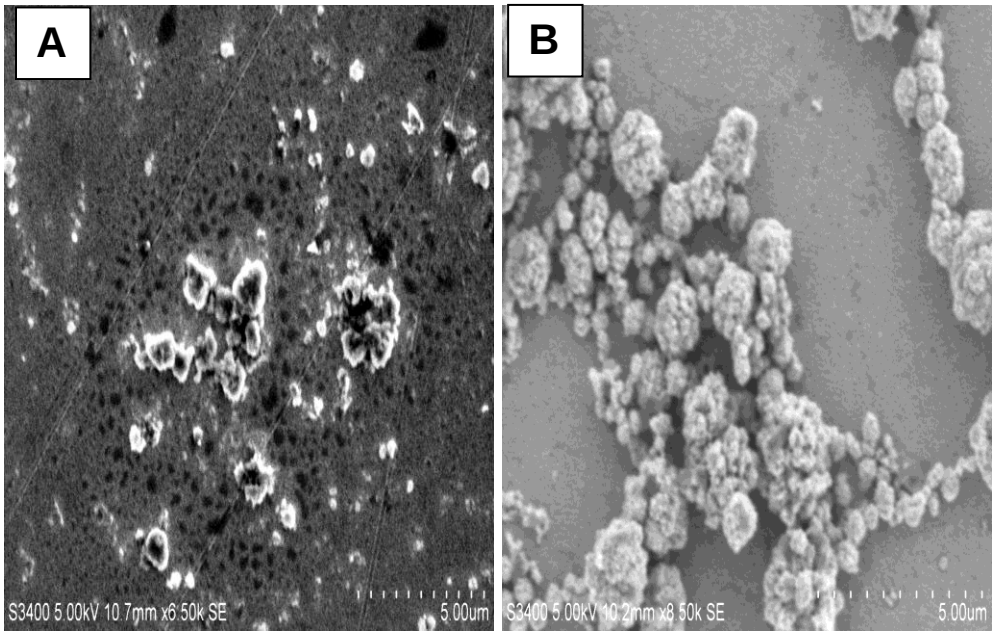

Figure 3.11: Scanning electron micrograph (SEM) images of gold electrodes after dropcasting the centrifuged desorbed platinum deposits onto the surface. Platinum had initially been deposited onto **unmodified** gold electrode with a nucleation potential of -1600 mV for 20 ms and a growth potential of -200 mV for 30s **(A)**, and a nucleation pulse of -1600 mV for 20 ms and a growth potential of -200 mV for 60 s **(B)**.

3.2.4.2 Characterisation of the platinum nanoparticles desorbed from self-assembled monolayer templated gold

3.2.4.2.1 Voltammetric characterisation of platinum nanoparticles desorbed from self-assembled monolayer templated gold

The same experiments described above were carried out with the self-assembled monolayer templated nanoparticles. All of the same parameters were used, except that the platinum was deposited into the defect sites of the monolayer instead of across the electrode surface. A CV of a bare gold disc electrode in sulfuric acid is compared with that of a bare gold disc electrode cycled in the desorbed nanoparticle solution, shown in Figure 3.12. These results are when the platinum was deposited with a nucleation pulse of -1600 mV for 20 ms, along with a growth pulse of -200 mV for 60 s. This growth method was chosen as it was determined to be the best one for the DNA detection application in the following Chapter.

Looking at Figure 3.12, there is a huge difference between these two CVs; mainly the appearance of a large platinum oxide reduction peak at 0.3 V when cycled in the desorbed suspension and the large water reduction peak at -0.4 V also. These both show that there is a large amount of platinum present in the suspension. Although as explained above in Section 3.2.4.1.1, a direct comparison cannot be made between this CV and when the platinum is initially deposited onto the electrode due to the many different processes occurring during this experiment. However, what can be determined is more platinum may be present in this suspension than in the non-templated platinum suspension, due to the larger current achieved and the large hydrogen adsorption/desorption peak.

These results look promising for using the templated nanoparticles for the DNA detection assay, as it shows that the platinum desorbs and remains in suspension. By using the self-assembled monolayer template, the shape of the nanoparticles should be better than that found for deposition onto the bare gold electrode; however SEM imaging will confirm this, and if the shape is retained after desorption.

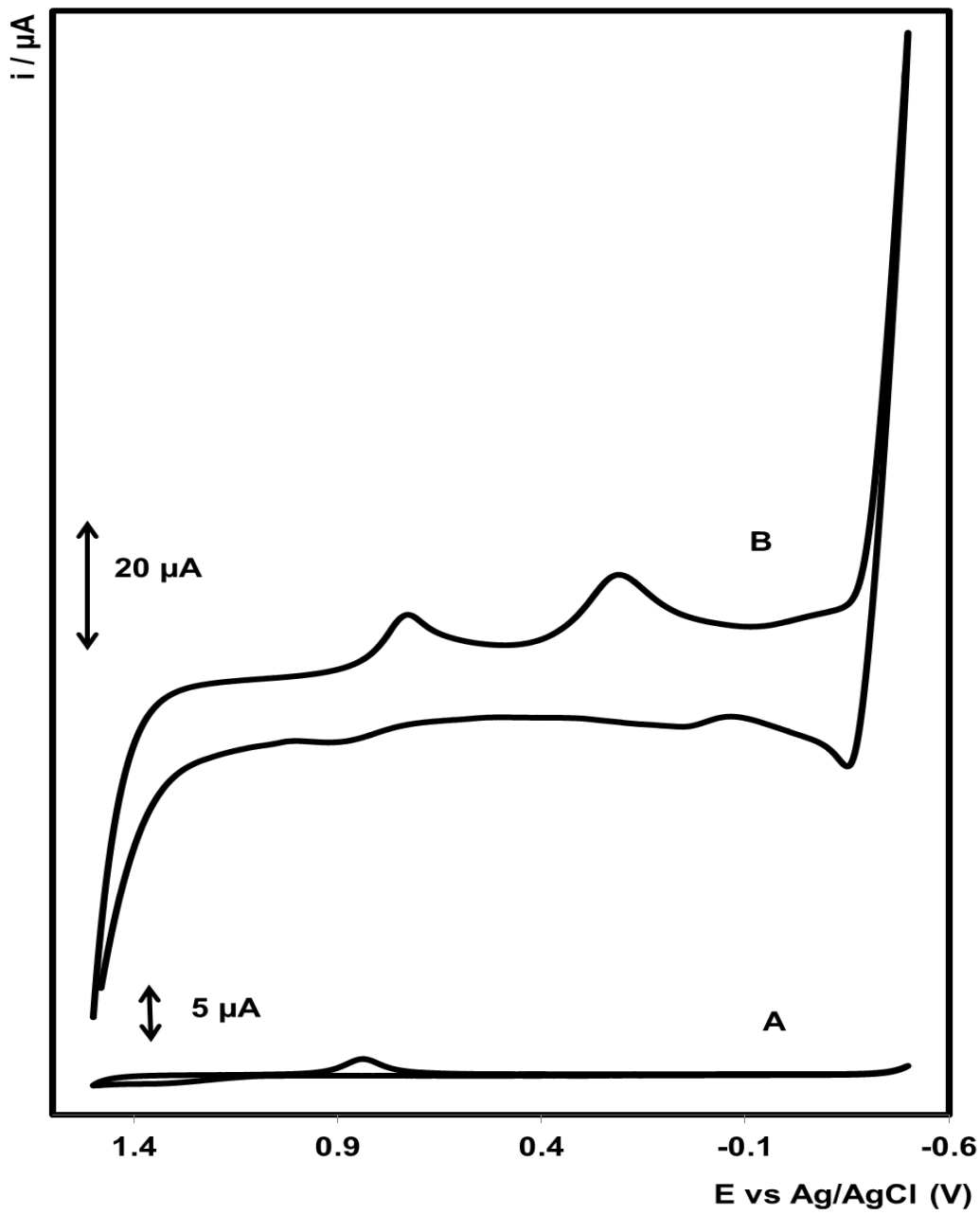

Figure 3.12: Cyclic voltammograms of: **(A)** 2 mm unmodified gold electrode, **(B)** bare gold electrode cycled in the desorbed platinum solution in 0.05 M H_2SO_4. The platinum was initially deposited onto a self-assembled monolayer modified gold disc electrode using a nucleation pulse of -1600 mV for 20 ms, and a growth pulse of -200 mV for 60 s, and were desorbed using a current jump. The voltammograms have been displaced vertically for clarity of presentation.

3.2.4.2.2 SEM characterisation of platinum nanoparticles desorbed from self-assembled monolayer templated gold

Figure 3.13 A and Figure 3.13 B shows SEM images of platinum nanoparticles that were initially grown into the defect sites on self-assembled monolayer modified gold disc electrodes, using a -1600 mV nucleation potential for 20 ms, followed by a growth potential of -200 mV for both 30 s and 60 s respectively; these particles were then desorbed into suspension, centrifuged, and dropcast onto the surface of the gold electrodes and allowed to dry. The corresponding SEM images are shown below.

It is extremely clear that depositing the platinum into defects within the self-assembled monolayer and desorbing them creates well defined nanoparticles. As explained previously, when the growth potential is applied, the particles don't always grow up from all of the nucleation sites; this varies depending on the growth potential applied, and the stability of the nuclei on the surface. This means that the density of nanoparticles can be controlled, along with the size. This is shown with all of the other potentials and time investigated, which are displayed in full in the appendix. However, for the DNA detection assay application, a large density of nanoparticles is desirable which is what is produced by the -1600 mV nucleation pulse for 20 ms, followed by the -200 mV growth pulse for 60 s. These give reasonably size monodisperse, high density nanoparticles.

These platinum deposits are shown to retain their shape when desorbed from the SAM modified electrode. This is due to the template; it allows the particle to be attached to the surface by a narrow wire of platinum, which can easily be broken by applying the current during the stripping process. In comparison to the non-templated deposits, this is an advantage, as it allows a clean break and a nicely shaped particle, as opposed to the size and shape polydisperse particles found after the desorption of the non-templated particles.

These particles allow also for the nanoparticle to have a dual function, which was also required for this application. When the platinum is grown through the

template, it continues over the top of the monolayer into a “mushroom” shape. The top exposed layer can be functionalised prior to desorption, as these SEM images show that the shape of the particles are kept post-desorption. This leaves the exposed under side for catalysis, when the nucleic acid strand is hybridised for detection. This application is shown in the next Chapter.

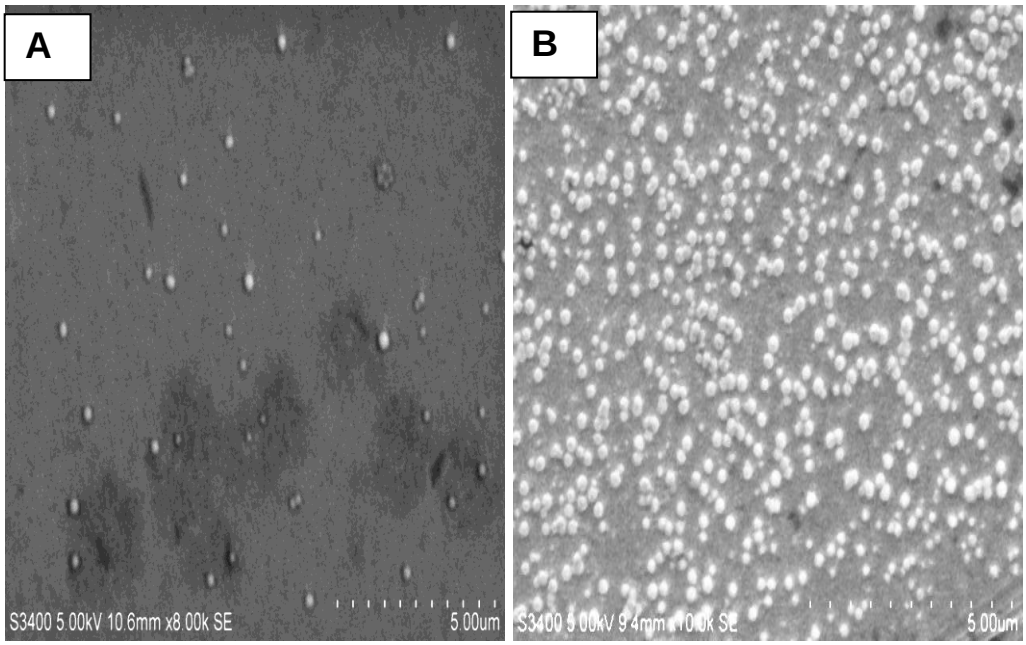

Figure 3.13: Scanning electron micrograph (SEM) images of a gold electrode after dropcasting the centrifuged desorbed platinum nanoparticles onto the surface. Platinum had initially been deposited onto self-assembled monolayer modified gold electrode with a nucleation potential of -1600 mV for 20 ms and a growth potential of -200 mV for 30s **(A)**, and a nucleation pulse of -1600 mV for 20 ms and a growth potential of -200 mV for 60 s **(B)**.

3.3 CONCLUSIONS

The electrochemical deposition of platinum nanoparticles onto gold disc electrodes was investigated. The influence of the applied potential was examined by varying the potentials and examining the resulting nanoparticles. It was found by applying a very large overpotential for a short time (20 ms), followed by a longer growth pulse at a lower overpotential, allowed the size and density of the nanoparticles to be controlled.

Two methods to control the size and density of the platinum nanoparticles were investigated. The platinum nanoparticles were electrodeposited onto bare gold disc electrodes, and also into defects within a self-assembled monolayer formed on gold disc electrodes. By modifying the surface of the electrode, nanoscale defects sites were formed on the surface within which the platinum could be initially deposited and then grow over the edge of the monolayer, forming mushroom shaped nanoparticles, which could be advantageous for the DNA assay application of the platinum nanoparticles that is required here, as it separates the two functions of the nanoparticle.

The optimum parameters for creating a high density of size monodisperse nanoparticles were investigated by using a wide range of potentials for both the nucleation potential and for the growth potential, and also by varying the length of the growth time. It was determined that the optimum nanoparticles were obtained by applying a nucleation potential of -1600 mV for 20 ms, then changing the potential to -200 mV and allowing the nanoparticles to grow for 60 s, on the self-assembled monolayer modified gold disc electrode. This high nucleation potential at a short burst allowed the surface of the electrode to be nucleated with the platinum, with a sufficient decrease in the diffusion zone coupling to not increase particle size polydispersity. The longer growth pulse at the lower overpotential allowed the nanoparticles to be grown up from these nucleation sites. Many different nucleation and growth potentials were investigated, and it was shown that by varying these parameters, along with varying the growth times, the size and density of the particles could be

controlled. This is because at different growth potentials, a different amount of platinum particles will grow up from the nucleation sites. For the applications demonstrated in later chapters, a high density of particles were needed, and therefore these potentials were determined to be the best for this case.

The self-assembled monolayer template gave more structure to the nanoparticle, which again benefits the later applications, as they can have a dual function when functionalised on the top side with a nucleic acid, and have the clean underside for electrocatalysis. Size monodisperse nanoparticles are needed for electrocatalysis in a nucleic acid assay, as the electrocatalytic current is proportional to the size of the nanoparticle. At low concentration of nucleic acid, when there may be a small number of nanoparticles bound to the electrode, if these particles are polydisperse in size, the electrocatalytic current will be significantly varied, and therefore detection of low concentrations of nucleic acids may not be accurate.

The advantages of using a template-free system are that it can be achieved over a large area, and has a shorter fabrication process, as the SAM does not need to grow. However, by using the SAM template, the particle size and distribution is tighter, the particles are easier to desorb and retain their shape after desorption, and they are asymmetric which is beneficial for applications. The electrocatalytic efficiency of both particles will be looked at in Chapter 4.

3.4 REFERENCES

1. Dong, H.; Jin, S.; Ju, H.; Hao, K.; Xu, L.; Lu, H.; Zhang, X. Trace and Label-Free MicroRNA Detection Using Oligonucleotide Encapsulated Silver Nanoclusters as Probes. *Anal. Chem.* **2012***, 84*, 8670-8674.

2. Chen, S.; Yuan, R.; Chai, Y.; Hu, F. Electrochemical sensing of hydrogen peroxide using metal nanoparticles: a review. *Microchim. Acta* **2013***, 180*, 15-32.

3. Shandost-fard, F.; Salimi, A.; Khezrian, S. Highly selective and sensitive adenosine aptasensor based on platinum nanoparticles as catalytical label for amplified detection of biorecognition events through H2O2 reduction. *Biosens. Bioelectron.* **2014***, 53*, 355-362.

4. Polsky, R.; Gill, R.; Kaganovsky, L.; Willner, I. Nucleic acid-functionalized Pt nanoparticles: Catalytic labels for the amplified electrochemical detection of biomolecules. *Anal. Chem.* **2006***, 78*, 2268-2271.

5. Steele, B.; Heinzel, A. Materials for fuel-cell technologies. *Nature* **2001***, 414*, 345-352.

6. Luo, J.; Wang, L.; Mott, D.; Njoki, P. N.; Lin, Y.; He, T.; Xu, Z.; Wanjana, B. N.; Lim, I. -. S.; Zhong, C. Core/Shell Nanoparticles as Electrocatalysts for Fuel Cell Reactions. *Adv Mater* **2008***, 20*, 4342-4347.

7. Zhang, X.; Lu, W.; Da, J.; Wang, H.; Zhao, D.; Webley, P. A. Porous platinum nanowire arrays for direct ethanol fuel cell applications. *Chem. Commun.* **2009**, 195-197.

8. Suntivich, J.; Gasteiger, H. A.; Yabuuchi, N.; Nakanishi, H.; Goodenough, J. B.; Shao-Horn, Y. Design principles for oxygen-reduction activity on perovskite oxide catalysts for fuel cells and metal-air batteries. *Nat. Chem.* **2011***, 3*, 546-550.

9. Kloke, A.; von Stetten, F.; Zengerle, R.; Kerzenmacher, S. Strategies for the Fabrication of Porous Platinum Electrodes. *Adv Mater* **2011***, 23*, 4976-5008.

10. El Roustom, B.; Sine, G.; Foti, G.; Comninellis, C. A novel method for the preparation of bi-metallic (Pt-Au) nanoparticles on boron doped diamond (BDD) substrate: application to the oxygen reduction reaction. *J. Appl. Electrochem.* **2007***, 37*, 1227-1236.

11. Birtcher, R.; Donnelly, S.; Schlutig, S. Nanoparticle ejection from Au induced by single Xe ion impacts. *Phys. Rev. Lett.* **2000***, 85*, 4968-4971.

12. Hirasawa, M.; Shirakawa, H.; Hamamura, H.; Egashira, Y.; Komiyama, H. Growth mechanism of nanoparticles prepared by radio frequency sputtering. *J. Appl. Phys.* **1997***, 82*, 1404-1407.

13. Kaatz, F.; Chow, G.; Edelstein, A. Narrowing Sputtered Nanoparticle Size Distributions. *J. Mater. Res.* **1993***, 8*, 995-1000.

14. Dokoutchaev, A.; James, J.; Koene, S.; Pathak, S.; Prakash, G.; Thompson, M. Colloidal metal deposition onto functionalized polystyrene microspheres. *Chem. Mat.* **1999***, 11*, 2389-2399.

15. Jana, N.; Gearheart, L.; Murphy, C. Wet chemical synthesis of silver nanorods and nanowires of controllable aspect ratio. *Chem. Commun.* **2001**, 617-618.

16. Bertino, M. F.; Gadipalli, R. R.; Martin, L. A.; Story, J. G.; Heckman, B.; Guha, S.; Leventis, N. Patterning porous matrices and planar substrates with quantum dots. *J. Sol Gel Sci. Technol.* **2006***, 39*, 299-306.

17. Fukushima, M.; Yanagi, H.; Hayashi, S.; Suganuma, N.; Taniguchi, Y. Fabrication of gold nanoparticles and their influence on optical properties of dye-doped sol-gel films. *Thin Solid Films* **2003***, 438*, 39-43.

18. Ke, J.; Su, W.; Howdle, S. M.; George, M. W.; Cook, D.; Perdjon-Abel, M.; Bartlett, P. N.; Zhang, W.; Cheng, F.; Levason, W.; Reid, G.; Hyde, J.; Wilson, J.; Smith, D. C.; Mallik, K.; Sazio, P. Electrodeposition of metals from supercritical fluids. *Proc. Natl. Acad. Sci. U. S. A.* **2009***, 106*, 14768-14772.

19. Dharmadasa, I.; Haigh, J. Strengths and advantages of electrodeposition as a semiconductor growth technique for applications in macroelectronic devices. *J. Electrochem. Soc.* **2006***, 153*, G47-G52.

20. Spain, E.; Brennan, E.; McArdle, H.; Keyes, T. E.; Forster, R. J. High Sensitivity DNA Detection Based on Regioselectively Decorated Electrocatalytic Nanoparticles. *Anal. Chem.* **2012***, 84*, 6471-6476.

21. Liu, H.; Penner, R. Size-selective electrodeposition of mesoscale metal particles in the uncoupled limit. *J Phys Chem B* **2000***, 104*, 9131-9139.

22. Liu, H.; Favier, F.; Ng, K.; Zach, M.; Penner, R. Size-selective electrodeposition of meso-scale metal particles: a general method. *Electrochim. Acta* **2001***, 47*, 671-677.

23. Penner, R. Mesoscopic metal particles and wires by electrodeposition. *J Phys Chem B* **2002***, 106*, 3339-3353.

24. Niu, L.; Li, Q.; Wei, F.; Wu, S.; Liu, P.; Cao, X. Electrocatalytic behavior of Pt-modified polyaniline electrode for methanol oxidation: Effect of Pt deposition modes. *J Electroanal Chem* **2005***, 578*, 331-337.

25. Peng, Z.; Yang, H. Designer platinum nanoparticles: Control of shape, composition in alloy, nanostructure and electrocatalytic property. *Nano Today* **2009***, 4*, 143-164.

26. Ueda, M.; Dietz, H.; Anders, A.; Kneppe, H.; Meixner, A.; Plieth, W. Double-pulse technique as an electrochemical tool for controlling the preparation of metallic nanoparticles. *Electrochim. Acta* **2002***, 48*, 377-386.

27. Sheridan, E.; Hjelm, J.; Forster, R. J. Electrodeposition of gold nanoparticles on fluorine-doped tin oxide: Control of particle density and size distribution. *J Electroanal Chem* **2007***, 608*, 1-7.

28. Sandmann, G.; Dietz, H.; Plieth, W. Preparation of silver nanoparticles on ITO surfaces by a double-pulse method. *J Electroanal Chem* **2000***, 491*, 78-86.

CHAPTER 4

ELECTROCHEMICAL DNA BIOSENSOR BASED ON PLATINUM NANOPARTICLES

4.1 INTRODUCTION

The detection and quantitation of specific nucleic acid sequences continues to grow in importance and as a field of increasing interest.[1,2] The robust, low cost detection of low concentrations of nucleic acid based biomarkers of disease or specific mutations requires highly sensitive detection strategies to be developed so that the disease can be detected before any clinical symptoms appear.[3]

DNA and RNA can be important biomarkers of disease, i.e. they can be found in body fluid or tissue when disease is present. A strong emphasis is now being placed on the development of point-of-care devices which can determine the concentration of these biomarkers in different sample matrices such as blood, saliva, urine, etc.[4]

The DNA target of interest in this chapter is the gram positive bacterium Staphylococcus Aureus, which is responsible for mastitis in cows, and a range of other illnesses in humans, ranging from minor skin infections,[5] for example cellulitis and cutaneous abscesses, scalded skin syndrome,[6], pimples and boils, to more serious infections such as meningitis,[7] pneumonia,[5], toxic shock syndrome[6], food poisoning[8] and sepsis.

Symptoms of mastitis in cattle are abnormalities in the udder such as swelling, redness and hardness, or in the milk such as watery appearance, flakes or clots. Milk from cows with mastitis also has a higher somatic cell count (SCC). Generally speaking, the higher the somatic cell count, the lower the milk quality.[9] Current methods of detection include:[10]

- California Mastitis Test; this indirectly measures the SCC in milk by breaking down the somatic cells and measuring the viscosity of the released nucleic acids in proportion to the leukocyte number.
- Portacheck; this is an enzymatic reaction to determine the SCC.
- Fossomatic SCC; this uses optical fluorescence to determine the SCC.

- Delaval cell counter; this also uses optical fluorescence to determine the SCC but uses a different stain to do so.
- Electrical Conductivity Test; this measures the increase in conductance in milk in relation to the increases level of ions present due to inflammation.
- Culture tests; this identifies the different organisms involved in causing mastitis.
- pH tests; the pH of milk rises due to mastitis.
- Enzymes; assays are used to detect enzymes which are present or elevated due to mastitis.

A major disadvantage of these assays is that they are used to detect mastitis in the milk, when milk has already been produced by the infected cow. By developing a method to detect the DNA from the mastitis causing microorganism when it is present in low concentrations in blood, perhaps even before symptoms appear, treatment could begin earlier and could prevent loss of income to the farmer by avoiding producing spoiled milk.

This chapter describes the development of a sensitive electrochemical sensor for the detection of the single stranded DNA associated with the mastitis causing pathogen Staphylococcus Aureus. Current methods of DNA detection include PCR, gel electrophoresis and southern blotting.[11] These methods are time consuming, labour intensive, expensive and require specialised equipment, along with having low sensitivity. One of the main challenges in creating an electrochemical detection platform is amplifying the biorecognition events so that they can be easily detected. For example, metal nanoparticles can be used to amplify the recognition event in DNA hybridisation.[12-14]

Previous work by our group reported hemispherical metal nanoparticles that are regioselectively functionalised on one side with DNA can detect a target strand of DNA at concentrations as low as picomolar without the need for amplification, e.g., by PCR, of the target.[15,16] Hemispherical gold nanoparticles were obtained by laying a defective self-assembled monolayer on the electrode before deposition, using a HRP label for DNA detection. Hemispherical platinum nanoparticles have also been made and utilised in a

similar manner. In contrast, the detection comes from the electrocatalytic platinum nanoparticle label on the DNA instead of the HRP label. In this chapter, the platinum nanoparticles that have been optimized in Chapter 3 are used for electrocatalysis in order to improve the sensitivity and signal achieved during DNA detection. As illustrated in Figure 4.1, in this model the capture DNA strand is immobilised onto the gold disc electrode surface via a 5' thiol terminal on the DNA strand. The target DNA is complementary to a section of the capture strand. The platinum nanoparticles are formed at a different electrode, and regioselectively functionalised with probe strand DNA. When the probe DNA functionalised nanoparticles are desorbed from the electrode surface, the target DNA hybrid is exposed to the nanoparticle/probe DNA suspension; as the probe DNA strand is complementary to the end of the target DNA strand, a fully hybridised sequence is formed, with the platinum nanoparticle at the end of the sequence. These binding events can then be detected using hydrogen peroxide reduction at the platinum nanoparticle.[17,18]

As the amount of platinum brought to the surface of the electrode depends on the amount of target DNA present, the signal generated is proportional to the target concentration. The objective is that the platinum nanoparticle increases the detection sensitivity by amplifying the signal generated by the target binding event. This is in contrast to current nucleic acid detection strategies that amplify the nucleic acid itself, such a PCR or NASBA. By using a hemispherical nanoparticle that is regioselectively functionalised, the two functions of the nanoparticle are separated; the curved upper side is for biorecognition and the underside is for signal generation. By separating the two functions, it is intended that a larger electrocatalytic current is generated because the peroxide does not have to move through the nucleic acid capture strands.

The advantage of this approach is that it does not require nucleic acid amplification, making it easier to incorporate into a point-of-care device that is user friendly. It also means that this system should also be applicable to other diseases, as it is not dependent on the specific target pathogen strand.

4.2 RESULTS AND DISCUSSION

4.2.1 Electrode Formation and Characterisation

The target DNA concentration was determined by measuring the difference in the electrocatalytic reduction current at the platinum nanoparticles, Δi, before and after the addition of 2 mM hydrogen peroxide to a solution of deoxygenated 0.01 M H_2SO_4.

Figure 4.2 shows an SEM image of this fully hybridised electrode at which the assay is performed. In this case the target DNA concentration is 1 µM. Some of the platinum nanoparticles are highlighted for clarity. This shows that there are many binding events occurring on the electrode, and therefore there is a large amount of platinum present on the surface for catalysis during the DNA detection assay.

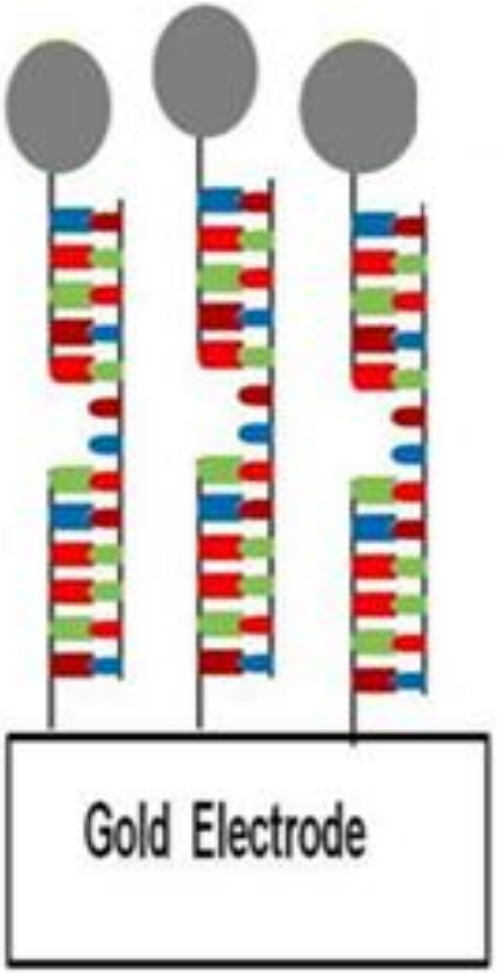

Figure 4.1: Schematic diagram of platinum nanoparticle modified gold electrode, hybridised with capture, target and probe DNA.

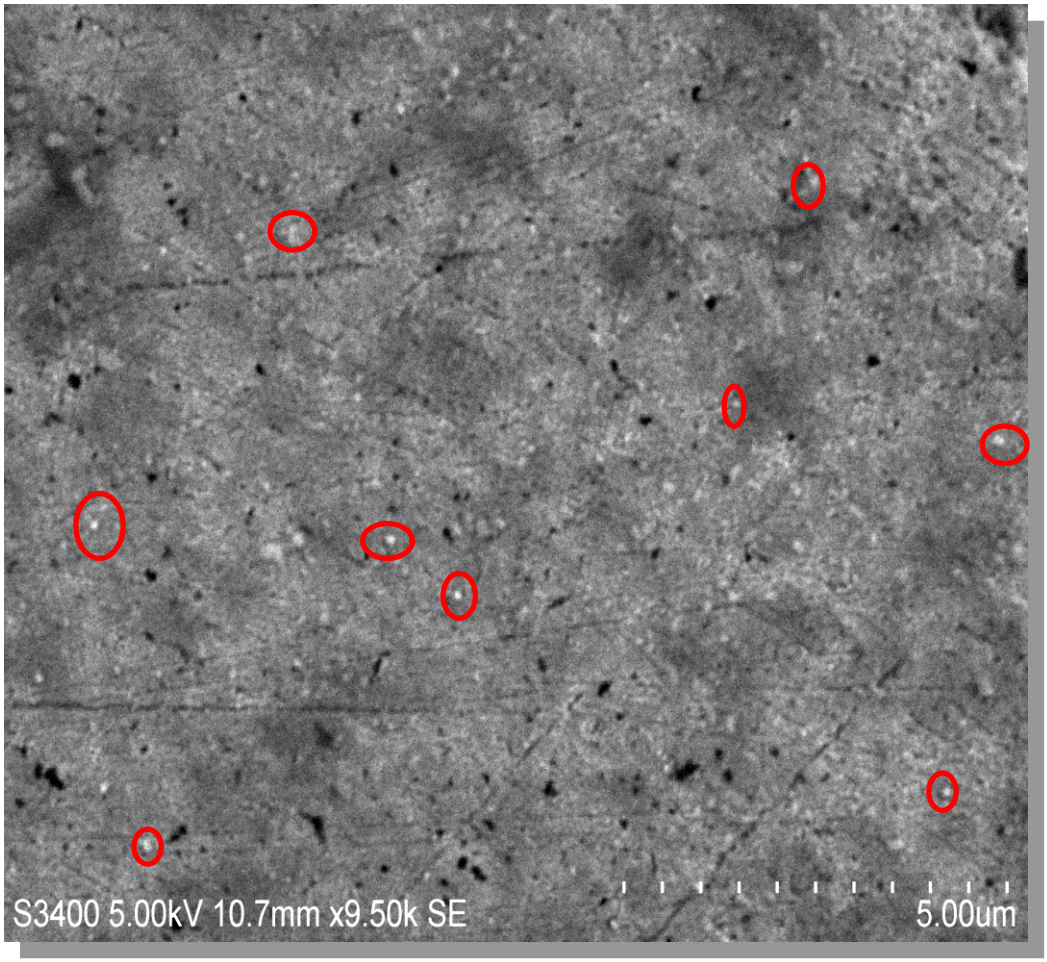

Figure 4.2: SEM image of gold slide modified with platinum nanoparticles which are immobilised to the surface via capture, target and probe DNA hybridisation.

4.2.2 Electrochemical Detection of DNA

The potential that is applied was -0.25 V which is obtained from a CV of platinum; it is a point where there are no redox processes occurring, but at an overpotential. The shape of the transient is due to Butler-Volmer kinetics; as a highly negative overpotential is applied, the rate of the reaction increases. The current will decay to almost zero after approximately 5 min. The initial current was approximately 0.01 µA for each concentration; when 2 mM hydrogen peroxide was added, the biosensor responded rapidly. Each concentration reached a steady state current in 300 – 1200 s, depending on the target concentration.

The current due to H_2O_2 reduction is being measured here. The limiting factor of the current is the radial diffusion of H_2O_2 to the platinum nanoparticles. As the H_2O_2 is reduced at the platinum surface, a layer of diminished peroxide surrounds the platinum. H_2O_2 in the bulk solution will diffuse to the platinum, but this diffusion rate is very slow, at approx. 10^{-5} cm^2/s. This diffusion limits the current and is what causes the transient to plateau. The magnitude of the current is influenced by the area of platinum, which depends on the target concentration as it is through complementary DNA hybridisation that the platinum is brought to the electrode surface; therefore for higher concentrations of target DNA, there is more platinum and a greater current.

For higher concentrations, a longer time is required for the current to plateau. This could be due to the diffusion zones of the nanoparticles overlapping if the particles are close together on the surface. This would mean that diffusion is much less efficient than isolated nanoparticles, and it takes longer to reach equilibrium.

However, the response time of this biosensor is still very fast. A steady-state current is achieved in 20 min after H_2O_2 injection, even for the highest concentrations, which is a very quick response time. The implications of this fast response time is of great benefit for point-of-care diagnostics, as the biosensor could be used in clinical settings, without having to wait for lengthy

amplification processes, such as PCR or NASBA which take hours to complete.

Using a concentration range of target DNA from 1 μM to 1 aM the electrocatalytic properties of the platinum nanoparticles towards H_2O_2 was investigated. The calibration plot of the semi-log concentration of DNA vs. Δi is shown in Figure 4.4. The observation that the change in current increases with log [DNA] rather than [DNA] suggests that the current response is influenced by the H_2O_2, as well as the DNA concentration.

The calibration curve gives a sigmoidal response, which is characteristic of this type of curve. There is an upper and a lower limit. The lower limit is the concentration of target DNA, which in this calibration curve is 10 aM. The upper limit depends on the area of the electrode available for the platinum nanoparticles to fit onto the surface. This is not an issue in this instance, as there is not enough target strands present to hybridise to all of the capture on the surface to then make a complete monolayer of nanoparticles. The current generated is also a factor in this. As mentioned above, the current generated is limited by the diffusion of the H_2O_2, so as more platinum nanoparticles are hybridised to the surface, they have the ability to form aggregates, that are microelectrode in size on the surface, and therefore the diffusion takes longer. This accounts for the current not increasing in proportion to the target concentration increasing.

However, the current still increases as the concentration increases over many orders of magnitude. Each concentration is selective and has a large current range between each concentration, as shown in Table 4.1; each concentration has a significant current associated with it, varying from 2.84 to 0.54 mA. Even at very low concentrations the standard deviations are low for three replicate measurements involving three independently prepared electrodes. This is due to the size monodisperse nanoparticles that are made in Chapter 3.

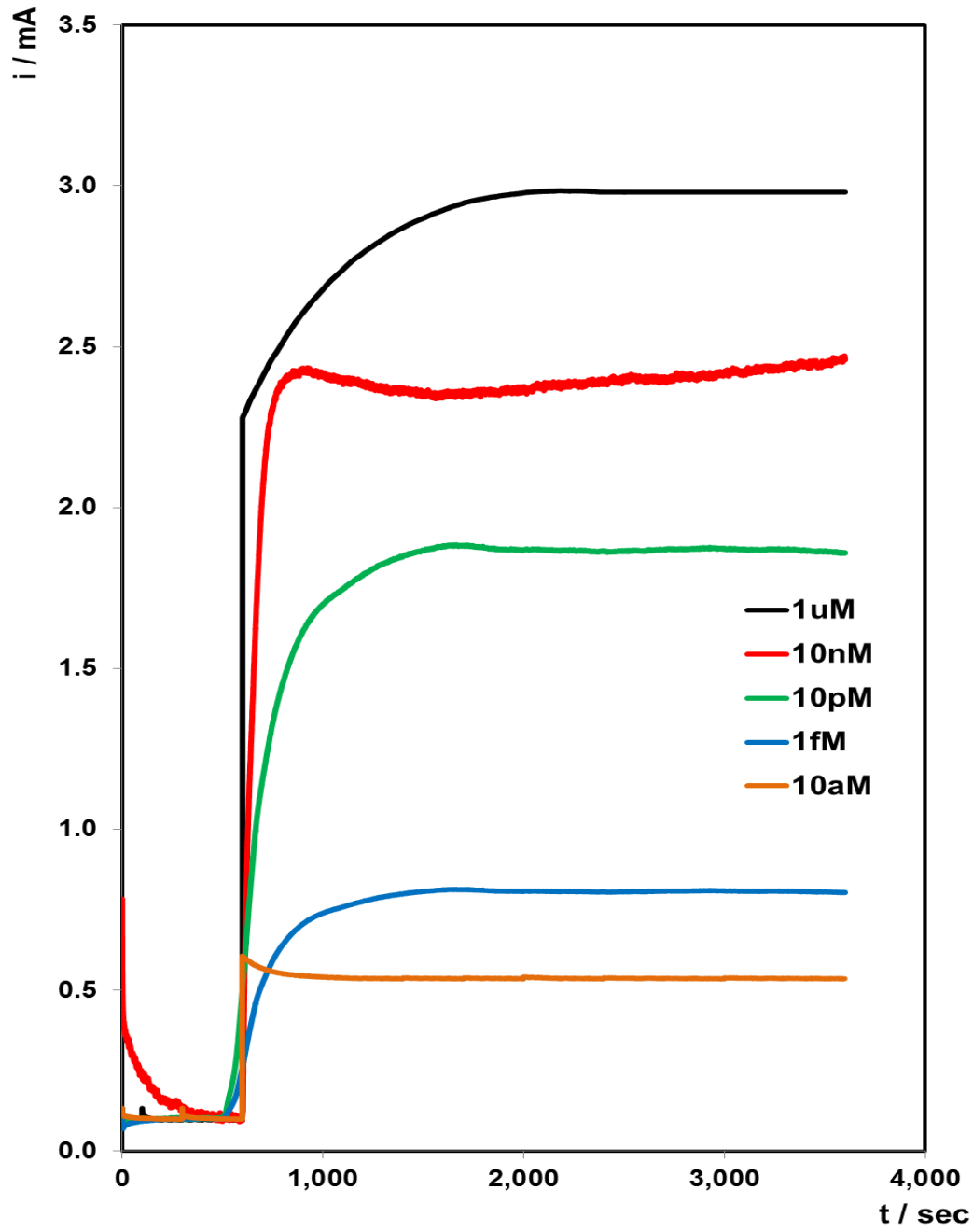

Figure 4.3: Amperometric i-t curves for individual gold electrodes functionalised with ss-DNA (1 µM capture strand, 1 µM probe strand with platinum nanoparticle label, and varying concentrations of target strand, as labelled). Potential applied is -0.25 V in 0.01 M H_2SO_4. Difference in current response before and after the addition of 2 mM H_2O_2 is measured.

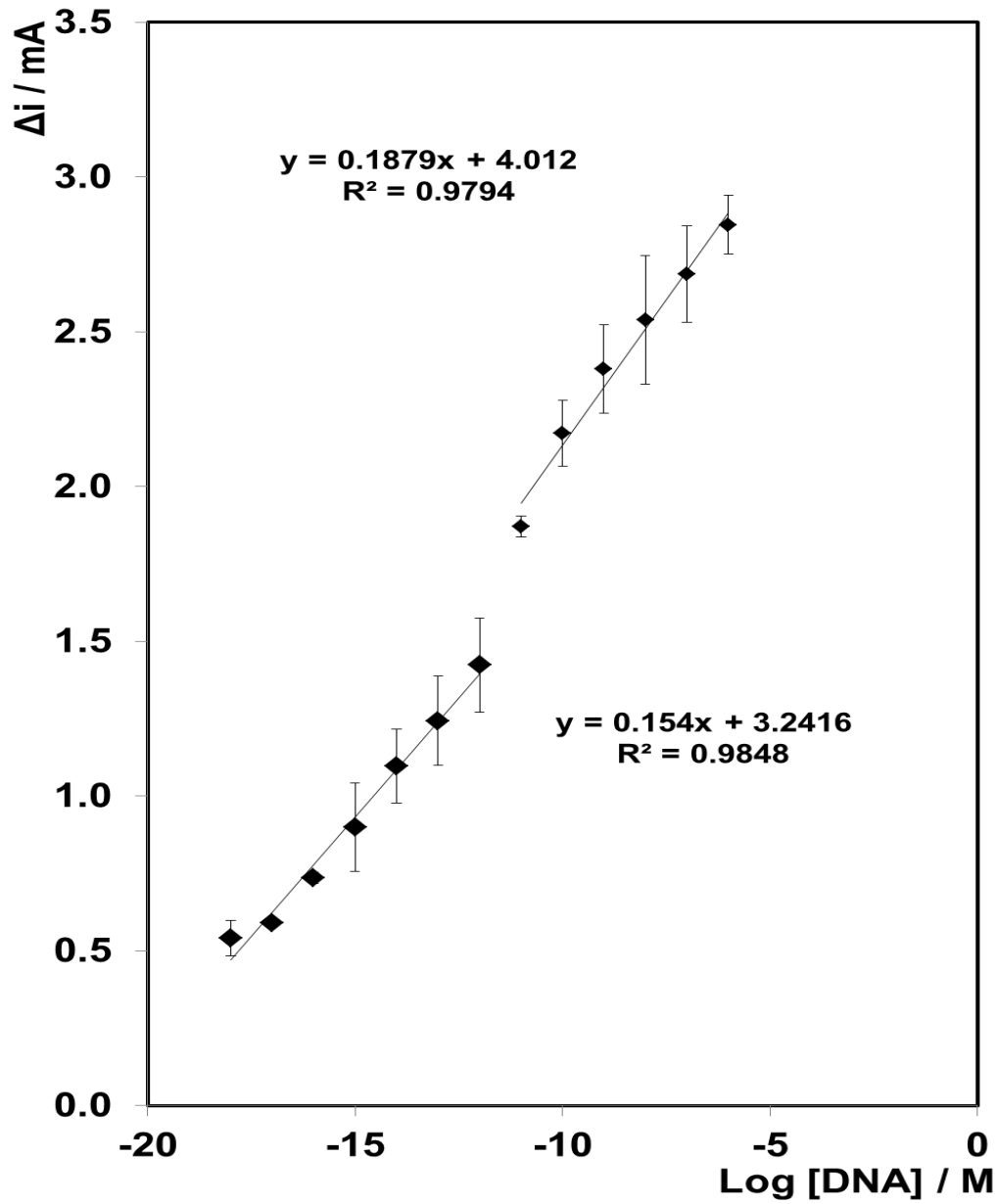

Figure 4.4: Electrochemical detection of sequence specific S. Aureus pathogen DNA concentration. The Y axis is the difference in current before and after addition of 2 mM of H_2O_2 (Δi). The applied potential is -0.25 V in 0.01 M H_2SO_4. Where error bars are not visible, they are smaller than, or comparable to, the size of the symbols.

Table 4.1: Change in current before and after the injection of H_2O_2 for varying concentrations of target DNA.

Concentration of target DNA (M)	Log [DNA]	Average Δi (mA)	Standard Deviation
1.00E-18	-18	0.54	0.06
1.00E-17	-17	0.59	0.01
1.00E-16	-16	0.74	0.02
1.00E-15	-15	0.90	0.14
1.00E-14	-14	1.10	0.12
1.00E-13	-13	1.24	0.14
1.00E-12	-12	1.42	0.15
1.00E-11	-11	1.87	0.03
1.00E-10	-10	2.17	0.11
1.00E-09	-9	2.38	0.14
1.00E-08	-8	2.54	0.21
1.00E-07	-7	2.69	0.16
1.00E-06	-6	2.84	0.09

4.2.2.1 Control Experiments

Various control studies were also carried out. Shown in Figure 4.5 is a calibration curve of the full electrode (as Figure 4.4) and also the calibration curve which used platinum deposits that were initially deposited onto a bare unmodified gold disc electrode; i.e. platinum nanoparticles that were also studied in Chapter 3. Using regioselectively functionalised, hemi-spherical platinum nanoparticles clearly generates a much larger signal. This biosensor is ten times more sensitive than the non-templated platinum nanoparticles. While a significant current is achieved by using these nanoparticles, the dynamic range isn't very large; the change in current increases from 0.34 to 0.83 from 1 aM to 1 μM concentrations, which doesn't give much resolution between each concentration. The reason for the decrease in sensitivity between the two different types of particles is due to the size and shape of the non-templated deposits. As explained in Chapter 3, when platinum is deposited directly onto the gold electrode, the deposition process isn't controlled and therefore large masses of platinum are formed. These masses are much less catalytically efficient than the regioselectively functionalised hemispherical particles, due to the size polydispersity as shown in Chapter 3. Hence there is less of a current change during detection. By only functionalising the top curved side of the particle with probe DNA, and leaving the clean underside to be bare for catalysis, the particle has a dual function that is clearly separated, allowing for a more sensitive biosensor.

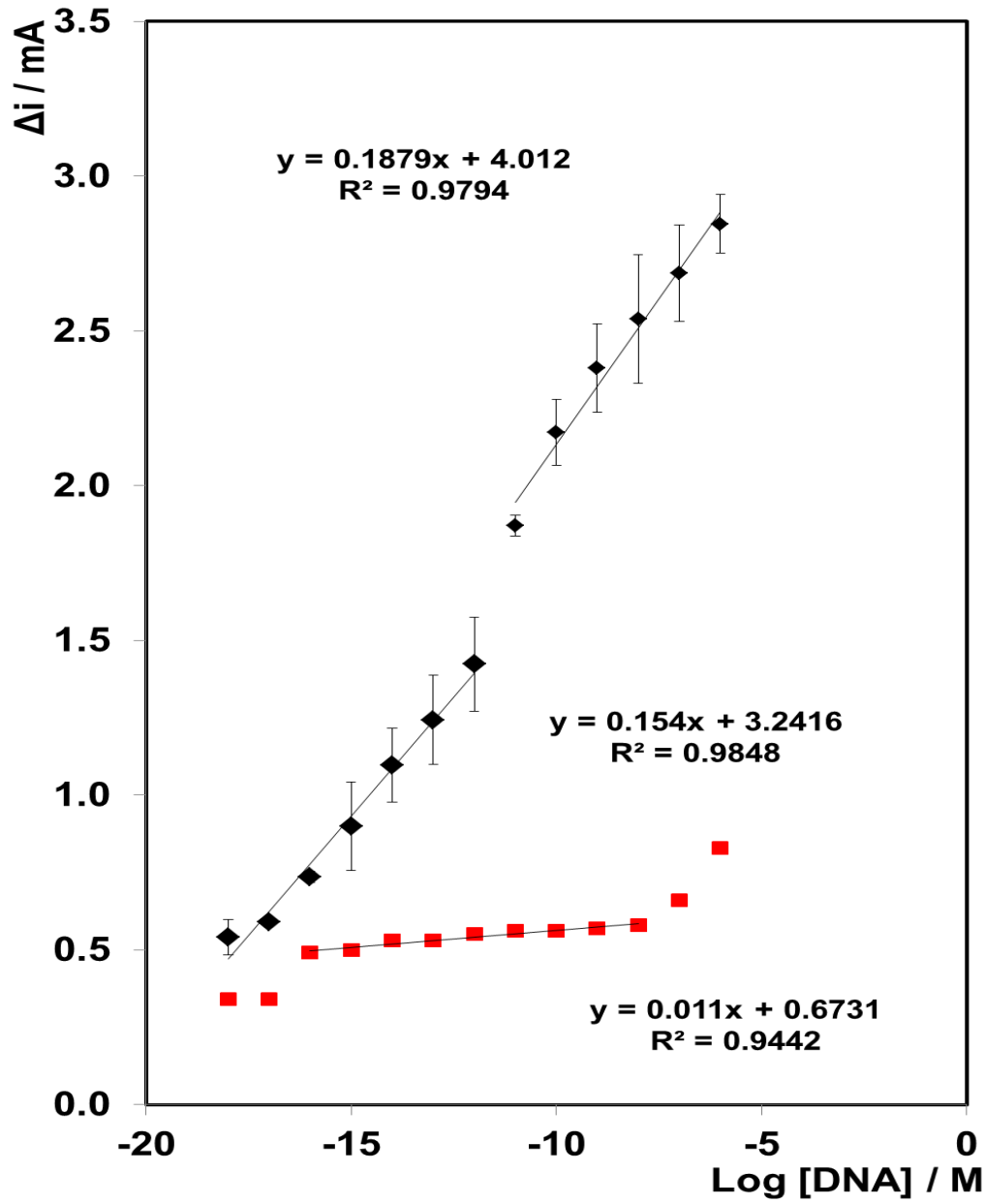

Figure 4.5: Electrochemical detection of sequence-specific S. Aureus pathogen DNA concentration; (♦) represents a full electrode; (■) represents an assay with platinum initially deposited onto an unmodified gold disc electrode. The Y axis is the difference in current before and after addition of 2mM of H_2O_2 (Δi). Potential applied is -0.25 V in 0.01 M H_2SO_4. Where error bars are not visible, they are smaller than, or comparable to, the size of the symbols.

Figure 4.6 shows a comparison of the i-t curve of the complementary hybridised ssDNA electrode with 1µM of target DNA and labelled with the regioselectively modified platinum nanoparticles, with the i-t curve of a gold disc electrode that is modified with the complementary hybridised DNA with a 1 µM of target DNA, without any platinum nanoparticle labels. There is a significant difference in these i-t curves, as there is no platinum present. Even the initial current before the addition of the peroxide is significant lower, due to no background current being produced from the platinum particles. The only current is coming from the underlying gold disc electrode, which is negligible.

Figure 4.7 compares the calibration curve of the fully complementary hybridised electrode that has hemispherical regioselectively functionalised platinum nanoparticles brought to the surface via target DNA hybridisation, to that of an electrode without any platinum nanoparticles, but with varying concentrations of the target DNA strand. As mentioned, the catalytic current in this case arises from the underlying, DNA-modified gold electrode. As expected, when the probe strand is not labelled, it's hybridisation to the target strand does not produce a large current, and it does not vary between different concentrations, as the amount of target present on the electrode surface would not affect the catalytic activity when the probe strand that it is hybridising to is unlabelled. The sensitivity of the gold disc electrode, modified with unlabelled DNA is almost 100 times lower than that of the hemispherical platinum nanoparticle assay. This reflects the poor electrocatalytic properties of the unlabelled DNA modified gold disc electrode.

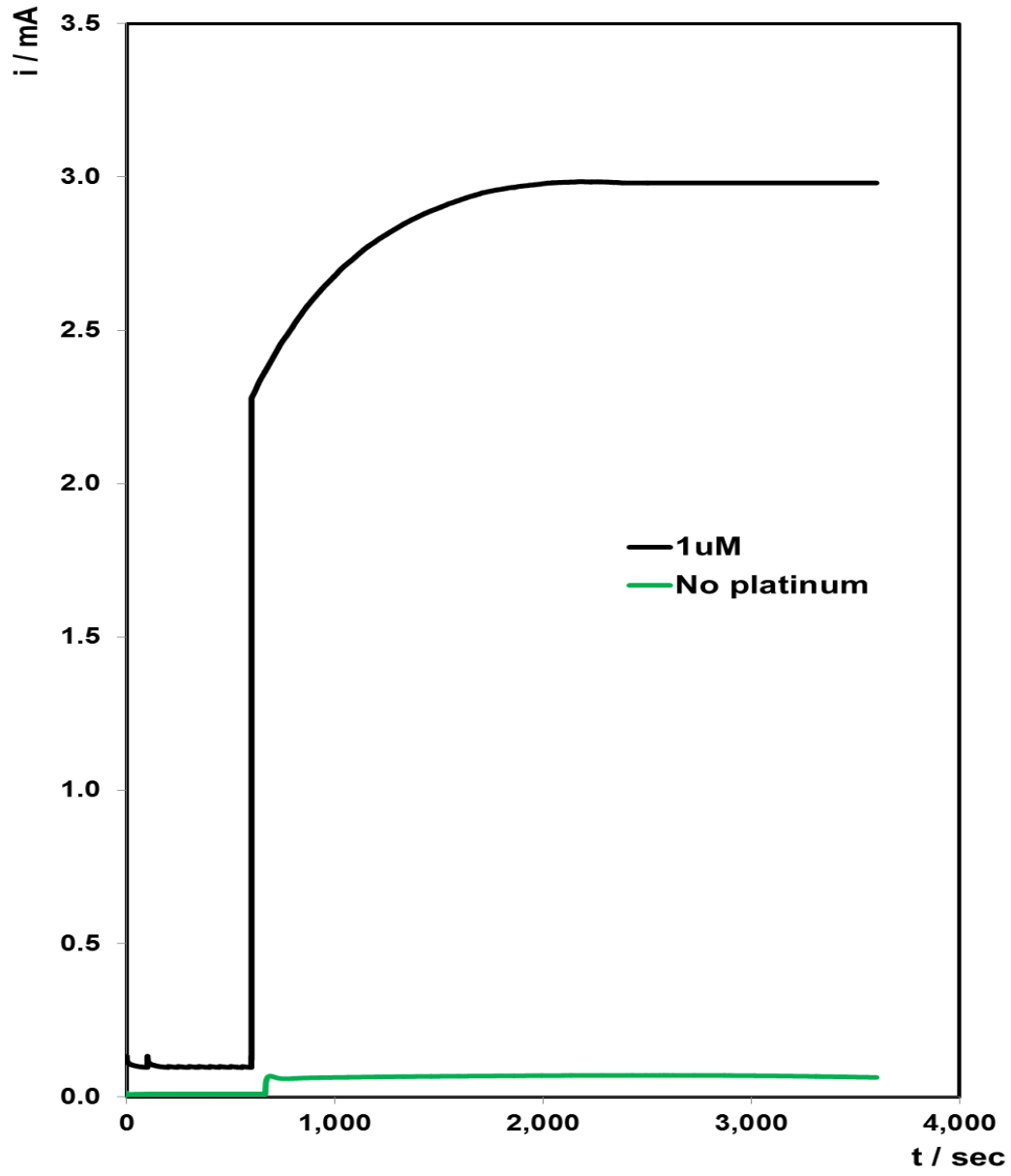

Figure 4.6: Amperometric i-t curve for a gold disc electrode functionalised with complementary ssDNA strands with a target DNA concentration of 1 µM and labelled with platinum nanoparticles (black line); and for a gold disc electrode functionalised with complementary ssDNA strands with a target DNA concentration of 1 µM, with no platinum label (green line). Potential applied is -0.25 V in 0.01 M H_2SO_4. Difference in current response before and after the addition of 2 mM H_2O_2 is displayed.

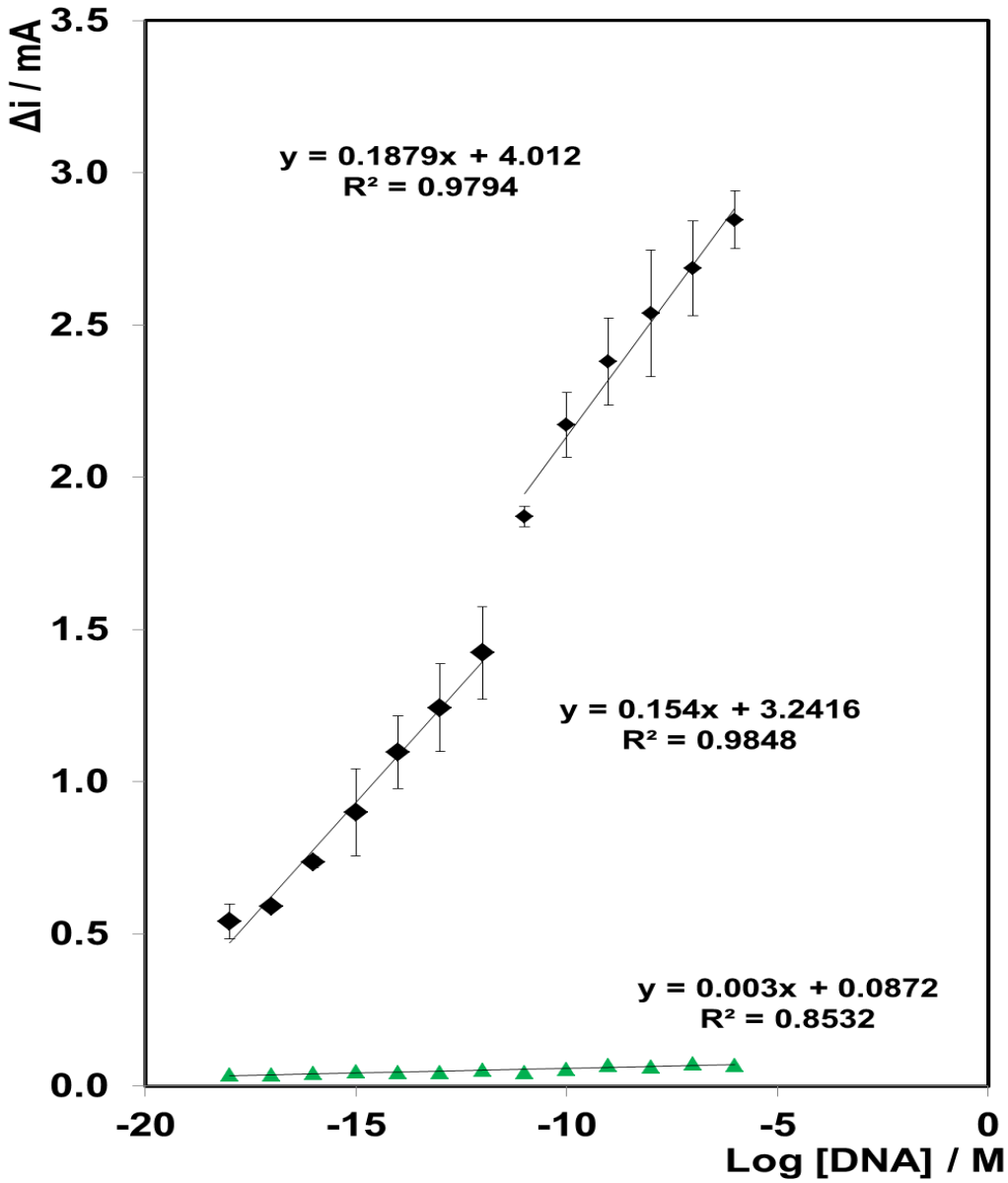

Figure 4.7: Electrochemical detection of sequence-specific S. Aureus pathogen DNA concentration; (♦) represents a full electrode; (▲) represents an electrode with no platinum. The Y axis is the difference in current before and after addition of 2mM of H_2O_2 (Δi). Potential applied is -0.25 V in 0.01 M H_2SO_4. Where error bars are not visible, they are smaller than, or comparable to, the size of the symbols

Investigations were carried out to probe the non-specific adsorption of the assay and to demonstrate the need for each hybridisation step; the results are displayed below in Figures 4.8 and 4.9 in bar chart format. Figure 4.8 shows a comparison of the fully hybridised electrode with regioselectively functionalised hemispherical platinum nanoparticles to various mismatches where the target concentration used is 1 µM while. Figure 4.9 shows the results where the concentration of the target strand of DNA is 1 pM.

Figure 4.8 (b) shows a decrease of approximately 97 % in the current between the assay using hemispherical, regioselectively functionalised platinum nanoparticles, and the assay carried out on the electrode when the nanoparticles have been desorbed. This shows that even after the desorption process is carried out on the electrode, there may still be some platinum present on the surface of the electrode. This has been shown by previous results in Chapter 3 also, so the change in current shown here in somewhat expected. As mentioned previously, the platinum nanowire that grows through the monolayer is the point at which the hemispherical nanoparticle should detach from the electrode surface during the desorption process, so it would be expected that this nanowire of platinum would remain on the surface of the electrode. This is what is giving the change in current when the peroxide is added to the solution.

Figure 4.8 (c) compares the signals obtained when the DNA functionalised deposits are desorbed from an unmodified, non-templated gold electrode surface, i.e. with no monolayer present. This has been shown in a calibration curve in Figure 4.5, however in this format the difference is just as apparent. There is a 70 % decrease when non-templated platinum nanoparticles are used, at a 1 µM target DNA concentration. Figure 4.9 (c) shows the same experiments but using a 1 pM concentration of target DNA. At this concentration there is a 61 % decrease in the change in current from the full electrode. This difference is due to the platinum nanoparticles not being templated when they are initially deposited, and hence they are clustered together and not regular in size or in shape. This shows that these non-templated nanoparticles aren't as suitable for DNA detection, as they give a much lower signal than the templated nanoparticles.

Figure 4.8 (d) compares the signals obtained for the DNA detection when there are no platinum nanoparticles present, as shown also in the calibration curve in Figure 4.7. For the 1 µM target concentration, there is a 98 % decrease in comparison to the full electrode. In Figure 4.9 (d), for a 1 pM target DNA concentration, there is a 97 % decrease when the platinum nanoparticles are omitted from the assay. The signal that is achieved here could be described as the background signal for this system, as it shows that there is very little catalysis of peroxide by just the underlying gold electrode, and by incorporating the nanoparticles into the biosensor, there is a massive enhancement for DNA detection, showing that it is the platinum nanoparticles that catalyse the peroxide and are required for accurate analysis.

Figures 4.8 and 4.9 (e) - (g) show how the biosensor is affected by removal of one of the strands of DNA, for 1 µM and 1 pM target DNA concentration respectively.

Figure 4.8 and 4.9 (e) show the change in current when the bare gold electrode is exposed to the target DNA strand. The change in current here is negligible and is attributed to a very limited degree of electrocatalysis occurring at the bare, underlying gold disc electrode. This low background when the nanoparticles are absent is significant since it is the signal-to-noise ratio rather than the absolute magnitude of the response that is important for ultrasensitive detection. The current is low because target DNA can only physisorb onto the surface of the electrode.

Similarly in Figure 4.8 and 4.9 (f), the probe and platinum nanoparticles are both omitted from the assay. In this case the target DNA strand can hybridise to the capture DNA strand that is bound to the electrode via a thiol bond. However, as mentioned previously, it is the platinum nanoparticles that generate the electrocatalytic current, so when they are omitted, there is minimal change in the current for the DNA detection. This is true for both the 1 µM target DNA strand and for the 1 pM target DNA strand.

In Figures 4.8 and 4.9 (g), there is no target DNA strand present; the bare electrode is functionalised with the thiolated capture strand, and is then exposed to the probe-platinum nanoparticles suspension. As the probe strand

immobilised on the platinum nanoparticles is not complementary to the capture DNA strand on the electrode surface, they are not expected to hybridise. Hence, even though the electrode is exposed to platinum nanoparticles, they are not brought to the surface via DNA hybridisation and therefore give a negligible change in current when compared to when they are attached to the surface of the electrode. This result is significant since it indicates that non-specific adsorption is not a significant issue in this system.

These results are very promising as they show that the assay using the regioselectively functionalised hemispherical platinum nanoparticles is extremely selective to any changes to the fully complementary target DNA strand.

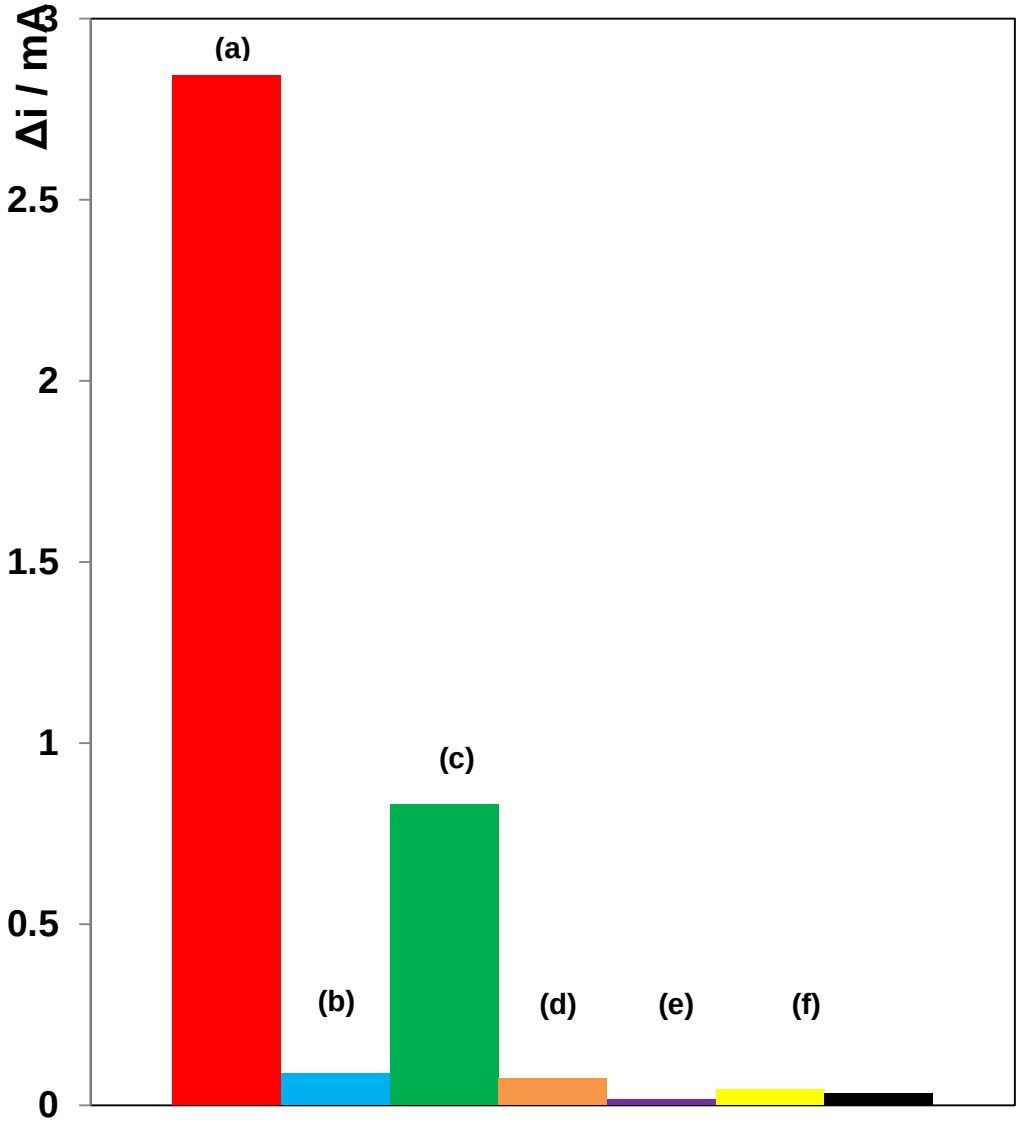

Figure 4.8: Comparison of the change in current of (a) a fully hybridised electrode with hemispherical regioselectively modified platinum nanoparticles; (b) the electrode from which the platinum has been desorbed by a current jump; (c) a fully hybridised electrode with non-templated platinum deposits; (d) without the platinum label; (e) electrode with target DNA; (f) electrode without the probe and platinum nanoparticle label; (g) without the target DNA. Concentration of capture, target and probe DNA strands are 1 µM. Concentration of H_2O_2 added is 2 mM. Potential applied is -0.25 V in 0.01 M H_2SO_4.

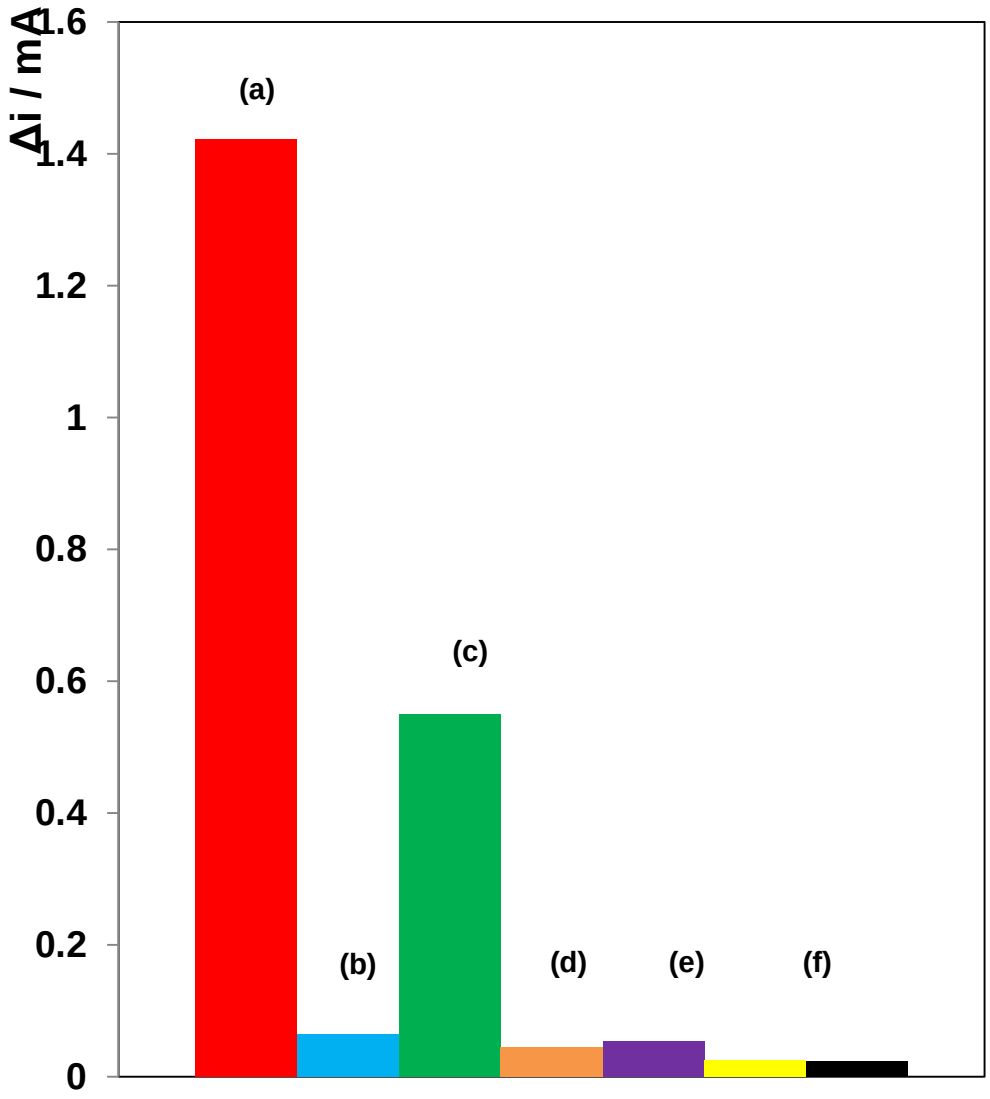

Figure 4.9: Comparison of the change in current of (a) a fully hybridised electrode with hemispherical platinum nanoparticles; (b) the electrode from which the platinum has been desorbed; (c) a fully hybridised electrode with non-templated platinum deposits; (d) without the platinum label; (e) electrode with target DNA; (f) electrode without the probe and platinum nanoparticle label; (g) without the target DNA. Concentration of capture and probe DNA strands are 1 µM. Concentration of target DNA is 1 pM. Concentration of H_2O_2 added is 2 mM. Potential applied is -0.25 V in 0.01 M H_2SO_4.

4.2.3 Comparison of Regioselectively Functionalised Platinum Nanoparticles to Uniformly Functionalised Commercial Platinum Nanoparticles

In order to investigate the impact of regioselective functionalisation of the nanoparticles on the DNA assay performance, spherical platinum nanoparticle that were 63 nm ± 5 nm in size were uniformly functionalised with probe DNA and tested in the same way to the electrochemically grown particles.

The uniform platinum nanoparticles were functionalised with the probe strand DNA to form a DNA layer on the surface of the nanoparticle. All other parameters were as before and explained in Chapter 2; the target DNA concentration range was from 1 µM to 1 aM, the incubation times and the experimental parameters remained the same.

Figure 4.10 illustrates the difference between the DNA detection currents for the regioselective, electrochemically deposited platinum nanoparticles, and the uniformly functionalised platinum nanoparticles. As shown, the electrochemically deposited platinum nanoparticles generate a larger current for a given concentration of DNA. The regioselectively functionalised nanoparticles have a change in current of up to four times greater than that for the uniformly functionalised nanoparticles, at the highest concentrations, as shown in Table 4.2. While an acceptable linear response is observed for concentrations from 1 µM to 1 aM, and a significant change in current is generated for these uniform particles, the current change isn't as wide as for the hemispherical particles. Significantly, the average change in current varies from 0.67 µA to 0.41 µA from the 1 µM to 1 aM, i.e., the response is very insensitive to the target concentration. Because the values are so close together, an accurate detection would be much harder to achieve and a highly reproducible response at each concentration is required. However, the system is reproducible, as shown by the low standard deviation and small error bars. The lower electrocatalytic currents and analytical sensitivity observed suggests that while the DNA layer is sufficiently porous to allow the hydrogen peroxide

access to the surface of the platinum nanoparticle, electrocatalysis is relatively less efficient.

The sensitivity of the response using the regioselectively modified hemispherical platinum nanoparticles is over an order of magnitude better than the uniformly modified spherical nanoparticles, due to more efficient electrocatalysis at the bare underside of the hemispherical particles. Thus, the physical separation of the two functions of the nanoparticles, i.e. the molecular recognition where the DNA is functionalised on the curved upper side of the nanoparticle, and the signal generation, where the electrocatalysis occurs on the bare underside of the particle when desorbed, leads to a significant improvement in the overall analytical performance of the assay.

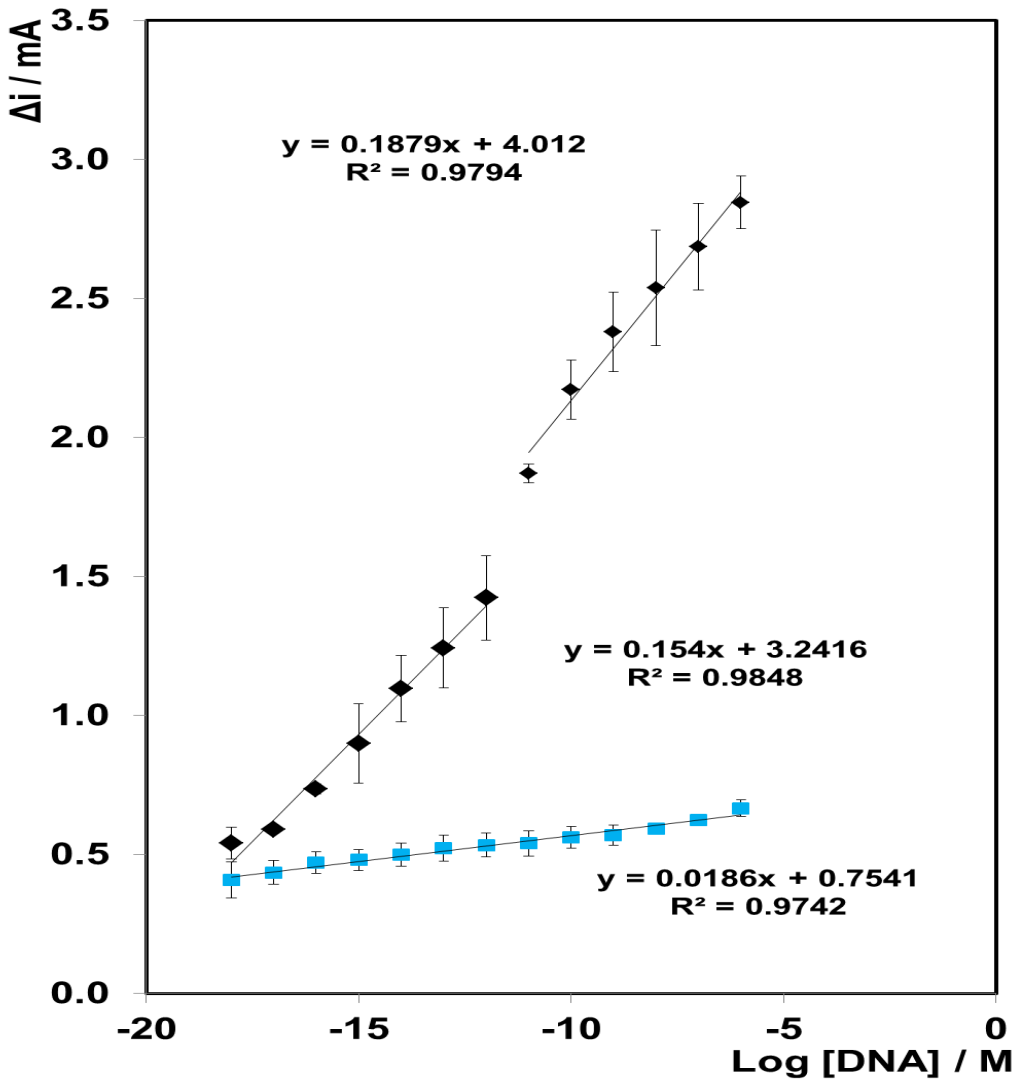

Figure 4.10: Comparison of the amperometric DNA detection between regioselective, electrochemically deposited PtNPs (♦) and uniform PtNPs (■), both functionalised with DNA corresponding to the pathogen, S. Aureus. Electrolyte is 0.01 M H_2SO_4. Target concentrations range from 1 µM to 1 aM. Concentration of H_2O_2 is 2 mM. Potential applied is -0.25 V. Where error bars are not visible, they are smaller than, or comparable to, the size of the symbols

Table 4.2: Change in current before and after the injection of H_2O_2 for varying concentrations of target DNA when labelled with uniformly functionalised spherical nanoparticles.

Concentration of DNA (M)	Log [DNA]	Average Δi (mA)	Standard Deviation
1.00E-18	-18	0.41	0.06
1.00E-17	-17	0.43	0.04
1.00E-16	-16	0.47	0.04
1.00E-15	-15	0.48	0.04
1.00E-14	-14	0.50	0.04
1.00E-13	-13	0.52	0.05
1.00E-12	-12	0.53	0.04
1.00E-11	-11	0.54	0.05
1.00E-10	-10	0.56	0.04
1.00E-09	-9	0.57	0.04
1.00E-08	-8	0.59	0.02
1.00E-07	-7	0.62	0.02
1.00E-06	-6	0.67	0.03

4.3 CONCLUSION

In conclusion, hemispherical platinum nanoparticles were produced by electrodeposition within a defective monolayer on a gold disc electrode. A double potential step electrodeposition method was used which allowed nucleation sites to form when a large overpotential was applied for 20 ms. Following this, a longer growth pulse was applied at a lower overpotential so the nanoparticles could grow at a steady rate up from the nucleation sites. This created size monodisperse nanoparticles.

Prior to desorption, the rounded top side of the platinum nanoparticles was functionalised with thiolated probe strand DNA complementary to that found within S. aureus mastitis. The DNA modified nanoparticles were then released by applying a fixed current which is thought to melt, by resistive heating, the nanowire connecting the particle to the surface of the electrode through the monolayer defect sites. This released the nanoparticles into suspension without damaging the adsorbed DNA since the time constant for particle release is shorter than that for DNA desorption.

When the target DNA strand is labelled with the platinum nanoparticle via probe DNA hybridisation, it then can form a sandwich assay by hybridisation with the complementary capture DNA strand that is immobilised on to a clean, bare gold disc electrode via a thiol group on the capture strand.

The current associated with the reduction of hydrogen peroxide at the platinum nanoparticles varies linearly with the target DNA concentration between concentrations of 1 aM and 1 µM. There is wide dynamic range, with each concentration being resolved with excellent reproducibility, (typically 2 – 15 %) even at the lowest concentrations.

When compared to platinum nanoparticles that are formed without the monolayer defect template, the sensitivity of the hemispherical, templated nanoparticles are over an order of magnitude larger, showing that the template gives more electrocatalytic nanoparticles, grown with more control than without

the template, so that they are size monodisperse is this reflected in the low concentration reproducibility. They also have the clean bare underside to the particle for the hydrogen peroxide catalysis to occur. However, the fabrication process for the templated particles is longer. When the platinum label is removed completely, the sensitivity decreases further by an order of magnitude, showing that the platinum is necessary for the electrocatalytic reduction and change in current. The biosensor is also extremely selective and has low non-specific adsorption, with each step able to discriminate against interferences with excellent accuracy, as there is minimal current.

Regioselectively functionalised hemispherical nanoparticles are also more efficient for DNA detection, when compared to commercial, spherical, uniformly functionalised platinum nanoparticles. Once again, the sensitivity is over an order of magnitude larger for the electrochemically deposited platinum nanoparticles. This shows that by physically separating the two functions of the nanoparticles, i.e. the molecular recognition and the electrocatalysis, the analytical performance increases.

The application of the platinum nanoparticles to the reduction of hydrogen peroxide demonstrates that the nanoparticle surface can be functionalised using thiolated DNA, which can further be used to detect a target DNA pathogen strand. Furthermore, the larger surface area of the nanoparticles make then ideal for adsorption of many biomarkers, such as enzymes, protein and RNA, not just DNA strands.

4.4 REFERENCES

1. Wang, J. From DNA biosensors to gene chips. *Nucleic Acids Res.* **2000***, 28*, 3011-3016.

2. Chang, C.; Chang, W.; Wang, C.; Wang, J.; Mai, J. D.; Lee, G. Nucleic acid amplification using microfluidic systems. *Lab Chip* **2013***, 13*, 1225-1242.

3. Wang, J. Electrochemical biosensors: Towards point-of-care cancer diagnostics. *Biosens. Bioelectron.* **2006***, 21*, 1887-1892.

4. Gubala, V.; Harris, L. F.; Ricco, A. J.; Tan, M. X.; Williams, D. E. Point of Care Diagnostics: Status and Future. *Anal. Chem.* **2012***, 84*, 487-515.

5. Lina, G.; Piemont, Y.; Godail-Gamot, F.; Bes, M.; Peter, M.; Gauduchon, V.; Vandenesch, F.; Etienne, J. Involvement of Panton-Valentine leukocidin-producing Staphylococcus aureus in primary skin infections and pneumonia. *Clin. Infect. Dis.* **1999***, 29*, 1128-1132.

6. Becker, K.; Friedrich, A.; Lubritz, G.; Weilert, M.; Peters, G.; von Eiff, C. Prevalence of genes encoding pyrogenic toxin superantigens and exfoliative toxins among strains of Staphylococcus aureus isolated from blood and nasal specimens. *J. Clin. Microbiol.* **2003***, 41*, 1434-1439.

7. Schlesinger, L.; Ross, S.; Schaberg, D. Staphylococcus-Aureus Meningitis - a Broad-Based Epidemiologic-Study. *Medicine* **1987***, 66*, 148-156.

8. Jarraud, S.; Peyrat, M.; Lim, A.; Tristan, A.; Bes, M.; Mougel, C.; Etienne, J.; Vandenesch, F.; Bonneville, M.; Lina, G. A highly prevalent operon of enterotoxin gene, forms a putative nursery of superantigens in Staphylococcus aureus (vol 166, pg 669, 2001). *J. Immunol.* **2001***, 166*, 4260-4260.

9. Nickerson, S.; Owens, W.; Boddie, R. Symposium - Mastitis in Dairy Heifers - Mastitis in Dairy Heifers - Initial Studies on Prevalence and Control. *J. Dairy Sci.* **1995***, 78*, 1607-1618.

10. Viguier, C.; Arora, S.; Gilmartin, N.; Welbeck, K.; O'Kennedy, R. Mastitis detection: current trends and future perspectives. *Trends Biotechnol.* **2009***, 27*, 486-493.

11. Ghosh, I.; Stains, C. I.; Ooi, A. T.; Segal, D. J. Direct detection of double-stranded DNA: molecular methods and applications for DNA diagnostics. *Mol. Biosyst.* **2006***, 2*, 551-560.

12. Hansen, J. A.; Mukhopadhyay, R.; Hansen, J. O.; Gothelf, K. V. Femtomolar electrochemical detection of DNA targets using metal sulfide nanoparticles. *J. Am. Chem. Soc.* **2006***, 128*, 3860-3861.

13. Mirkin, C. A.; Letsinger, R. L.; Mucic, R. C.; Storhoff, J. J. A DNA-based method for rationally assembling nanoparticles into macroscopic materials. *Nature* **1996***, 382*, 607-609.

14. Polsky, R.; Gill, R.; Kaganovsky, L.; Willner, I. Nucleic acid-functionalized Pt nanoparticles: Catalytic labels for the amplified electrochemical detection of biomolecules. *Anal. Chem.* **2006***, 78*, 2268-2271.

15. Spain, E.; Brennan, E.; McArdle, H.; Keyes, T. E.; Forster, R. J. High Sensitivity DNA Detection Based on Regioselectively Decorated Electrocatalytic Nanoparticles. *Anal. Chem.* **2012***, 84*, 6471-6476.

16. Spain, E.; Miner, B.; Keyes, T. E.; Forster, R. J. Regio selective functionalisation of gold nanoparticles with DNA. *Chemical Communications* **2012***, 48*, 838-840.

17. Cui, K.; Song, Y.; Yao, Y.; Huang, Z.; Wang, L. A novel hydrogen peroxide sensor based on Ag nanoparticles electrodeposited on DNA-networks modified glassy carbon electrode. *Electrochemistry Communications* **2008***, 10*, 663-667.

18. Zhang, Y.; Yuan, R.; Chai, Y.; Wang, J.; Zhong, H. Amperometric biosensor for nitrite and hydrogen peroxide based on hemoglobin immobilized on gold nanoparticles/polythionine/platinum nanoparticles modified glassy carbon electrode. *Journal of Chemical Technology and Biotechnology* **2012***, 87*, 570-574.

CHAPTER 5

MICROFLUIDIC DISC FOR ULTRASENSITIVE DETECTION OF miRNA USING ELECTROCATALYTIC PLATINUM NANOPARTICLES

5.1 INTRODUCTION

As discussed previously, biomarkers are increasingly seen and used as non-invasive tools to support diagnosis, prognosis and treatment decisions for disorders of the central nervous system.[1-3] For many situations, a rapid, point-of-care/use sample-to-answer device that is capable of taking a blood, or minimally processed sample, is highly desirable. This Chapter reports on the development of a centrifugal microfluidic device for the detection of a miRNA biomarker that is important in epilepsy.

Epilepsy is a common neurological disease. It is characterised by an enduring predisposition to generate epileptic seizures.[4,5] Seizures can be highly unpredictable for many patients. Diagnosis can also be challenging and can rely heavily on clinical examination and history alone. The primary tool used for prognosis in newly diagnosed epilepsy has been the electroencephalogram, which is invaluable but also costly and technically demanding. Also, in patients whose electroencephalogram demonstrates no evidence of epileptiform activity, they face a high level of uncertainty as to their diagnosis and future after an unprovoked seizure. Identifying a biomarker associated with epilepsy in biofluid such a blood, urine or cerebrospinal fluid, would vastly improve the diagnosis, prognosis, care and treatment of the patient.[6] Many efforts have been focussed on areas such as antibodies to neuronal antigens, infectious markers, inflammatory markers, white blood cells and associated cell adhesion molecules paediatric syndromes, and treatment-related biomarkers; however these have been largely unsuccessful and have presented varying challenges.[6]

A promising class of biomarkers for epilepsy are microRNA.[7] MicroRNA (miRNA) are small, 18-25 nucleotide-long, non-coding RNA molecules that regulate protein function in cells post-transcriptionally.[8,9] A number of miRNA have been found to be unique to the brain, including miR-134, which is a key component in the response to neuronal activity.[10,11] Recent studies reported upregulation of miR-134 in rodent and human epilepsy and have shown that

silencing miR-134 had long-lasting seizure-suppressive effects in mice.[12,13] Recent work has also shown the altering miRNA levels in blood following seizures in rodents,[14] and in epilepsy patients.[15]

This shows that the analysis of the miRNA content in biofluids of epilepsy patients may support diagnosis, predict seizures or treat the patient effectively.

Previous work has shown that miR-134 can be detected from serum samples and show highly linear correlation with Taqman-based PCR.[16] A huge advantage of this is that the miRNA can be detected without the need for amplification involved in PCR, leading to a much simpler and quicker detection method. In the method reported here, platinum nanoparticles are regioselectively labelled with probe strand miRNA complementary to the miR134 target in a nucleic acid sandwich assay. The platinum nanoparticle is brought to the surface of the electrode via miRNA hybridisation complementary to the target. The target concentration is detected by the current associated with the reduction of hydrogen peroxide at the electrode surface.

In order to further improve this, a point-of-care method of analysis is required, to detect epilepsy biomarkers as a routine detection strategy in a clinical setting.

Centrifugal platforms for bioanalytical assays have been investigated for more than 40 years.[17,18] Centrifugal microfluidic platforms offer many advantages over chip-based microfluidic systems, including:

- A minimal amount of instrumentation is needed for movement of fluid, and no external pumps are required. This therefore allows the entire network to be contained within the disc.
- Inexpensive materials such as polycarbonate or poly(methyl methacrylate) can be used to mass produce the discs. These can also be manufactured so that they can be disposed of in an economical manner.
- Centrifugal pumping is not dependant on physicochemical properties of the fluid, such as pH, ionic strength or chemical composition. This allows many different types of fluids to be successfully pumped through

a microfluidic centrifugal platform, such a blood, mucous, urine or milk.[19]

Centrifugal platforms have been developed for different nucleic acid detection. However, many of these require the nucleic acid to be amplified by methods such as PCR[20,21], LAMP[22] and RCA [23]. These have some disadvantages though, as they require thermal cycling, can have large background noise, complicated primers required for amplification, and can sometimes give false positives.[24]

In this chapter, electrocatalytic platinum nanoparticles are functionalised with probe strand miRNA that are complementary to a particular region of the target, miR-134, and are used to detect this target strand without PCR amplification of the target. Thiol terminated probe strand miRNA are immobilised onto spherical platinum nanoparticles and these are pre-loaded into a microfluidic disc, along with the target miRNA, miR-134. Capture miRNA that is complementary to part of the target miRNA are immobilised via thiol bonding to a bare gold electrode, and is assembled into a microfluidic disc. Using a triggering system, and by controlling the force at which the disc is spinning on an experimental spin stand, the pre-loaded target miRNA and probe-functionalised platinum nanoparticles can be released at specific times, for a specific duration, in order to expose the capture strand functionalised to each step, to attach the electrocatalytic particles to the electrode surface, via the target miRNA hybridisation. When the electrode is fully functionalised, electrochemical detection is carried out on the disc, by connecting the external contact of the electrode to a potentiostat.

5.2 RESULTS AND DISCUSSION

5.2.1 Microfluidic Disc

5.2.1.1 Disc design and assembly

The design of this disc was based off previously published centrifugal microfluidic discs that developed the method of using dissolvable film (DF) tabs to allow event triggered flow of the fluid through the device.[25,26] The designing of each layer was carried out in solid works by Eadaoin Carthy and David Boyle using CAD software.

The microfluidic discs were assembled using nine layers in total - four layers of poly(methyl methacrylate) (PMMA) and five layers of pressure sensitive adhesive (PSA). Larger voids such as reservoirs and vents were machined in PMMA layers using a CO_2 laser cutter (Epilog Zing, USA). PMMA layers were 0.5 mm, 1.5 mm or 2 mm thick. Small features such as microchannels and lower channels were created from voids cut out in PSA using a knife-cutter (Graphtec). The layers used were as follows:

- **Layer 1:** Vents (1.5 mm PMMA).
- **Layer 2:** Microchannels (PSA).
- **Layer 3:** Reservoirs (1.5 mm PMMA).
- **Layer 4:** Dissolvable Film, DF cover (PSA).
- **Layer 5:** DF Support (PSA).
- **Layer 6:** Midlayer (0.5 mm PMMA).
- **Layer 7:** Lower Channels (PSA).
- **Layer 8:** Electrode Cover (PSA).
- **Layer 9:** Base (2 mm PMMA).

These layers are shown in Figure 5.1 in a cascade format, to view each layer of disc. Figure 5.2 is a photograph of the top view of the disc and Figure 5.3 shows a labelled image of each chamber.

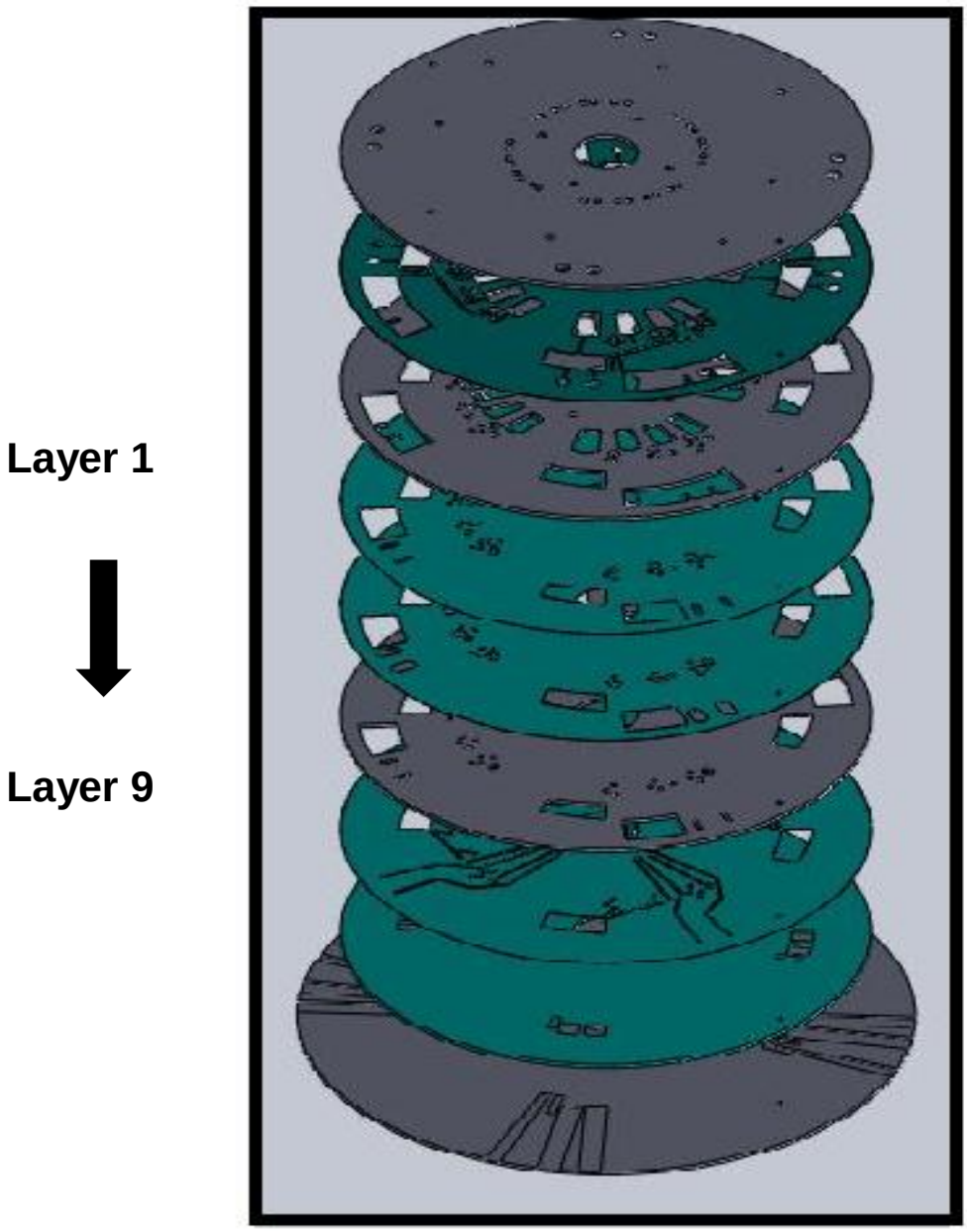

Figure 5.1: Exploded view of disc assembly. The grey layers are PMMA. The green layers are PSA.

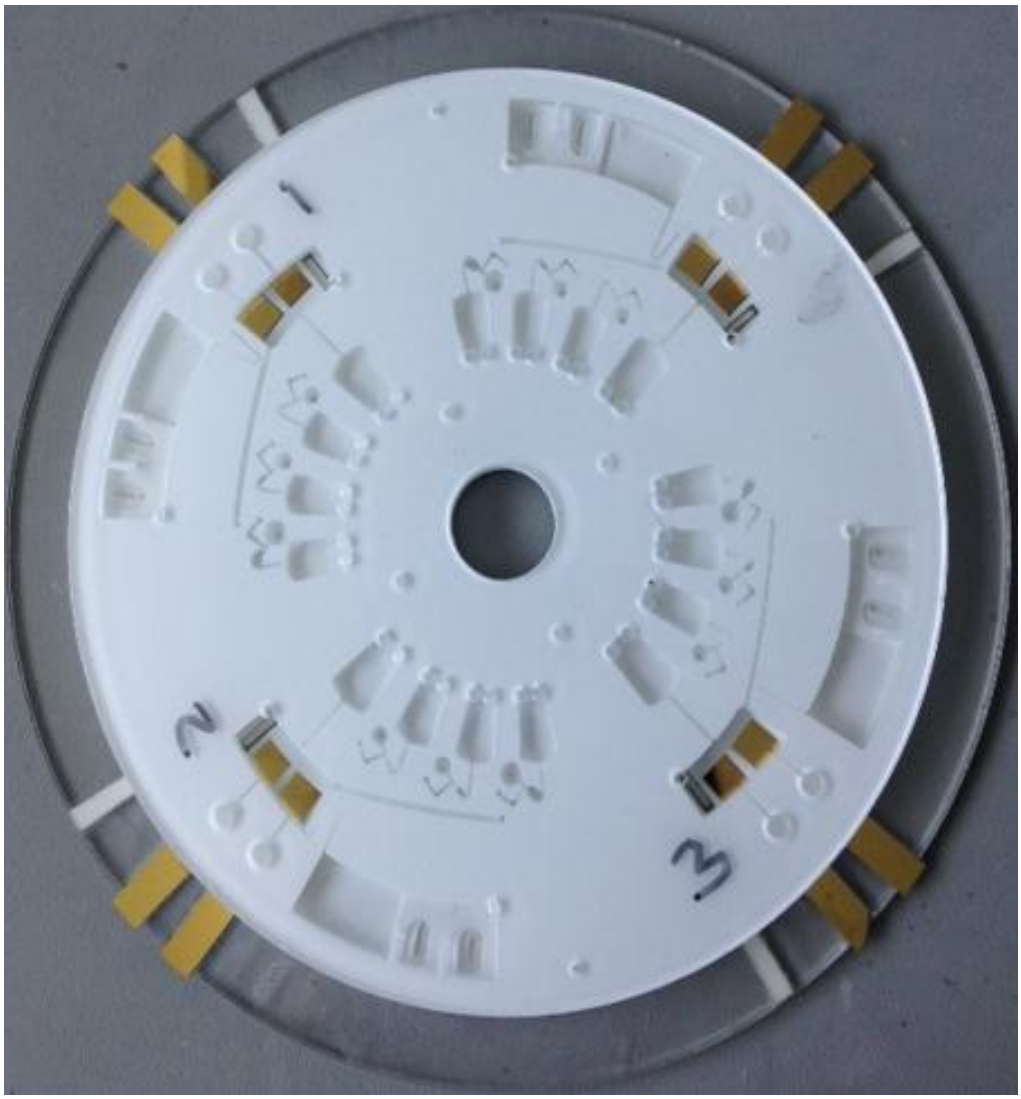

Figure 5.2: Image of fully assembled microfluidic disc with integrated electrodes.

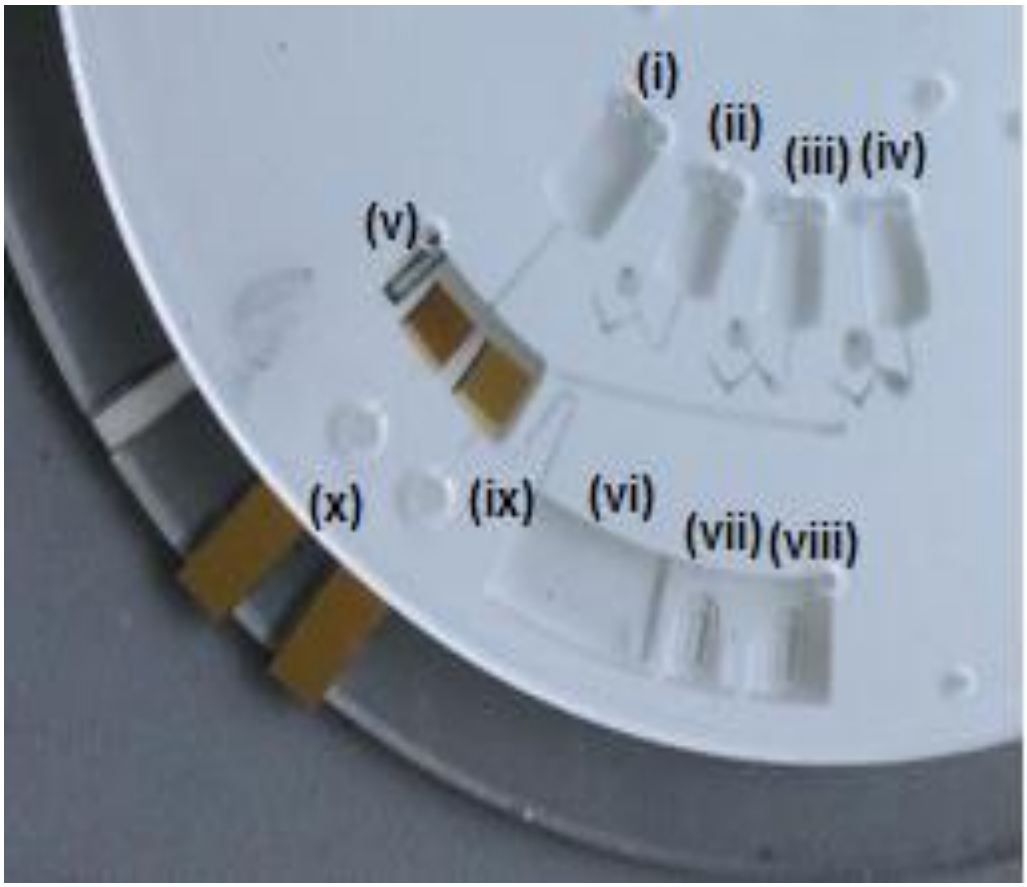

Figure 5.3: Labelled section of disc. Chamber (i) – (iv) are preloaded with (i) target miRNA strands, (ii) PBS wash step, (iii) PtNP labelled probe miRNA strands, (iv) PBS wash step/electrolyte. Chamber (v) is the electrode chamber with ITO reference, gold working electrode and gold counter electrode. Chamber (vi) is the waste chamber, with an overflow system implemented at (vii) and (vii); these contain DF tabs. (ix) is the siphon between the electrode chamber and the waste chamber. Labelled at (x) are the vents for the electrode chamber.

The device was designed to allow the preloading of the chambers, (i) – (iv); two vents were placed at the top of each chamber, one to inject the sample prior to spinning, the other to relieve the air pressure when the fluid was being injected, so the air or fluid wasn't pushed through the channels. A vent was also placed above the electrode chamber (v) to allow the injection of peroxide. A vent was placed at the end of the waste chamber (viii) to relieve the air pressure when the fluid entered the waste chamber.

A major issue in the design of the device was gas evolution when the hydrogen peroxide was added into the electrode chamber (v). Gases are produced during hydrogen peroxide reduction (oxygen and hydrogen gas), and as the volume of the electrode chamber is small, if there are no vents for the gas to escape from the chamber, the fluid will be pushed out and no electrochemical detection can be carried out. This occurred during testing of the device and vents and channels were placed in different areas of the disc to attempt to alleviate the pressure. A wide channel with a vent was placed from the top right corner of the electrode chamber initially. However this did not have any affect as the entry to the channel in the electrode chamber was too far from the working electrode where the gas evolution was occurring. Vents were places above the electrode chamber, so no channels were needed and the gas could be released as soon as it was produced. However, this caused some leaking issues from the electrode chamber as the fluid inside it could spill out if the disc was tilted and spun. The optimum vents were eventually placed below the electrode chamber, with short channels leading from the chamber to the vents (labelled as (x) in Figure 5.3). The entrance to the vents in the electrode chamber was above the electrode, so the gas could pass straight into the channel and out the vent. When the peroxide was injected into the electrode chamber via the injection vent on the top left of the chamber, a piece of tape was placed over this opening; this ensured that the gas produced would only escape from the vents and channels designed for it.

A siphon was used between the electrode chamber and the waste chamber, shown at label (ix) in Figure 5.3. This was used to prevent the fluid from flowing from the electrode chamber to the waste chamber prematurely, to allow sufficient incubation time. When the disc is spun on the spin stand at a high

spin rate, the fluid cannot rise above the curve in the siphon channel as the centrifugal force is stronger than the capillary force.[27,28] By slowing down the spin rate, the capillary force is then able to surpass the centrifugal force, which allows the fluid to prime the sample so it can flow into the waste chamber, when required.

The dissolvable film (DF) tabs used here are made of polyvinyl alcohol (PVA), and attached to double sided PSA to create adhesive tabs. Two different shapes were used, circular and slot shaped. The circular tabs were used for the load film (LF) at the sample chambers (i) – (iv). The slot-shaped tabs were used for the control film (CF) at the waste chambers.

The valving technology used here, uses the arrival of a liquid at one location to prompt the release of another liquid at another, distant location on the disc by a connecting pneumatic channel. This enables the multi-step fluid handling sequence that is required to make the sandwich assay used for the nucleic acid detection. An overflow system was implemented in the waste chambers also; this means that only when the second sample chamber (ii) has emptied into the waste chamber, it then flowed into the overflow part of the waste chamber (vii), which contains a CF. When this CF was wetted, it vented the pneumatic channel (Lower channels, Layer 7) permitting the sample chamber (iii) to advance, and wet and dissolve the LF. This liquid could then flow into the electrode chamber. When this pneumatic chamber (iii) was vented, the liquid can only flow into the electrode chamber and not back through the venting channel into the waste; this was achieved through a physical barrier by extending the microchannels linking the CF and LF (lower channels, layer 7) radially inward of the fluid in the sample chamber; this forces the fluid into the electrode chamber. The full triggering system is explained in the following section also.

The discs were aligned using an assembly jig. Previously prepared DF tabs were placed in the Layer 5 (DF support) and covered by Layer 4 (DF cover). Between each assembly step, the discs were rolled using a temperature-controlled lamination press (Hot Roll Laminator, Chemsultant Int., US) to ensure proper sealing.

Many types of glue were tested to glue the electrodes into the raster base. These included super glue, araldite, and Loctite adhesives. However due to their composition, many of the glues tried cracked the base which then caused leaks, or did not dry correctly causing the electrodes to crack or give a “tacky” finish. The glue that worked most efficiently was the 3M spray adhesive glue. This was used to glue the electrodes into the rastered base. Four sets of three electrodes were assembled into each base; gold on silica slides as the working and counter electrode and ITO as the reference electrode. The gold electrodes were cleaned by washing with ethanol and deionised water, and dried under a steady stream of nitrogen. Prior to assembly, the working electrode was functionalised with the capture miRNA strands. To glue the electrodes into the rastered base, the base was first cleaned with isopropanol and dried under nitrogen. A thin layer of glue was applied using a pipette tip to the edges of the raster base where the electrodes slot in. The top of the rastering was avoided as much as possible, as this is the area of the electrodes that is in the electrochemical cell when the nucleic acid detection is being carried out, and if glue were to get onto the surface of the electrode it would affect the results. The electrode were placed into the rastered base using tweezers and gently pushed into position, avoiding the top of the electrode where the detection occurs. The PSA electrode cover was heated prior to gluing to 70oC. Once all of the electrodes were glued into place, this layer was taken from the oven and immediately placed onto the base, over the electrodes. By heating this layer, the PSA melted slightly, allowing it to mould onto the base and electrodes, filling in any possible gaps. The top of the disc was then applied to the base and rolled under the pressure roller slowly to seal. The whole disc was then clamped overnight under the roller to allow the glue to dry.

5.2.1.2 Triggering System of Microfluidic Disc

Once the disc was assembled, the four sample chambers (i) – (iv) were preloaded; (i) contained the target miRNA strand of varying concentrations, (ii) contained a PBS wash step, (iii) contained the platinum nanoparticle labelled probe miRNA strands, and (iv) contained the PBS wash step/electrolyte.

The disc was mounted on an experimental spin stand.[26,29,30] The discs were spun on a computer controlled motor. A stroboscopic light source, a sensitive, short exposure time camera and the motor are synchronized using custom electronics and visualise the hydrodynamics on the rotating disc. Due to the software used, images are acquired as single files at a rate of ~6 Hz. Each image is imprinted with a time stamp accurate to 1 s. The images are cropped to region of interest. Each step involved in the system is explained below and visualised in Figure 5.4. The discs were tested at varying rates of rotation, ranging from 1 Hertz to 35 Hertz, depending on the stage of testing.

Image A: The sample chambers (i) – (iv) were preloaded as described.

Image B: A spin rate of 15 Hz was applied. The forced the contents of chamber (i) into the electrode chamber (v). This was left to incubate for 30 min, so the target miRNA could hybridise to the capture miRNA immobilised on the surface of the working electrode.

The siphon between the electrode chamber (v) and the waste chamber (vi) (shown as (ix) on Figure 5.3) prevents the flow of the sample into the waste. After the 30 min incubation time, the spin rate was slowed down to 1 Hz; this allowed the siphon to prime.

Image C: Once the siphon was primed, the spin rate was increased to 10 Hz, to force the sample into the waste chamber.

Image D: Once the entire sample was in the waste chamber, the spin rate was increased to 30 Hz. This high spin rate released the sample chamber (ii) which flowed into the electrode chamber. This is a wash step, so the fluid can flow over the electrode and through the siphon into the waste chamber.

As an overflow system was implemented here, the fluid overflows from the waste chamber (vi) into the overflow chamber (vii). This wetted the DF tab in the chamber, releasing the pressure in the lower channel, allowing the DF tab at chamber (iii) to become wet.

Image E: As the DF tab of chamber (iii) was wetted, the spin rate was increased to 35 Hz to allow this chamber to empty into the electrode chamber. This chamber contained the probe functionalised platinum nanoparticles and was left for 30 min to incubate, to allow the probe to hybridise to the target miRNA on the surface of the working electrode.

When the incubation time was complete, the spin rate was slowed down once again to prime the siphon and allow flow into the waste chamber. Another overflow system was implemented here; as the volume increased, the fluid flowed into waste chamber (viii) and wetted the DF tab in this chamber, releasing the pressure in the lower channels, so the DF tab at sample chamber (iv) can be wetted also.

Image F: The spin rate was increased to 35 Hz once again, to allow the release of the liquid in chamber (iv) into the electrode chamber, where it remained for electrochemical testing.

The disc was removed from the spin stand and the external elements of the electrodes were connected to a potentiostat for testing.

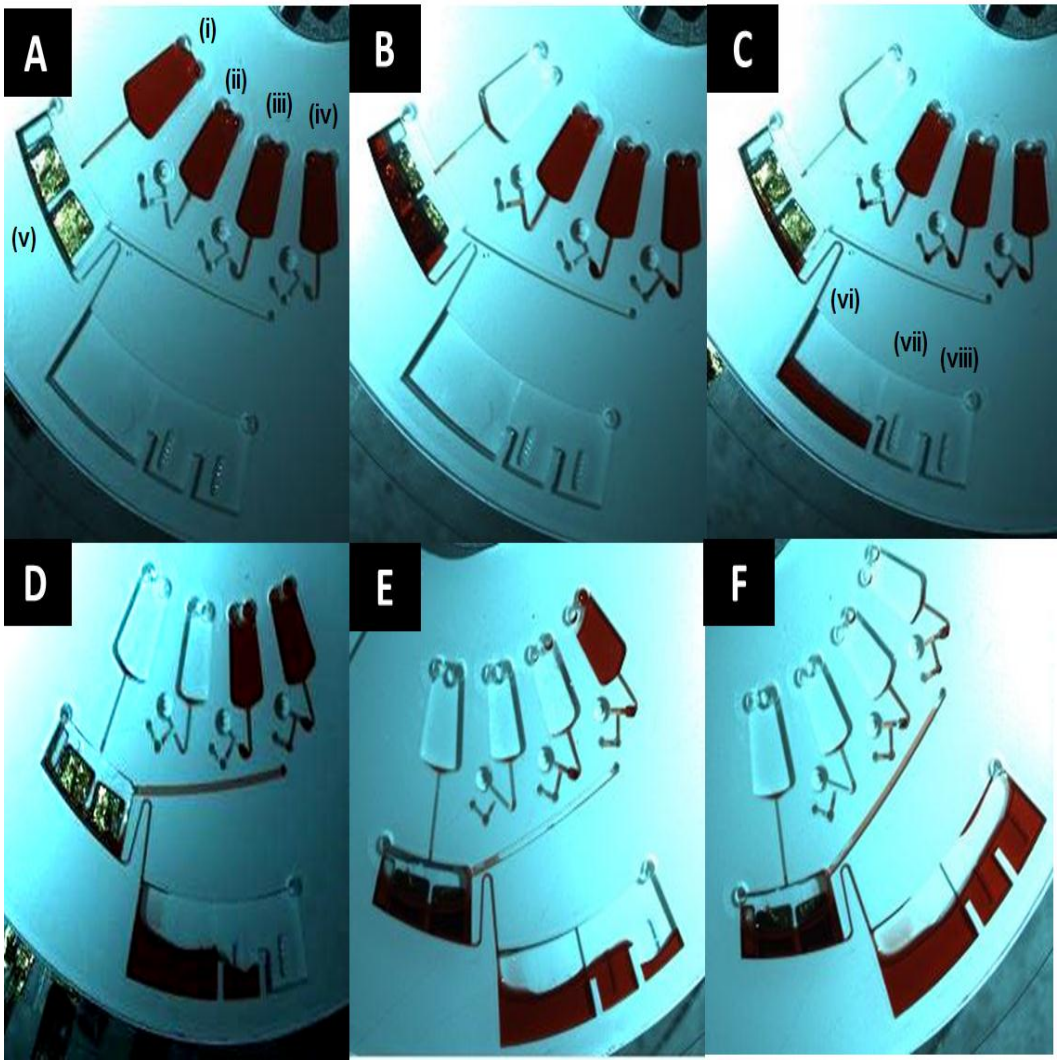

Figure 5.4: Stepwise display of triggering system to allow complete functionalisation of the working electrode in the incubation chamber. Each image is cropped to show just one section of the disc. Red food dye is preloaded into the chambers instead of samples for visualisation purposes only. Chambers (i) – (iv) are the preloaded sample chambers. Chamber (v) is the electrode chamber. Chamber (vi) is the waste chamber, with (vii) and (viii) as the overflow of the waste.

5.2.2 Step-wise hybridisation of miRNA inside microfluidic device

5.2.2.1 Electrochemical impedance studies for the modification of the electrodes with miRNA

Electrochemical impedance spectroscopy is emerging as a powerful method for detection in biosensors, as explained in more detail in Chapter 1. These biosensors can be classed as faradaic and non-faradaic. Faradaic means that the current generated is from the oxidation and reduction of a redox species at the electrode; non-faradaic means that the current generated is from the moment of electrolyte ions, adsorption/desorption, etc., at the electrode interface. Changes in the EIS spectra can be related to the change in resistance and capacitance of the interface, thus providing insights into the effects of surface modification. Non-faradaic biosensors have been described as being more amenable to point-of-care applications, as there is no additional reagent required.[31] As there is no redox probe in the system described here, it is therefore non-faradaic EIS. The movement of the ions in the electrolyte is being measured here.

In this study, Nyquist plots were utilised to study the change in charge transfer resistance after the capture miRNA layer was formed on the bare gold electrode, after the complementary target miRNA strand was hybridised to the capture strand, and again after this was labelled with a platinum nanoparticle via target-probe complementary hybridisation.

A dilute electrolyte of 1 mM DPBS was used. The electrodes were connected to the potentiostat, while the parts of the electrode that are functionalised with the miRNA are confined in the sample chamber of the disc. The EIS measurements were performed at an open circuit potential at an ac amplitude of 25 mV and at a frequency range from 0.01 Hz to 100 kHz. The results are shown in Figure 5.4 – Figure 5.7.

Figure 5.5 shows an overlay of the Nyquist plot after each step. The Nyquist plot is composed of an imaginary part (Z'') and a real part (Z'). The diameter of the semi-circle represents the charge transfer resistance (R_{ct}) at the electrode surface, which corresponds to any surface modification. The bare gold electrode has an R_{ct} value of 618 Ω. When modified with the capture miRNA strand, via thiol functionalisation to the gold electrode, the R_{ct} value increases to 886 Ω. This is due to the miRNA partially blocking the electrode surface as the capture layer is formed. There is little change to the R_{ct} value when the target miRNA strand is immobilised to the surface of the electrode via capture strand hybridisation. A previous study by Riedel et al showed that when a ssDNA immobilised on the surface of the electrode was hybridised to a complementary target strand, the R_{ct} value decreased as the length of the overhang of target DNA increased.[32] This would account for the similarities of the Nyquist plots, as there is an overhang of 12 base pairs when the target is hybridised to the capture miRNA strand. When the probe miRNA strand and platinum nanoparticles are included on the surface of the electrode the R_{ct} value increases to 1186 Ω. Although the inclusion of nanoparticles has been shown to improve the electron transfer ability to a solution phase redox active probe, in this case because there is miRNA immobilised on the surface of the nanoparticle, this increases the negative charge of the electrode surface, which increases the resistance as shown.[33]

In a Bode plot, the data obtained from the impedance experiment is displayed in a different way to the Nyquist plot, i.e. it takes the frequency at which each resistance value is obtained at into account, whereas the Nyquist plot does not. This accounts for the difference in the Bode plot in Figure 5.6, when there is no change in the Nyquist plot. As the Bode Plot is affected more by the capacitance, this shows that towards a higher frequency, there is a difference when the target miRNA is hybridised to the capture miRNA. This is confirmed when the data is fit to the equivalent circuit model in the next section, as the capacitance calculated from that decreases from 1.9×10^{-8} to 6.8×10^{-9} when the target is hybridised.

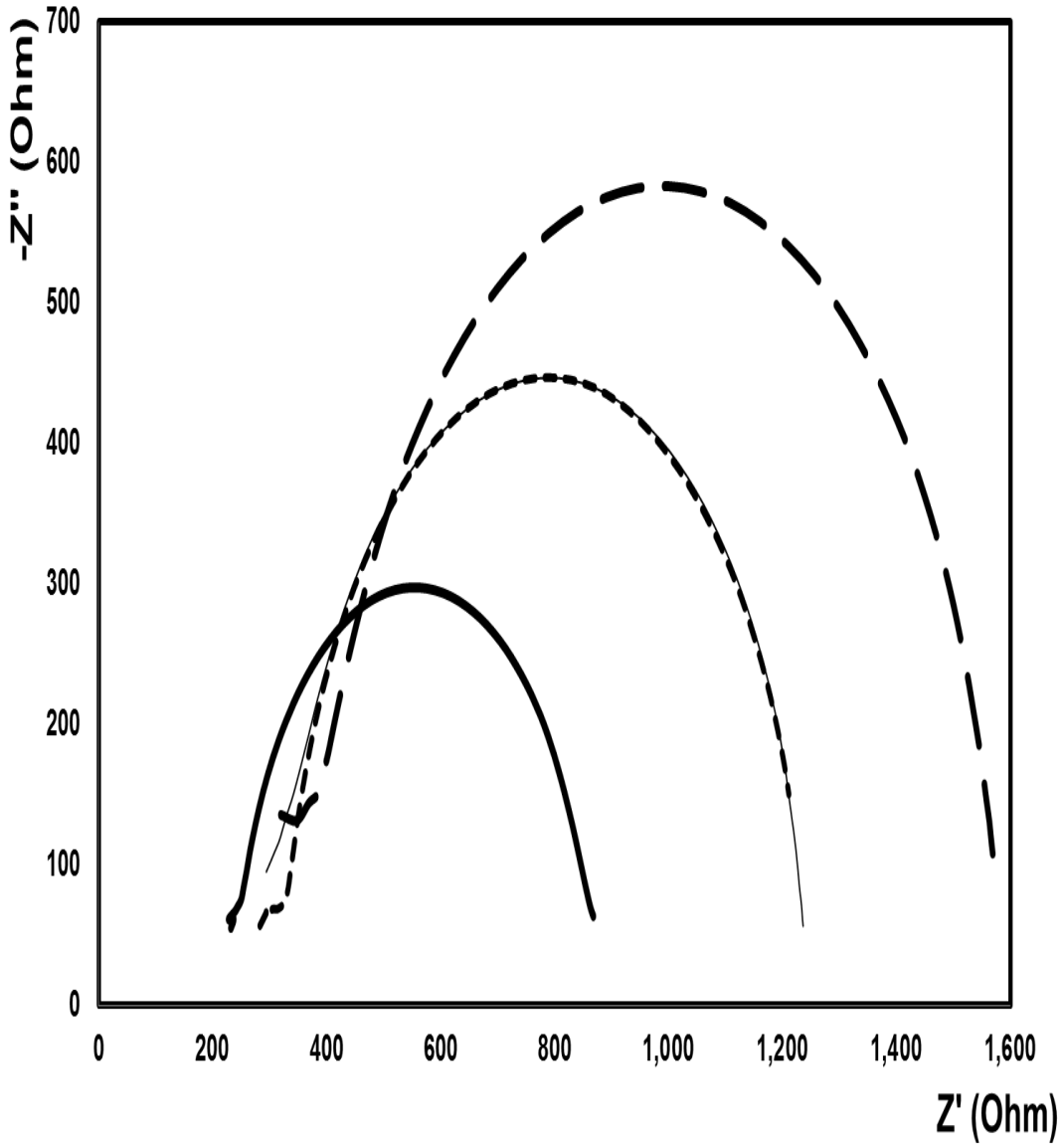

Figure 5.5: Nyquist plots of a bare gold electrode (thick black line), after capture miRNA (short dashed line), after target miRNA (thin black line) and after probe miRNA-PtNP (long dashed line). The EIS were recorded in the presence of 1 mM DPBS at a frequency range between 0.01 Hz and 100,000 Hz using an ac amplitude of 25 mV and the dc potential set to the open circuit potential of 0.1 V.

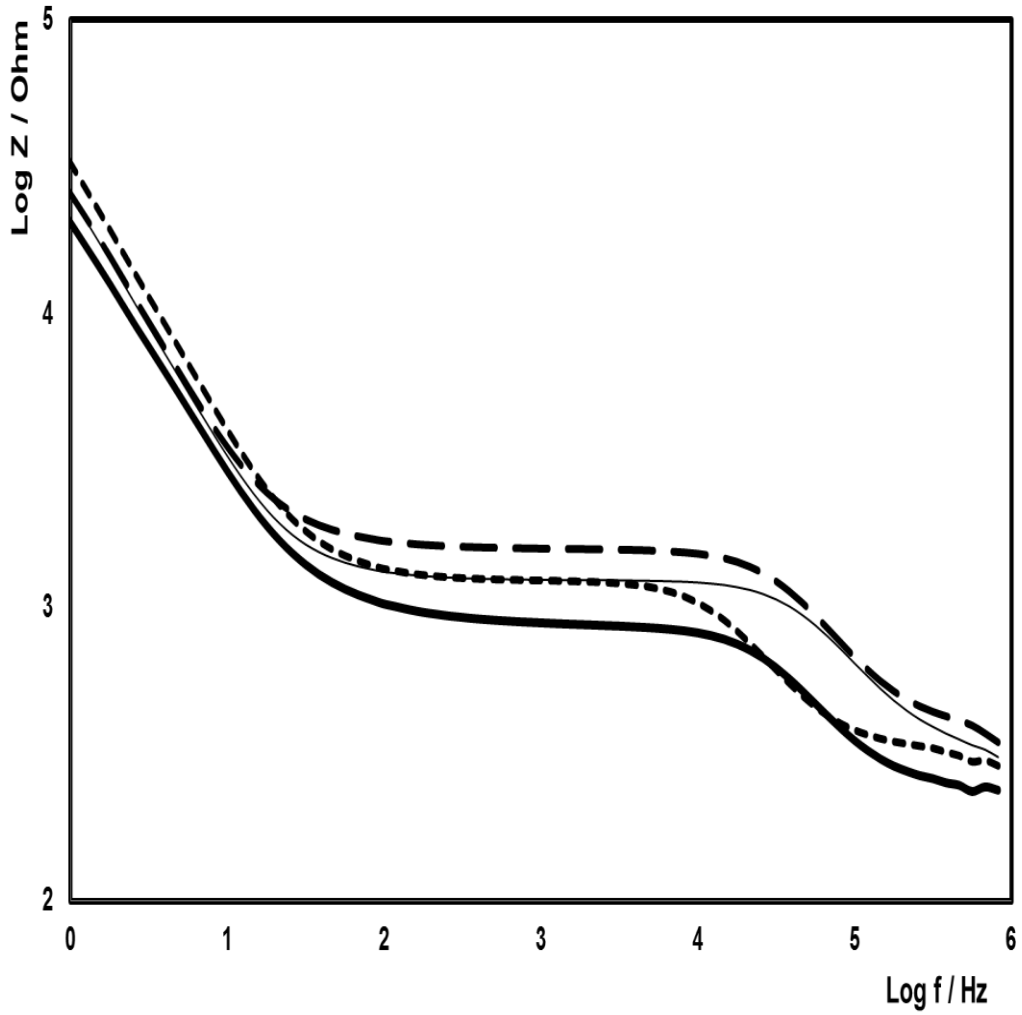

Figure 5.6: Bode plot for a bare gold electrode (thick black line), after capture miRNA (short dashed line), after target miRNA (thin black line) and after probe miRNA-PtNP (long dashed line). The EIS were recorded in the presence of 1 mM DPBS at a frequency range between 0.01 Hz and 100,000 Hz using an ac amplitude of 25 mV and the dc potential set to the open circuit potential of 0.1 V.

5.2.2.1.1 Equivalent Circuit Model

Impedance spectra can be modelled using an electrical equivalent circuit whose components are optimised to replicate the experimental response. In this way, the relative contributions from the capacitors and resistances associated with different components in the assay, e.g., solution phase resistance or the change in capacitance due to analyte binding, can be quantified and deconvoluted from the overall response. An electrical circuit can consist of electrical components, such as resistors, capacitors, inductors, etc., and components that have no electrical analogy, such as constant phase elements, Warburg impedances, etc. These can be parallel or in series. When building the equivalent circuit, it is essential that the various components correspond to meaningful electrochemical processes in the experimental cell.

Figure 5.7 illustrates the electrical equivalent circuit model that describes the capture miRNA and target miRNA modified gold electrode. The circuit consists of the solution resistance (R_{sol}) in series with a parallel combination of the component for the resistance of the capture miRNA / target miRNA layer on the electrode surface ($R_{cap/tar}$) and the Constant Phase Element of the capture miRNA / target miRNA layers. The circuit uses Constant Phase Elements (CPE) instead of pure capacitors to account for surface defects on both the electrode surface and the capture miRNA / target miRNA layers. This model simplifies and consolidates certain components, e.g., the resistance could be further broken down into components representing contributions from the capture monolayer and the intrinsic electrode resistance. However, since this simplified model accurately reflects the experimentally observed behaviour, more complex models were not used.

The solid lines in Figure 5.8 and Figure 5.9 correspond to the fitted values obtained using the equivalent circuit. Figure 5.8 shows the Nyquist plot and the Bode plot for the capture miRNA on the gold electrode (solid shapes), overlaid with the fitted values (solid line). Figure 5.9 show the Nyquist and the Bode plots when the target miRNA strand is hybridised to the capture miRNA strand (solid shapes), overlaid with the fitted values (solid line). It is clear that

they are in very good agreement with the experimental data. Chi-squared (χ^2) values of 2.3 x 10^{-4} for the fit for the capture and 9.0 x 10^{-4} for the fit for the target were observed which further indicate the good agreement between the experimental data and the model data obtained from the equivalent circuit.

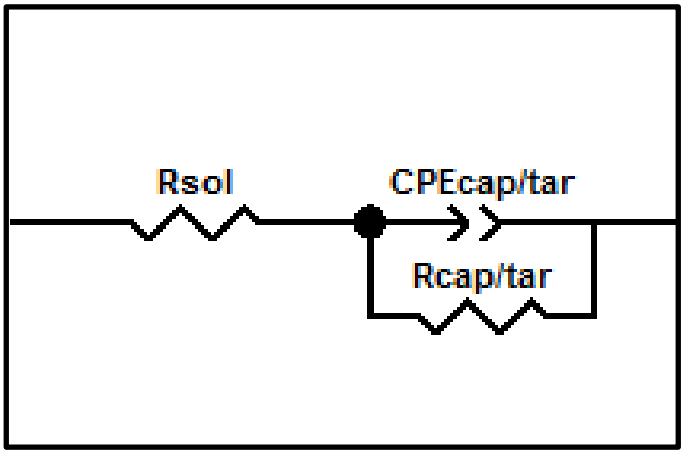

Figure 5.7: Equivalent circuit model used to fit the measured electrochemical impedance spectroscopy data.

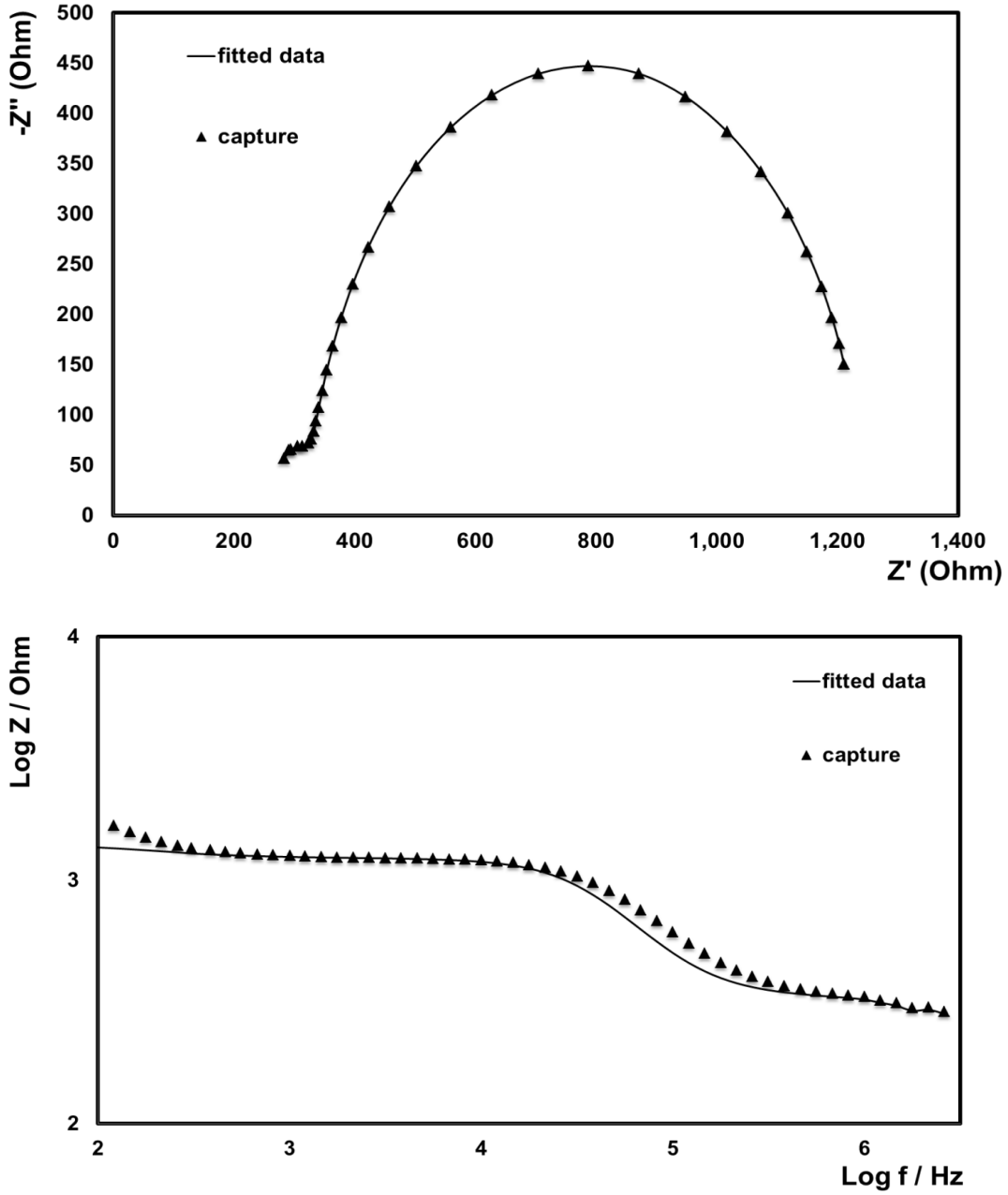

Figure 5.8: Nyquist and Bode plots showing change in impedance for the gold electrode following modification with 1 µM capture miRNA strands (▲). The solid lines correspond to the fitted values obtained using the equivalent circuit model shown in Figure 5.7. All measurements were carried out in 1 mM DPBS buffer electrolyte. The frequency range used was between 0.01 Hz and 100,000 Hz with an ac amplitude of 25 mV and the dc potential set to the open circuit potential of 0.1 V.

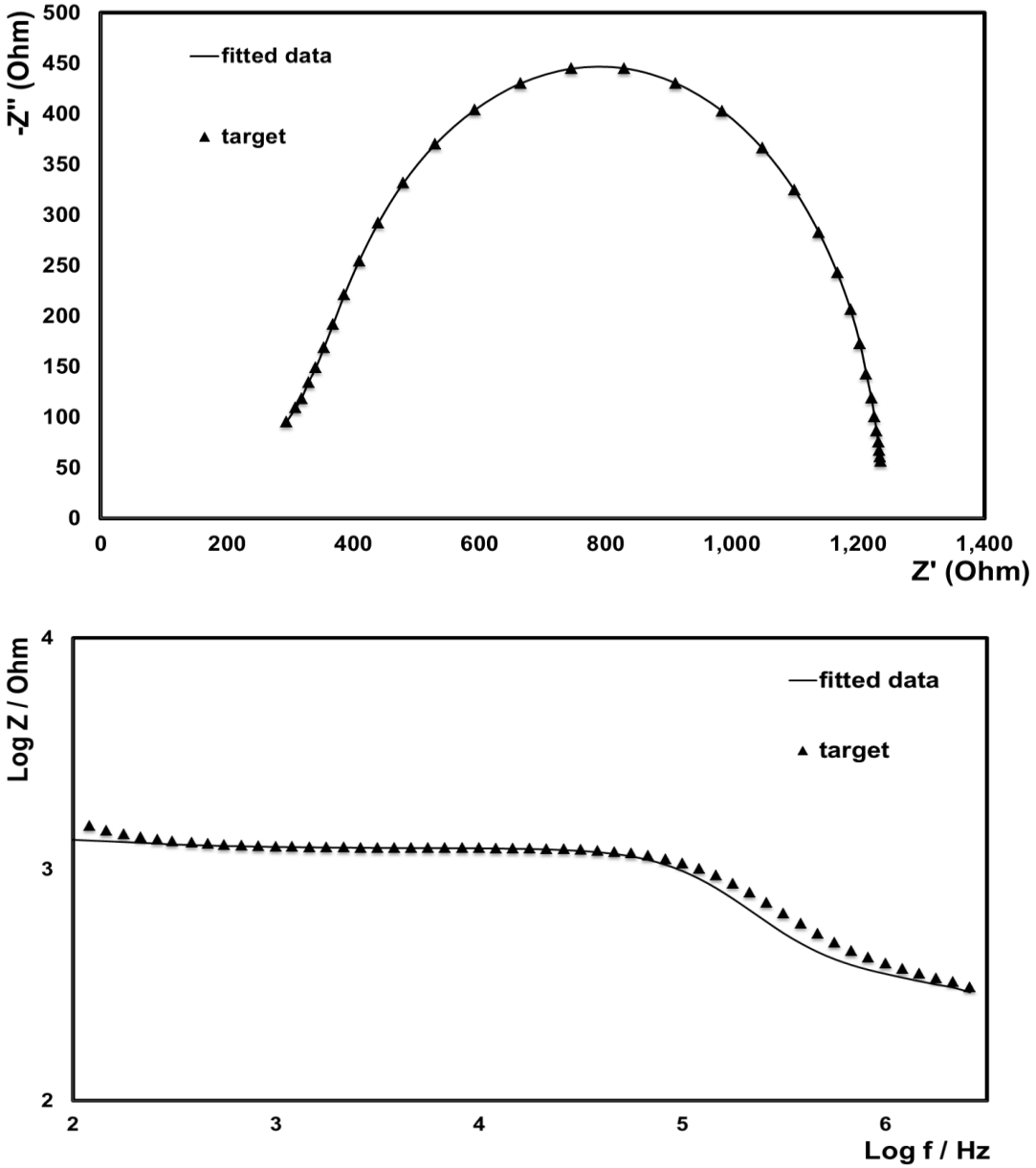

Figure 5.9: Nyquist and Bode plots showing change in impedance for the gold electrode following modification with 1 µM capture and hybridised with complementary 1 µM target miRNA strands (▲). The solid lines correspond to the fitted values obtained using the equivalent circuit model shown in Figure 5.7. All measurements were carried out in 1 mM DPBS buffer electrolyte. The frequency range used was between 0.01 Hz and 100,000 Hz with an ac amplitude of 25 mV and the dc potential set to the open circuit potential of 0.1 V.

5.2.3 Detection of miRNA

5.2.3.1 Electrochemical Impedance Spectroscopy measurement for the Detection of miRNA

Once the electrode was characterised for each step of the hybridisation process, detection of varying concentrations of the target miRNA strand were carried out also.

For this section, the disc was pre-loaded as explained. It was spun on the experimental spin stand as previously shown in Section 5.2.1.2, in order to expose the working electrode to each concentration of miRNA and allowed to hybridise before labelling with platinum nanoparticles. Varying concentrations of the target miRNA were pre-loaded into the target miRNA chamber on each section of the disc, in order to obtain the EIS measurement for differing concentrations. The EIS measurements were then carried out on the disc in 1 mM DPBS and the results are displayed in Figure 5.10 – Figure 5.12.

Binding of the platinum nanoparticles to the electrode surface would be expected to change the impedance properties of the interface, by changing both the resistance and capacitance, and therefore would allow for a sensitive detection method. As the platinum nanoparticles are brought to the surface of the electrode via complementary target miRNA binding to the probe strand on the nanoparticle, the number of platinum nanoparticles on the surface of the electrode depends on the concentration of the target miRNA. Varying concentrations of the target were used, from 1 µM to 1 aM.

The Nyquist plots in Figure 5.10 show the relationship between the real and imaginary components of the impedance. The intercept at the real axis (Z') corresponds to the solution resistance. A semi-circle forms from high to low frequencies, which corresponds to the capacitive and resistive properties of the modified electrode. The charge transfer resistance of the electrode systematically decreases as the target miRNA concentration decreases. This

is due to the decrease in the negative charge associated with lowering the concentration of the miRNA, which therefore decreases the resistance as shown. The R_{ct} values decreases from 1201 Ω for 1 μM target miRNA concentration to 661 Ω for 1 aM target miRNA concentration.

Figure 5.11 displays a calibration plot of the intercept of the real axis (Z') vs the log of the target miRNA concentration. As shown, the change in Z' value (Ohms) decreases linearly from 1 μM to 1 aM of target miRNA, with a correlation coefficient of R^2 = 0.9763, and a large slope indicating high sensitivity. These results are very encouraging, and suggest that this sensor can detect low concentrations of miRNA using label-free electrochemical impedance spectroscopy.

Reproducibility is extremely important in biosensors. There are many factors that contribute to the reproducibility in this biosensor, including:

- The density of the capture miRNA strand on the electrode surface;
- The density of probe miRNA strand functionalised on the platinum nanoparticles;
- Defects in the surface of the electrode substrate ;
- Sample volumes.

Along with many possible contributing factors from the microfluidic device, such as:

- Dust particles between the layers of the disc;
- Varying pressure when rolling the layers;
- The glue used to stick the electrodes onto the base.

Figure 5.12 shows a calibration curve of the R_{ct} values vs the log of the target miRNA concentration for an n = 3 assay. There is a clear dependence on the interfacial resistance on concentration as presented in Figure 5.12. As the total dynamic range is over 12 orders of magnitude, there isn't a large change in the resistance between each concentration. Therefore each of the above points mentions are major contributors to the reproducibility and would need to be extremely precise. Although the error bars may look large, there is in fact only a 4 – 9 % error on each data point, which is acceptably low.

Overall, EIS can be used for the detection of target miRNA strands, with promising results. However, the R_{ct} range between varying target miRNA concentration is not very wide, which may cause issues for exact concentration detection, as there may be some overlap in the values.

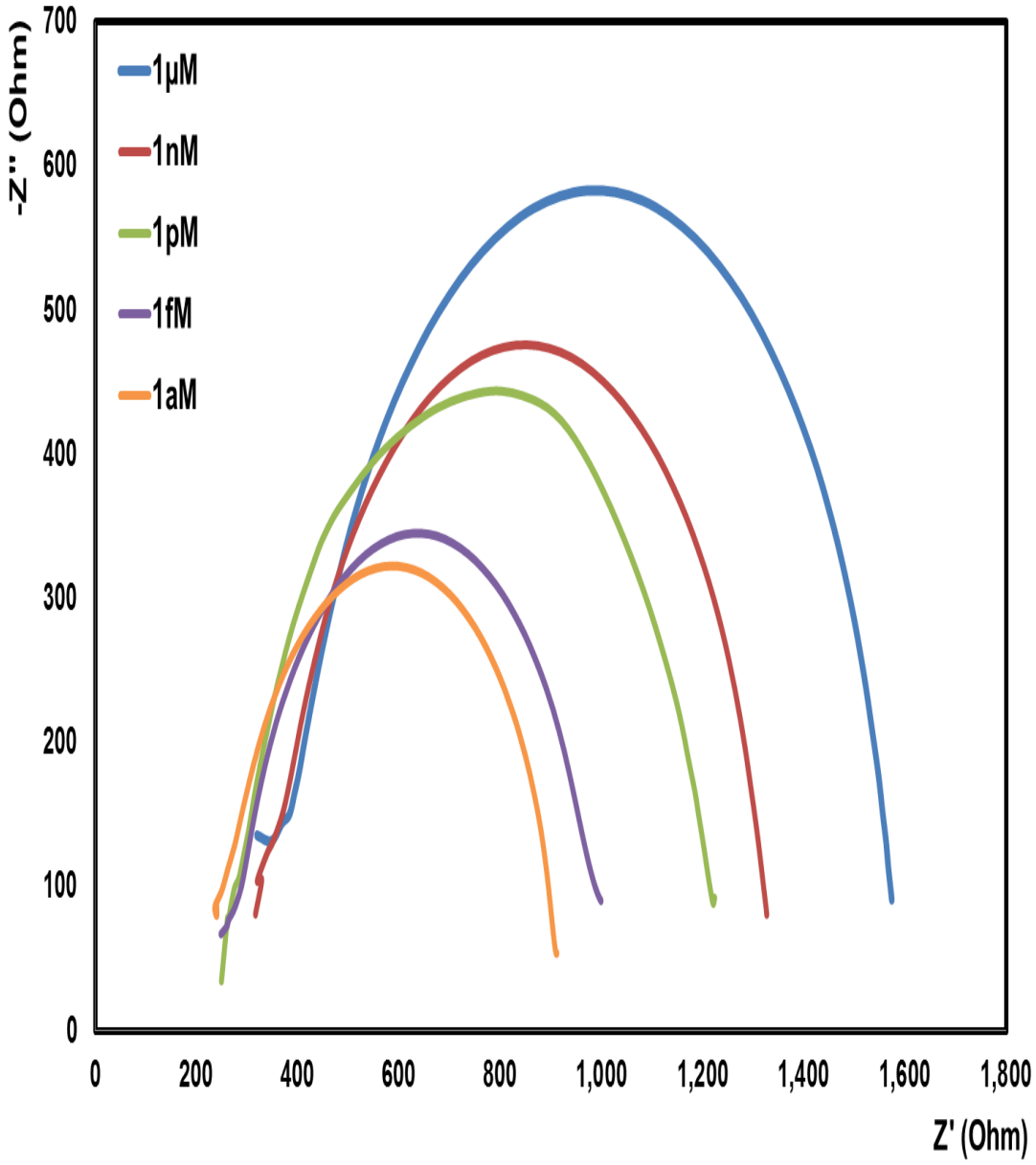

Figure 5.10: Nyquist plots recorded in 1 mM DPBS of a gold electrode modified with miRNA labelled with platinum nanoparticles. The concentration of the target strand of miRNA was varied from 1 μM to 1 aM. The EIS were recorded at a frequency range between 0.01 Hz and 100,000 Hz using an ac amplitude of 25 mV and the dc potential set to the open circuit potential of 0.1 V.

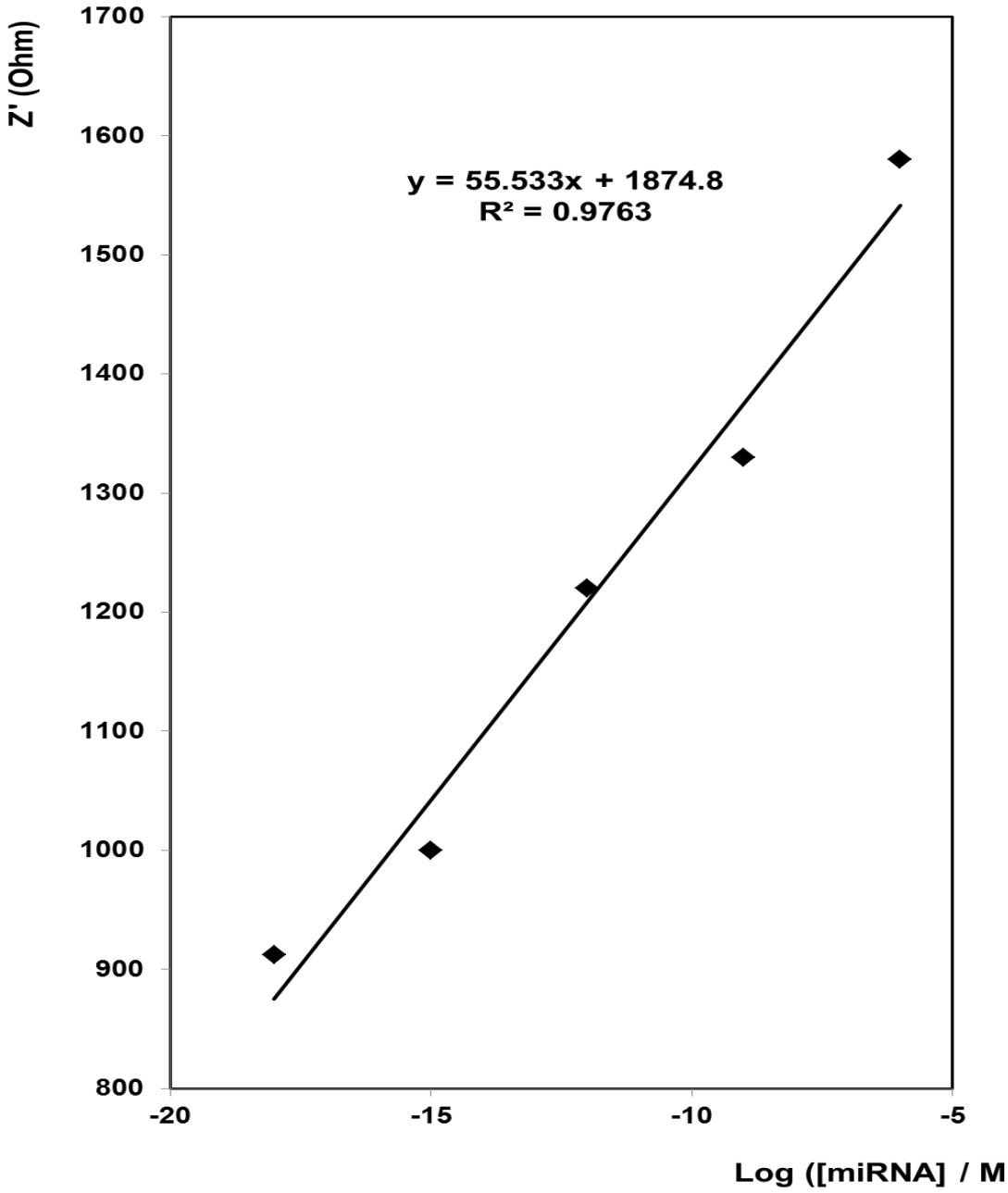

Figure 5.11: Calibration curve of the detection of miR-134 target strand miRNA. The target concentration is varied from 1 aM to 1 µM. The Y axis is the resistance value obtained from the Nyquist plot.

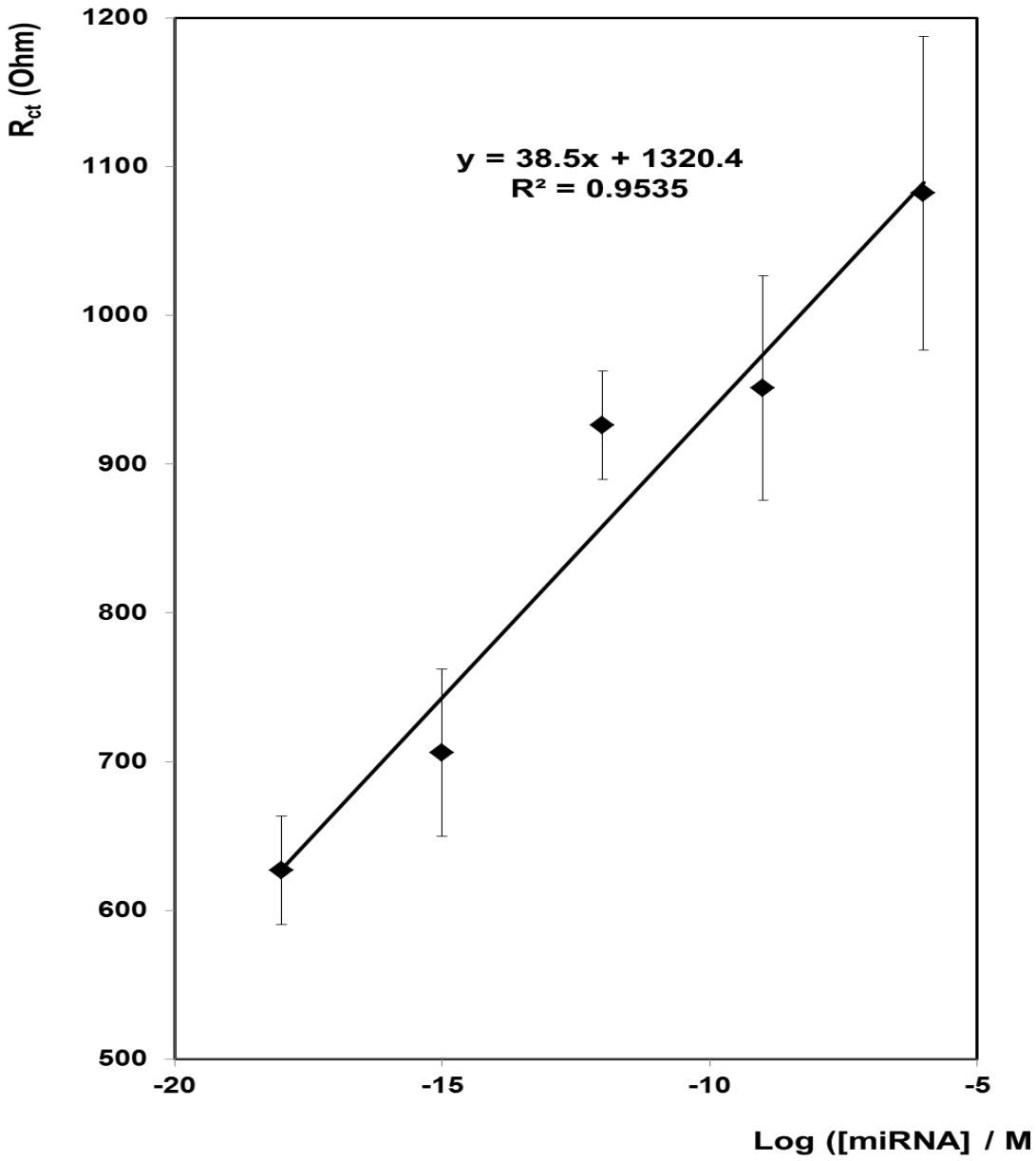

Figure 5.12: Calibration curve of the detection of miR-134 target strand miRNA. The target concentration is varied from 1 aM to 1 µM. The Y axis is the R_{ct} values obtained from the Nyquist plots. Each concentration is obtained in triplicate.

5.2.3.1.1 Equivalent Circuit Model

Figure 5.13 illustrates the electrical equivalent circuit model that describes the electrode after complete complementary hybridisation and labelling with the platinum nanoparticles. The circuit is as explained previously; it consists of the solution resistance (R_{sol}) in series with a parallel combination of the component for the resistance of the platinum nanoparticle on the electrode surface via complementary miRNA hybridisation (R_{PtNP}) and the Constant Phase Element of the platinum nanoparticle-miRNA layers (CPE_{PtNP}). The circuit uses Constant Phase Elements (CPE) instead of pure capacitors to account for surface defects on the electrode surface due to the presence of varying amounts of platinum nanoparticles.

The solid lines in Figure 5.14 correspond to the fitted values obtained using the equivalent circuit. Figure 5.14 shows the Nyquist plot for each of the varying target miRNA concentrations (solid shapes), overlaid with the fitted values (solid line). Once again, it is clear that the fitted values are in very good agreement with the experimental data with Chi-squared (χ^2) values between 10^{-3} and 10^{-4} being observed for every sample; the exact values are included in the table.

Table 5.1 shows the best-fit values for the resistances and capacitance extracted from the equivalent circuit model. It gives the R_{ct} values for each concentration, which show that they are in correlation to the R_{ct} values plotted in the calibration curve, Figure 5.12. The errors listed here are for the best fit model shown in Figure 5.13; the errors are all small, with the percentage error less than 10% for each concentration fit.

The capacitance values for a clean electrode would be expected to be tens of $\mu F/cm^2$. The capacitance values shown in Table 5.1 are dramatically lower than this at 10^{-9} F. This is consistent with a low dielectric constant, which confirms that there is miRNA modification on the electrode and that the capture layer on the electrode is dense. This low capacitance figure is also associated with the blocking properties of the nanoparticles on the electrode surface.

Table 5.1: Equivalent Circuit Model Parameters of a gold electrode modified with miRNA labelled with PtNPs. Varying concentrations of the target miRNA were used.

	χ^2	Rsol	Rsol (Err)	Rsol (Err%)	CPEnp	CPEnp - (Err)	CPEnp - (Err%)	Rnp	Rnp (Err)	Rnp (Err%)
1uM	2.3787 x 10^{-4}	366	3.1	0.85	5.87E-09	3.44E-10	5.85	1235	7.89	0.64
1nM	3.7679 x 10^{-4}	337.1	2.5	0.76	7.34E-09	4.20E-10	5.72	1009	5.48	0.54
1pM	1.0239 x 10^{-3}	267.7	3.2	1.19	7.76E-09	7.69E-10	9.90	958.6	10.19	1.06
1fM	1.1341 x 10^{-4}	267.5	1.5	0.58	1.17E-08	5.79E-10	4.95	740.5	4.20	0.57
1aM	1.2125 x 10^{-3}	229.1	2.4	1.05	8.87E-09	7.38E-10	8.32	695.4	4.84	0.70

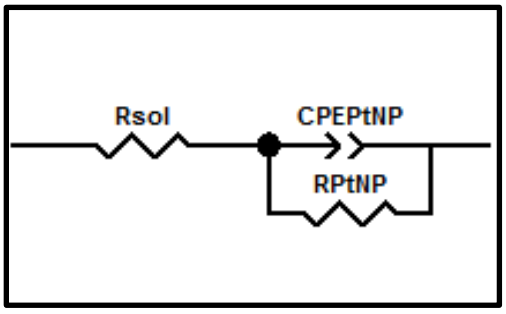

Figure 5.13: Equivalent circuit model used to fit the measured electrochemical impedance spectroscopy data.

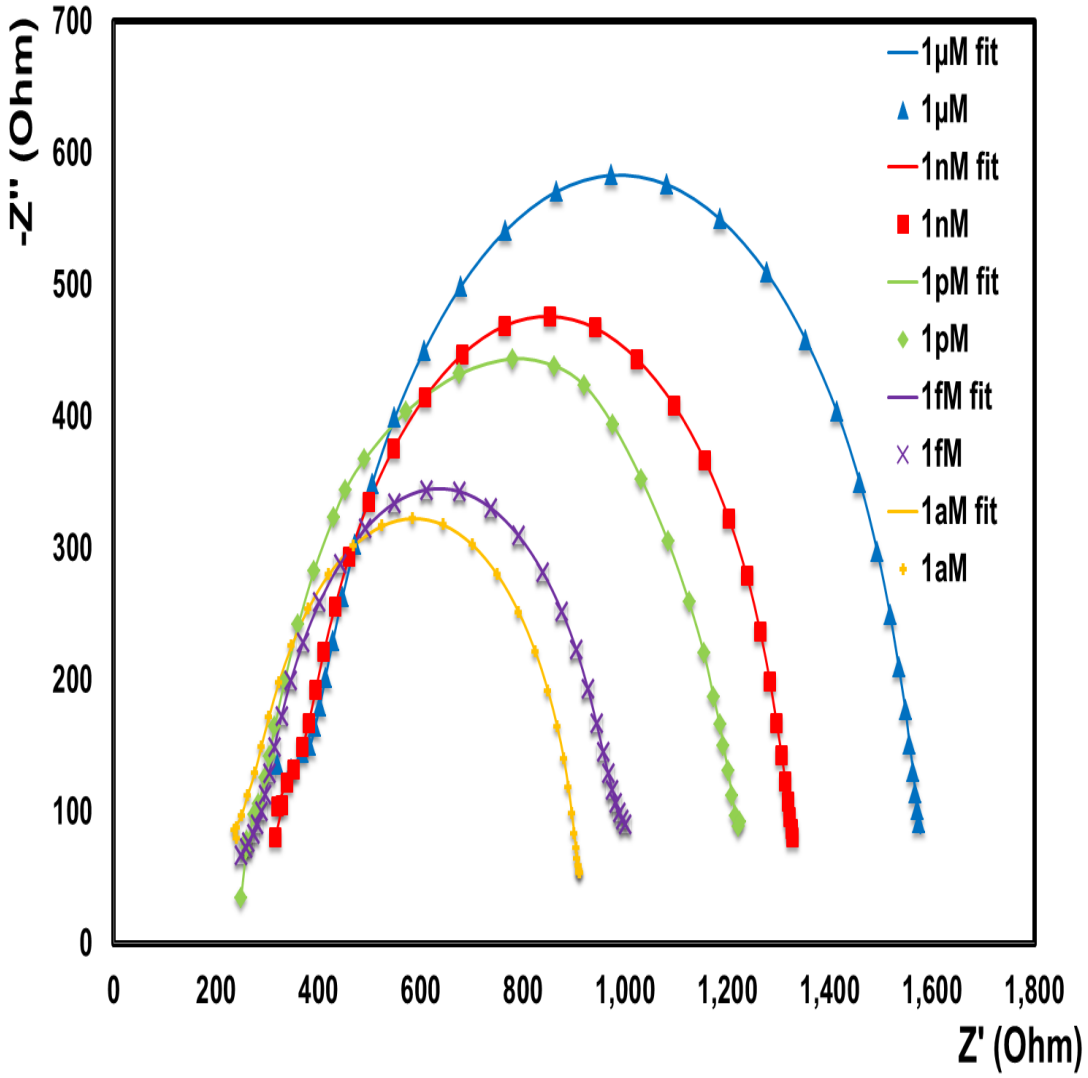

Figure 5.14: Nyquist and plots showing change in impedance for the gold electrode following modification with 1 μM capture miRNA strands, hybridised with varying concentrations of target strand miRNA and labelled with complementary probe strand modified PtNPs (solid shapes). The solid lines correspond to the fitted values obtained using the equivalent circuit model shown in Figure 5.7. All measurements were carried out in 1 mM DPBS buffer electrolyte. The frequency range used was between 0.01 Hz and 100,000 Hz with an ac amplitude of 25 mV and the dc potential set to the open circuit potential of 0.1 V.

5.2.3.2 Electrocatalytic Detection of miRNA

Electrocatalytic detection of miRNA was performed inside the microfluidic disc. As previous, the platinum nanoparticles that are confined on the gold electrode surface by miRNA complementary hybridisation are capable of electrocatalysing the reduction of hydrogen peroxide, generating a current whose magnitude is directly proportional to the number of nanoparticles on the surface of the electrode. The number of nanoparticles on the surface of the electrode depends directly on the concentration of target miRNA, as that is the strand that brings the nanoparticle to the surface. Therefore a calibration curve can be constructed by varying the target miRNA concentration.

Platinum nanoparticles that were uniformly functionalised with probe strand miRNA were used in this study. Although in Chapter 4 it was concluded that the regioselectively functionalised nanoparticles were more efficient at DNA detection by having more bare platinum available for peroxide reduction, a wide current range from 0.67 mA to 0.41 mA was still produced for the uniformly functionalised nanoparticles. The uniformly functionalised nanoparticles also have many advantages such as, they are quicker to synthesise as a monolayer does not need to be formed prior to deposition and there is more area free for probe miRNA immobilisation. The time constraint is a major disadvantage in a microfluidic disc, as the purpose of having a point-of-care device is to have a rapid detection of the pathogen that is being tested. Therefore, having pre-made miRNA functionalised platinum nanoparticles that can be loaded into the disc is a major advantage.

Concentrations ranging from 1 µM to 1 aM of the target miRNA strand were studied. A fixed potential is applied to the electrode, and the current decays to almost zero after approximately 5 min. The difference in reduction current was measured before and after the addition of 20 µM hydrogen peroxide to the sample chamber of the disc, which is already containing 1 mM DPBS. DPBS was used for the electrocatalytic assay in this biosensor, as there is a significant amount of gas evolution produced when peroxide is added to sulfuric acid. As the volume of the sample chamber is small in comparison to

previous studies, it cannot hold the gas, or let it vent out as quickly as it is produced. This causes issues as the chamber fills with air and pushes the electrolyte out, giving inaccurate results. By using DPBS the gas evolution is much lower, and can be vented from the sample chamber and therefore does not affect the measurements. Using the uniformly functionalised platinum nanoparticles also decreases the gas evolution as the current response is less, due to less bare platinum available for catalysis.

The current responses of three different concentrations are displayed in Figure 5.14. The initial current was measured at approximately 0.3 μA. When the hydrogen peroxide was added, the biosensor responded rapidly; the response current rises to reach a stable current response again. In 60 to 240 s, the maximum current is reached, depending on the initial concentration of miRNA. The rate at which a steady current is achieved is dependent on the amount of platinum present on the electrode, as it is the platinum that is driving the catalysis. As the amount of platinum is dependent on the target miRNA concentration, the higher the concentration on target miRNA, the more platinum nanoparticles present, and therefore the current takes longer to reach a steady state.

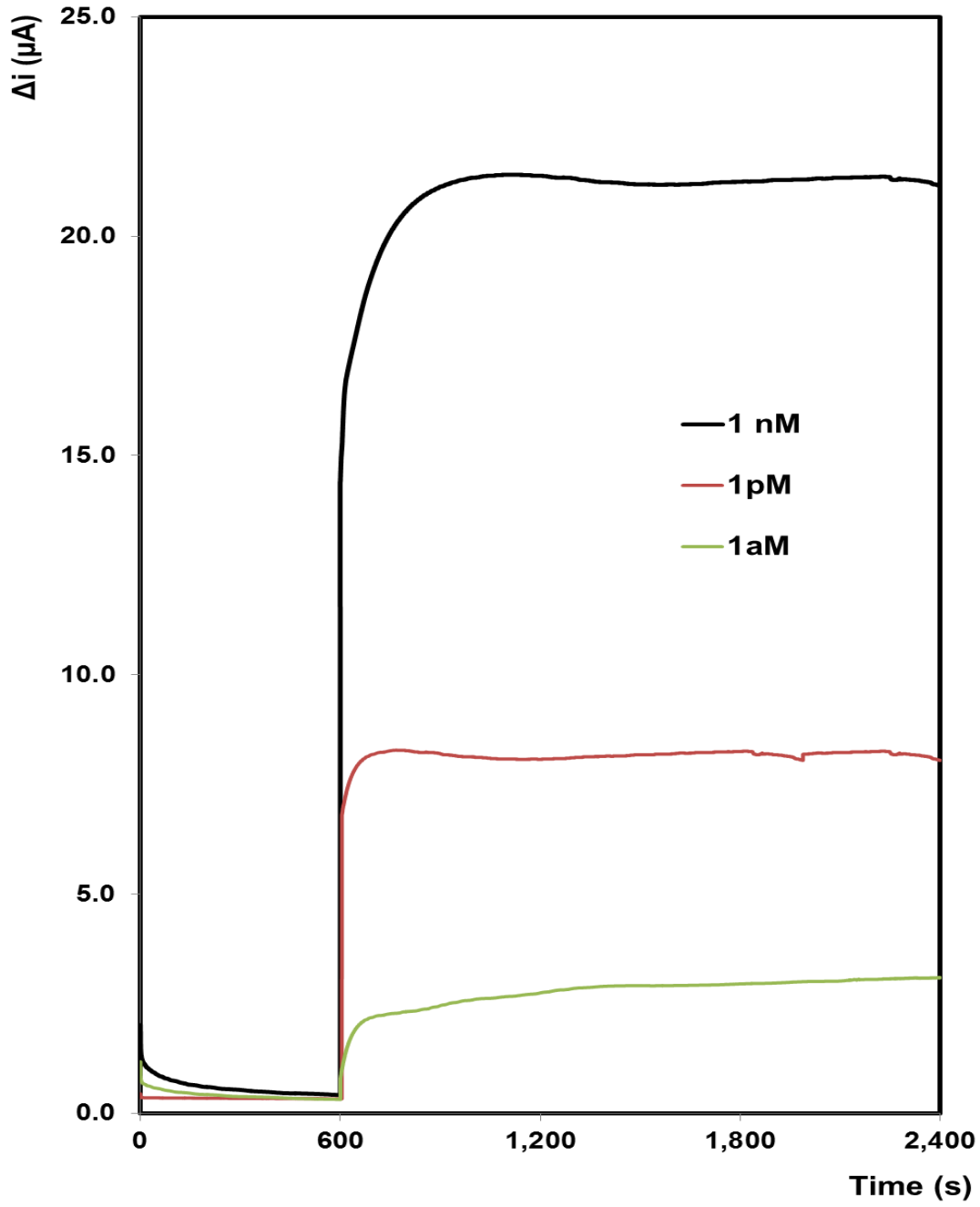

Figure 5.15: Amperometric i-t curves for gold electrodes functionalised with 1 μM miRNA capture strands, varying concentrations of miRNA target stands (as shown in legend) and 1 μM miRNA probe strands labelled with platinum nanoparticles. Potential applied is -0.25 V in 1 mM DPBS. The difference in current before and after the addition of 20 μM H_2O_2 is displayed.

Using a concentration range of target DNA from 1 µM to 1 aM the electrocatalytic properties of the platinum nanoparticles towards H_2O_2 was investigated. The calibration plot of the semi-log concentration vs. Δi is shown in Figure 5.16. The change in current increases with log [miRNA] rather than [miRNA]; this suggests that the current response is influenced by the [H_2O_2], as well as the miRNA concentration.

Figure 5.16 shows that the change in current decreases linearly from 1 µM to 1 pM of target miRNA, with a correlation coefficient of R^2 = 0.9999, with a high sensitivity, shown by the large slope, and a wide dynamic range over six orders of magnitude. As shown in Table 5.2, the current change varies from 6 µA to 40 µA, with low standard deviations being observed for all concentrations investigated.

The shape of this calibration curve is typical of an S-shaped calibration curve, i.e. it will have an upper and a lower detection limit. Limit of detection is the minimum concentration at which the analyte can be distinguished from the assay background. The LOD of this system was determined to be 1 x 10^{-12} M, or 1 pM, as this is the point on the curve when the current no longer depends on the concentration. Therefore, the lower two target miRNA concentrations, 1 fM and 1 aM are below the LOD and can't be accurately detected.

By comparing the currents obtained for this calibration curve to those obtained previously for the other uniform platinum nanoparticles shown in Chapter 4 for the detection of mastitis DNA target, the current generated here is much lower. This could be attributed to a couple of reasons. First of all, the electrolyte is changed from 0.01 M H_2SO_4 to 1 mM DPBS. The concentration of peroxide is also reduced from 2 mM to 20 µM. Both of these changes are to reduce the gas produced during the hydrogen peroxide reduction, which would affect the catalytic activity slightly, due to less hydrogen peroxide present for reduction, and less hydrogen ions available in the solution from the sulfuric acid.

However, the signal generated is significant given the low concentrations of the target used and shows the ability of a self-contained microfluidic biosensor, where all steps can be carried out inside the disc.

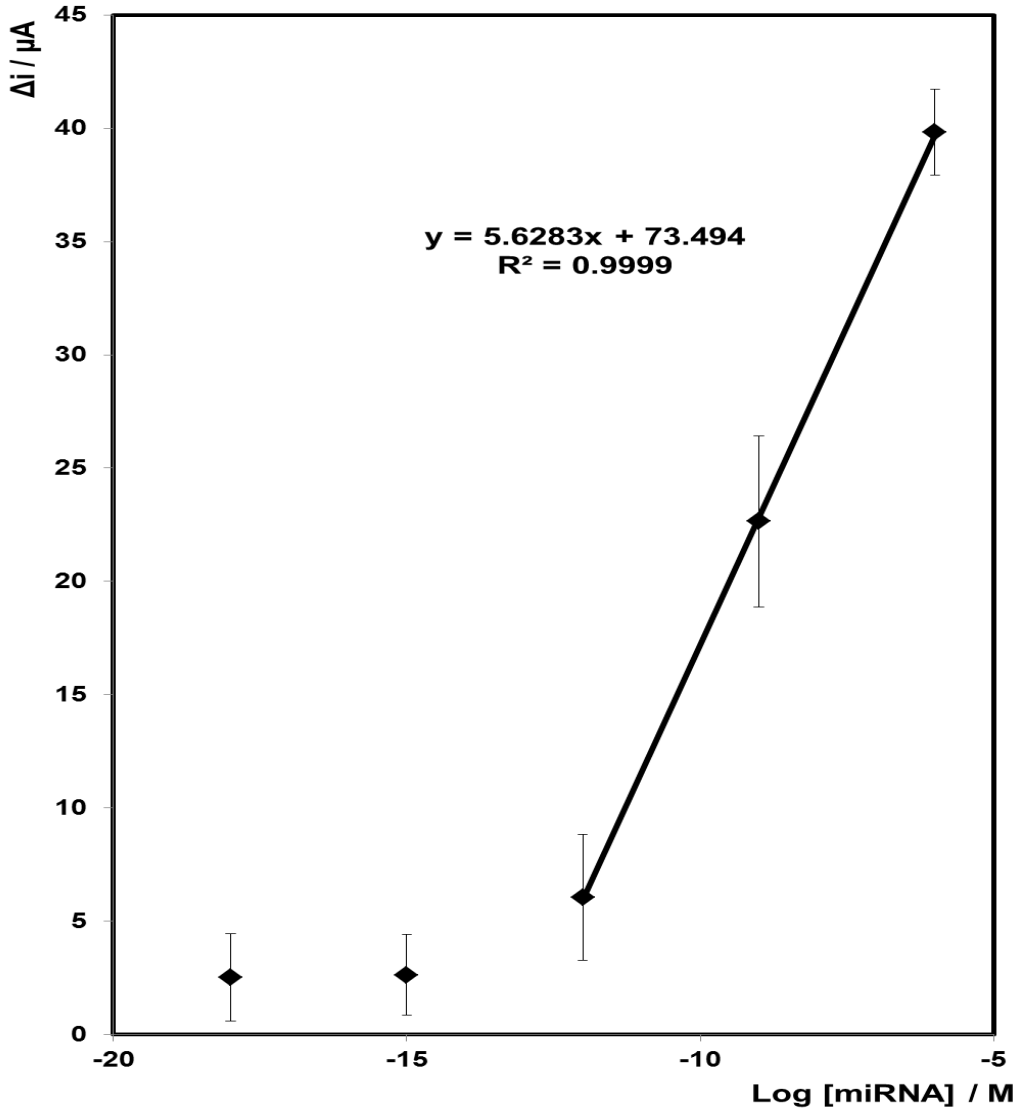

Figure 5.16: Electrochemical detection of sequence specific miR-134 miRNA pathogen. The Y axis is the difference in current before and after the addition of 20 μM H_2O_2. The applied potential is -0.25 V in 1 mM DPBS.

Table 5.2: Change in current before and after the injection of H_2O_2 for varying concentrations of miRNA.

Concentration of miRNA (M)	Log [DNA]	Average Δi (μA)	Standard Deviation
1.00E-18	-18	2.5	1.924954
1.00E-15	-15	2.6	1.776869
1.00E-12	-12	6.1	2.78585
1.00E-9	-9	22.7	3.783706
1.00E-6	-6	39.8	1.89702

5.2.3.3 Control Studies

A control study was carried out to show the electrocatalytic activity of the bare electrode and where the miRNA was immobilised and hybridised onto the electrode without the platinum nanoparticle label. The current-time transients are displayed in Figure 5.17, with the corresponding average change in current values displayed in Table 5.3.

The current generated from a bare electrode causes an average current change of 1.81 μA. The current generated from both the capture miRNA strand functionalised gold electrode, and with the target miRNA strand hybridised to the electrode surface, both cause an average current change of 1.49 μA and 1.58 μA respectively.

The reason that the current generated for the bare gold electrode is slightly higher than when it is functionalised with miRNA is due to the fact that there would be some electrocatalytic activity coming from the underlying gold also, especially when it is clean gold, unmodified by the miRNA. Therefore, when the gold is bare, it will cause a slight current jump when the hydrogen peroxide is added, as it will reduce the hydrogen peroxide also. When the capture miRNA is immobilised on the surface of the electrode, it blocks some of the gold, which cause a slight decrease in the average current jump. Most of the peroxide can still permeate through the miRNA layer, which is why the current doesn't decrease by a large amount. By exposing the functionalised electrode to the target miRNA strand, the target will hybridise to the complementary capture miRNA strand. This will not change the current associated, as the peroxide can still permeate through the miRNA strands to the gold as before, and as the target miRNA is unlabelled, the current will not increase because there is no platinum present for the electrocatalytic hydrogen peroxide reduction. This shows the low background current associate with the biosensor, which also reflects the poor electrocatalytic properties of a miRNA modified gold electrode, and shows the need for a platinum nanoparticle label.

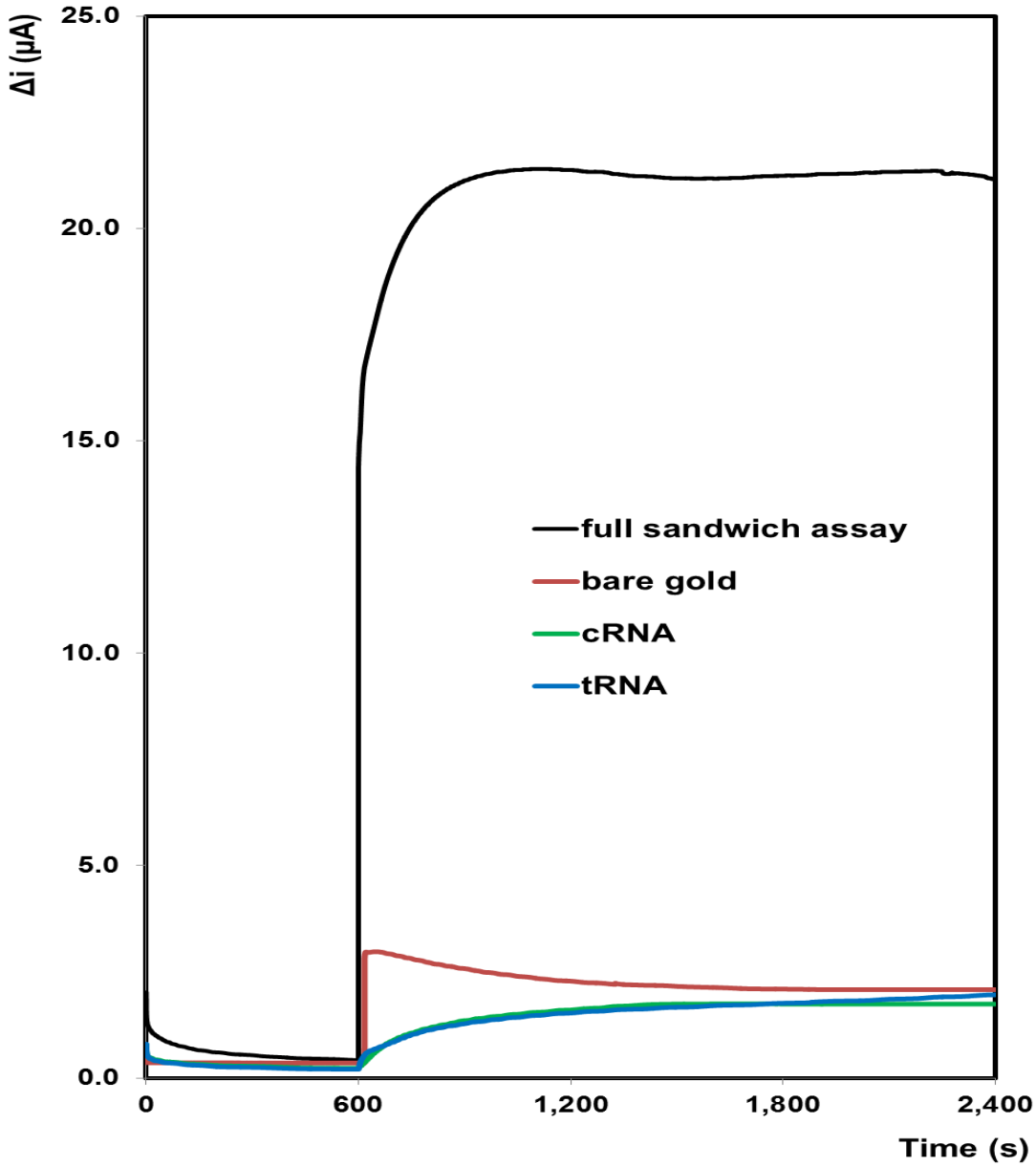

Figure 5.17: Amperometric i-t curves for a bare gold electrode (red line), a gold electrode functionalised with 1 μM capture miRNA (cRNA, green line), a gold electrode functionalised with 1 μM capture miRNA and hybridised to 1 μM target miRNA (tRNA, blue line), and a gold electrode functionalised with capture, 1 nM target and probe miRNA labelled with platinum nanoparticles (full sandwich assay, black line). Potential applied is -0.25 V in 1 mM DPBS. The difference in current before and after the addition of 20 μM H_2O_2 is displayed.

Table 5.3: Change in current before and after the injection of H_2O_2 for varying stages of the hybridisation process.

	Average Δi (μA)	**Standard Deviation**
Bare	1.8	0.266
cRNA	1.5	0.170
tRNA	1.6	0.118
Full sandwich assay with 1 nM target miRNA	22.7	3.784

5.4 CONCLUSION

In conclusion, target miRNA, associated with epilepsy is detected inside a microfluidic disc using two methods: electrochemical impedance spectroscopy and electrocatalytic reduction of peroxide at functionalised platinum nanoparticles functionalised with probe strand nucleic acids.

A microfluidic disc is assembled with nine layers of PMMA and PSA. The gold electrode is pre-functionalised with capture miRNA that is complementary to part of the target miRNA strand. This electrode is then assembled into the base of the disc, with bare gold as the counter electrode and ITO as the reference electrode. This disc uses an event triggered system; the valving technology used utilises the arrival of a liquid at one location to prompt the release of another liquid at another, distant location on the disc by a connecting pneumatic channel. The disc is pre-loaded with target miRNA, probe miRNA-functionalised platinum nanoparticles and DPBS into the relevant chambers. It is then spun on an experimental spin stand at different rates of rotation, to control the flow of liquid, and the release of differing chambers.

By pre-loading each of the chambers with each step of the hybridisation process, and releasing them systematically and allowing each liquid to incubate for the required time, a sandwich assay is formed on the gold electrode with the target miRNA bringing the platinum nanoparticle to the surface of the electrode, via complementary hybridisation with the probe miRNA that is immobilised on the platinum nanoparticle via a thiol head group. Once fully hybridised, the external elements of the electrode are attached to a potentiostat to detect the concentration of target miRNA in the disc.

Electrochemical Impedance Spectroscopy (EIS) is performed on the electrode with the fully hybridised sequence labelled with platinum nanoparticles. Different concentrations of the target miRNA were used. A calibration plot showing the log [miRNA] vs the Z' value from the Nyquist plot is displayed, showing that the Z' value varies linearly with the varying concentration, with a

standard deviation of 2 – 9 %. These results are fit to an equivalent circuit model and the measured data is in very good agreement to the fitted data for each concentration investigated.

The current associated with the reduction of hydrogen peroxide at the platinum nanoparticles is measured as is shown to vary linearly with concentration between target miRNA concentrations of 1 pM and 1 µM. The limit of detection is calculated to be 1 pM of the target miRNA concentration. Uniformly functionalised platinum nanoparticles are used, and a significant current is achieved after the injections of 20 µM of H_2O_2 that varies between each target miRNA concentration.

The ability to detect target miRNA strands associated with epilepsy inside a microfluidic disc is a huge step forward for biosensing applications, as it is inexpensive, sensitive and rapid. While there are some challenges involved in the reproducibility of some of the data points, that are touched on in the chapter, the results displayed here are extremely encouraging, due to the wide dynamic range and low limits of detection. The issues that arise due to reproducibility are all solvable, and can be improved on. The advantages of this system include the low limit of detection, wide dynamic range, and the rapid response time for target miRNA detection. This system is also versatile and can be utilised for many different pathogens or biomarkers; as there are four sample chambers present on the device, four samples can be tested simultaneously.

5.5 REFERENCES

1. Hampel, H.; Frank, R.; Broich, K.; Teipel, S. J.; Katz, R. G.; Hardy, J.; Herholz, K.; Bokde, A. L. W.; Jessen, F.; Hoessler, Y. C.; Sanhai, W. R.; Zetterberg, H.; Woodcock, J.; Blennow, K. Biomarkers for Alzheimer's disease: academic, industry and regulatory perspectives. *Nat. Rev. Drug Discov.* **2010***, 9*, 560-574.

2. Zetterberg, H.; Blennow, K. Biomarker evidence for uncoupling of amyloid build-up and toxicity in Alzheimer's disease. *Alzheimers. Dement.* **2013***, 9*, 459-462.

3. Zetterberg, H.; Smith, D. H.; Blennow, K. Biomarkers of mild traumatic brain injury in cerebrospinal fluid and blood. *Nat. Rev. Neurol.* **2013***, 9*, 201-210.

4. Chang, B.; Lowenstein, D. Mechanisms of disease - Epilepsy. *N. Engl. J. Med.* **2003***, 349*, 1257-1266.

5. Fisher, R. S.; Acevedo, C.; Arzimanoglou, A.; Bogacz, A.; Cross, J. H.; Elger, C. E.; Engel, J., Jr.; Forsgren, L.; French, J. A.; Glynn, M.; Hesdorffer, D. C.; Lee, B. I.; Mathern, G. W.; Moshe, S. L.; Perucca, E.; Scheffer, I. E.; Tomson, T.; Watanabe, M.; Wiebe, S. ILAE Official Report: A practical clinical definition of epilepsy. *Epilepsia* **2014***, 55*, 475-482.

6. Hegde, M.; Lowenstein, D. H. The search for circulating epilepsy biomarkers. *Biomark. Med.* **2014***, 8*, 413-427.

7. Henshall, D. C. MicroRNA and epilepsy: profiling, functions and potential clinical applications. *Curr. Opin. Neurol.* **2014***, 27*, 199-205.

8. Fabian, M. R.; Sonenberg, N.; Filipowicz, W. Regulation of mRNA Translation and Stability by microRNAs. *Annu. Rev. Biochem.* **2010***, 79*, 351-379.

9. Friedman, R. C.; Farh, K. K.; Burge, C. B.; Bartel, D. P. Most mammalian mRNAs are conserved targets of microRNAs. *Genome Res.* **2009***, 19*, 92-105.

10. Schratt, G.; Tuebing, F.; Nigh, E.; Kane, C.; Sabatini, M.; Kiebler, M.; Greenberg, M. A brain-specific microRNA regulates dendritic spine development. *Nature* **2006***, 439*, 283-289.

11. Fiore, R.; Khudayberdiev, S.; Christensen, M.; Siegel, G.; Flavell, S. W.; Kim, T.; Greenberg, M. E.; Schratt, G. Mef2-mediated transcription of the miR379-410 cluster regulates activity-dependent dendritogenesis by fine-tuning Pumilio2 protein levels. *EMBO J.* **2009***, 28*, 697-710.

12. Peng, J.; Omran, A.; Ashhab, M. U.; Kong, H.; Gan, N.; He, F.; Yin, F. Expression Patterns of miR-124, miR-134, miR-132, and miR-21 in an Immature Rat Model and Children with Mesial Temporal Lobe Epilepsy. *J. Mol. Neurosci.* **2013***, 50*, 291-297.

13. Jimenez-Mateos, E. M.; Engel, T.; Merino-Serrais, P.; McKiernan, R. C.; Tanaka, K.; Mouri, G.; Sano, T.; O'Tuathaigh, C.; Waddington, J. L.; Prenter, S.; Delanty, N.; Farrell, M. A.; O'Brien, D. F.; Conroy, R. M.; Stallings, R. L.; DeFelipe, J.; Henshall, D. C. Silencing microRNA-134 produces neuroprotective and prolonged seizure-suppressive effects. *Nat. Med.* **2012***, 18*, 1087-+.

14. Gorter, J. A.; Iyer, A.; White, I.; Colzi, A.; van Vliet, E. A.; Sisodiya, S.; Aronica, E. Hippocampal subregion-specific microRNA expression during epileptogenesis in experimental temporal lobe epilepsy. *Neurobiol. Dis.* **2014***, 62*, 508-520.

15. Wang, J.; Tan, L.; Tan, L.; Tian, Y.; Ma, J.; Tan, C.; Wang, H.; Liu, Y.; Tan, M.; Jiang, T.; Yu, J. Circulating microRNAs are promising novel biomarkers for drug-resistant epilepsy. *Sci Rep* **2015***, 5*, 10201.

16. Spain, E.; Jimenez-Mateos, E. M.; Raoof, R.; ElNaggar, H.; Delanty, N.; Forster, R. J.; Henshall, D. C. Direct, non-amplified detection of

microRNA-134 in plasma from epilepsy patients. *RSC Adv.* **2015***, 5*, 90071-90078.

17. Gorkin, R.; Park, J.; Siegrist, J.; Amasia, M.; Lee, B. S.; Park, J.; Kim, J.; Kim, H.; Madou, M.; Cho, Y. Centrifugal microfluidics for biomedical applications. *Lab Chip* **2010***, 10*, 1758-1773.

18. Ducree, J.; Haeberle, S.; Lutz, S.; Pausch, S.; von Stetten, F.; Zengerle, R. The centrifugal microfluidic bio-disk platform. *J Micromech Microengineering* **2007***, 17*, S103-S115.

19. Madou, M.; Zoval, J.; Jia, G.; Kido, H.; Kim, J.; Kim, N. Lab on a CD. *Annu. Rev. Biomed. Eng.* **2006***, 8*, 601-628.

20. Lien, K.; Lee, W.; Lei, H.; Lee, G. Integrated reverse transcription polymerase chain reaction systems for virus detection. *Biosens. Bioelectron.* **2007***, 22*, 1739-1748.

21. Miao, B.; Peng, N.; Li, L.; Li, Z.; Hu, F.; Zhang, Z.; Wang, C. Centrifugal Microfluidic System for Nucleic Acid Amplification and Detection. *Sensors* **2015***, 15*, 27954-27968.

22. Myers, F. B.; Henrikson, R. H.; Bone, J.; Lee, L. P. A Handheld Point-of-Care Genomic Diagnostic System. *PLoS One* **2013***, 8*, e70266.

23. Lin, X.; Chen, Q.; Liu, W.; Li, H.; Lin, J. A portable microchip for ultrasensitive and high-throughput assay of thrombin by rolling circle amplification and hemin/G-quadruplex system. *Biosens. Bioelectron.* **2014***, 56*, 71-76.

24. Chang, C.; Chang, W.; Wang, C.; Wang, J.; Mai, J. D.; Lee, G. Nucleic acid amplification using microfluidic systems. *Lab Chip* **2013***, 13*, 1225-1242.

25. Gorkin, R.,III; Nwankire, C. E.; Gaughran, J.; Zhang, X.; Donohoe, G. G.; Rook, M.; O'Kennedy, R.; Ducree, J. Centrifugo-pneumatic valving utilizing dissolvable films. *Lab on a Chip* **2012***, 12*, 2894-2902.

26. Kinahan, D. J.; Kearney, S. M.; Dimov, N.; Glynn, M. T.; Ducree, J. Event-triggered logical flow control for comprehensive process integration of multi-step assays on centrifugal microfluidic platforms. *Lab on a Chip* **2014**, *14*, 2249-2258.

27. Gorkin, R.; Soroori, S.; Southard, W.; Clime, L.; Veres, T.; Kido, H.; Kulinsky, L.; Madou, M. Suction-enhanced siphon valves for centrifugal microfluidic platforms. *Microfluidics and Nanofluidics* **2012**, *12*, 345-354.

28. Nwankire, C. E.; Donohoe, G. G.; Zhang, X.; Siegrist, J.; Somers, M.; Kurzbuch, D.; Monaghan, R.; Kitsara, M.; Burger, R.; Hearty, S.; Murrell, J.; Martin, C.; Rook, M.; Barrett, L.; Daniels, S.; McDonagh, C.; O'Kennedy, R.; Ducree, J. At-line bioprocess monitoring by immunoassay with rotationally controlled serial siphoning and integrated supercritical angle fluorescence optics. *Anal. Chim. Acta* **2013**, *781*, 54-62.

29. Grumann, M.; Brenner, T.; Beer, C.; Zengerle, R.; Ducree, J. Visualization of flow patterning in high-speed centrifugal microfluidics. *Rev. Sci. Instrum.* **2005**, *76*, 025101.

30. Kirby, D.; Siegrist, J.; Kijanka, G.; Zavattoni, L.; Sheils, O.; O'Leary, J.; Burger, R.; Ducree, J. Centrifugo-magnetophoretic particle separation. *Microfluidics and Nanofluidics* **2012**, *13*, 899-908.

31. Daniels, J. S.; Pourmand, N. Label-free impedance biosensors: Opportunities and challenges. *Electroanalysis* **2007**, *19*, 1239-1257.

32. Riedel, M.; Kartchemnik, J.; Schoening, M. J.; Lisdat, F. Impedimetric DNA Detection-Steps Forward to Sensorial Application. *Anal. Chem.* **2014**, *86*, 7867-7874.

33. Liu, S.; Wei, W.; Wang, Y.; Fang, L.; Wang, L.; Li, F. Ultransensitive electrochemical detection of nucleic acid by coupling an autonomous cascade target replication and enzyme/gold nanoparticle-based post-amplification. *Biosensors & bioelectronics* **2016**, *80*, 208-214.

CHAPTER 6

TRIANGULAR SILVER NANOPLATES: PROPERTIES AND ULTRASENSITIVE DETETCTION OF miRNA

6.1 INTRODUCTION

Neuroblastoma is a paediatric cancer of the sympathetic nervous system that is responsible for approximately 15 % of all childhood cancer deaths.[1] It is one of the most common solid tumours in children, and these tumours are noted for their wide heterogeneity in clinical behaviours, ranging from spontaneous regression to aggressive clinical course and death due to disease.[2] Diagnosis can be very challenging as many of the symptoms can be attributed to other less serious causes, and the age at which the patient is diagnosed can greatly affect their prognosis and treatment.[3]

Recently, a 22 base miRNA signature, miR-132-3p, has been implicated in the pathogenesis of neuroblastoma.[4,5] This miRNA has been associated with carcinogenesis and aggressive progression of various tumours including lung cancer[6], gastric cancer[7], osteosarcoma[8] and ovarian cancer.[9] However, the concentration of miRNA in samples for detection is typically extremely low, i.e., picomolar or lower. Current methods of miRNA analysis involve complex strategies such as Reverse Transcriptase PCR (RT-PCR),[10,11] or microarrays[12]. These methods have disadvantages including the short and inflexible templates characteristics of the target and similarities in sequence between miRNA families. They are also more prone to human and handling error.[13] Many direct detection methods `do not have the necessary sensitivity to detect the ultralow copy numbers of miRNA and cannot be deployed away from centralised laboratories. Therefore, there is an unmet clinical need for methods that can directly detect ultralow concentrations of miRNA without the need for prior amplification methods.

The target miRNA in question here, miR-132-3p is used in two different ways, as shown in Scheme 6.1. Firstly, the triangular silver nanoplates are functionalised with probe strand miRNA, complementary to the target strand. These labelled nanoplates are then used for the electrocatalytic detection of the target miRNA on the surface of a gold disc electrode. They are also immobilised in gold microcavity arrays for a different detection method.

As previously explored, electrocatalytic metal nanoparticles can be used as a detection method by immobilising probe nucleic acids on the surface of the nanoparticle, and then complementary hybridisation to the target nucleic acid in question to bring the nanoparticle to the electrode surface. We have shown how this method of nucleic acid detection functions extremely well for platinum nanoparticles, by giving a large current change when the peroxide is injected into the biosensor. However silver is also another metal that shows electrocatalytic activity toward the reduction of hydrogen peroxide[14-16] and therefore can be used in a similar way. In this study, triangular silver nanoplates will be used for electrocatalytic detection of nucleic acids, as it has been shown that triangular shaped nanoparticles have greater catalytic activity when compared to spherical or cubic shaped nanoparticles.[17] A previous amperometric biosensor used triangular silver nanoparticles in conjunction with glucose oxidase for the detection of glucose.[18] In this study, 1 µM was the limit of detection reached by this system, and it was proven that by adding triangular silver prisms into the system, the current response was 16 times greater.

Beyond the optimisation of the particle shape and size for detection, the nature of the surface onto which they are captured can also significantly influence the optical and electrochemical responses generated. For example, the fabrication of ordered nanoporous arrays of gold with varying pore diameters has previously been demonstrated.[19] These arrays have strong plasmonic fields which deliver excellent Raman signals and vary both with the metal used, and the dimensions of the nanopore. These plasmonic fields can be exploited to yield very significant enhancements in the Raman intensity from a species trapped on or near the surface. Nanoparticles immobilised within the microcavities can contribute to the generation of extremely strong electromagnetic fields and can dramatically enhance Raman responses when the cavity mode is resonant with the captured nanoparticle mode.[20-22] For example, regioselectively functionalised platinum nanoparticles have been immobilised in a microcavity array via DNA hybridisation.[23] These immobilised nanoparticles retain their electrocatalytic activity inside the microcavities and can generate significantly higher current for the reduction of hydrogen peroxide

than a planar surface by changing the nature of the diffusion field which can improve the sensitivity of DNA detection. The benefit of having the nanoparticles in a microcavity is that they can generate high Raman signal intensities which can be used to indicate when the hybridisation has occurred, as there is a twofold enhancement in the Raman intensity when the nanoparticle is present.

The benefit in this instance in using silver nanoplates is that silver is SERS active.[24-26] Xu et al have recently used silver nanoparticles to detect multiplex diseases at attomolar level by SERS.[27] Wu et al have also detected the aptamer of a cancer biomarker, alpha fetoprotein, by SERS and have achieved a limit of detection of 0.097 aM.[28]

There is also benefit in using triangular shaped nanoparticles as they have been shown to have unique optical properties that can be tuned to many different biosensing opportunities.[29-32] In SERS, "hotspots" are created between the nanoparticles to produce intense electromagnetic fields that increase the Raman intensity of the molecules located in these regions. By using triangular silver nanoplates, these hotspots can occur at the edges or the tips of the triangular shape, and could operate individually as a highly sensitive SERS substrate.[33]

In this study, both SERS and electrocatalytic detection of miRNA is reported and their performances compared. The triangular silver nanoplates has been immobilised on a gold disk electrode, and inside a gold microcavity by complementary miRNA hybridisation with the target miRNA strand, miR-132-3p.

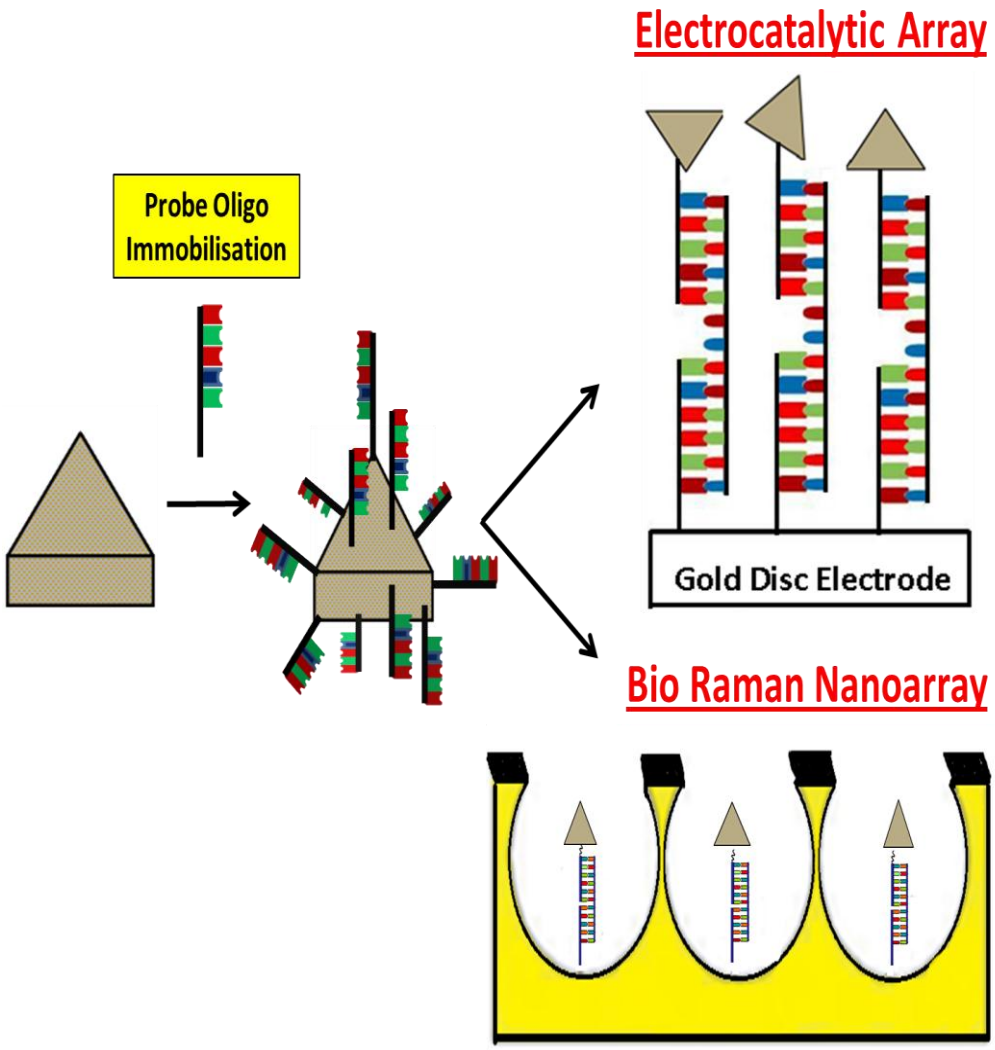

Scheme 6.1: Fabrication of the microcavity array. A closely packed layer of probe strand miRNA is formed on TSNPs. These probe-functionalised TSNPs are then hybridised to the target miRNA strand and then hybridised with a capture miRNA surface. This is performed on both a clean planar 2mm gold disc electrode for the electrochemical array, and inside a 5 µm gold microcavity, for the bio Raman array.

6.2 RESULTS AND DISCUSSION

6.2.1 Characterisation of Triangular Silver Nanoplates

Triangular silver nanoplates were used in two different ways in this study, as shown in Scheme 6.1. The triangular silver nanoplates were initially functionalised with probe strand miRNA that is complementary to part of the target miRNA strand associated with neuroblastoma. The probe miRNA strands were immobilised onto the surface of the silver nanoplates via a thiol terminus on the probe miRNA strand.

The miRNA functionalised triangular silver nanoplates were immobilised on the surface of a gold disc electrode, and also inside gold microcavities. Both of these immobilisation methods involve immobilising a capture miRNA strand onto the gold via a thiol end group. The target miRNA is then hybridised to the complementary capture miRNA strand, followed by hybridising the remaining section of the target miRNA to the probe miRNA strand on the triangular silver nanoplate, bringing it onto the electrode surface for analysis. This is shown in Scheme 6.1, and the method can be found in more detail in Chapter 2, Section 2.3.8 and Section 2.3.9.

The following characterisation methods confirm the probe miRNA immobilisation onto the triangular silver nanoplates, and also the fully hybridised electrode / gold microcavities.

6.2.1.1 UV

Noble metal nanoparticles exhibit a strong ultraviolet (UV) – visible (Vis) absorption band that is not present in the spectrum of the bulk metal. This absorption band results when the incident photon frequency is resonant with

the collective oscillation of the conductions electrodes and is known as the local surface plasmon resonance (LSPR).[29,34-36] As the triangular silver nanoplates can be optically tuned from the visible to NIR wavelengths; by changing the size of the nanoplates, its surface plasmon resonance will change, so it can be tuned for whatever properties are required.[37,38]

Figure 6.1 show an overlay of two absorbance spectra if the triangular silver nanoplates before and after the immobilisation of the probe strand miRNA on the surface of the nanoplate. Previous work by Wu et al[39] has shown that for triangular silver nanoparticles, three bands are present in the absorbance spectrum, relating to the in-plane dipole, the in-plane quadrupole, and the out-of-plane quadrupole; these are observed at approximately 528nm, 428nm and 340 nm respectively, with the in-plane bands being the strongest. These correspond to the spectrum shown in Figure 6.1, as there are peaks at 520nm, 400 nm and 338nm. They have also shown that there is a red shift as the edge length increased, and the wide bands are attributed to a percentage of inhomogeneity of shape and size in the samples, which is to be expected. These peaks have also been observed by Chen et al,[40] and they have determined that the shift in comparison to “perfect” triangular nanoplates is due to the truncated nature of these triangular silver nanoplates. When the probe miRNA strand is immobilised on the surface of the nanoplate, there is a shift in the absorbance band, and a band appears at 260 nm.[41,42]

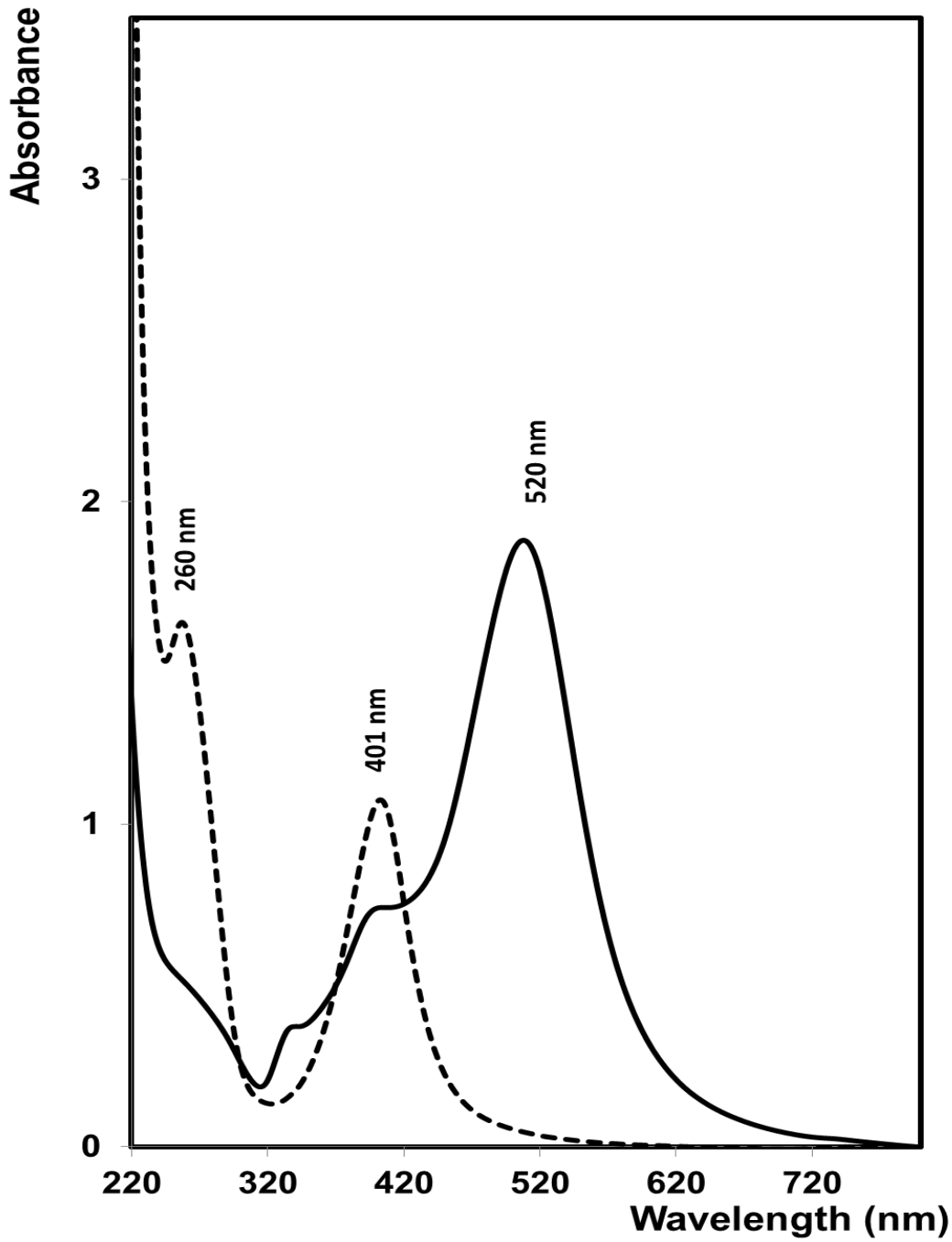

Figure 6.1: Overlaid absorption spectra of pristine triangular silver nanoplates (black line) and triangular silver nanoplates following immobilisation of probe strand miRNA via a thiol head group.

6.2.1.2 FESEM

Field-Emission Scanning Electron Microscopy (FESEM) is a versatile non-destructive technique that can reveal detailed information about the morphology of the material surface.

Figure 6.2 shows FESEM images of the triangular silver nanoplates immobilised inside the gold microcavities via complementary miRNA hybridisation. As these cavities are very large in comparison to the triangular silver nanoplates (approximately 100 nm nanoplates within 5 µm cavities), the image in Figure 6.2A has been zoomed in to show the presence of the triangular silver nanoplates.

This shows that the nanoplates have retained their shape throughout the probe miRNA strand functionalisation and complementary target miRNA hybridisation process, and that they can successfully be immobilised inside the microcavities, using the method outlined. The absolute count of triangular silver nanoplates is 20±3 triangular silver nanoplates per cavity, when using a target miRNA concentration of 1 µM.

6.2.1.3 EDX

Energy dispersive X-ray (EDX) spectroscopy is a characterisation technique used for the elemental analysis or chemical composition of sample.[40] Its characterisation capabilities are largely due to the fundamental principle that each element has a unique atomic structure, allowing a unique set of peaks to appear on its X-ray emission spectrum.

Figure 6.3 shows the EDX spectrum obtained from the triangular silver nanoplates immobilised inside the gold microcavity array. The EDX spectrum indicates the presence of silver with a relatively high purity of 75 at.% weight. The other peaks are gold peaks, which arise from the underlying gold microcavities.

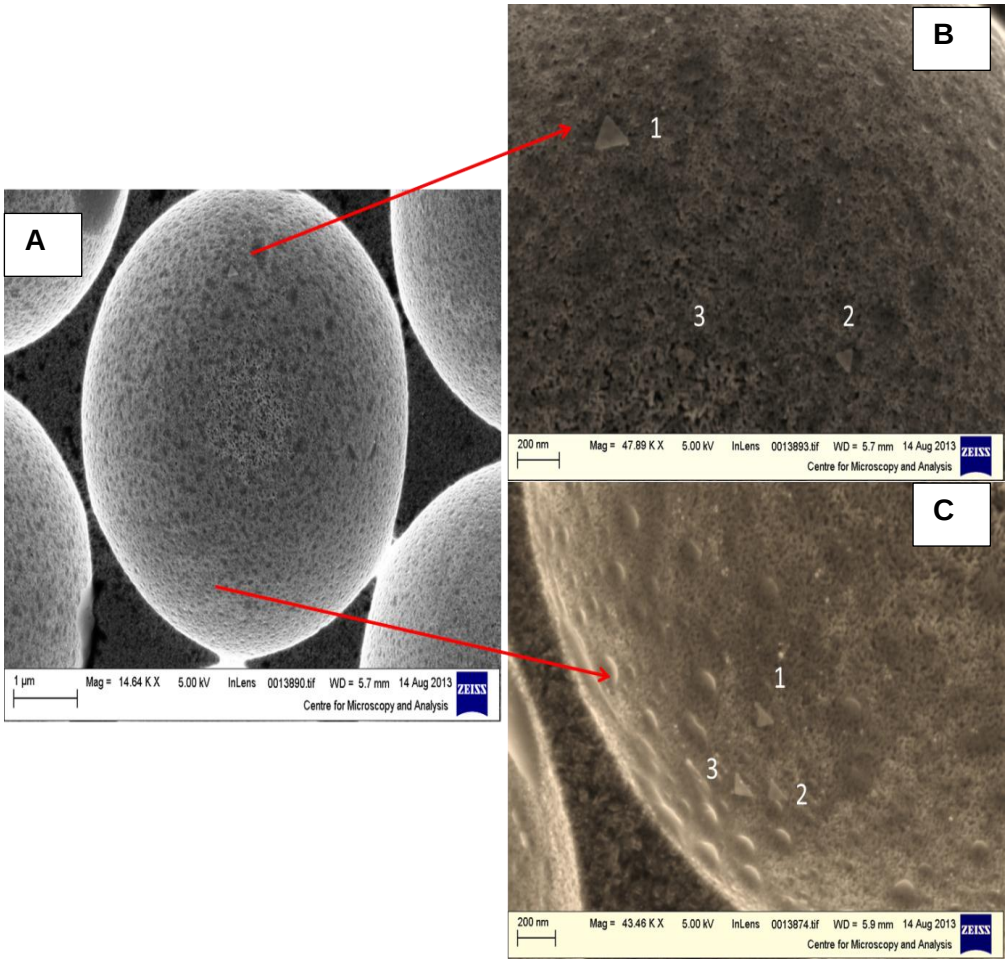

Figure 6.2: Field emission scanning electron micrographs of 5 µM gold cavities, containing TSNPs selectively localised within the cavities via RNA hybridisation. The concentration of the target RNA strand is 1 µM. Image B and C are a magnified portion of image A, to show the TSNPs. Some of the TSNPs have been highlighted and the sizes of them are as follows: B1 – 150 nm, B2 – 100 nm, B3 – 100 nm; C1 – 94 nm, C2 – 103 nm, C3 – 101 nm. The occupancy of each cavity is 20 TSNPs ± 3. (Images obtained by Dr Elaine Spain.)

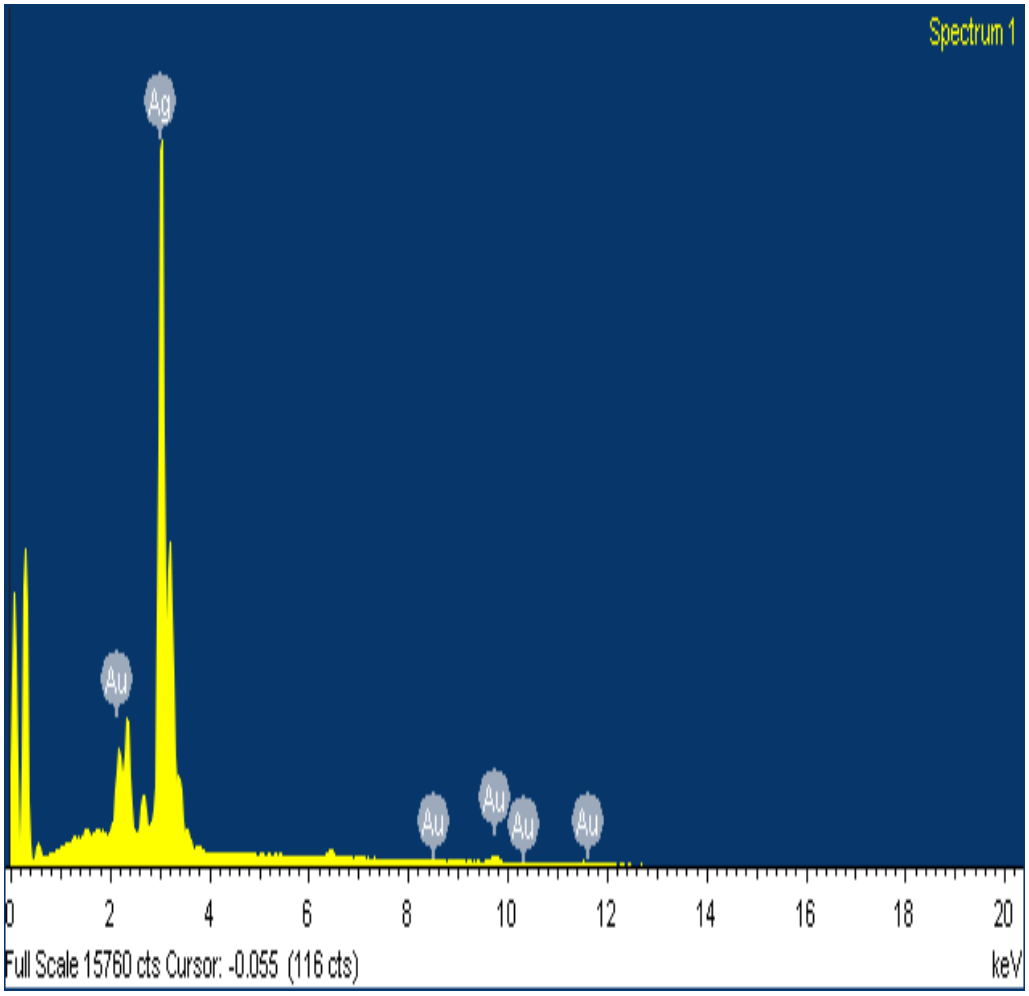

Figure 6.3: EDX spectrum of triangular silver nanoplates immobilised in gold microcavities via miRNA hybridisation. The spot size used was 100 nm. (Spectrum acquired by Dr Elaine Spain.)

6.2.3 Raman Detection of miRNA

Under certain conditions, Surface-Enhanced Raman Scattering (SERS) is a highly sensitive spectroscopic technique that has been used extensively for biochemical detection.[43,44] A potential advantage of the nanoparticle immobilised inside a microcavity is that both the cavity and the particle can provide plasmonic enhancement of Raman, giving rise to SERS and transport to and from the captured particles, e.g., the effect of stirring, can be influenced by the cavities. As mentioned previously, silver is among the most active metal for SERS, with enhancement factors as high as 10^{14} obtained for silver nanoparticles.[24] Factors that can further enhance SERS are the presence of sharp edges, which leads to "hot-spots" localised at the corners and edges.

Here, both triangular silver nanoplates and gold edge-coated triangular silver nanoplates have been functionalised with nucleic acids to enhance the Raman response from the oligonucleotides. To further amplify the Raman response, the nucleic acid sandwich assay is performed within a gold microcavity. The separation can be tuned to promote enhancement by adding more base pairs to, or taking base pairs away from the structure of the target strand, which controls the distance between the nanoparticle and the bottom of the gold microcavity. Two different types of the triangular nanoplates are studied in this case, to try and further optimise the Raman and electrocatalytic responses. The advantages of using both of these types of triangular nanoplates are that they are optically tuneable throughout the visible and near-infrared spectrum. They also can both be surface modified with bioreceptors such as nucleic acids in this case, via thiol head group bonding.

Figure 6.4 shows the SERS spectra of the completed hybridisation steps, using gold edge-coated triangular silver nanoplates (top spectrum) and triangular silver nanoplates (bottom spectrum). Many of the peaks can be credited to varying parts of the miRNA structure on the electrode surface.[45-49]

Some of the peaks can be attributed to the RNA structure like the ribose sugar, such as the peak at 368 cm^{-1} is the phosphate backbone, 867 cm^{-1} is the

ribose base linkage, 984 cm^{-1} is the C-O and C-C stretching, and the strong peaks at 1001 – 1020 cm^{-1} in both spectra are attributed to the C-C and C-O stretching of the ribose backbone.

There are also many miRNA peaks present in the spectra such as; 618 cm^{-1} (A ring deformation), 759 cm^{-1} (C ring), 788 cm^{-1} (C and U ring breathing), 1151 cm^{-1} (A stretching), 1162 cm^{-1} (C ring), 1245 cm^{-1} (U ring mode), 1307 cm^{-1} (C and A ring mode), 1430 cm^{-1} (G ring breathing). Also present are peaks that are attributed to the alkane thiol, such as 440 cm^{-1}, 1600 cm^{-1} (Au-S stretch) and 1160 cm^{-1} (C-C stretch).

These spectra display the feasibility of detecting RNA using this approach. Figure 6.4 shows that the extent of enhancement differs for the two different triangular nanoplates. The enhancement of the gold edge-coated triangular silver nanoplates is 10^4 times greater than that of the triangular silver nanoplates. The best SERS enhancement occurs when the plasmons overlap; therefore there is a greater enhancement where the gold edged nanoplates are used. The plasmonic field of the gold microcavities is from approximately 600 – 900 nm and the plasmon of the gold edge-coated triangular silver nanoplates is 784 nm. These plasmonic fields therefore overlap, along with the excitation wavelength used for the Raman spectroscopy measurements was 633 nm which can excite the cavity modes. The plasmon of the triangular silver nanoplates is 520 nm, which is outside of the plasmonic field of the gold cavities which reduces the magnitude of the enhancement observed. However, there is still a significant spectrum from the triangular silver nanoplates, which could still be used for detection. These results are important as they show that by tuning the plasmons of the cavities with that of the particles, and combining that with an excitation wavelength in the same range, an extremely large SERS enhancement can be achieved.

As the miRNA target separates the surface of the cavity and the nanoplates, different lengths of RNA strands could be explore to maximise the interaction between the nanoplates and the cavity fields. This could be further modified into a multiplexed array, by confining different capture RNA strands into different sections of the microcavity array, and using different metal

nanoparticles for each differing target miRNA for each different disease. This method should give different SERS enhancements, depending on the length of the miRNA in the cavity and on the metal attached to it in the sandwich assay, so different diseases could be detected simultaneously.

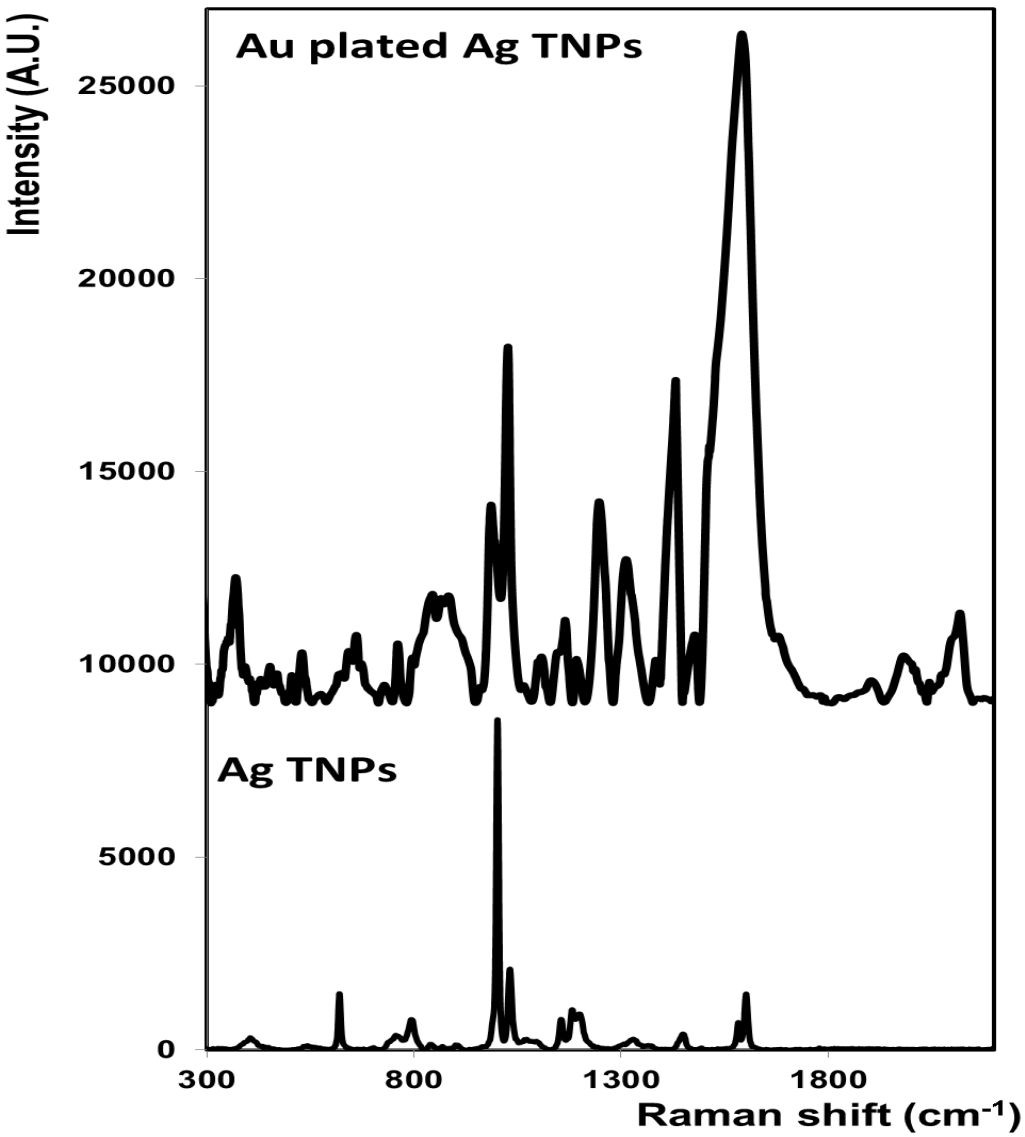

Figure 6.4: Raman spectra of mR-132-3p bound within a gold microcavity array in the presence of TSNPs (bottom) and gold plated TSNPs (top). The excitation wavelength is 633 nm.

6.2.4 Electrochemical miRNA Detection

The analytical performance of the triangular silver nanoplates using the electrocatalytic reduction of peroxide was investigated in sandwich assays. The difference in current before and after addition of hydrogen peroxide, which can be reduced at the nanoplates, was measured. The system was left to equilibrate for ten min prior to the peroxide addition and allowed to stabilise for thirty min after the addition of peroxide. The current generated is due to the number of triangular silver nanoplates on the electrode surface. As the number of triangular silver nanoplates on the surface of the electrode depends on the concentration of target miRNA, as that is the strand that brings the nanoplate to the surface via complementary miRNA binding, the current generated depends on the concentration of the target miRNA.

Figure 6.5 shows the dependence of the change in current on the log of the concentration of miRNA. Concentrations ranging from 1 aM to 1 µM were investigated. The difference in current was measured after the addition of 20 µM hydrogen peroxide. A linear response was obtained for concentrations of miRNA from sequence-specific neuroblastoma from 100 fM to 1 µM of target concentration, with a correlation coefficient of $R^2 = 0.9907$. The calibration plot is highly sensitive, as shown by the large slope and a wide dynamic range. Each concentration is selective and has a significant current change associated with it, arising from the efficient electrocatalysis. A signal is obtained for concentrations as low as 1 aM; however this does not fit into the linear portion of the calibration plot.

For the lower concentrations, from 10 fM to 1 aM, the calibration curve flattens and is no longer linear. This is typical of an S-shaped calibration curve, i.e. it will have an upper and a lower detection limit. The LOD of the system is calculated to be 10 fM, which correlates to the flattening of the calibration plot at this point. This means that concentrations below this point cannot be accurately detected by this method.

Also in Figure 6.5 is a calibration curve of a miRNA functionalised electrode without the triangular silver nanoplate label. Any catalytic current generated in this instance is from the underlying gold electrode. As expected, and as seen previously, when the probe strand is not labelled with an electrocatalytic nanoparticle, the target miRNA strand does not produce a significant current any current that is produced does not depend directly on the target concentration. The current produced here is only the underlying current, and does not vary as there is no label on the probe strand. The sensitivity of the gold electrode, modified with just unlabelled miRNA strands is over 350 times lower than that of the triangular silver nanoplates assay. This reflects the poor electrocatalytic properties of the unlabelled miRNA modified gold disc electrode.

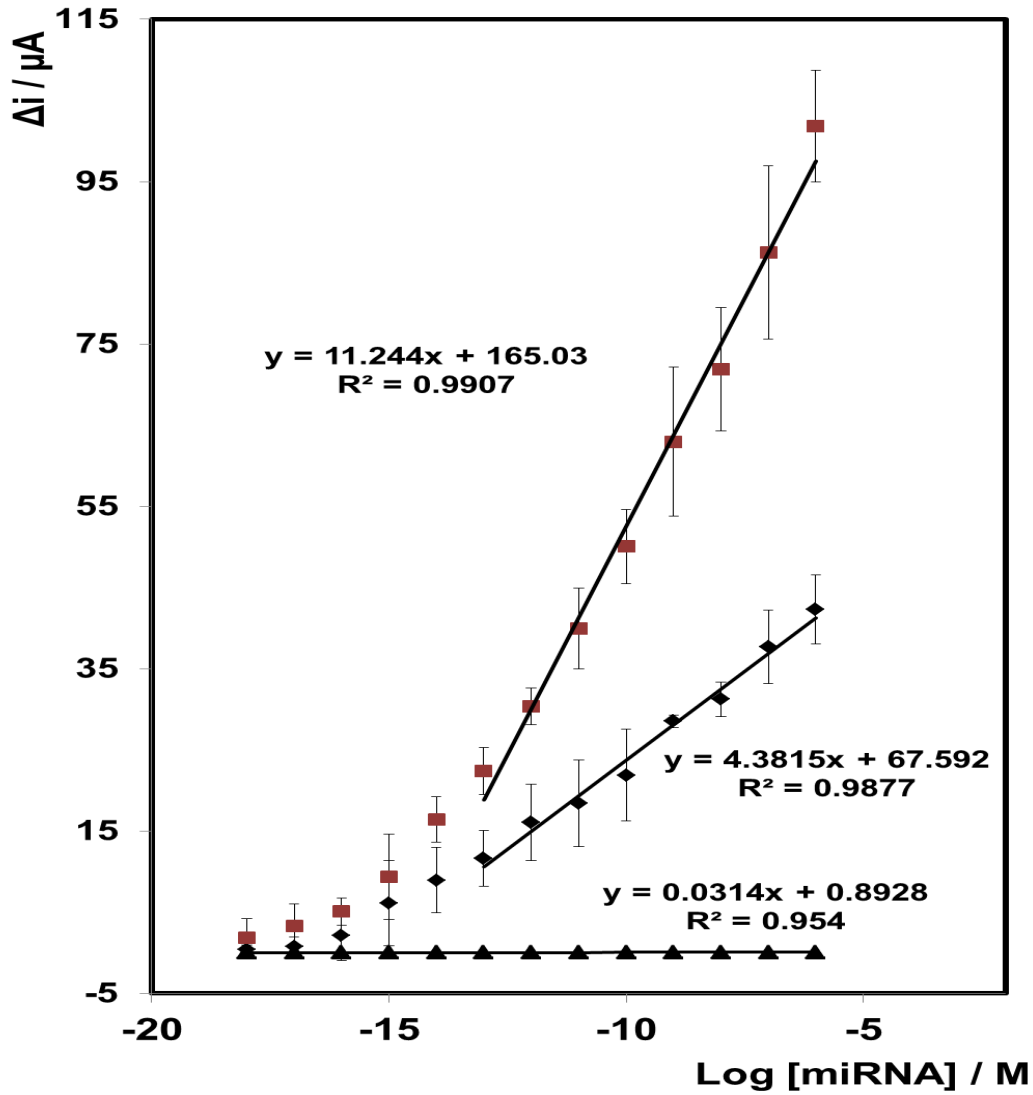

Figure 6.5: Dependence of the change in current before and after the addition of H_2O_2 on log[RNA] for a 2 mm gold disc electrode following hybridisation with TSNPs (■), and without any nanoplates (▲). In all cases, H_2O_2 in aqueous 0.01 M H_2SO_4 gives a concentration of 200 μM. The applied potential is -0.250 V. Where error bars are not visible, they are smaller than, or comparable to, the size of the symbols.

6.3 CONCLUSION

In conclusion, triangular silver nanoplates were used in two ways to directly detect the presence of a target miRNA strand, miR-132-3p, which has been linked to neuroblastoma, a paediatric cancer of the sympathetic nervous system. By immobilising probe strand miRNA, that is complementary to part of the target miRNA strand, on the surface of the triangular silver nanoplates via thiol head group, the target can be detect by electrocatalytic reduction of hydrogen peroxide at the silver nanoplate, and also by surface enhanced Raman spectroscopy, caused by the triangular silver nanoplate. The probe miRNA labelling on the triangular silver nanoplate has been confirmed by UV-Vis spectroscopy, as there is a shift the in silver peak, and the RNA peak appears.

Gold microcavity arrays were made by depositing gold through an array of 5 µm polystyrene spheres. The top, bare part of the gold was blocked using 11-mercaptoundecanoic acid; then the spheres were removed by sonication in THF. Capture miRNA, that is complementary in part to the target strand is immobilised in the microcavity via thiol binding. This is then hybridised with the target miRNA strand, followed by hybridisation with the probe miRNA modified triangular silver nanoplates. Confirmation of the immobilisation of the triangular silver nanoplates is achieved by EDX spectroscopy and FESEM, and the absolute count of triangular silver nanoplates is 20 ± 3 triangular silver nanoplates per cavity, when using a target miRNA concentration of 1 µM.

This sandwich assay was examined under Raman spectroscopy; as silver is highly SERS active. The nanoplates enhance the nucleic acid Raman signature, with gold edge-coated triangular silver nanoplates giving a 10^4 enhancement in comparison to the silver triangular silver nanoplates. This is due to the overlapping plasmonic fields of the gold cavities and the gold coated triangular silver nanoplates, and the excitation wavelength used. This shows that there is a lot of potential using this as a target miRNA detection method,

by tuning the plasmons, nanoparticles and target miRNA length to get a modified architecture for significant SERS enhancement.

The triangular silver nanoplates were also used in an electrocatalytic assay on planar gold disc electrodes by measuring the change in current before and after the injection of hydrogen peroxide. A significant current was achieved with a linear response from 100 fM to 1 µM target miRNA concentration. The limit of detection was determined to be 10 fM. By comparing this assay to an unlabelled assay, it is shown how the triangular silver nanoplates are essential for the electrocatalysis to occur. The sensitivity when there are no nanoparticles is over 300 times lower, with barely any current change after the injection of hydrogen peroxide.

In summary, this study demonstrates the electrochemical detection based on triangular silver nanoplates suitable for the detection of low-abundance molecular biomarkers, miR-132-3p of neuroblastoma. It also demonstrates the potential for SERS detection of biomarkers using triangular silver nanoplates that could be achieved by further slight modification.

6.4 REFERENCES

1. Brodeur, G. Neuroblastoma: Biological insights into a clinical enigma. *Nat. Rev. Cancer* **2003***, 3*, 203-216.

2. Chen, Y.; Stallings, R. L. Differential patterns of microRNA expression in neuroblastoma are correlated with prognosis, differentiation, and apoptosis. *Cancer Res.* **2007***, 67*, 976-983.

3. Cheung, N. V.; Dyer, M. A. Neuroblastoma: developmental biology, cancer genomics and immunotherapy. *Nat. Rev. Cancer* **2013***, 13*, 397-411.

4. Foley, N. H.; Bray, I.; Watters, K. M.; Das, S.; Bryan, K.; Bernas, T.; Prehn, J. H. M.; Stallings, R. L. MicroRNAs 10a and 10b are potent inducers of neuroblastoma cell differentiation through targeting of nuclear receptor corepressor 2. *Cell Death Differ.* **2011***, 18*, 1089-1098.

5. Stallings, R. L.; Foley, N. H.; Bray, I. M.; Das, S.; Buckley, P. G. MicroRNA and DNA methylation alterations mediating retinoic acid induced neuroblastoma cell differentiation. *Semin. Cancer Biol.* **2011***, 21*, 283-290.

6. Zhang, B.; Lu, L.; Zhang, X.; Ye, W.; Wu, J.; Xi, Q.; Zhang, X. Hsa-miR-132 Regulates Apoptosis in Non-Small Cell Lung Cancer Independent of Acetylcholinesterase. *J. Mol. Neurosci.* **2014***, 53*, 335-344.

7. Liu, X.; Yu, H.; Cai, H.; Wang, Y. The expression and clinical significance of miR-132 in gastric cancer patients. *Diagn. Pathol.* **2014***, 9*, 57.

8. Yang, J.; Gao, T.; Tang, J.; Cai, H.; Lin, L.; Fu, S. Loss of microRNA-132 predicts poor prognosis in patients with primary osteosarcoma. *Mol. Cell. Biochem.* **2013***, 381*, 9-15.

9. Chung, Y.; Bae, H.; Song, J.; Lee, J. K.; Lee, N. W.; Kim, T.; Lee, K. Detection of MicroRNA as Novel Biomarkers of Epithelial Ovarian Cancer

From the Serum of Ovarian Cancer Patient. *International Journal of Gynecological Cancer* **2013***, 23*, 673-679.

10. Kunder, R.; Jalali, R.; Sridhar, E.; Moiyadi, A.; Goel, N.; Goel, A.; Gupta, T.; Krishnatry, R.; Kannan, S.; Kurkure, P.; Deopujari, C.; Shetty, P.; Biyani, N.; Korshunov, A.; Pfister, S. M.; Northcott, P. A.; Shirsat, N. V. Real-time PCR assay based on the differential expression of microRNAs and protein-coding genes for molecular classification of formalin-fixed paraffin embedded medulloblastomas. *Neuro-oncology* **2013***, 15*, 1644-1651.

11. Jacobsen, N.; Andreasen, D.; Mouritzen, P. Profiling MicroRNAs by Real-Time PCR. *Methods Mol. Biol.* **2011***, 732*, 39-54.

12. Wu, D.; Hu, Y.; Tong, S.; Williams, B. R. G.; Smyth, G. K.; Gantier, M. P. The use of miRNA microarrays for the analysis of cancer samples with global miRNA decrease. *RNA-Publ. RNA Soc.* **2013***, 19*, 876-888.

13. Kong, W.; Zhao, J.; He, L.; Cheng, J. Q. Strategies for Profiling MicroRNA Expression. *J. Cell. Physiol.* **2009***, 218*, 22-25.

14. Safavi, A.; Maleki, N.; Farjami, E. Electrodeposited Silver Nanoparticles on Carbon Ionic Liquid Electrode for Electrocatalytic Sensing of Hydrogen Peroxide. *Electroanalysis* **2009***, 21*, 1533-1538.

15. Tammeveski, L.; Erikson, H.; Sarapuu, A.; Kozlova, J.; Ritslaid, P.; Sammelselg, V.; Tammeveski, K. Electrocatalytic oxygen reduction on silver nanoparticle/multi-walled carbon nanotube modified glassy carbon electrodes in alkaline solution. *Electrochem. Commun.* **2012***, 20*, 15-18.

16. Chen, S.; Yuan, R.; Chai, Y.; Hu, F. Electrochemical sensing of hydrogen peroxide using metal nanoparticles: a review. *Microchim. Acta* **2013***, 180*, 15-32.

17. Bansal, V.; Li, V.; O'Mullane, A. P.; Bhargava, S. K. Shape dependent electrocatalytic behaviour of silver nanoparticles. *Crystengcomm* **2010***, 12*, 4280-4286.

18. Shi, W.; Ma, Z. Amperometric glucose biosensor based on a triangular silver nanoprisms/chitosan composite film as immobilization matrix. *Biosens. Bioelectron.* **2010***, 26*, 1098-1103.

19. Mallon, C. T.; Jose, B.; Forster, R. J.; Keyes, T. E. Protein nanopatterning and release from gold nano-cavity arrays. *Chem. Commun.* **2010***, 46*, 106-108.

20. Jose, B.; Mallon, C. T.; Forster, R. J.; Keyes, T. E. Regio-selective decoration of nanocavity metal arrays: contributions from localized and delocalized plasmons to surface enhanced Raman spectroscopy. *Phys. Chem. Chem. Phys.* **2011***, 13*, 14705-14714.

21. Huang, F. M.; Wilding, D.; Speed, J. D.; Russell, A. E.; Bartlett, P. N.; Baumberg, J. J. Dressing Plasmons in Particle-in-Cavity Architectures. *Nano Lett.* **2011***, 11*, 1221-1226.

22. Cintra, S.; Abdelsalam, M.; Bartlett, P.; Baumberg, J.; Kelf, T.; Sugawara, Y.; Russell, A. Sculpted substrates for SERS. *Faraday Discuss.* **2006***, 132*, 191-199.

23. Mallon, C. T.; Spain, E.; Keyes, T. E.; Forster, R. J. DNA mediated immobilisation of electrocatalytic platinum nanoparticles in gold nanocavity arrays. *Chem. Commun.* **2013***, 49*, 1380-1382.

24. Kneipp, K.; Wang, Y.; Kneipp, H.; Perelman, L.; Itzkan, I.; Dasari, R.; Feld, M. Single molecule detection using surface-enhanced Raman scattering (SERS). *Phys. Rev. Lett.* **1997***, 78*, 1667-1670.

25. Xu, H.; Bjerneld, E.; Kall, M.; Borjesson, L. Spectroscopy of single hemoglobin molecules by surface enhanced Raman scattering. *Phys. Rev. Lett.* **1999***, 83*, 4357-4360.

26. Futamata, M.; Maruyama, Y.; Ishikawa, M. Microscopic morphology and SERS activity of Ag colloidal particles. *Vib. Spectrosc.* **2002***, 30*, 17-23.

27. Xu, L.; Yan, W.; Ma, W.; Kuang, H.; Wu, X.; Liu, L.; Zhao, Y.; Wang, L.; Xu, C. SERS Encoded Silver Pyramids for Attomolar Detection of Multiplexed Disease Biomarkers. *Adv Mater* **2015***, 27*, 1706-+.

28. Wu, X.; Fu, P.; Ma, W.; Xu, L.; Kuang, H.; Xu, C. SERS-active silver nanoparticle trimers for sub-attomolar detection of alpha fetoprotein. *Rsc Advances* **2015***, 5*, 73395-73398.

29. Haes, A. J.; Van Duyne, R. P. Preliminary studies and potential applications of localized surface plasmon resonance spectroscopy in medical diagnostics. *Expert Review of Molecular Diagnostics* **2004***, 4*, 527-537.

30. Haes, A. J.; Van Duyne, R. P. A nanoscale optical blosensor: Sensitivity and selectivity of an approach based on the localized surface plasmon resonance spectroscopy of triangular silver nanoparticles. *J. Am. Chem. Soc.* **2002***, 124*, 10596-10604.

31. Malinsky, M. D.; Kelly, K. L.; Schatz, G. C.; Van Duyne, R. P. Chain length dependence and sensing capabilities of the localized surface plasmon resonance of silver nanoparticles chemically modified with alkanethiol self-assembled monolayers. *J. Am. Chem. Soc.* **2001***, 123*, 1471-1482.

32. Zhang, J.; Sun, Y.; Zhang, H.; Xu, B.; Zhang, H.; Song, D. Preparation and application of triangular silver nanoplates/chitosan composite in surface plasmon resonance biosensing. *Anal. Chim. Acta* **2013***, 769*, 114-120.

33. Potara, M.; Boca, S.; Licarete, E.; Damert, A.; Alupei, M.; Chiriac, M. T.; Popescu, O.; Schmidt, U.; Astilean, S. Chitosan-coated triangular silver nanoparticles as a novel class of biocompatible, highly sensitive plasmonic platforms for intracellular SERS sensing and imaging. *Nanoscale* **2013***, 5*, 6013-6022.

34. Haynes, C.; Van Duyne, R. Nanosphere lithography: A versatile nanofabrication tool for studies of size-dependent nanoparticle optics. *J Phys Chem B* **2001***, 105*, 5599-5611.

35. Link, S.; El-Sayed, M. Spectral properties and relaxation dynamics of surface plasmon electronic oscillations in gold and silver nanodots and nanorods. *J Phys Chem B* **1999***, 103*, 8410-8426.

36. Mulvaney, P. Surface plasmon spectroscopy of nanosized metal particles. *Langmuir* **1996***, 12*, 788-800.

37. Charles, D. E.; Aherne, D.; Gara, M.; Ledwith, D. M.; Gun'ko, Y. K.; Kelly, J. M.; Blau, W. J.; Brennan-Fournet, M. E. Versatile Solution Phase Triangular Silver Nanoplates for Highly Sensitive Plasmon Resonance Sensing. *ACS Nano* **2010***, 4*, 55-64.

38. Si, G.; Shi, W.; Li, K.; Ma, Z. Synthesis of PSS-capped triangular silver nanoplates with tunable SPR. *Colloid Surf. A-Physicochem. Eng. Asp.* **2011***, 380*, 257-260.

39. Wu, C.; Zhou, X.; Wei, J. Localized Surface Plasmon Resonance of Silver Nanotriangles Synthesized by a Versatile Solution Reaction. *Nanoscale Res. Lett.* **2015***, 10*, 354.

40. Chen, S.; Carroll, D. Synthesis and characterization of truncated triangular silver nanoplates. *Nano Lett.* **2002***, 2*, 1003-1007.

41. Cavaluzzi, M.; Borer, P. Revised UV extinction coefficients for nucleoside-5'-monophosphates and unpaired DNA and RNA. *Nucleic Acids Res.* **2004***, 32*, e13.

42. Kanakis, C. D.; Tarantilis, P. A.; Polissiou, M. G.; Diamantoglou, S.; Tajmir-Riahi, H. A. An overview of DNA and RNA bindings to antioxidant flavonoids. *Cell Biochem. Biophys.* **2007***, 49*, 29-36.

43. David, C.; Guillot, N.; Shen, H.; Toury, T.; de la Chapelle, M. L. SERS detection of biomolecules using lithographed nanoparticles towards a reproducible SERS biosensor. *Nanotechnology* **2010***, 21*, 475501.

44. Tripp, R. A.; Dluhy, R. A.; Zhao, Y. Novel nanostructures for SERS biosensing. *Nano Today* **2008***, 3*, 31-37.

45. Cao, Y. W. C.; Jin, R. C.; Mirkin, C. A. Nanoparticles with Raman spectroscopic fingerprints for DNA and RNA detection. *Science* **2002***, 297*, 1536-1540.

46. Bell, S. E. J.; Sirimuthu, N. M. S. Surface-enhanced Raman spectroscopy (SERS) for sub-micromolar detection of DNA/RNA mononucleotides. *J. Am. Chem. Soc.* **2006***, 128*, 15580-15581.

47. Benevides, J. M.; Tsuboi, M.; Bamford, J. K. H.; Thomas, G. J. Polarized Raman spectroscopy of double-stranded RNA from bacteriophage phi 6: Local Raman tensors of base and backbone vibrations. *Biophys. J.* **1997***, 72*, 2748-2762.

48. Hobro, A. J.; Rouhi, M.; Blanch, E. W.; Conn, G. L. Raman and Raman optical activity (ROA) analysis of RNA structural motifs in Domain I of the EMCV IRES. *Nucleic Acids Res.* **2007***, 35*, 1169-1177.

49. Hobro, A. J.; Standley, D. M.; Ahmad, S.; Smith, N. I. Deconstructing RNA: optical measurement of composition and structure. *Physical Chemistry Chemical Physics* **2013***, 15*, 13199-13208.

CHAPTER 7

CONCLUSION AND FUTURE WORK

7.1 SUMMARY

This thesis reported on the synthesis and optimization of electrocatalytic platinum nanoparticles using the double potential step electrodeposition method, and application of these, and other electrocatalytic nanocomposites for the detection of nucleic acid strands that are associated with different diseases.

As the concentrations of biomarkers such as nucleic acids, can be extremely low at the early stages of diseases, an increased sensitivity and lower limits of detection are essential for successful detection. Biosensors are promising devices with are superior to traditional analytical methods due to their specificity, rapid response time, portability and ease of use. Due to the major advantages, it is clear that these devices are coming to the forefront in the field of point-of-care diagnostics. Therefore, this work focused on improving the sensitivity of nucleic acid biosensors through metal nanomaterials, and also the incorporation of this detection method into a fully integrated microfluidic device for point-of-care testing.

Following Chapters 1 and 2, which review the current state-of-the-art methods for nucleic acid detection using metal nanoparticles and the experimental strategies employed respectively, Chapter 3 reported on the synthesis and characterisation of platinum nanoparticles. A double potential step electrodeposition method was used to deposit platinum nanoparticles onto self-assembled monolayer templated and template-free gold electrodes in order to control the size and density of the platinum nanoparticles. By varying the nucleation and growth potentials, the size and density of the nanoparticles could be controlled. The self-assembled monolayer template allowed the nanoparticles to be regioselectively functionalised with a probe nucleic acid strand, before desorption into suspension and the particles retained their functionality after desorption.

These regioselectively functionalised nanoparticles can be multifunctional. By functionalising the nanoparticle in different areas, the nanoparticles can

selectively bind to each other in a way that is analogous to atoms. The length of these bonds and the angles at which they bind can be controlled also, by varying the surface functionalisation. These can then be further built on, to form ordered structures.

In Chapter 4, the detection of nucleic acids using the optimal platinum nanoparticles and electrocatalytic detection was reported. The current generated for the reduction of hydrogen peroxide varied linearly with target DNA concentration between 1 aM and 1 µM, with excellent reproducibility of between 2 – 15 %, even at the lowest concentrations. When compared to the nanoparticles formed without the monolayer template, the sensitivity (slope of the calibration curve) of the templated nanoparticles was over an order of magnitude larger, due to the templated particles being more size monodisperse. For uniformly functionalised platinum nanoparticles, the sensitivity was again over an order of magnitude lower demonstrating that separating the two functions of the nanoparticle, i.e. the molecular recognition side and the electrocatalytic side, greatly enhances the analytical performance.

In order to improve the sensitivity even further, ideally to be able to detect one binding event, the current associated with the arrival of a single nanoparticle would need to be large enough to measure. The lowest concentration on the calibration curve is equivalent to the binding of approximately 10,000 nanoparticles. So to detect just one binding event, this is the gap that needs to be overcome.

Chapter 5 reports on integrating the nucleic acid sandwich assay into a microfluidic device. The microfluidic disc was pre-loaded and used an event triggered system to carry out the hybridisation process fully inside the microfluidic device.

Electrochemical Impedance Spectroscopy was performed on the sandwich assay, with different concentrations of the target miRNA. The R_{ct} values increased linearly with increasing concentration, with a standard deviation of between just 2 – 9 %. These results were also fit to an equivalent circuit model and the measured data is in very good agreement to the fitted data. While the standard deviation is low, the range of response is also quite narrow over 12

orders of magnitude; this would be affected by the reproducibility factors of the system, such as the density of miRNA on the electrode surface, the density of the miRNA on the nanoparticle, defects on the electrode surface, plus all of the steps involved in the assembly of the device. However the results are encouraging, as there is a clear dependence of the interfacial resistance on concentration, and the precision of the reproducibility factors can all be solvable.

The electrocatalytic activity of the sandwich assay incorporated into the microfluidic disc and performance of the device was impressive with the hydrogen peroxide reduction current increasing linearly with increasing target mRNA concentrations from 1 pM to 1 µM, with a limit of detection of 1 pM. These results are extremely promising, due to the wide dynamic range, low limit of detection and rapid response time, along with the advantage of the full system contained inside an integrated microfluidic device.

In Chapter 6, triangular silver nanoplates were used in the sandwich assay to detect the target miRNA which in this case is a biomarker for Neuroblastoma. A linear response was achieved for the change in current before and after the addition of hydrogen peroxide from 100 fM to 1 µM target miRNA concentration, with a limit of detection of 10 fM. By comparing these results to that of an unlabeled assay, without any nanoplates present, the sensitivity is over 300 times larger when the triangular silver nanoplates are incorporated into the assay.

The triangular silver nanoplates were also immobilised in gold microcavity arrays via complementary miRNA hybridisation. As silver is SERS active, the nanoplates should enhance the nucleic acid Raman signature. Gold-edged triangular silver nanoplates were used as a comparison, and these nanoplates gave a 10^4 enhancement in comparison to the silver nanoplates. This is due to the overlapping plasmonic fields between the gold nanocavities, the gold-edged nanoplates and the excitation wavelength used. Even though in this instance a systematic dependence of the Raman signal on the target concentration wasn't achieved, the results show that there is a huge potential for this detection method to be successful, by tuning the plasmons,

nanoparticles and target miRNA length to get a modified architecture for significant SERS enhancement.

Overall, this thesis shows that electrocatalytic nanoparticles are excellent for nucleic acid detection and are highly sensitive over a wide range of target nucleic acid concentrations, and offer a large signal enhancement over planar gold electrodes. The sandwich assay used here can also be used for a wide variety of target nucleic acids, simply by changing the capture and probe nucleic acid sequences for complementary hybridisation to the target. It can also be tailored by changing the nanoparticle to different shapes, sizes or metals, in order to achieve the greatest signal required for the detection needed. The integrated microfluidic device is a major step forward for point-of-care diagnostics, and can also be used for a wide variety of nucleic acid targets.

Another application for this system and the high sensitivity and wide dynamic ranges achieved here, would be for the detection of environmental pollutants. While they would decay over time, it would get more difficult to detect as time went on, and the concentration got lower. By implementing the system described here, ultralow concentrations could be detected, so the decay could be monitored over time.

APPENDIX A

Comparison of the electrochemical area (E.A.) and surface roughness factor (S.R.). values of the gold oxide reduction and platinum oxide reduction peaks of a bare gold disc electrode, before and after platinum deposition from a 1mM chloroplatinic acid hydrate solution in 0.5 M H_2SO_4 and after desorption of the platinum nanoparticles, using a current jump.

*A nucleation potential of **-1000 mV** is applied for **20 ms** and **0 to -600 mV** growth pulses applied for **30 s** and **60 s**.*

E_{growth}		30 s $E.A._{Au}$	30 s $S.R._{Au}$	30 s $E.A._{Pt}$	30 s $S.R._{Pt}$	60 s $E.A._{Au}$	60 s $S.R._{Au}$	60 s $E.A._{Pt}$	60 s $S.R._{Pt}$
0mV	Unmodified	0.039	1.23	0.000	0.00	0.049	1.55	0.000	0.00
	PtNPs	0.034	1.09	0.002	0.07	0.047	1.50	0.004	0.12
	Stripped	0.075	2.39	0.000	0.00	0.066	2.10	0.000	0.00
-100mV	Unmodified	0.042	1.34	0.000	0.00	0.050	1.59	0.000	0.00
	PtNPs	0.041	1.30	0.006	0.18	0.048	1.52	0.007	0.23
	Stripped	0.095	3.03	0.000	0.00	0.094	2.99	0.000	0.00
-200mV	Unmodified	0.046	1.45	0.000	0.00	0.051	1.61	0.000	0.00
	PtNPs	0.041	1.30	0.009	0.30	0.049	1.55	0.014	0.45
	Stripped	0.088	2.80	0.000	0.00	0.098	3.12	0.000	0.00
-300mV	Unmodified	0.049	1.56	0.000	0.00	0.046	1.47	0.000	0.00
	PtNPs	0.046	1.48	0.010	0.31	0.042	1.33	0.016	0.51
	Stripped	0.063	2.02	0.000	0.00	0.115	3.67	0.000	0.00
-400mV	Unmodified	0.047	1.50	0.000	0.00	0.049	1.55	0.000	0.00
	PtNPs	0.045	1.42	0.009	0.28	0.044	1.40	0.010	0.31
	Stripped	0.079	2.51	0.000	0.00	0.108	3.44	0.000	0.00
-500mV	Unmodified	0.046	1.48	0.000	0.00	0.047	1.49	0.000	0.00
	PtNPs	0.045	1.42	0.006	0.20	0.044	1.40	0.008	0.25
	Stripped	0.075	2.39	0.000	0.00	0.101	3.23	0.000	0.00
-600mV	Unmodified	0.050	1.58	0.000	0.00	0.050	1.60	0.000	0.00
	PtNPs	0.048	1.53	0.004	0.12	0.049	1.57	0.006	0.19
	Stripped	0.067	2.12	0.000	0.00	0.097	3.10	0.000	0.00

*A nucleation potential of **-1200 mV** is applied for **20 ms** and **0 to -600 mV** growth pulses applied for **30 s** and **60 s**.*

E_{growth}		30 s $E.A._{Au}$	30 s $S.R._{Au}$	30 s $E.A._{Pt}$	30 s $S.R._{Pt}$	60 s $E.A._{Au}$	60 s $S.R._{Au}$	60 s $E.A._{Pt}$	60 s $S.R._{Pt}$
0mV	Unmodified	0.049	1.56	0.000	0.00	0.051	1.62	0.000	0.00
	PtNPs	0.033	1.04	0.009	0.28	0.039	1.23	0.011	0.34
	Stripped	0.052	1.65	0.000	0.00	0.053	1.70	0.000	0.00
-100mV	Unmodified	0.047	1.49	0.000	0.00	0.048	1.54	0.000	0.00
	PtNPs	0.030	0.96	0.011	0.34	0.024	0.78	0.019	0.61
	Stripped	0.049	1.55	0.000	0.00	0.050	1.60	0.000	0.00
-200mV	Unmodified	0.050	1.60	0.000	0.00	0.048	1.54	0.000	0.00
	PtNPs	0.027	0.87	0.038	1.21	0.018	0.56	0.056	1.78
	Stripped	0.052	1.65	0.000	0.00	0.052	1.65	0.000	0.00
-300mV	Unmodified	0.047	1.49	0.000	0.00	0.047	1.49	0.000	0.00
	PtNPs	0.021	0.67	0.040	1.26	0.021	0.67	0.046	1.45
	Stripped	0.051	1.61	0.000	0.00	0.050	1.60	0.000	0.00
-400mV	Unmodified	0.049	1.57	0.000	0.00	0.049	1.57	0.000	0.00
	PtNPs	0.034	1.09	0.023	0.72	0.030	0.97	0.032	1.02
	Stripped	0.053	1.70	0.000	0.00	0.050	1.60	0.000	0.00
-500mV	Unmodified	0.047	1.49	0.000	0.00	0.046	1.45	0.000	0.00
	PtNPs	0.027	0.87	0.011	0.35	0.028	0.90	0.016	0.51
	Stripped	0.050	1.60	0.000	0.00	0.047	1.50	0.000	0.00
-600mV	Unmodified	0.042	1.35	0.000	0.00	0.049	1.57	0.000	0.00
	PtNPs	0.025	0.80	0.006	0.20	0.028	0.90	0.015	0.48
	Stripped	0.047	1.50	0.000	0.00	0.052	1.65	0.040	0.00

*A nucleation potential of **-1400 mV** is applied for **20 ms** and **0 to -600 mV** growth pulses applied for **30 s** and **60 s**.*

E_{growth}		30 s $E.A._{Au}$	30 s $S.R._{Au}$	30 s $E.A._{Pt}$	30 s $S.R._{Pt}$	60 s $E.A._{Au}$	60 s $S.R._{Au}$	60 s $E.A._{Pt}$	60 s $S.R._{Pt}$
0mV	Unmodified	0.044	1.41	0.000	0.00	0.047	1.51	0.000	0.00
	PtNPs	0.035	1.12	0.017	0.54	0.034	1.09	0.021	0.68
	Stripped	0.059	1.89	0.000	0.00	0.058	1.84	0.000	0.00
-100mV	Unmodified	0.051	1.61	0.000	0.00	0.047	1.50	0.000	0.00
	PtNPs	0.047	1.51	0.038	1.20	0.032	1.01	0.044	1.39
	Stripped	0.060	1.90	0.000	0.00	0.056	1.78	0.000	0.00
-200mV	Unmodified	0.049	1.56	0.000	0.00	0.050	1.60	0.000	0.00
	PtNPs	0.015	0.48	0.095	3.01	0.018	0.56	0.111	3.54
	Stripped	0.053	1.70	0.000	0.00	0.052	1.65	0.000	0.00
-300mV	Unmodified	0.043	1.37	0.000	0.00	0.047	1.50	0.000	0.00
	PtNPs	0.031	0.98	0.084	2.67	0.006	0.20	0.061	1.93
	Stripped	0.055	1.76	0.000	0.00	0.052	1.67	0.000	0.00
-400mV	Unmodified	0.047	1.49	0.000	0.00	0.046	1.47	0.000	0.00
	PtNPs	0.029	0.93	0.032	1.01	0.029	0.92	0.187	5.96
	Stripped	0.053	1.68	0.000	0.00	0.053	1.70	0.000	0.00
-500mV	Unmodified	0.050	1.58	0.000	0.00	0.050	1.59	0.000	0.00
	PtNPs	0.034	1.08	0.031	0.98	0.033	1.04	0.032	1.01
	Stripped	0.053	1.70	0.000	0.00	0.059	1.89	0.000	0.00
-600mV	Unmodified	0.046	1.48	0.000	0.00	0.040	1.26	0.000	0.00
	PtNPs	0.035	1.12	0.013	0.40	0.030	0.96	0.019	0.59
	Stripped	0.053	1.68	0.000	0.00	0.050	1.60	0.000	0.00

*A nucleation potential of **-1600 mV** is applied for **20 ms** and **0 to -600 mV** growth pulses applied for **30 s** and **60 s**.*

E_{growth}		30 s $E.A._{Au}$	30 s $S.R._{Au}$	30 s $E.A._{Pt}$	30 s $S.R._{Pt}$	60 s $E.A._{Au}$	60 s $S.R._{Au}$	60 s $E.A._{Pt}$	60 s $S.R._{Pt}$
0mV	Unmodified	0.046	1.46	0.000	0.00	0.051	1.62	0.000	0.00
	PtNPs	0.035	1.12	0.028	0.90	0.037	1.19	0.047	1.51
	Stripped	0.063	2.01	0.000	0.00	0.056	1.79	0.000	0.00
-100mV	Unmodified	0.050	1.59	0.000	0.00	0.045	1.42	0.000	0.00
	PtNPs	0.043	1.38	0.042	1.34	0.032	1.01	0.062	1.98
	Stripped	0.062	1.97	0.216	6.88	0.053	1.68	0.000	0.00
-200mV	Unmodified	0.051	1.62	0.000	0.00	0.049	1.57	0.000	0.00
	PtNPs	0.043	1.38	0.119	3.79	0.038	1.21	0.238	7.59
	Stripped	0.037	1.18	0.052	1.67	0.062	1.98	0.004	0.12
-300mV	Unmodified	0.050	1.59	0.000	0.00	0.048	1.54	0.000	0.00
	PtNPs	0.041	1.32	0.100	3.19	0.030	0.96	0.143	4.56
	Stripped	0.067	2.12	0.000	0.00	0.057	1.80	0.000	0.00
-400mV	Unmodified	0.051	1.61	0.000	0.00	0.050	1.59	0.000	0.00
	PtNPs	0.041	1.30	0.046	1.46	0.027	0.87	0.117	3.74
	Stripped	0.062	1.99	0.000	0.00	0.058	1.84	0.000	0.00
-500mV	Unmodified	0.046	1.47	0.000	0.00	0.044	1.40	0.000	0.00
	PtNPs	0.037	1.17	0.038	1.21	0.039	1.23	0.061	1.93
	Stripped	0.054	1.71	0.000	0.00	0.053	1.70	0.000	0.00
-600mV	Unmodified	0.043	1.38	0.000	0.00	0.049	1.56	0.000	0.00
	PtNPs	0.037	1.18	0.021	0.67	0.041	1.31	0.031	0.98
	Stripped	0.056	1.79	0.000	0.00	0.062	1.98	0.000	0.00

*A nucleation potential of -**1800 mV** is applied for **20 ms** and **0 to -600 mV** growth pulses applied for **30s** and **60 s**.*

E_{growth}		30 s $E.A._{Au}$	30 s $S.R._{Au}$	30 s $E.A._{Pt}$	30 s $S.R._{Pt}$	60 s $E.A._{Au}$	60 s $S.R._{Au}$	60 s $E.A._{Pt}$	60 s $S.R._{Pt}$
0mV	Unmodified	0.041	1.32	0.000	0.00	0.038	1.20	0.000	0.00
	PtNPs	0.040	1.28	0.012	0.39	0.037	1.17	0.024	0.75
	Stripped	0.140	4.45	0.000	0.00	0.108	3.45	0.000	0.00
-100mV	Unmodified	0.039	1.23	0.000	0.00	0.046	1.45	0.000	0.00
	PtNPs	0.038	1.20	0.014	0.45	0.044	1.40	0.031	0.99
	Stripped	0.115	3.65	0.000	0.00	0.088	2.79	0.000	0.00
-200mV	Unmodified	0.046	1.46	0.000	0.00	0.041	1.30	0.000	0.00
	PtNPs	0.046	1.45	0.037	1.19	0.037	1.19	0.046	1.45
	Stripped	0.060	1.90	0.000	0.00	0.074	2.36	0.000	0.00
-300mV	Unmodified	0.049	1.56	0.000	0.00	0.051	1.61	0.000	0.00
	PtNPs	0.041	1.32	0.038	1.20	0.047	1.50	0.044	1.39
	Stripped	0.063	2.01	0.000	0.00	0.060	1.90	0.000	0.00
-400mV	Unmodified	0.041	1.30	0.000	0.00	0.041	1.32	0.000	0.00
	PtNPs	0.039	1.25	0.033	1.05	0.040	1.27	0.035	1.10
	Stripped	0.042	1.35	0.000	0.00	0.083	2.65	0.000	0.00
-500mV	Unmodified	0.046	1.48	0.000	0.00	0.037	1.19	0.000	0.00
	PtNPs	0.046	1.48	0.041	1.30	0.035	1.13	0.019	0.61
	Stripped	0.044	1.40	0.000	0.00	0.088	2.81	0.000	0.00
-600mV	Unmodified	0.041	1.29	0.000	0.00	0.048	1.53	0.000	0.00
	PtNPs	0.038	1.20	0.019	0.59	0.045	1.42	0.024	0.75
	Stripped	0.052	1.67	0.000	0.00	0.091	2.91	0.000	0.00

Scanning electron microscopy (SEM) images of a gold electrode after electrochemical deposition of platinum using the double pulse potential method.

*Platinum had been deposited onto **unmodified** gold electrode with a nucleation potential of -**1000 mV** for **20 ms** and a growth potential of **0 mV to -600 mV** for **30s**.*

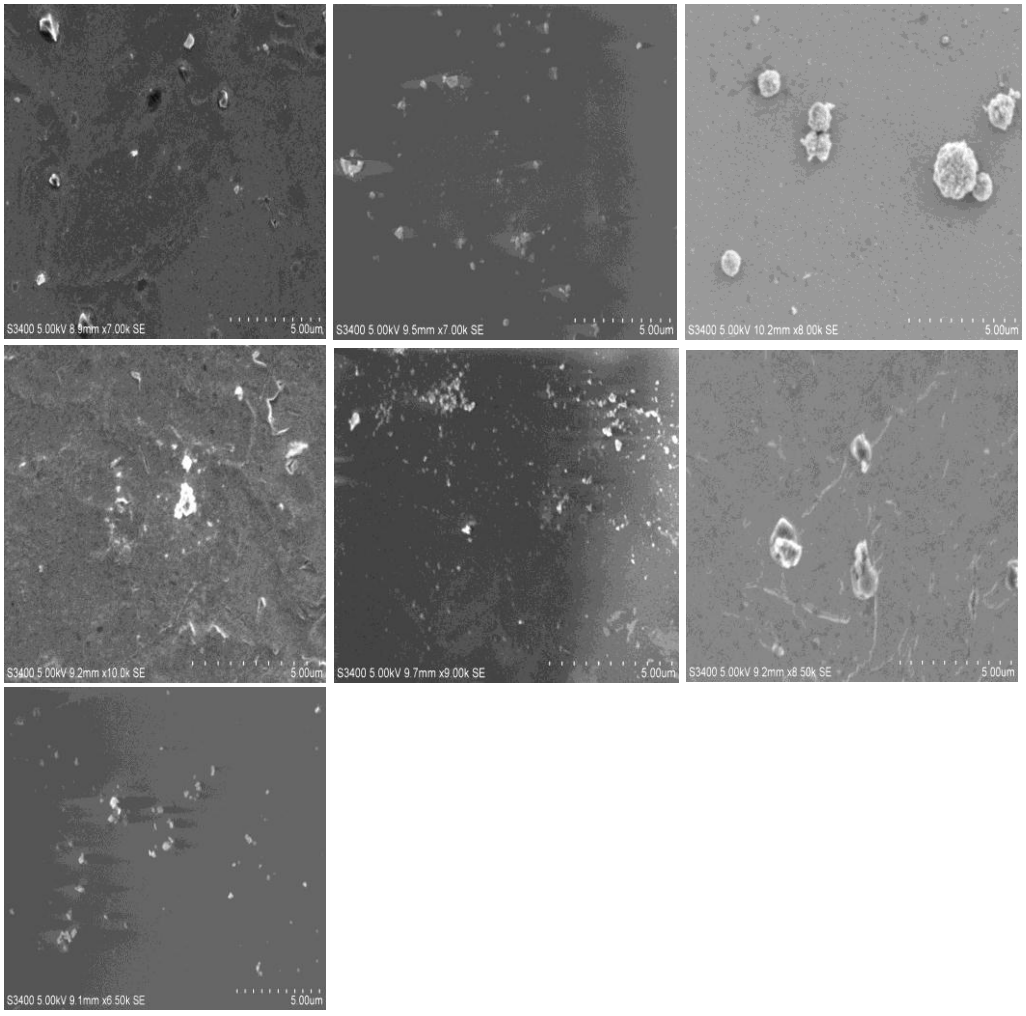

*Platinum had been deposited onto **unmodified** gold electrode with a nucleation potential of -**1200 mV** for **20 ms** and a growth potential of **0 mV to -600 mV** for **30s**.*

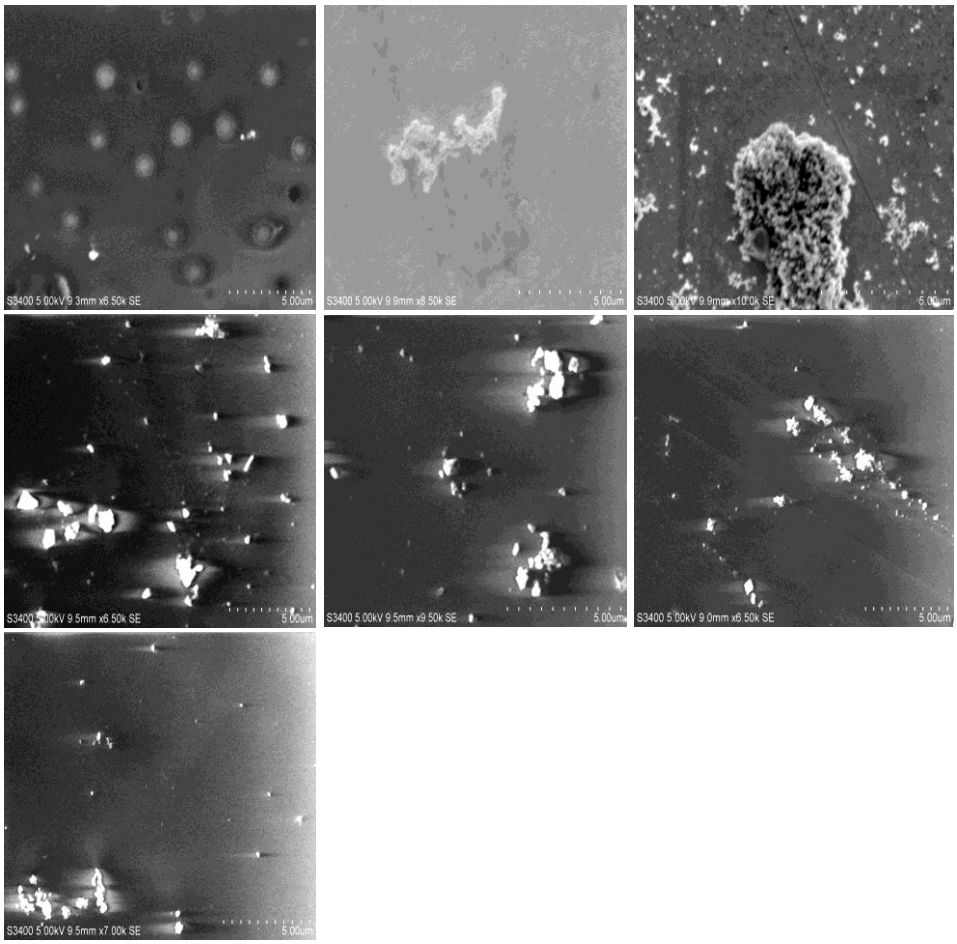

*Platinum had been deposited onto **unmodified** gold electrode with a nucleation potential of -**1400 mV** for **20 ms** and a growth potential of **0 mV to -600 mV** for **30s**.*

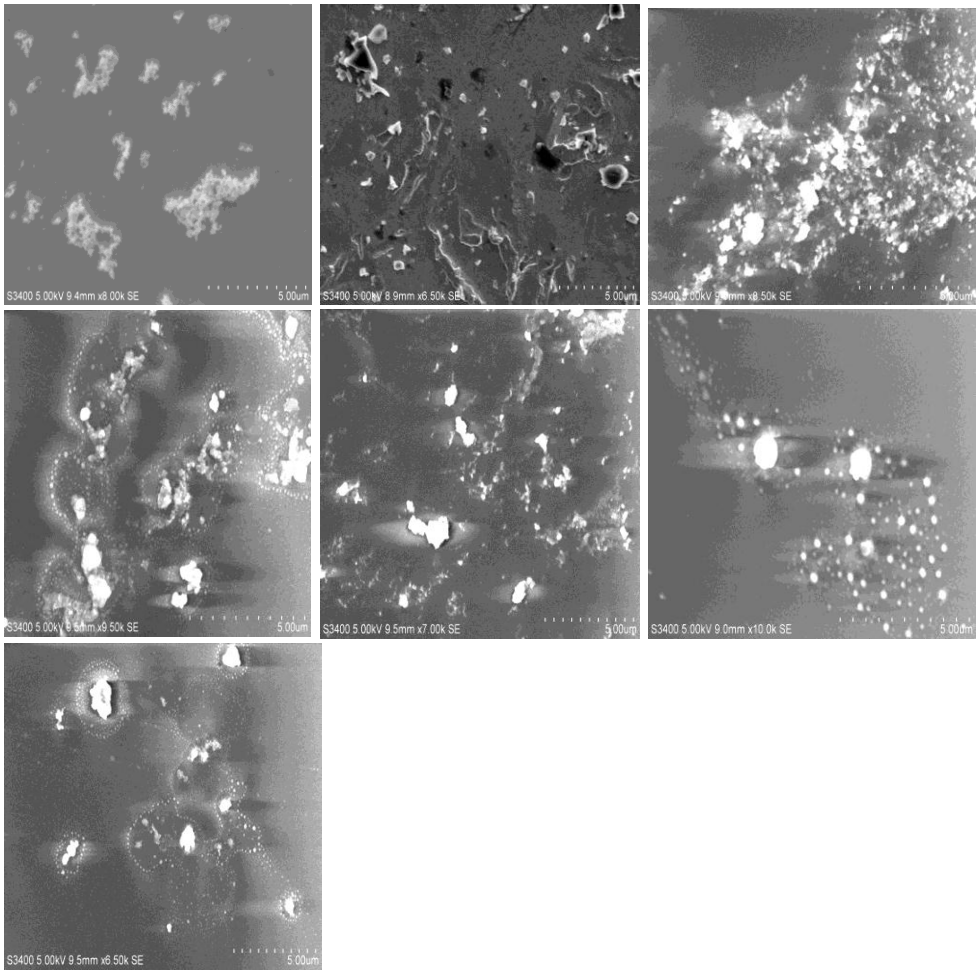

Platinum had been deposited onto ***unmodified*** *gold electrode with a nucleation potential of -****1600 mV*** *for* ***20 ms*** *and a growth potential of* ***0 mV to -600 mV*** *for* ***30s****.*

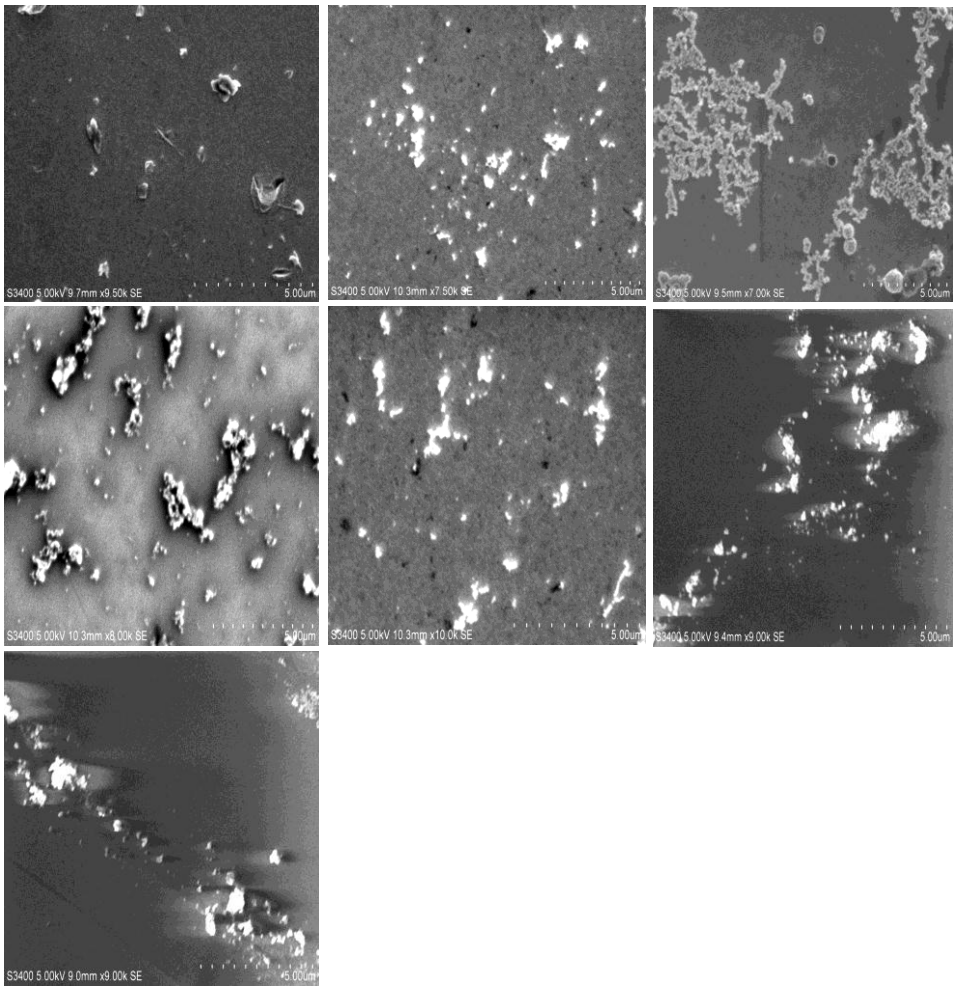

*Platinum had been deposited onto **unmodified** gold electrode with a nucleation potential of -**1800 mV** for **20 ms** and a growth potential of **0 mV to -600 mV** for **30s**.*

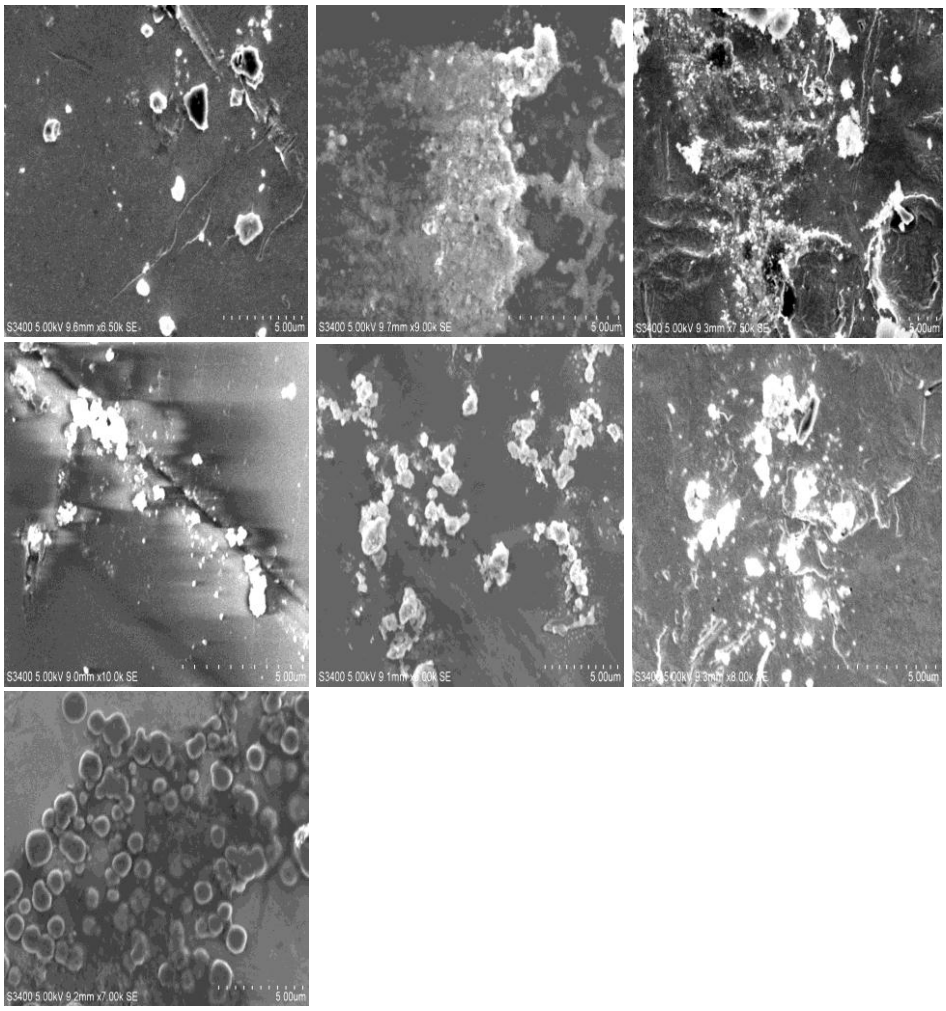

Scanning electron microscopy (SEM) images of a gold electrode after electrochemical deposition of platinum using the double pulse potential method.

*Platinum had been deposited onto **unmodified** gold electrode with a nucleation potential of -**1000 mV** for **20 ms** and a growth potential of **0 mV to -600 mV** for **60s**.*

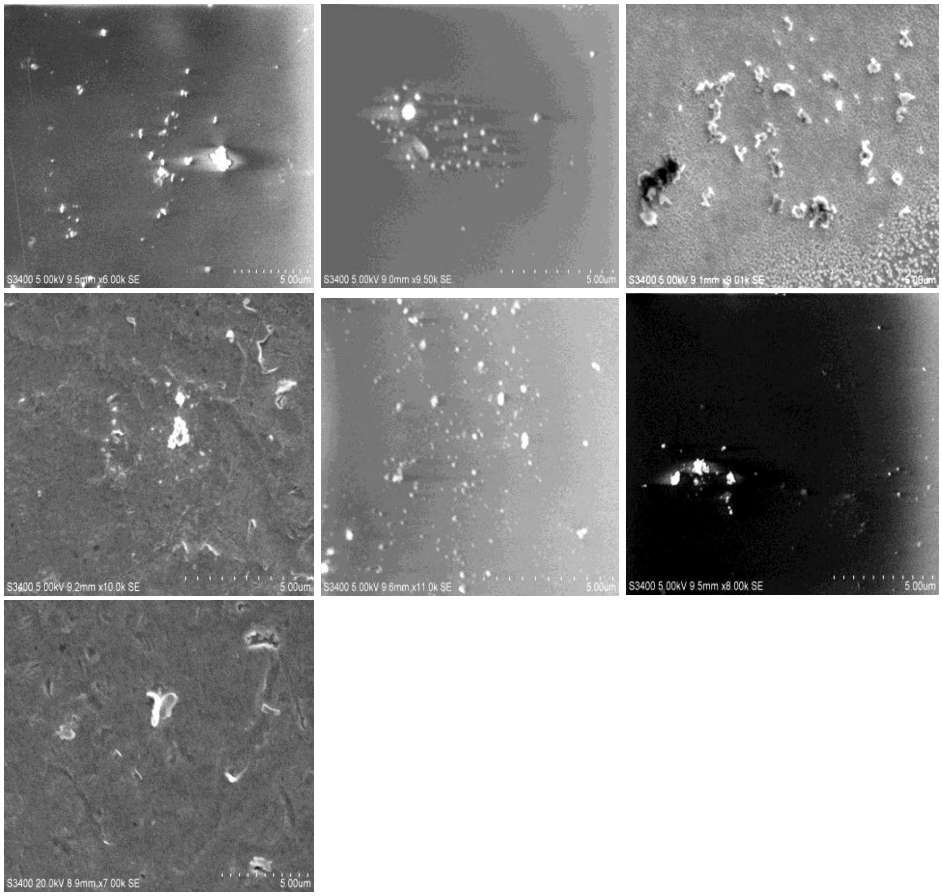

*Platinum had been deposited onto **unmodified** gold electrode with a nucleation potential of -**1200 mV** for **20 ms** and a growth potential of **0 mV to -600 mV** for **60s**.*

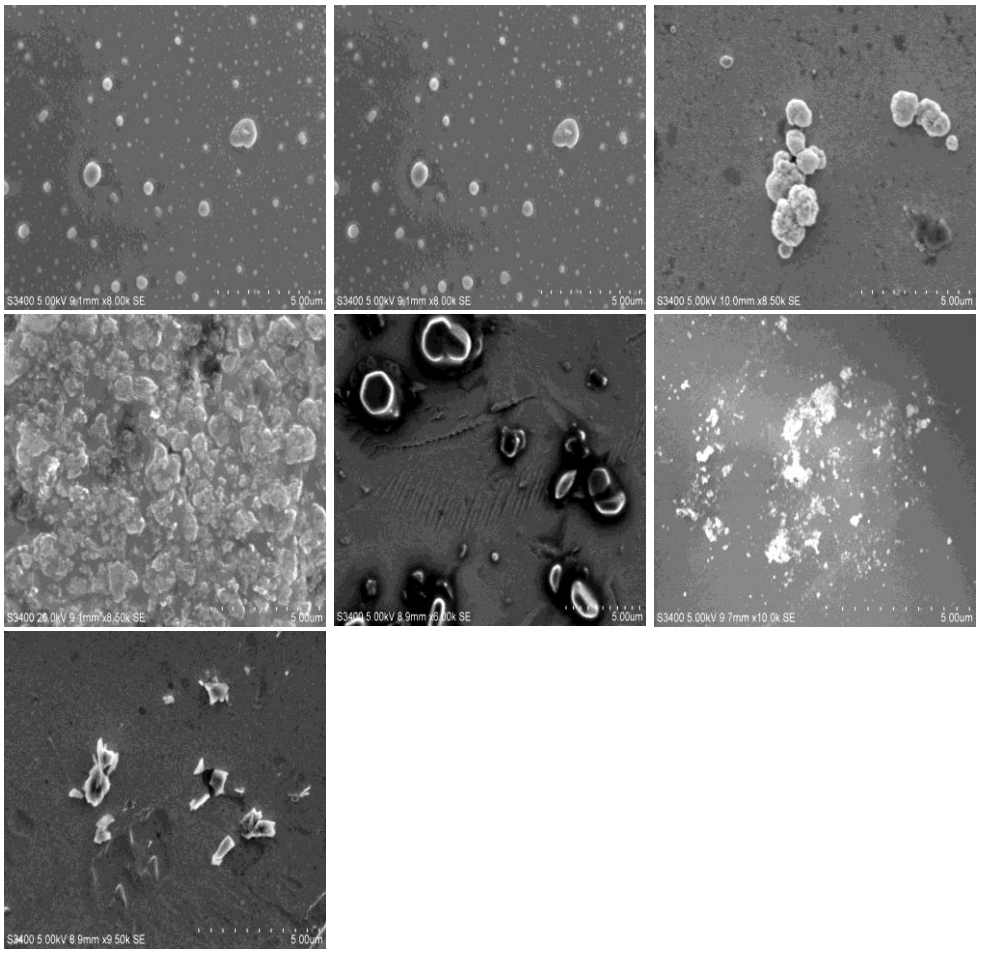

Platinum had been deposited onto ***unmodified*** *gold electrode with a nucleation potential of -****1400 mV*** *for* ***20 ms*** *and a growth potential of* ***0 mV to -600 mV*** *for* ***60s****.*

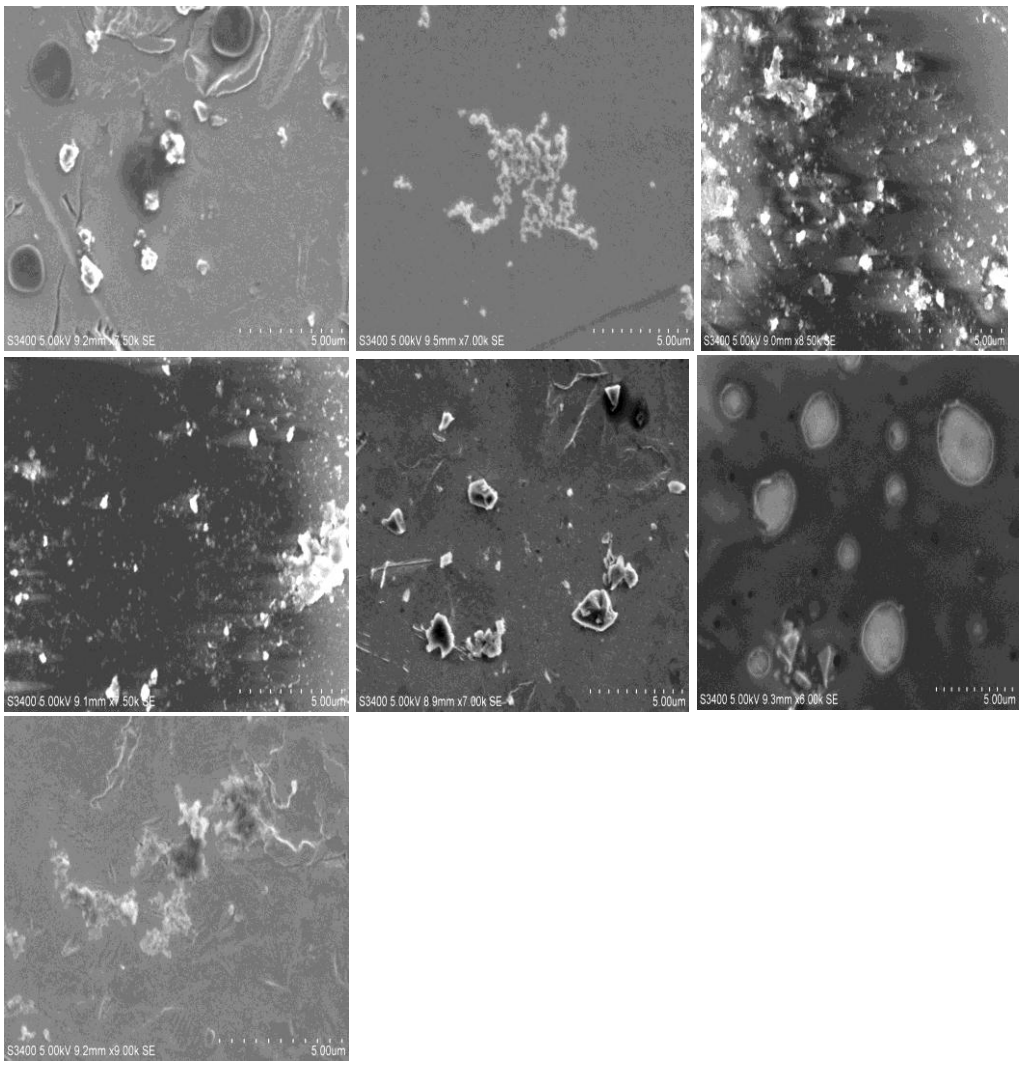

*Platinum had been deposited onto **unmodified** gold electrode with a nucleation potential of -**1600 mV** for **20 ms** and a growth potential of **0 mV to -600 mV** for **60s**.*

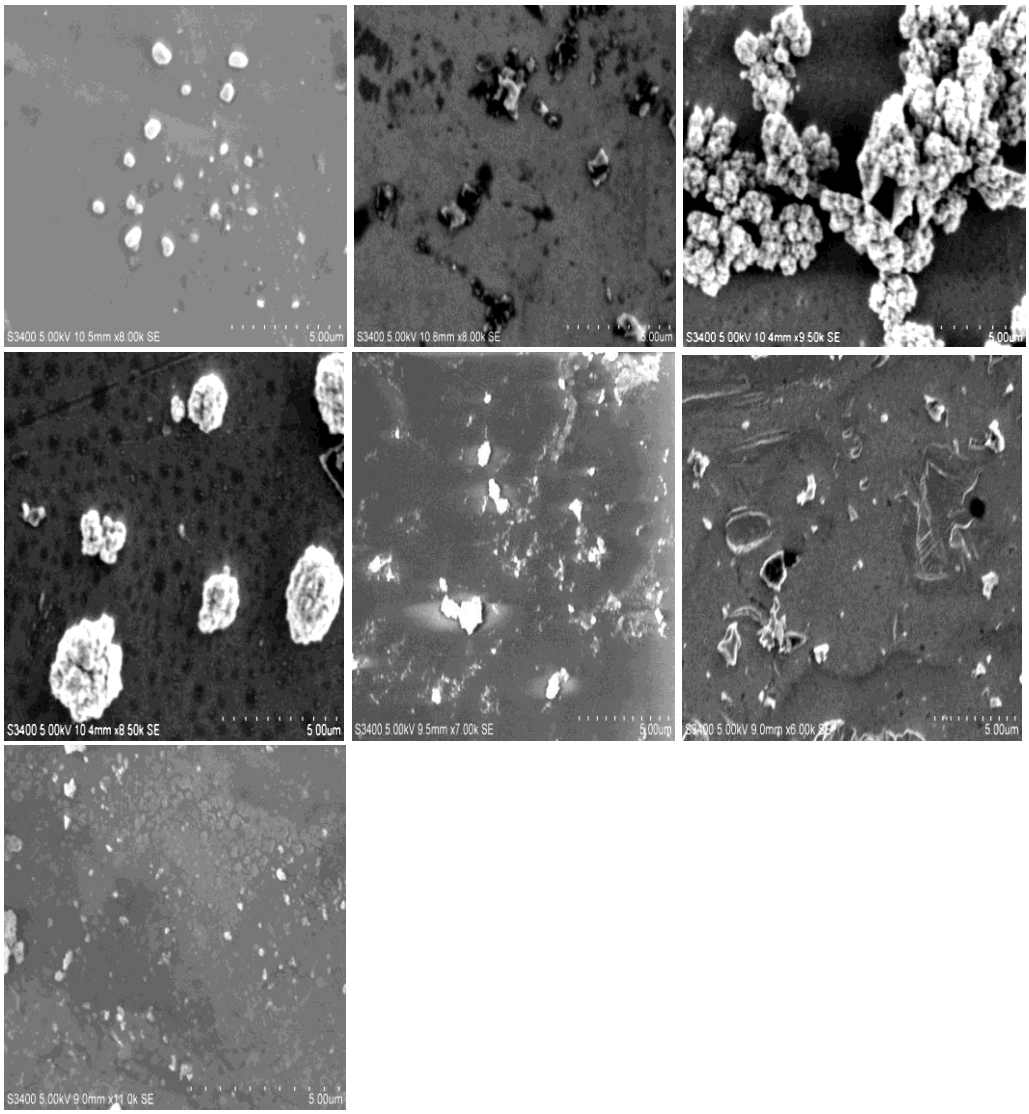

*Platinum had been deposited onto **unmodified** gold electrode with a nucleation potential of -**1800 mV** for **20 ms** and a growth potential of **0 mV to -600 mV** for **60s**.*

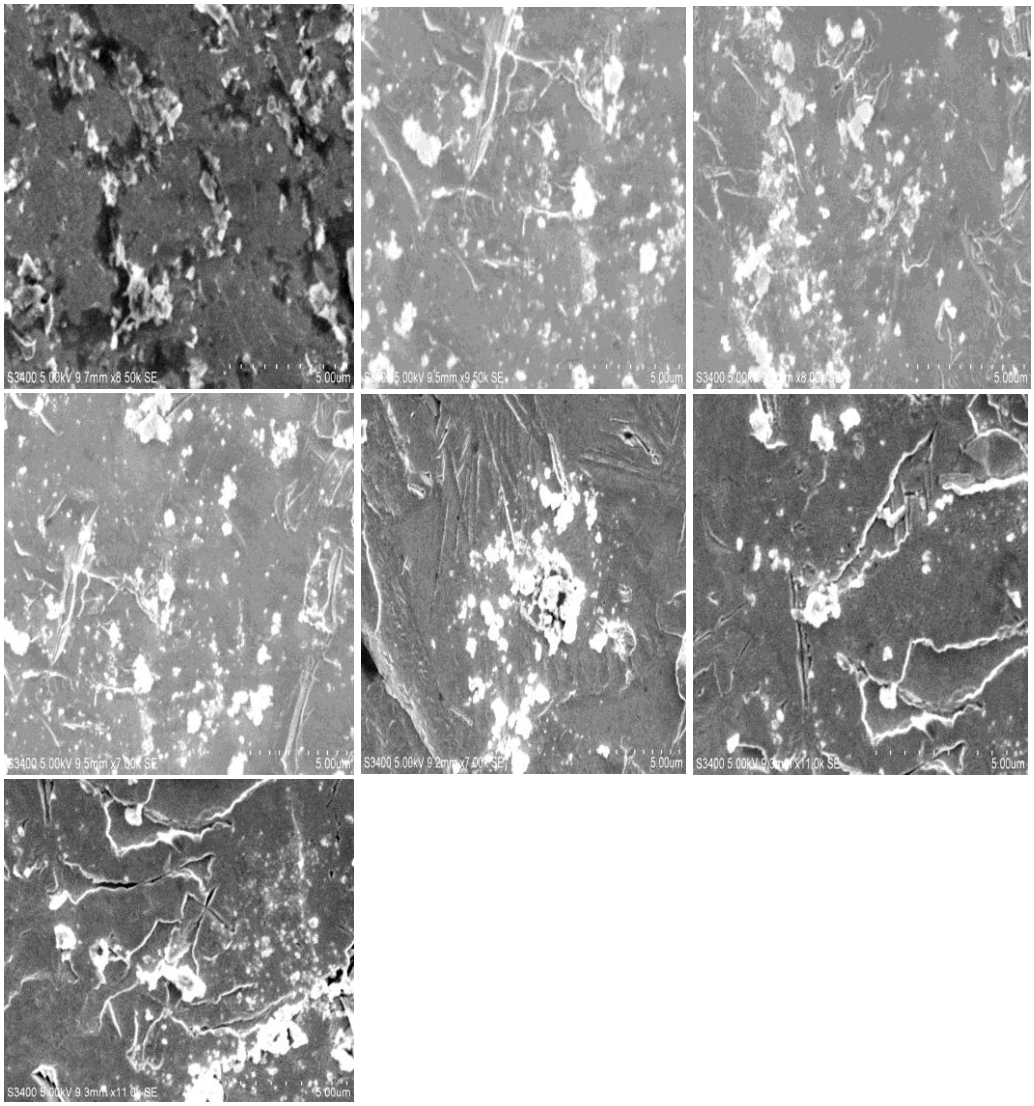

Comparison of the electrochemical area (E.A.) and surface roughness factor (S.R.) values of the gold oxide and platinum oxide peaks of a gold disc electrode after modification with an **alkanethiol monolayer**, after platinum deposition from a 1mM chloroplatinic acid hydrate solution in 0.5 M H_2SO_4 and after desorption of the platinum nanoparticles, using a current jump.

*A -**1000 mV** nucleation pulse is applied for **20 ms** and **0 to -600 mV** growth pulses applied for **30 s** and **60 s** onto a **modified** electrode.*

E_{growth}		30 s $E.A._{Au}$	30 s $S.R._{Au}$	30 s $E.A._{Pt}$	30 s $S.R._{Pt}$	60 s $E.A._{Au}$	60 s $S.R._{Au}$	60 s $E.A._{Pt}$	60 s $S.R._{Pt}$
0mV	Modified	0.050	1.59	0.000	0.00	0.047	1.49	0.000	0.00
	PtNPs	0.049	1.55	0.003	0.09	0.046	1.45	0.005	0.16
	Stripped	0.073	2.34	0.000	0.00	0.106	3.39	0.000	0.00
-100mV	Modified	0.048	1.54	0.000	0.00	0.049	1.56	0.000	0.00
	PtNPs	0.046	1.48	0.006	0.20	0.039	1.23	0.014	0.46
	Stripped	0.066	2.09	0.000	0.00	0.060	1.91	0.000	0.00
-200mV	Modified	0.045	1.43	0.000	0.00	0.048	1.53	0.000	0.00
	PtNPs	0.041	1.30	0.017	0.55	0.033	1.05	0.026	0.84
	Stripped	0.062	1.97	0.000	0.00	0.089	2.82	0.000	0.00
-300mV	Modified	0.048	1.54	0.000	0.00	0.047	1.50	0.000	0.00
	PtNPs	0.041	1.32	0.011	0.34	0.032	1.01	0.018	0.56
	Stripped	0.079	2.51	0.000	0.00	0.067	2.13	0.000	0.00
-400mV	Modified	0.050	1.60	0.000	0.00	0.046	1.45	0.000	0.00
	PtNPs	0.046	1.45	0.007	0.21	0.038	1.20	0.010	0.32
	Stripped	0.087	2.78	0.000	0.00	0.069	2.19	0.000	0.00
-500mV	Modified	0.045	1.43	0.000	0.00	0.046	1.48	0.000	0.00
	PtNPs	0.043	1.38	0.003	0.09	0.037	1.19	0.009	0.30
	Stripped	0.060	1.92	0.000	0.00	0.098	3.12	0.000	0.00
-600mV	Modified	0.049	1.57	0.000	0.00	0.049	1.56	0.000	0.00
	PtNPs	0.050	1.60	0.002	0.05	0.046	1.45	0.006	0.19
	Stripped	0.095	3.04	0.000	0.00	0.090	2.87	0.000	0.00

*A -**1200 mV** nucleation pulse is applied for **20 ms** and **0 to -600 mV** growth pulses applied for **30 s** and **60 s** onto a **modified** electrode.*

E_{growth}		30 s $E.A._{Au}$	30 s $S.R._{Au}$	30 s $E.A._{Pt}$	30 s $S.R._{Pt}$	60 s $E.A._{Au}$	60 s $S.R._{Au}$	60 s $E.A._{Pt}$	60 s $S.R._{Pt}$
0mV	Modified	0.035	1.12	0.000	0.00	0.035	1.10	0.000	0.00
	PtNPs	0.032	1.01	0.006	0.19	0.030	0.97	0.012	0.39
	Stripped	0.041	1.30	0.000	0.00	0.053	1.70	0.000	0.00
-100mV	Modified	0.038	1.20	0.000	0.00	0.042	1.34	0.000	0.00
	PtNPs	0.031	0.99	0.018	0.57	0.031	0.99	0.024	0.78
	Stripped	0.041	1.32	0.000	0.00	0.052	1.66	0.000	0.00
-200mV	Modified	0.037	1.18	0.000	0.00	0.044	1.39	0.000	0.00
	PtNPs	0.014	0.45	0.041	1.30	0.010	0.32	0.059	1.88
	Stripped	0.044	1.39	0.000	0.00	0.055	1.76	0.000	0.00
-300mV	Modified	0.034	1.09	0.000	0.00	0.047	1.49	0.000	0.00
	PtNPs	0.010	0.33	0.026	0.84	0.026	0.82	0.033	1.04
	Stripped	0.041	1.29	0.000	0.00	0.056	1.77	0.000	0.00
-400mV	Modified	0.035	1.11	0.000	0.00	0.050	1.58	0.000	0.00
	PtNPs	0.014	0.45	0.019	0.62	0.024	0.76	0.028	0.89
	Stripped	0.041	1.30	0.000	0.00	0.056	1.78	0.000	0.00
-500mV	Modified	0.034	1.07	0.000	0.00	0.046	1.45	0.000	0.00
	PtNPs	0.018	0.57	0.012	0.39	0.035	1.13	0.019	0.62
	Stripped	0.045	1.43	0.000	0.00	0.054	1.71	0.000	0.00
-600mV	Modified	0.038	1.22	0.000	0.00	0.049	1.55	0.000	0.00
	PtNPs	0.017	0.55	0.008	0.25	0.043	1.36	0.018	0.56
	Stripped	0.052	1.66	0.000	0.00	0.061	1.93	0.000	0.00

*A -**1400 mV** nucleation pulse is applied for **20 ms** and **0 to -600 mV** growth pulses applied for **30 s** and **60 s** onto a **modified** electrode.*

E_{growth}		30 s $E.A._{Au}$	30 s $S.R._{Au}$	30 s $E.A._{Pt}$	30 s $S.R._{Pt}$	60 s $E.A._{Au}$	60 s $S.R._{Au}$	60 s $E.A._{Pt}$	60 s $S.R._{Pt}$
0mV	Modified	0.036	1.16	0.000	0.00	0.034	1.09	0.000	0.00
	PtNPs	0.024	0.78	0.010	0.32	0.031	0.98	0.011	0.36
	Stripped	0.050	1.60	0.000	0.00	0.072	2.28	0.000	0.00
-100mV	Modified	0.037	1.19	0.000	0.00	0.035	1.13	0.000	0.00
	PtNPs	0.019	0.62	0.013	0.40	0.028	0.89	0.049	1.57
	Stripped	0.056	1.77	0.000	0.00	0.095	3.02	0.000	0.00
-200mV	Modified	0.032	1.03	0.000	0.00	0.035	1.12	0.000	0.00
	PtNPs	0.007	0.23	0.062	1.98	0.017	0.54	0.116	3.71
	Stripped	0.067	2.12	0.000	0.00	0.042	1.35	0.000	0.00
-300mV	Modified	0.034	1.07	0.000	0.00	0.032	1.03	0.000	0.00
	PtNPs	0.007	0.22	0.059	1.87	0.012	0.39	0.066	2.10
	Stripped	0.084	2.67	0.000	0.00	0.093	2.95	0.000	0.00
-400mV	Modified	0.033	1.04	0.000	0.00	0.033	1.05	0.000	0.00
	PtNPs	0.019	0.59	0.013	0.40	0.012	0.37	0.023	0.74
	Stripped	0.056	1.79	0.000	0.00	0.051	1.61	0.000	0.00
-500mV	Modified	0.035	1.10	0.000	0.00	0.031	1.00	0.000	0.00
	PtNPs	0.028	0.89	0.011	0.36	0.013	0.41	0.020	0.65
	Stripped	0.063	2.01	0.000	0.00	0.083	2.65	0.000	0.00
-600mV	Modified	0.035	1.11	0.000	0.00	0.036	1.16	0.000	0.00
	PtNPs	0.031	1.00	0.006	0.20	0.008	0.25	0.019	0.60
	Stripped	0.056	1.79	0.000	0.00	0.050	1.60	0.000	0.00

*A -**1600 mV** nucleation pulse is applied for **20 ms** and **0 to -600 mV** growth pulses applied for **30 s** and **60 s** onto a **modified** electrode.*

E_{growth}		30 s $E.A._{Au}$	30 s $S.R._{Au}$	30 s $E.A._{Pt}$	30 s $S.R._{Pt}$	60 s $E.A._{Au}$	60 s $S.R._{Au}$	60 s $E.A._{Pt}$	60 s $S.R._{Pt}$
0mV	Modified	0.034	1.08	0.000	0.00	0.036	1.16	0.000	0.00
	PtNPs	0.025	0.79	0.030	0.95	0.025	0.79	0.030	0.94
	Stripped	0.094	3.00	0.000	0.00	0.096	3.07	0.000	0.00
-100mV	Modified	0.035	1.11	0.000	0.00	0.034	1.09	0.000	0.00
	PtNPs	0.018	0.56	0.062	1.98	0.025	0.80	0.104	3.32
	Stripped	0.090	2.87	0.000	0.00	0.121	3.84	0.000	0.00
-200mV	Modified	0.035	1.10	0.000	0.00	0.040	1.27	0.000	0.00
	PtNPs	0.014	0.46	0.109	3.46	0.004	0.12	0.236	7.51
	Stripped	0.204	6.49	0.003	0.09	0.087	2.77	0.000	0.00
-300mV	Modified	0.038	1.20	0.000	0.00	0.033	1.04	0.000	0.00
	PtNPs	0.013	0.42	0.090	2.87	0.011	0.34	0.188	5.98
	Stripped	0.069	2.20	0.000	0.00	0.074	2.36	0.000	0.00
-400mV	Modified	0.034	1.08	0.000	0.00	0.033	1.06	0.000	0.00
	PtNPs	0.022	0.71	0.048	1.54	0.015	0.48	0.129	4.10
	Stripped	0.081	2.57	0.000	0.00	0.099	3.15	0.000	0.00
-500mV	Modified	0.033	1.05	0.000	0.00	0.034	1.09	0.000	0.00
	PtNPs	0.029	0.92	0.032	1.01	0.015	0.47	0.062	1.97
	Stripped	0.093	2.95	0.000	0.00	0.078	2.48	0.000	0.00
-600mV	Modified	0.032	1.02	0.000	0.00	0.035	1.11	0.000	0.00
	PtNPs	0.028	0.90	0.012	0.38	0.013	0.40	0.049	1.56
	Stripped	0.091	2.90	0.000	0.00	0.080	2.55	0.000	0.00

*A -**1800 mV** nucleation pulse is applied for **20 ms** and **0 to -600 mV** growth pulses applied for **30 s** and **60 s** onto a **modified** electrode.*

E_{growth}		30 s $E.A._{Au}$	30 s $S.R._{Au}$	30 s $E.A._{Pt}$	30 s $S.R._{Pt}$	60 s $E.A._{Au}$	60 s $S.R._{Au}$	60 s $E.A._{Pt}$	60 s $S.R._{Pt}$
0mV	**Modified**	0.032	1.02	0.000	0.00	0.036	1.16	0.000	0.00
	PtNPs	0.032	1.01	0.002	0.05	0.035	1.10	0.011	0.34
	Stripped	0.066	2.10	0.000	0.00	0.076	2.43	0.000	0.00
-100mV	**Modified**	0.035	1.10	0.000	0.00	0.033	1.05	0.000	0.00
	PtNPs	0.033	1.05	0.003	0.11	0.031	0.99	0.007	0.23
	Stripped	0.084	2.68	0.000	0.00	0.065	2.08	0.000	0.00
-200mV	**Modified**	0.036	1.14	0.000	0.00	0.035	1.10	0.000	0.00
	PtNPs	0.035	1.10	0.028	0.88	0.031	1.00	0.018	0.56
	Stripped	0.066	2.10	0.000	0.00	0.123	3.92	0.000	0.00
-300mV	**Modified**	0.032	1.02	0.000	0.00	0.038	1.20	0.000	0.00
	PtNPs	0.030	0.95	0.010	0.32	0.025	0.79	0.014	0.46
	Stripped	0.056	1.79	0.000	0.00	0.093	2.97	0.000	0.00
-400mV	**Modified**	0.035	1.12	0.000	0.00	0.034	1.09	0.000	0.00
	PtNPs	0.032	1.03	0.019	0.59	0.029	0.92	0.008	0.27
	Stripped	0.063	2.02	0.000	0.00	0.092	2.94	0.000	0.00
-500mV	**Modified**	0.033	1.06	0.000	0.00	0.035	1.10	0.000	0.00
	PtNPs	0.031	1.00	0.016	0.51	0.032	1.01	0.004	0.12
	Stripped	0.108	3.43	0.000	0.00	0.089	2.83	0.000	0.00
-600mV	**Modified**	0.036	1.14	0.000	0.00	0.032	1.03	0.000	0.00
	PtNPs	0.035	1.10	0.003	0.09	0.027	0.87	0.005	0.17
	Stripped	0.144	4.60	0.000	0.00	0.116	3.71	0.000	0.00

Scanning electron microscopy (SEM) images of a gold electrode after electrochemical deposition of platinum using the double pulse potential method.

*Platinum had been deposited onto a **monolayer template** with a nucleation potential of **-1000 mV** for **20 ms** and a growth potential of **0 mV to -600 mV** for **30 s**.*

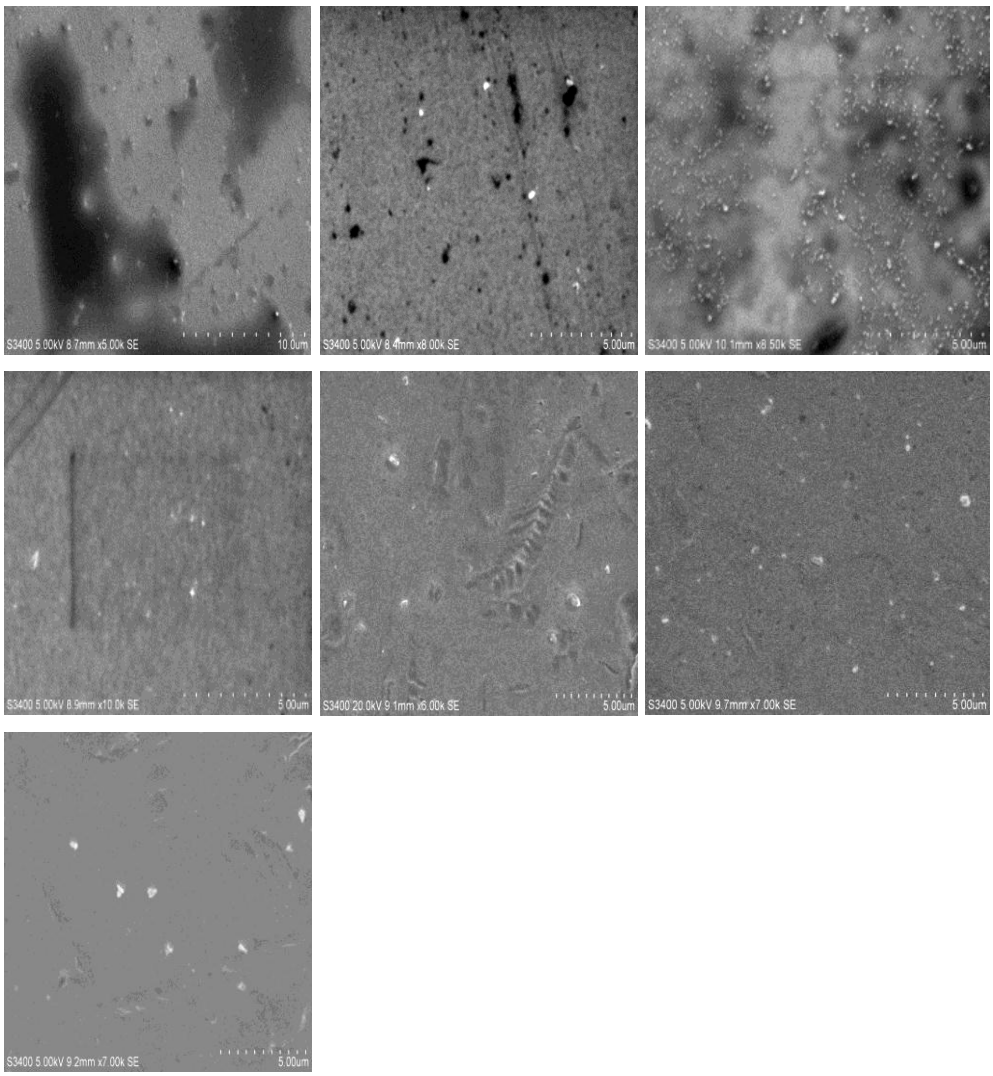

*Platinum had been deposited onto a **monolayer template** with a nucleation potential of **-1200 mV** for **20 ms** and a growth potential of **0 mV to -600 mV** for **30 s**.*

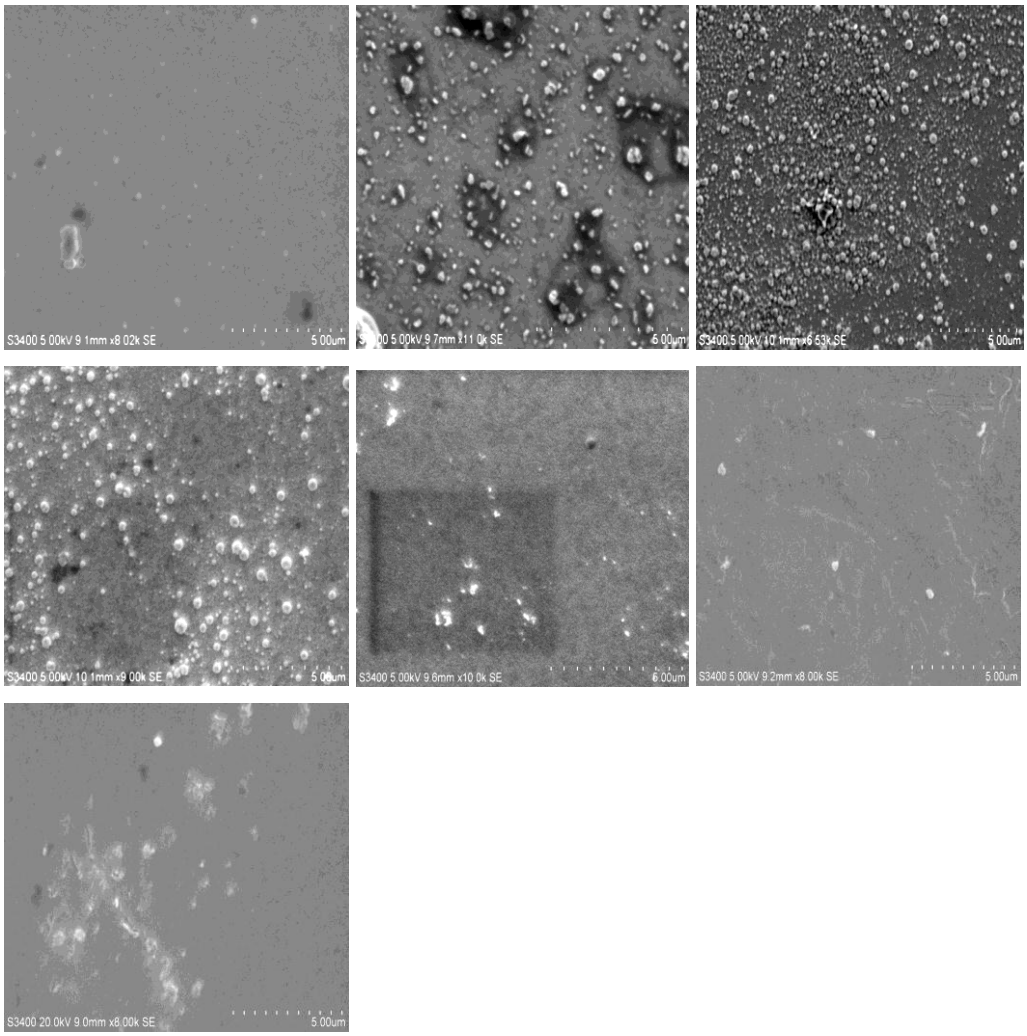

*Platinum had been deposited onto a **monolayer template** with a nucleation potential of **-1400 mV** for **20 ms** and a growth potential of **0 mV to -600 mV** for **30 s**.*

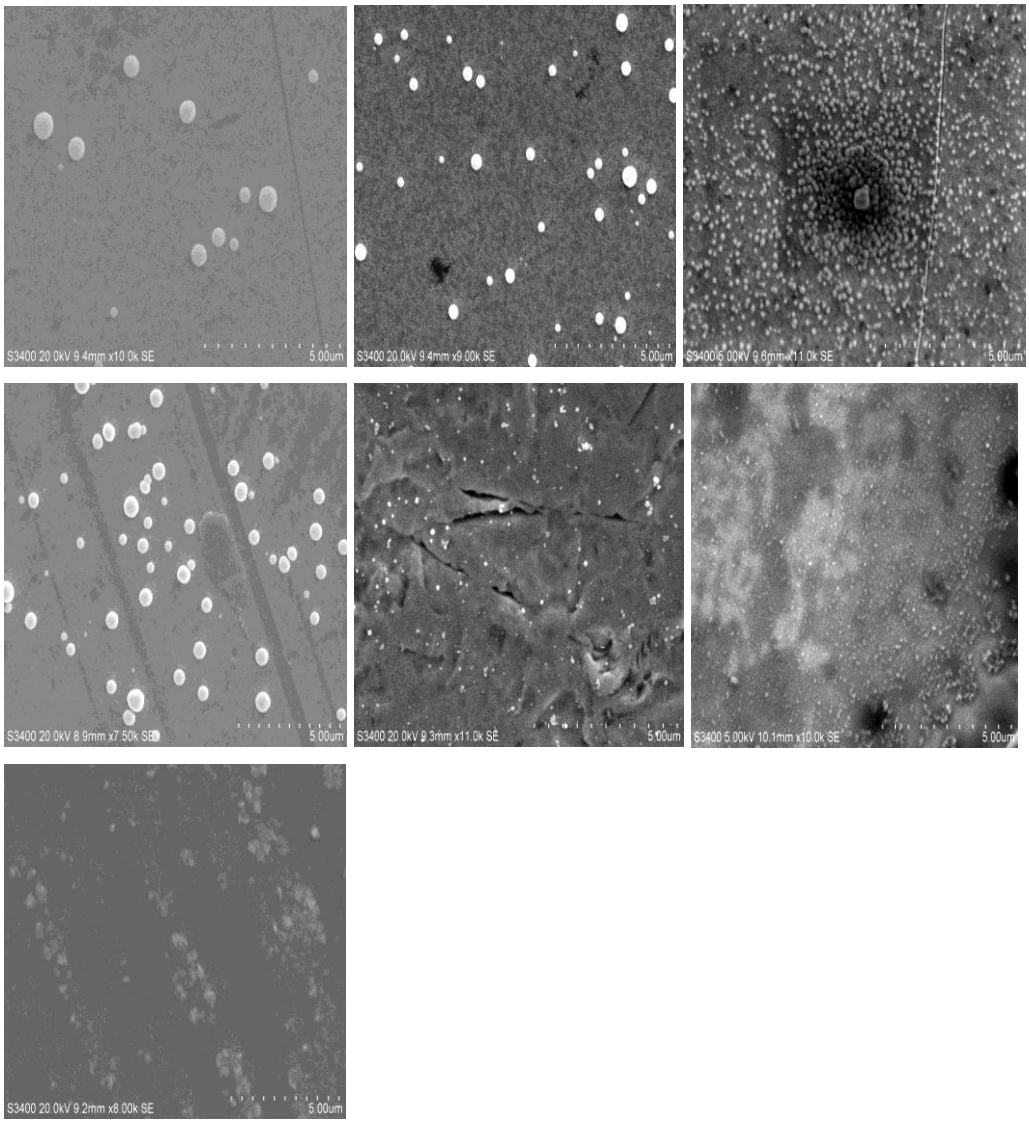

*Platinum had been deposited onto a **monolayer template** with a nucleation potential of **-1600 mV** for **20 ms** and a growth potential of **0 mV to -600 mV** for **30 s**.*

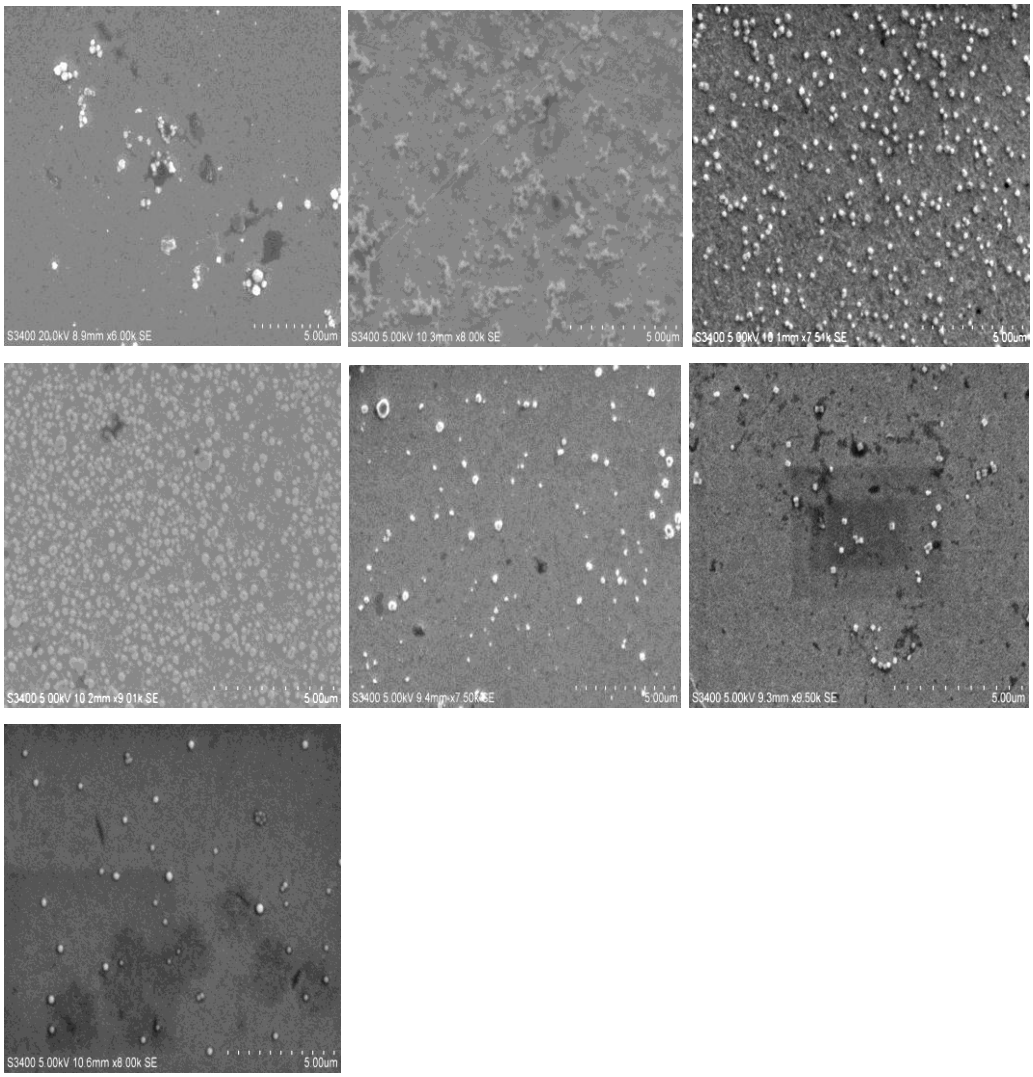

*Platinum had been deposited onto a **monolayer template** with a nucleation potential of **-1800 mV** for **20 ms** and a growth potential of **0 mV to -600 mV** for **30 s**.*

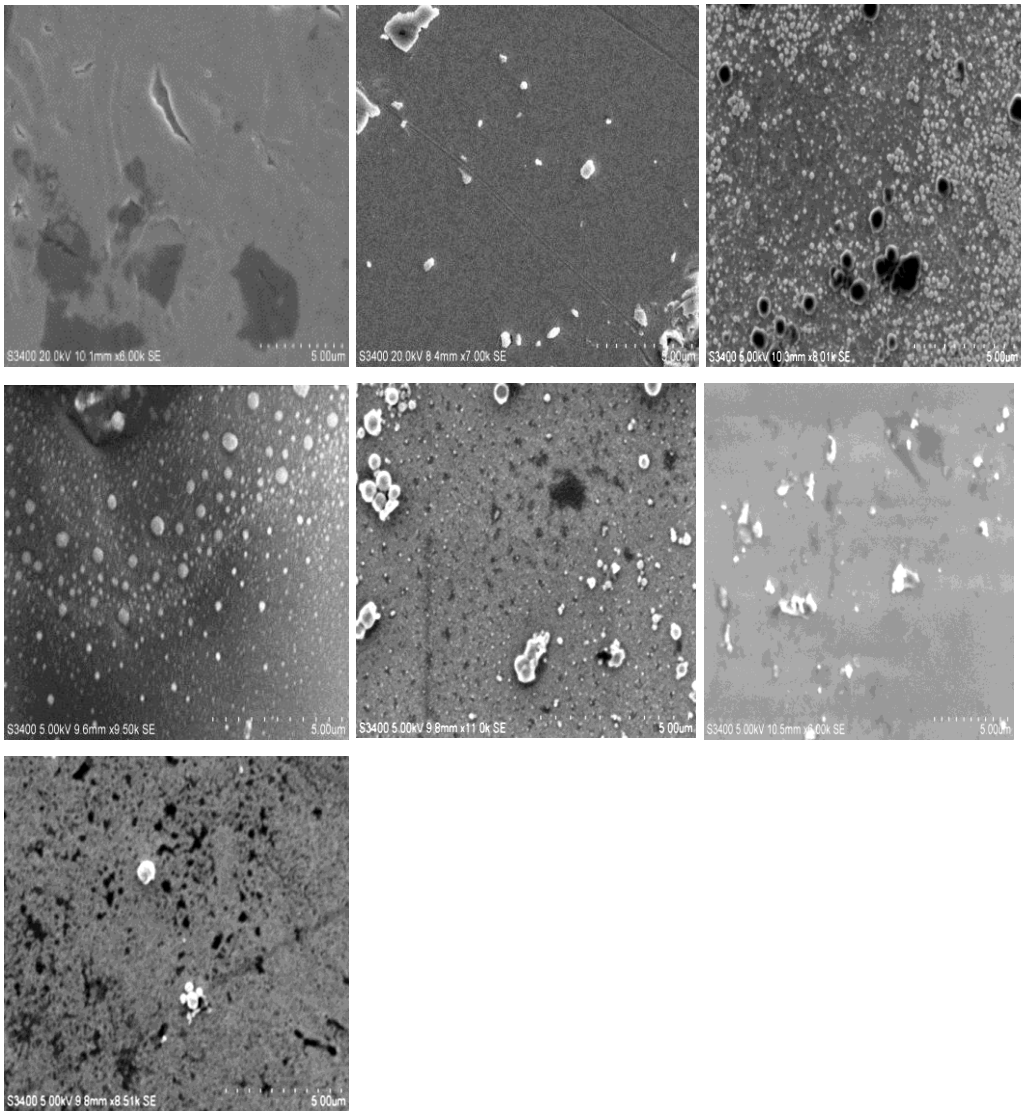

Scanning electron microscopy (SEM) images of a gold electrode after electrochemical deposition of platinum using the double pulse potential method.

*Platinum had been deposited onto a **monolayer template** with a nucleation potential of **-1000 mV** for **20 ms** and a growth potential of **0 mV to -600 mV** for **60 s.***

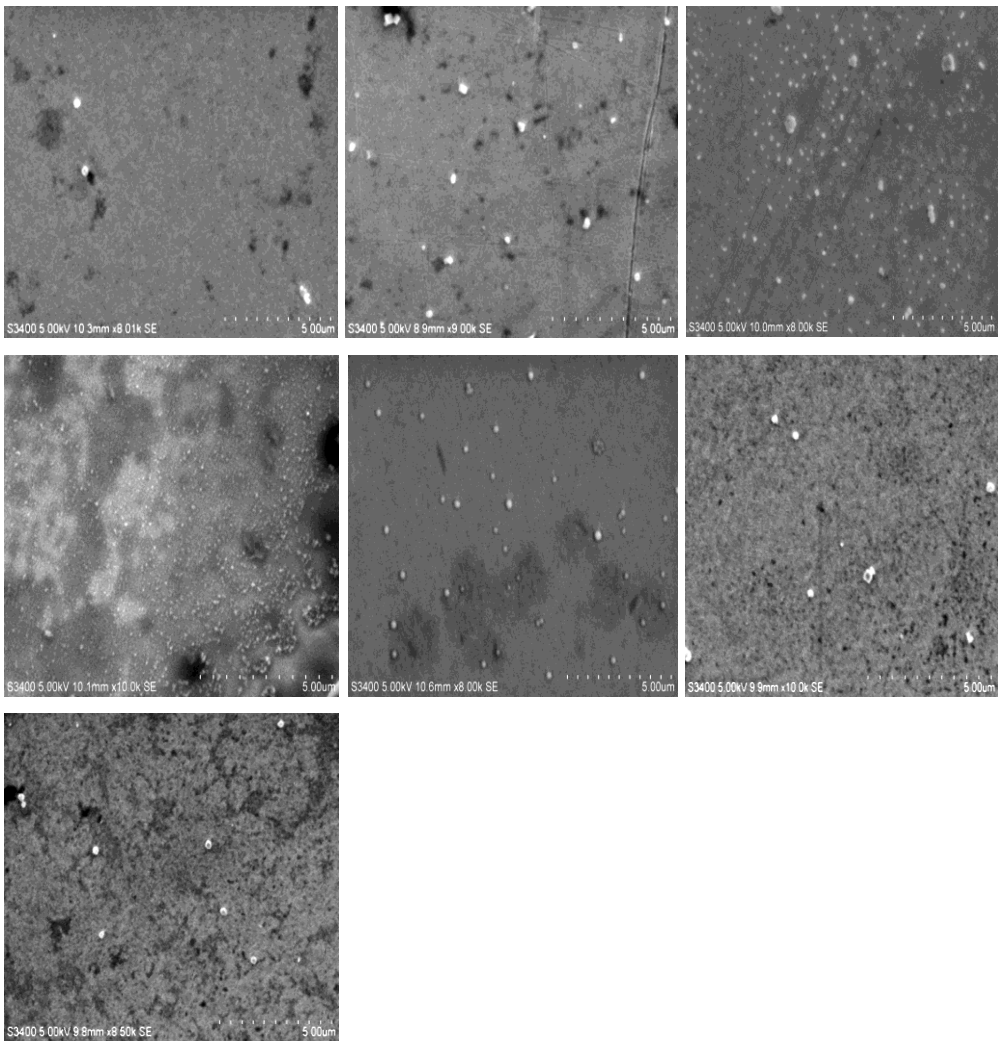

*Platinum had been deposited onto a **monolayer template** with a nucleation potential of **-1200 mV** for **20 ms** and a growth potential of **0 mV to -600 mV** for **60 s**.*

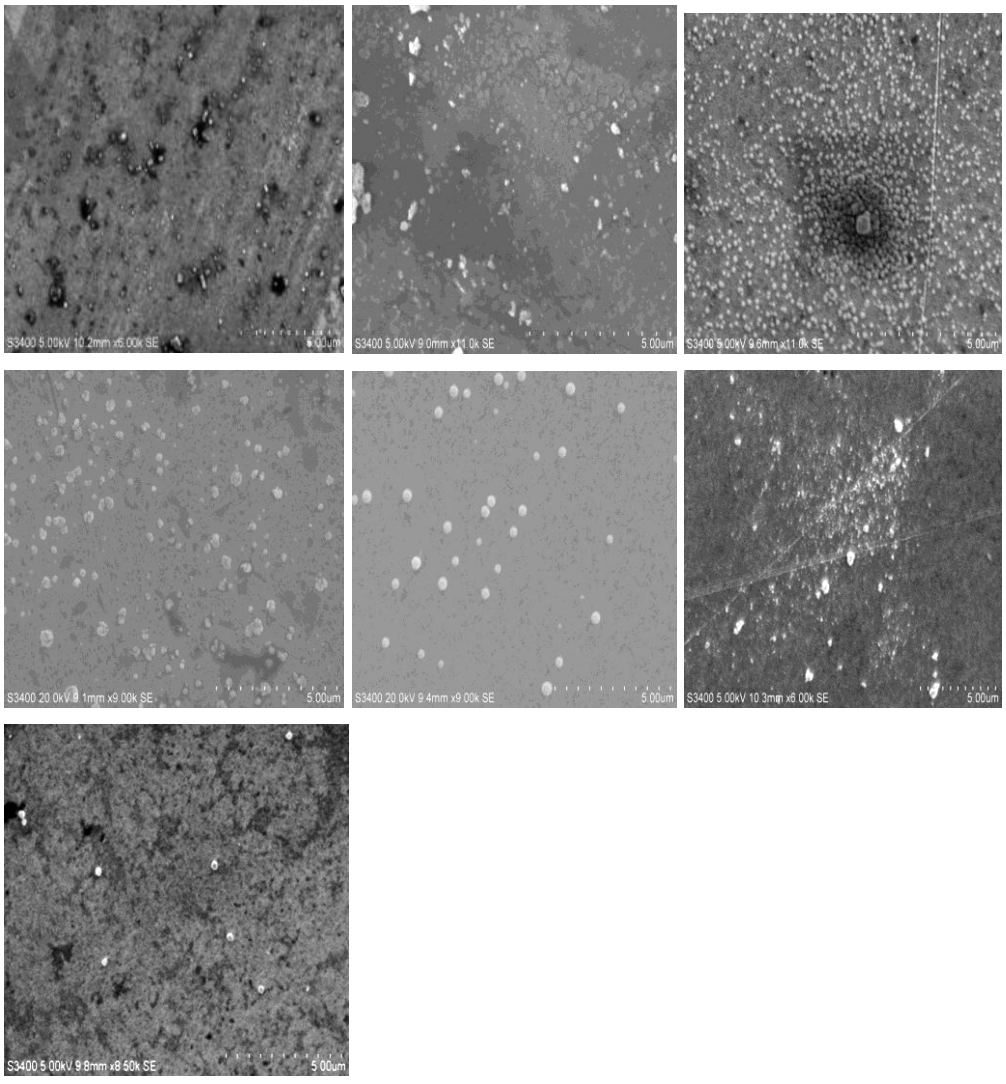

*Platinum had been deposited onto a **monolayer template** with a nucleation potential of **-1400 mV** for **20 ms** and a growth potential of **0 mV to -600 mV** for **60 s**.*

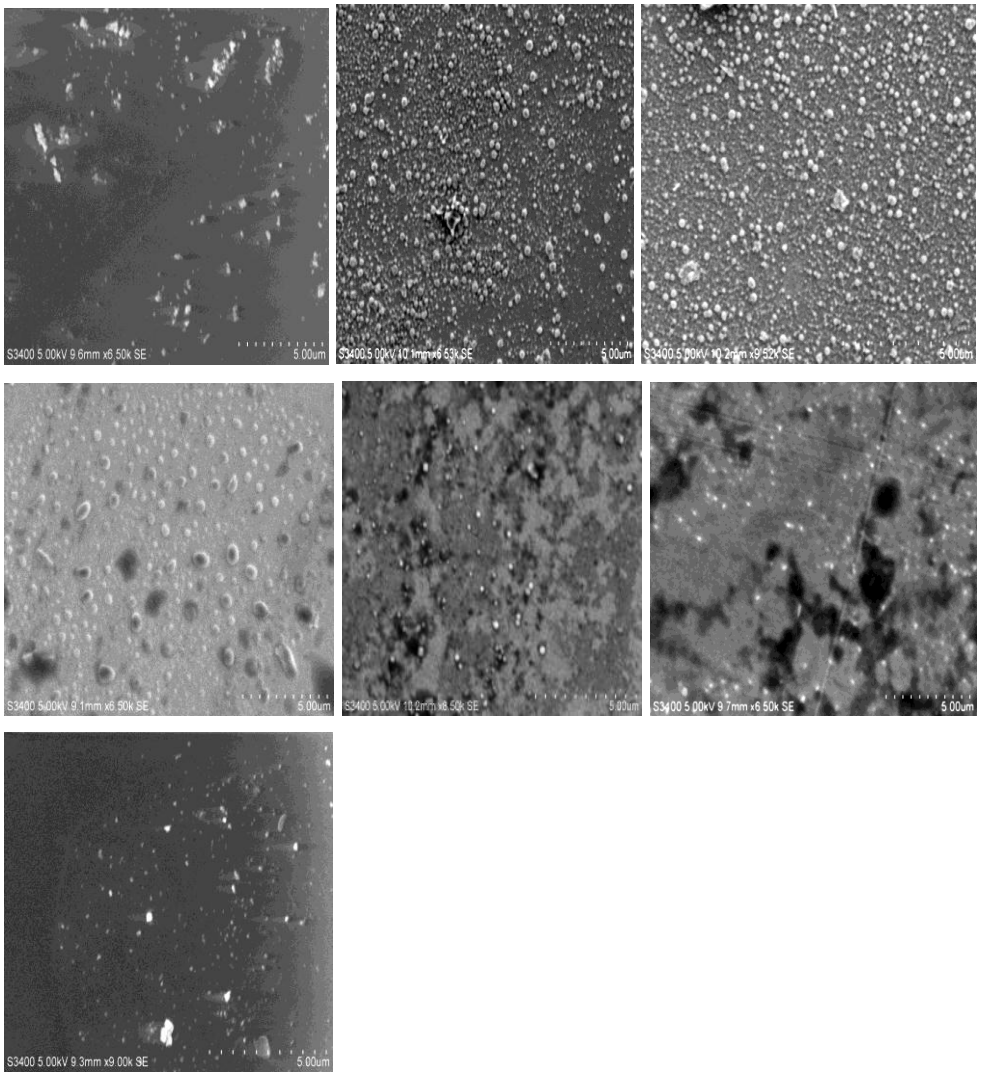

*Platinum had been deposited onto a **monolayer template** with a nucleation potential of **-1600 mV** for **20 ms** and a growth potential of **0 mV to -600 mV** for **60 s**.*

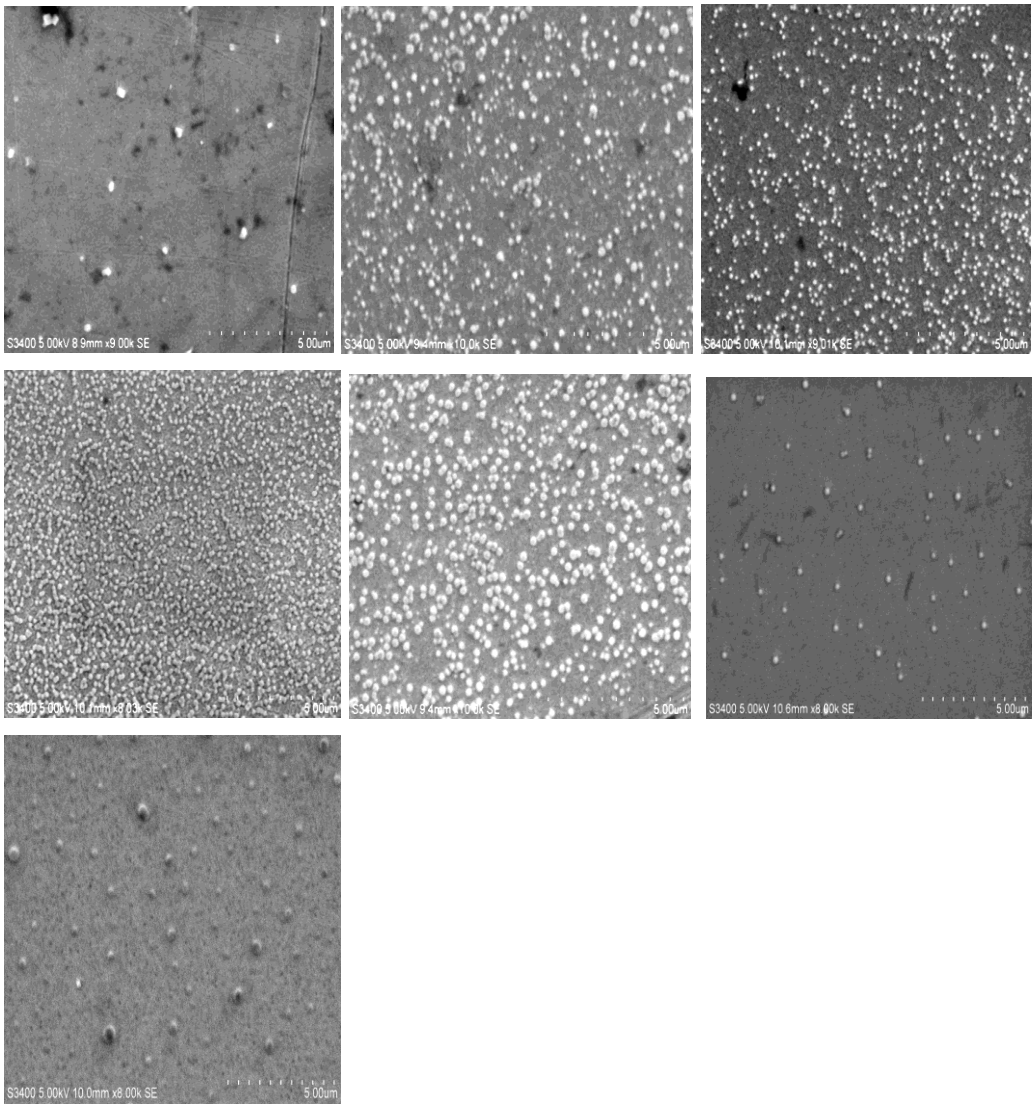

*Platinum had been deposited onto a **monolayer template** with a nucleation potential of **-1800 mV** for **20 ms** and a growth potential of **0 mV to -600 mV** for **60 s**.*

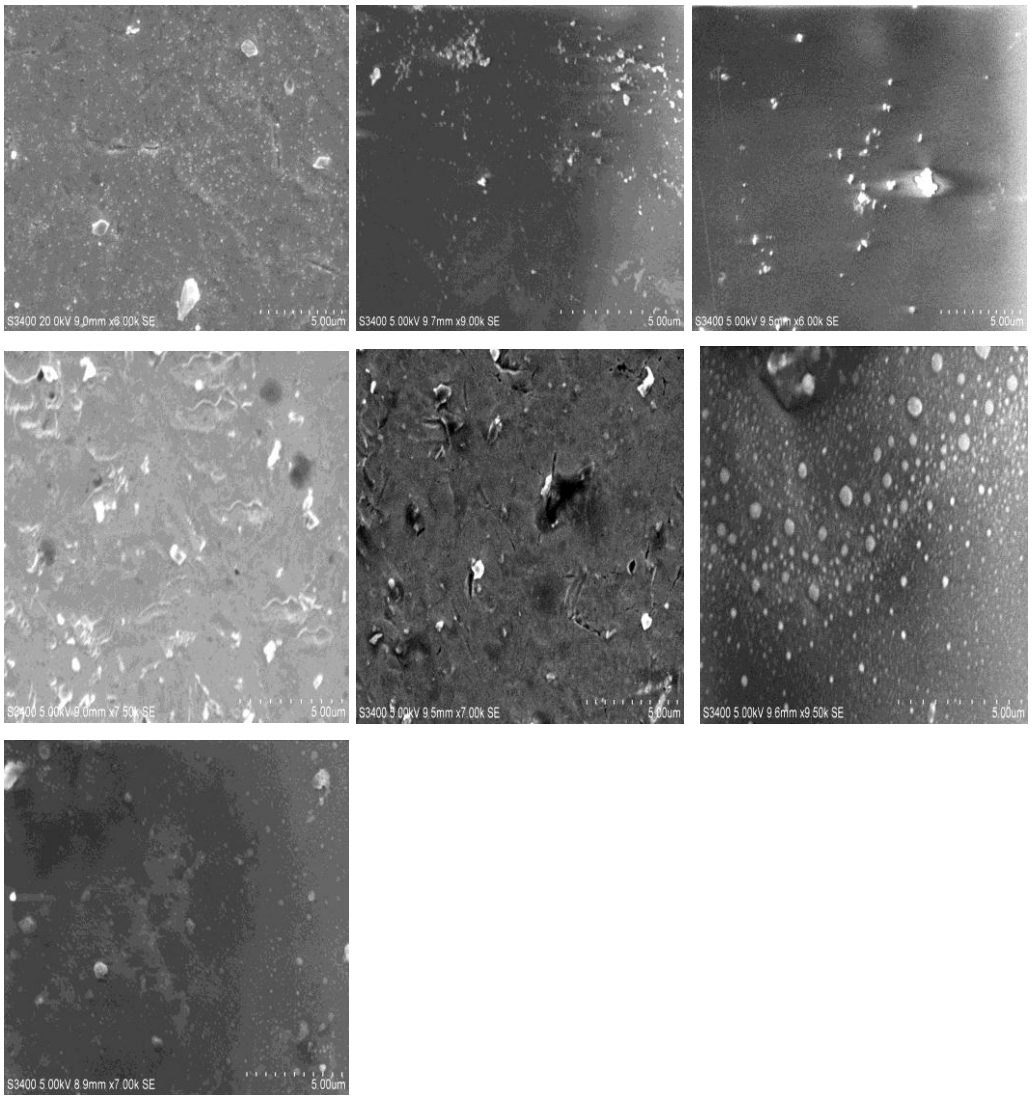

Scanning electron micrograph (SEM) images a gold electrode after dropcasting the centrifuged desorbed platinum nanoparticles onto the surface.

*Platinum had initially been deposited onto **unmodified** gold with a nucleation potential of **-1000 mV** for **20 ms** and a growth potential of **0 mV to -600 mV** for **30 s**.*

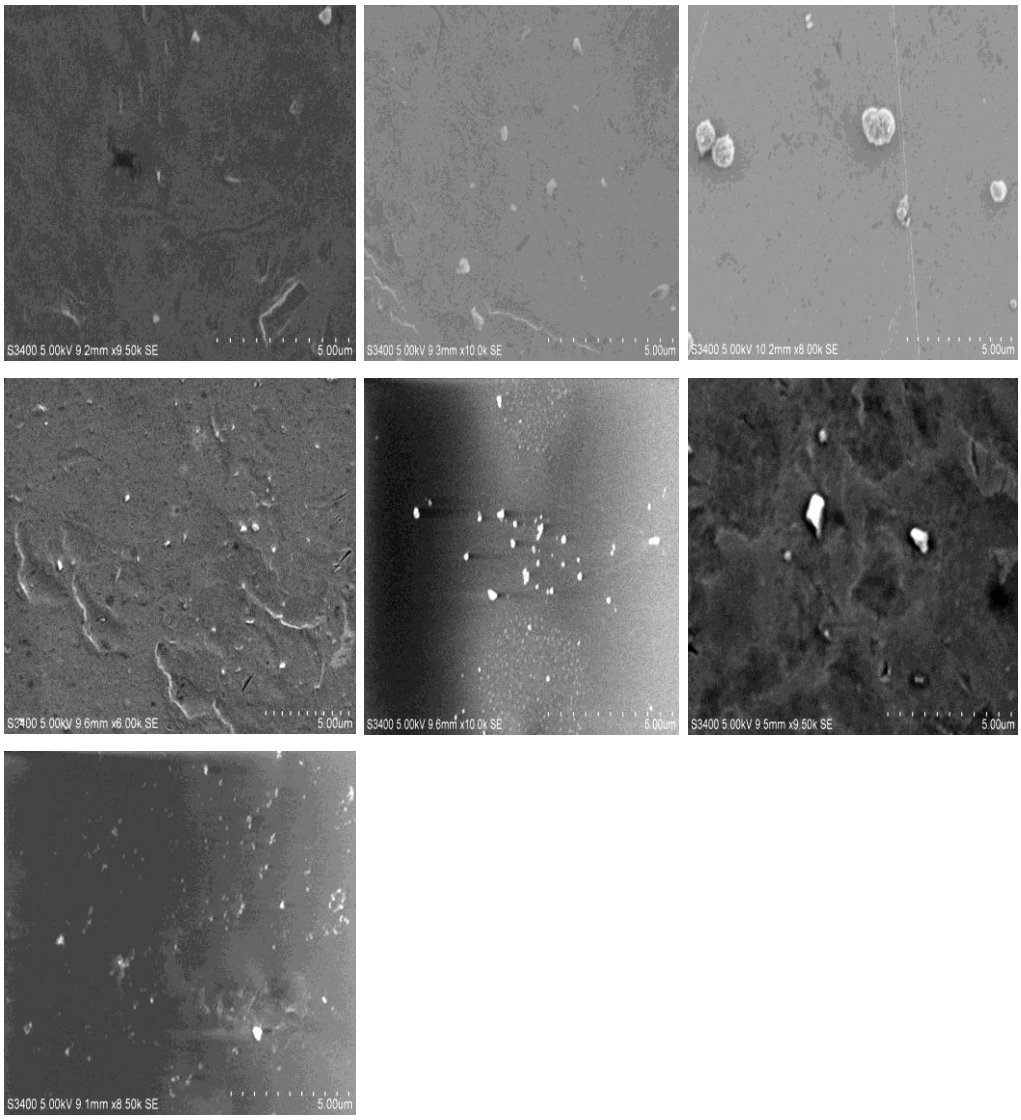

*Platinum had initially been deposited onto **unmodified** gold with a nucleation potential of **-1200 mV** for **20 ms** and a growth potential of **0 mV to -600 mV** for **30 s**.*

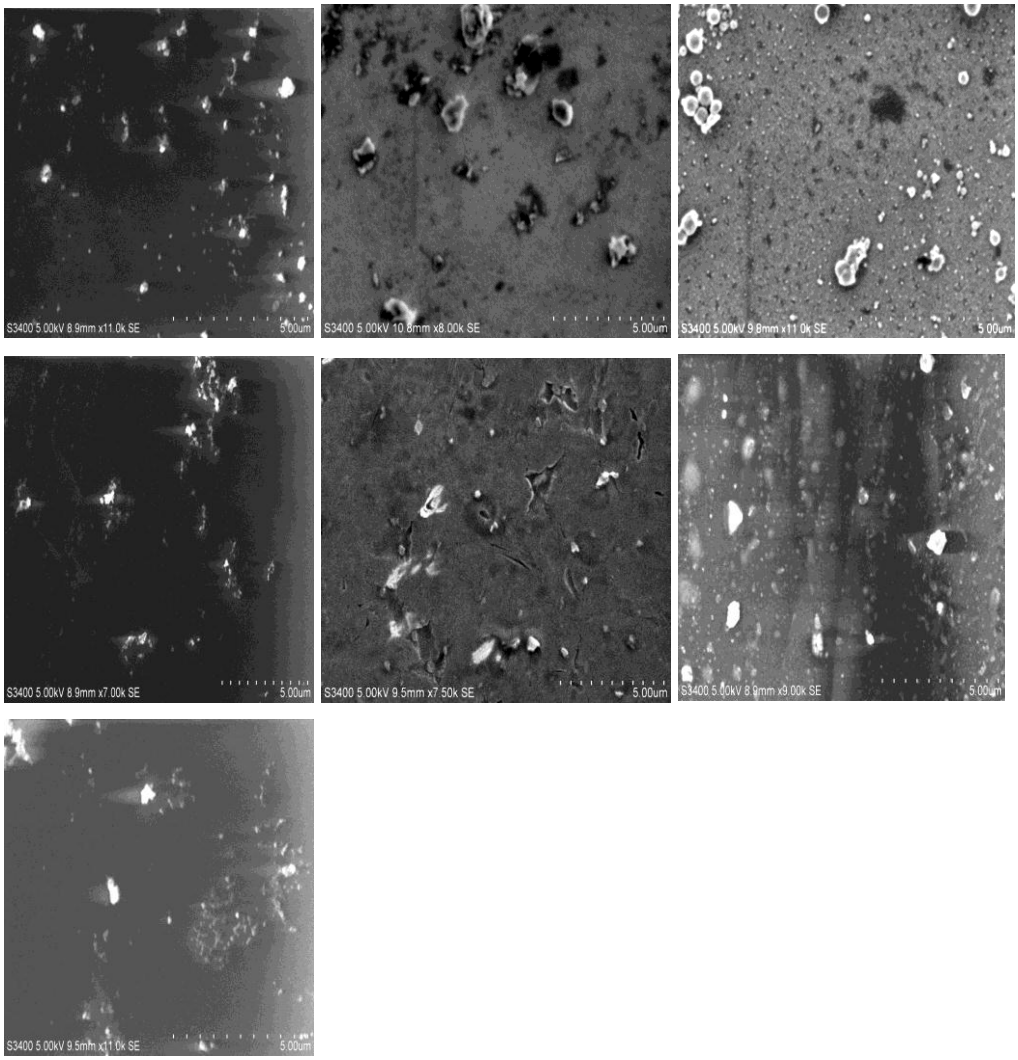

*Platinum had initially been deposited onto **unmodified** gold with a nucleation potential of **-1400 mV** for **20 ms** and a growth potential of **0 mV to -600 mV** for **30 s**.*

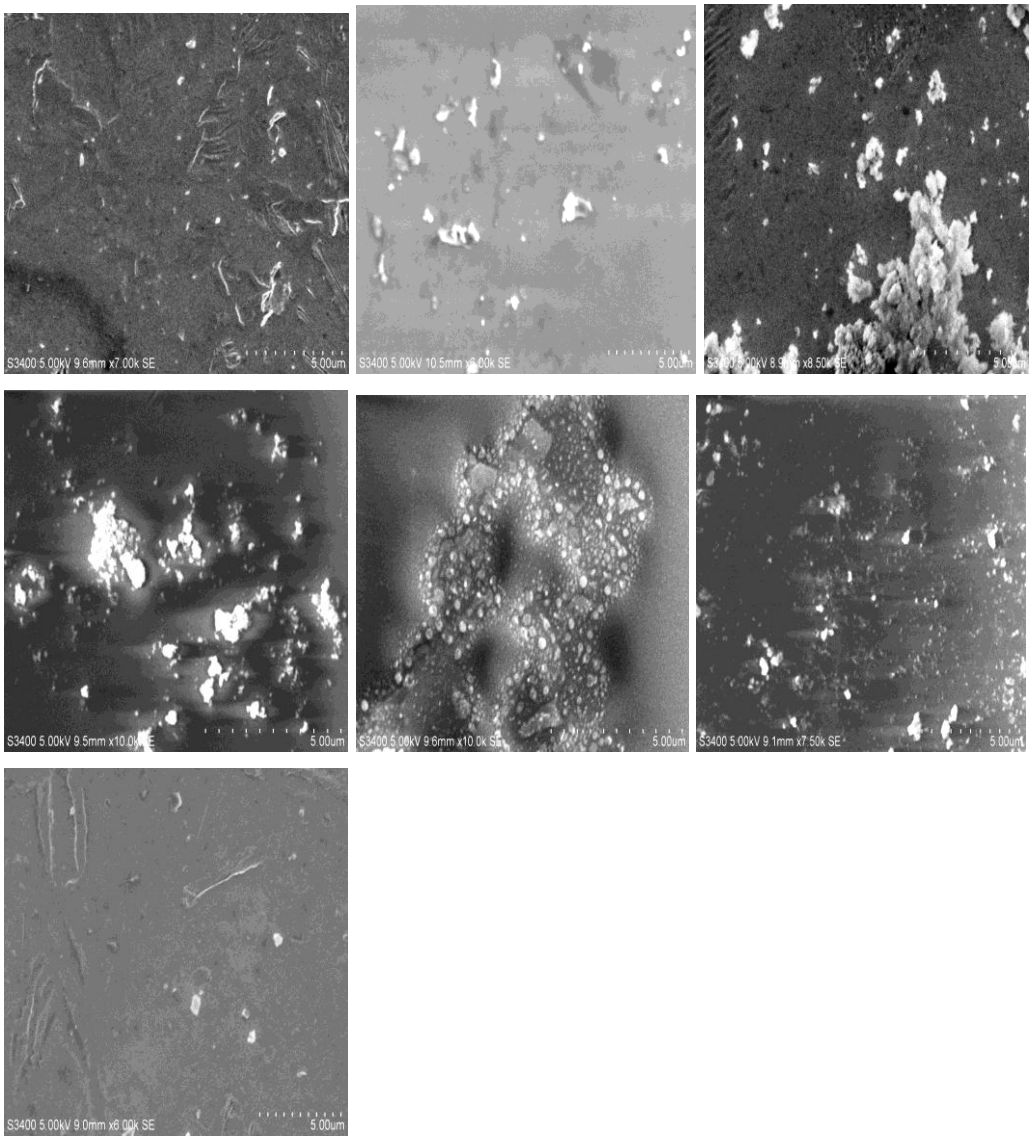

*Platinum had initially been deposited onto **unmodified** gold with a nucleation potential of **-1600 mV** for **20 ms** and a growth potential of **0 mV to -600 mV** for **30 s**.*

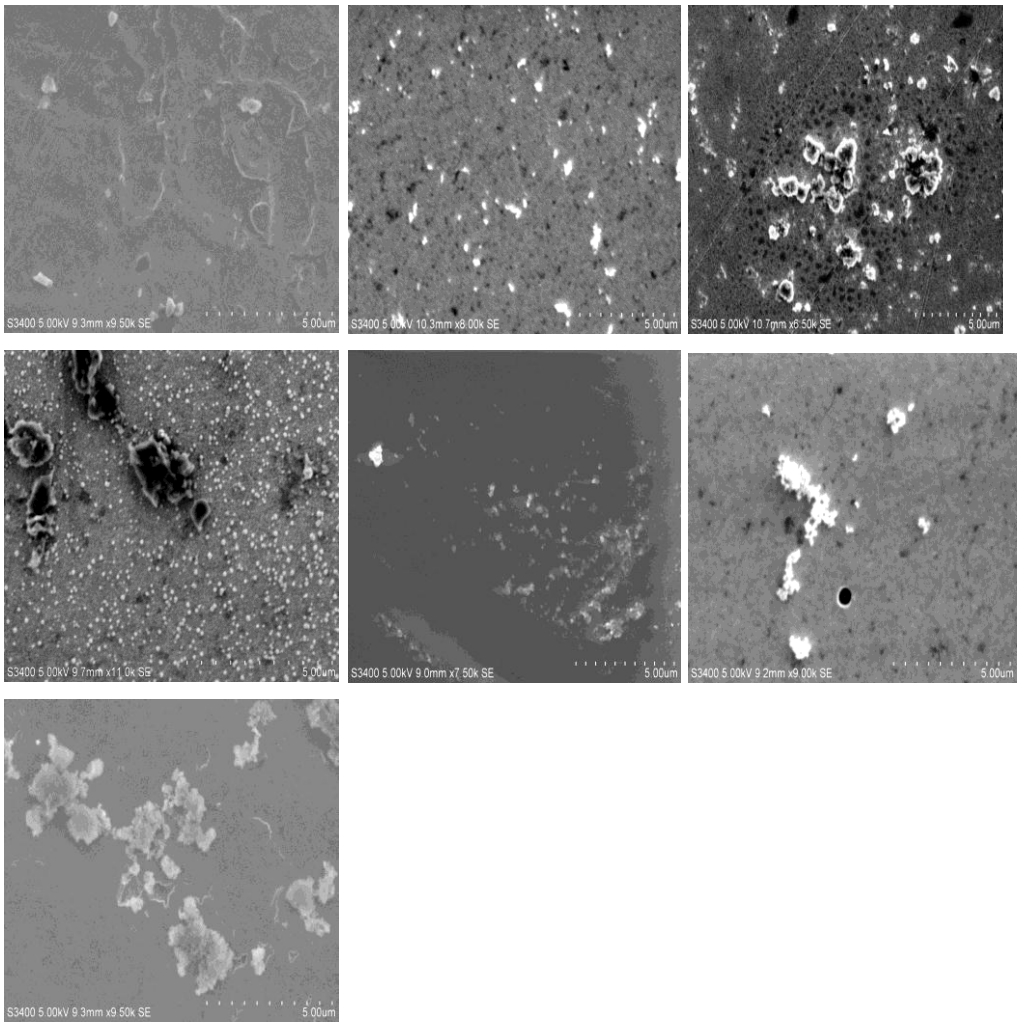

*Platinum had initially been deposited onto **unmodified** gold with a nucleation potential of **-1800 mV** for **20 ms** and a growth potential of **0 mV to -600 mV** for **30 s**.*

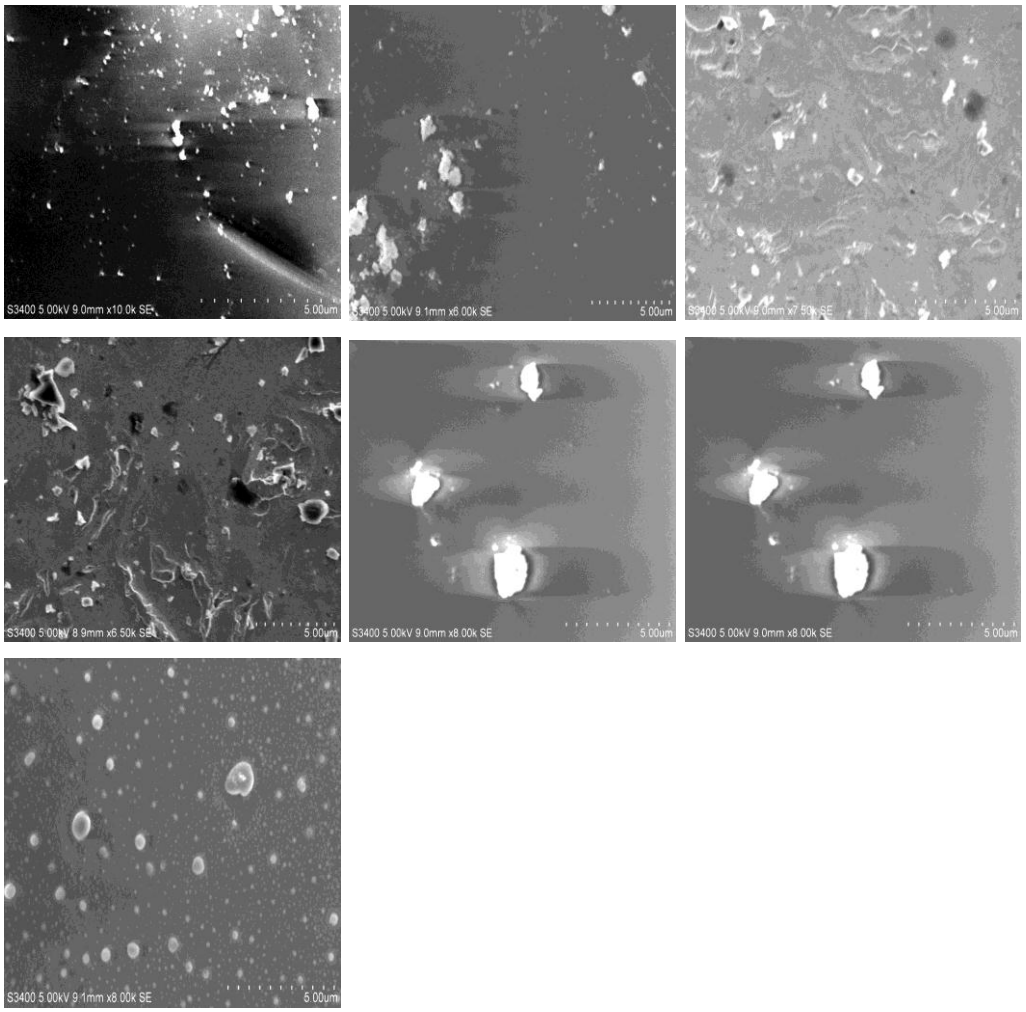

Scanning electron micrograph (SEM) images of a gold electrode after dropcasting the centrifuged desorbed platinum nanoparticles onto the surface.

*Platinum had initially been deposited onto **unmodified** gold with a nucleation potential of **-1000 mV** for **20 ms** and a growth potential of **0 mV to -600 mV** for **60 s**.*

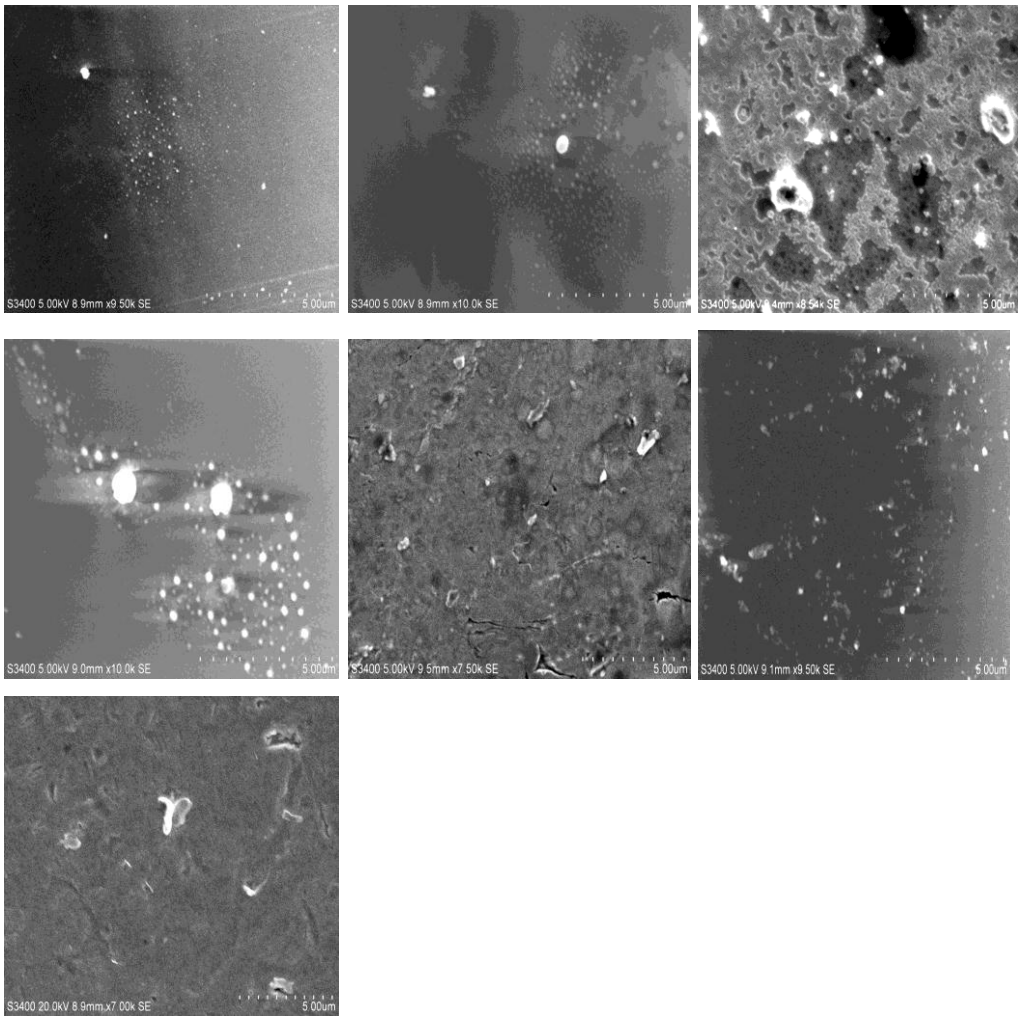

*Platinum had initially been deposited onto **unmodified** gold with a nucleation potential of **-1200 mV** for **20 ms** and a growth potential of **0 mV to -600 mV** for **60 s**.*

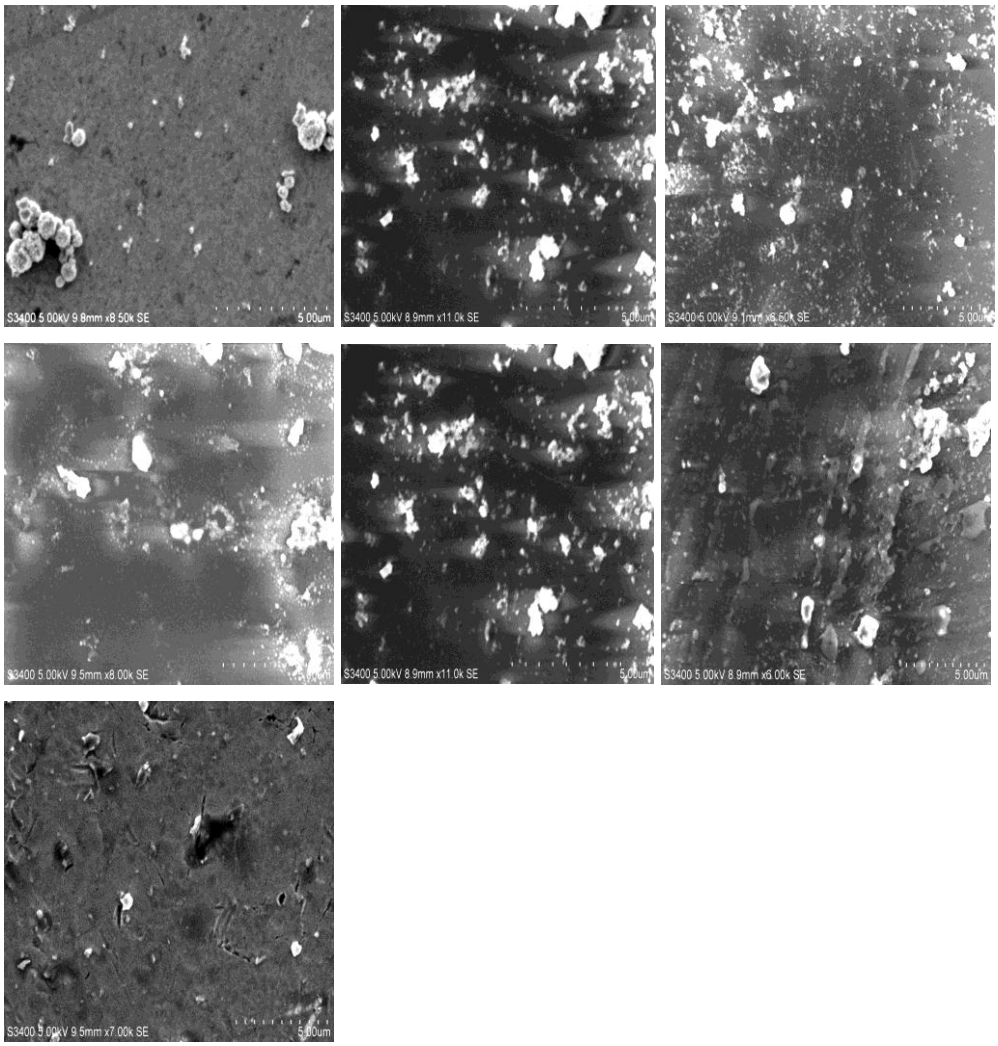

*Platinum had initially been deposited onto **unmodified** gold with a nucleation potential of **-1400 mV** for **20 ms** and a growth potential of **0 mV to -600 mV** for **60 s**.*

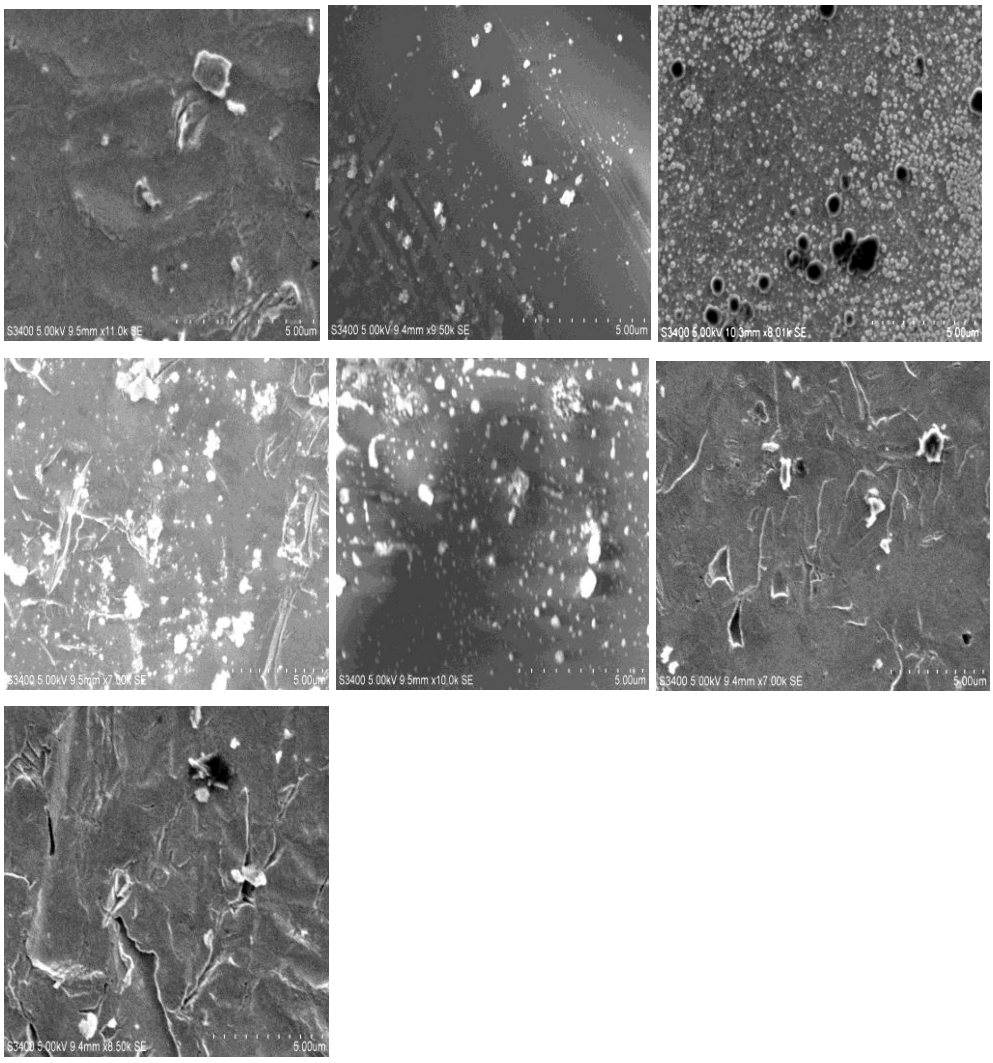

*Platinum had initially been deposited onto **unmodified** gold with a nucleation potential of **-1600 mV** for **20 ms** and a growth potential of **0 mV to -600 mV** for **60 s**.*

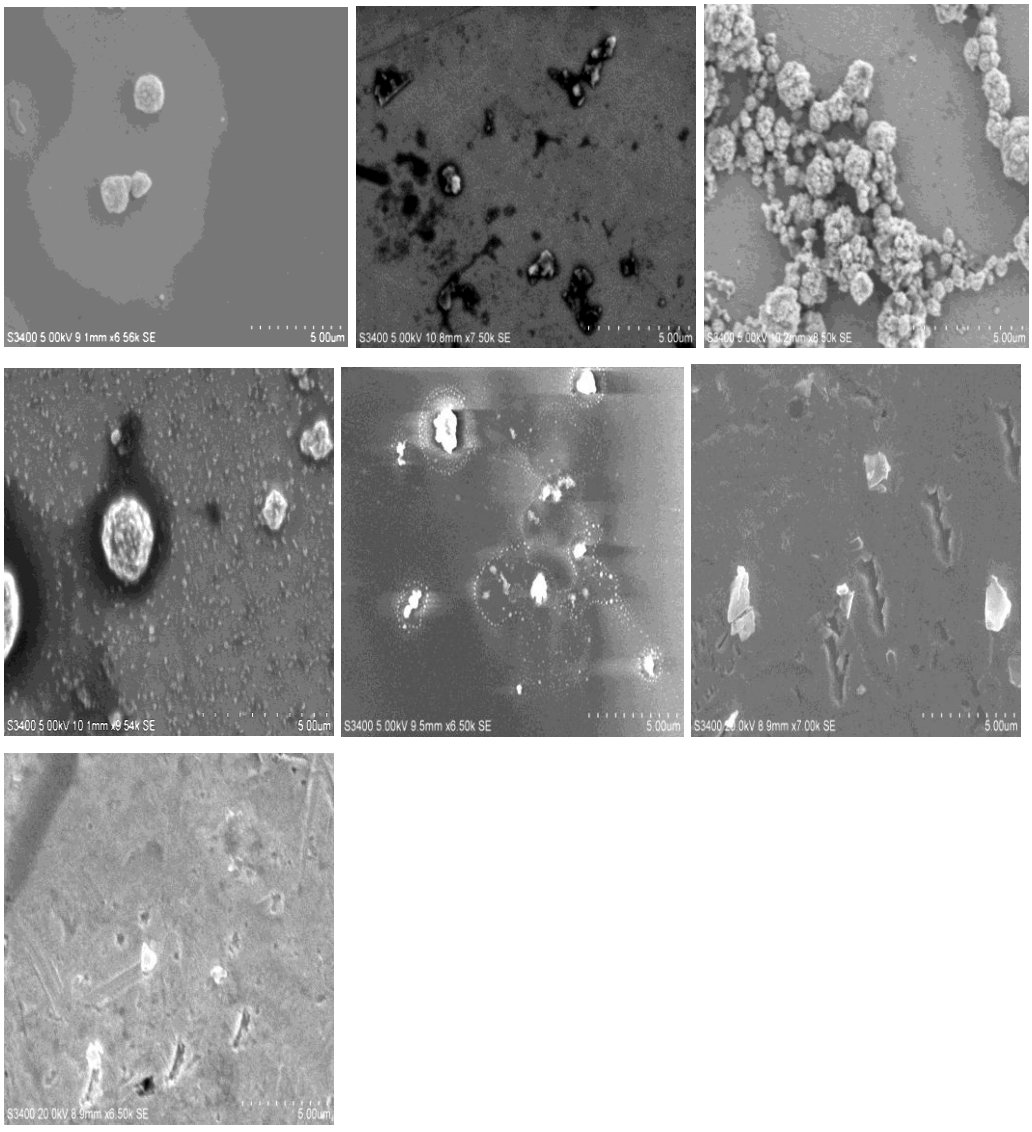

*Platinum had initially been deposited onto **unmodified** gold with a nucleation potential of **-1800 mV** for **20 ms** and a growth potential of **0 mV to -600 mV** for **60 s**.*

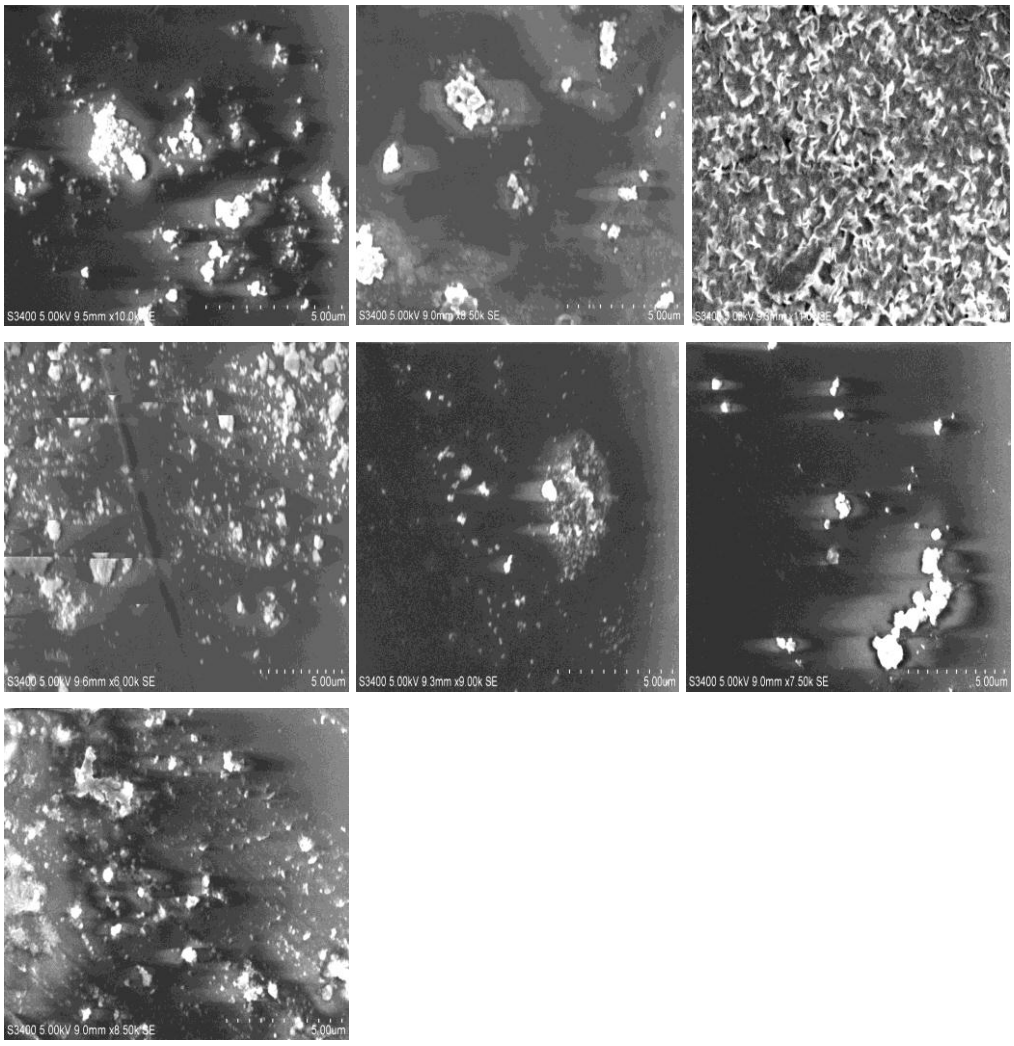

Scanning electron micrograph (SEM) images of a gold electrode after dropcasting the centrifuged desorbed platinum nanoparticles onto the surface.

Platinum had initially been deposited onto a ***self-assembled monolayer modified*** *gold electrode, with a nucleation potential of -1000 mV for 20 ms and a growth potential of* ***0 mV to -600 mV*** *for* ***30 s****.*

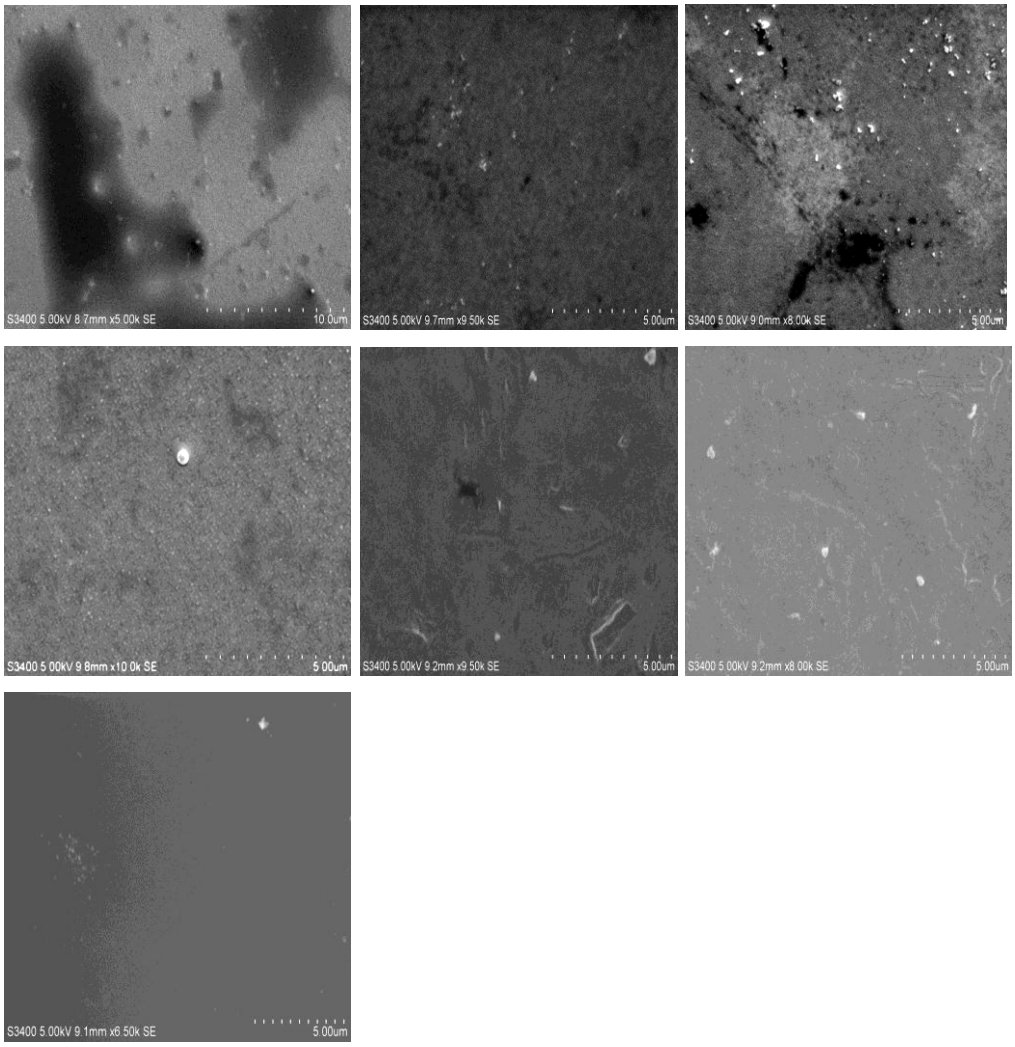

Platinum had initially been deposited onto a ***self-assembled monolayer modified*** *gold electrode, with a nucleation potential of -1200 mV for 20 ms and a growth potential of* ***0 mV to -600 mV*** *for* ***30 s****.*

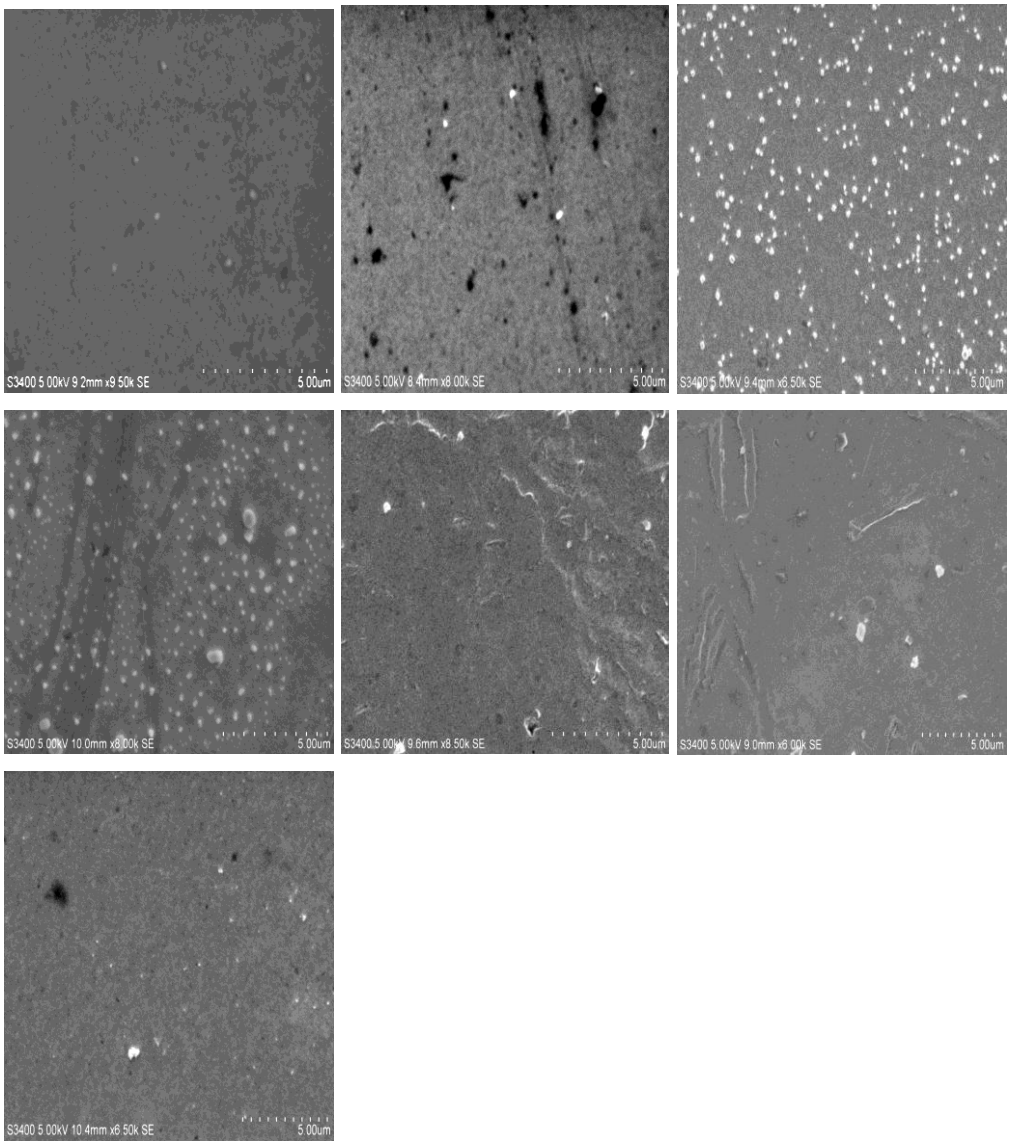

Platinum had initially been deposited onto a ***self-assembled monolayer modified*** *gold electrode, with a nucleation potential of* ***-1400 mV*** *for* ***20 ms*** *and a growth potential of* ***0 mV to -600 mV*** *for* ***30 s****.*

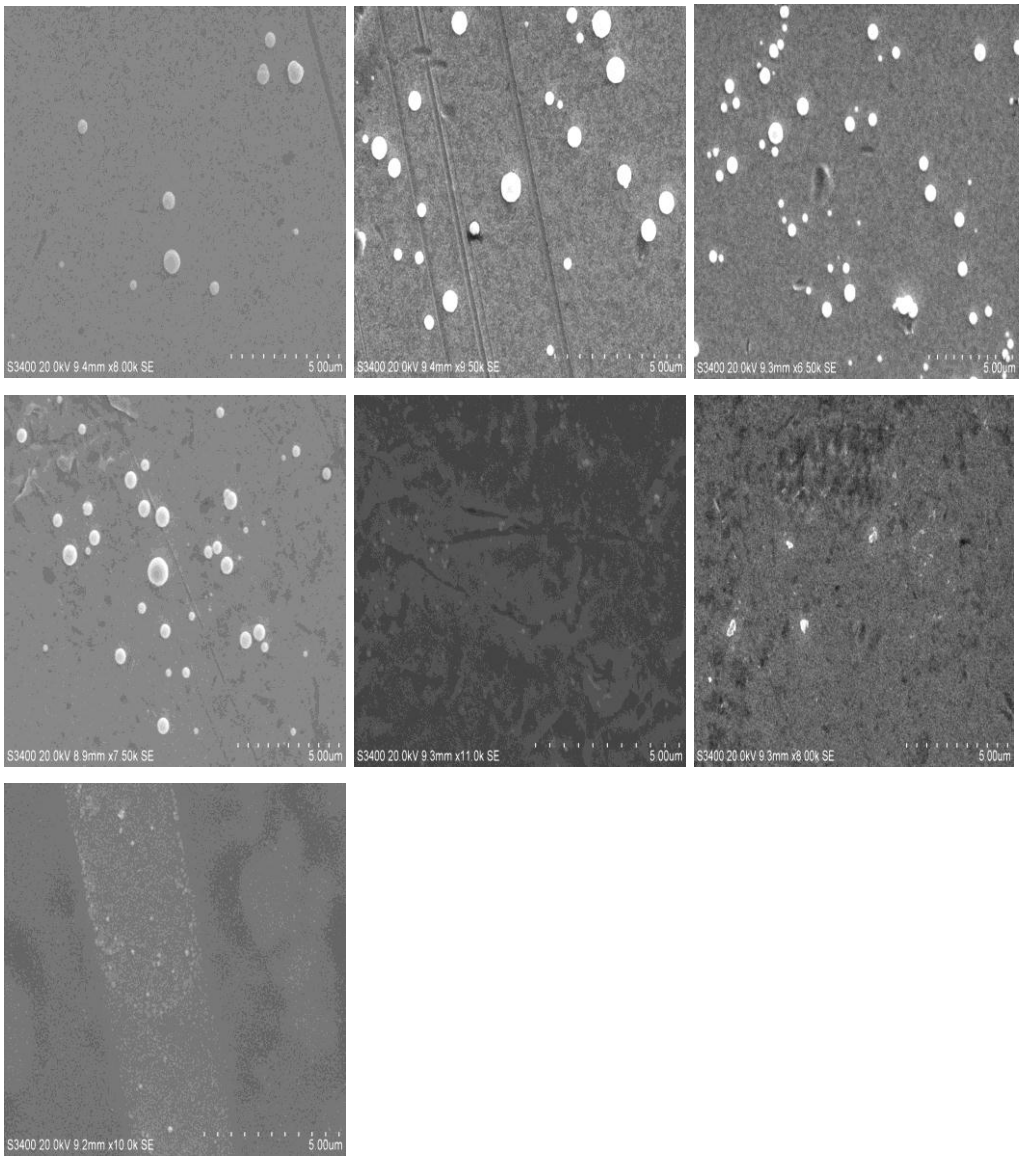

Platinum had initially been deposited onto a ***self-assembled monolayer modified*** *gold electrode, with a nucleation potential of* ***-1600 mV*** *for* ***20 ms*** *and a growth potential of* ***0 mV to -600 mV*** *for* ***30 s****.*

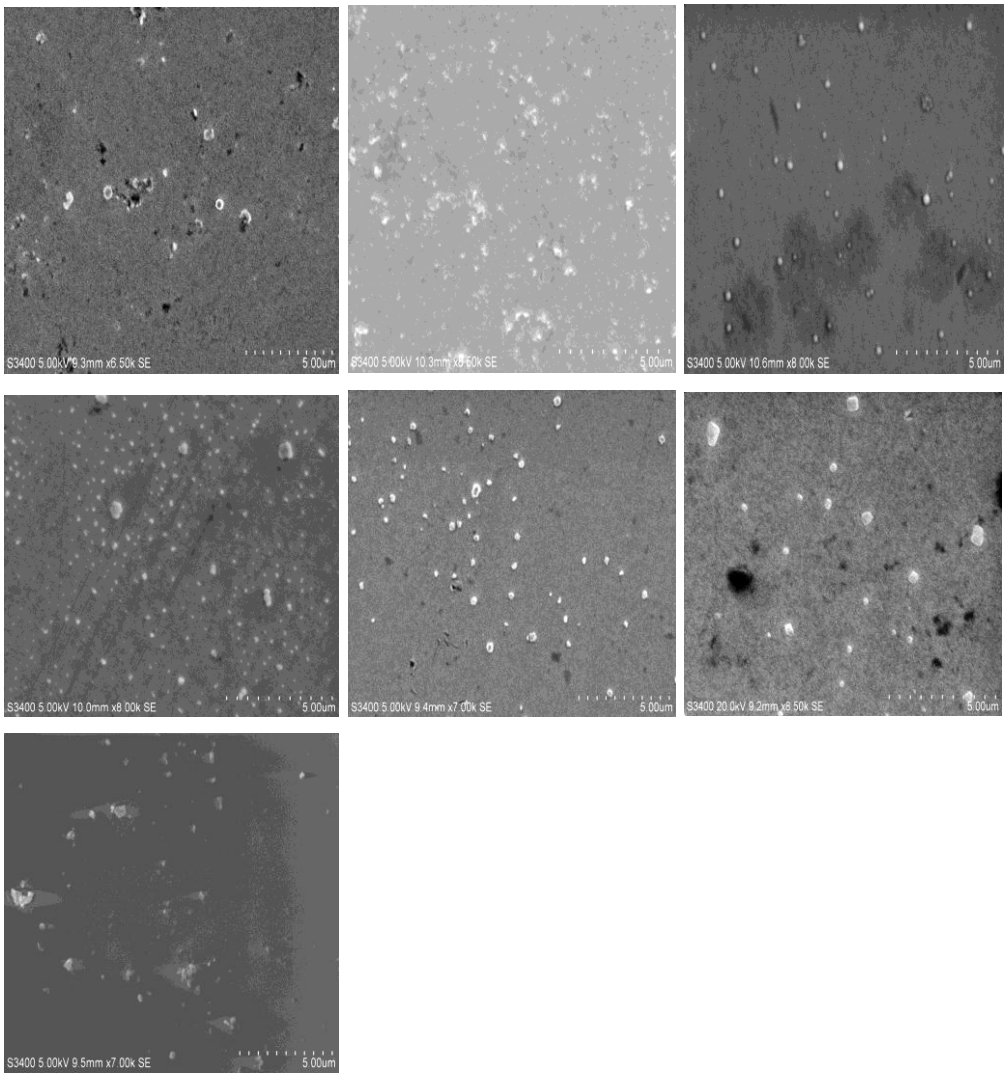

Platinum had initially been deposited onto a ***self-assembled monolayer modified*** *gold electrode, with a nucleation potential of* ***-1800 mV*** *for* ***20 ms*** *and a growth potential of* ***0 mV to -600 mV*** *for* ***30 s****.*

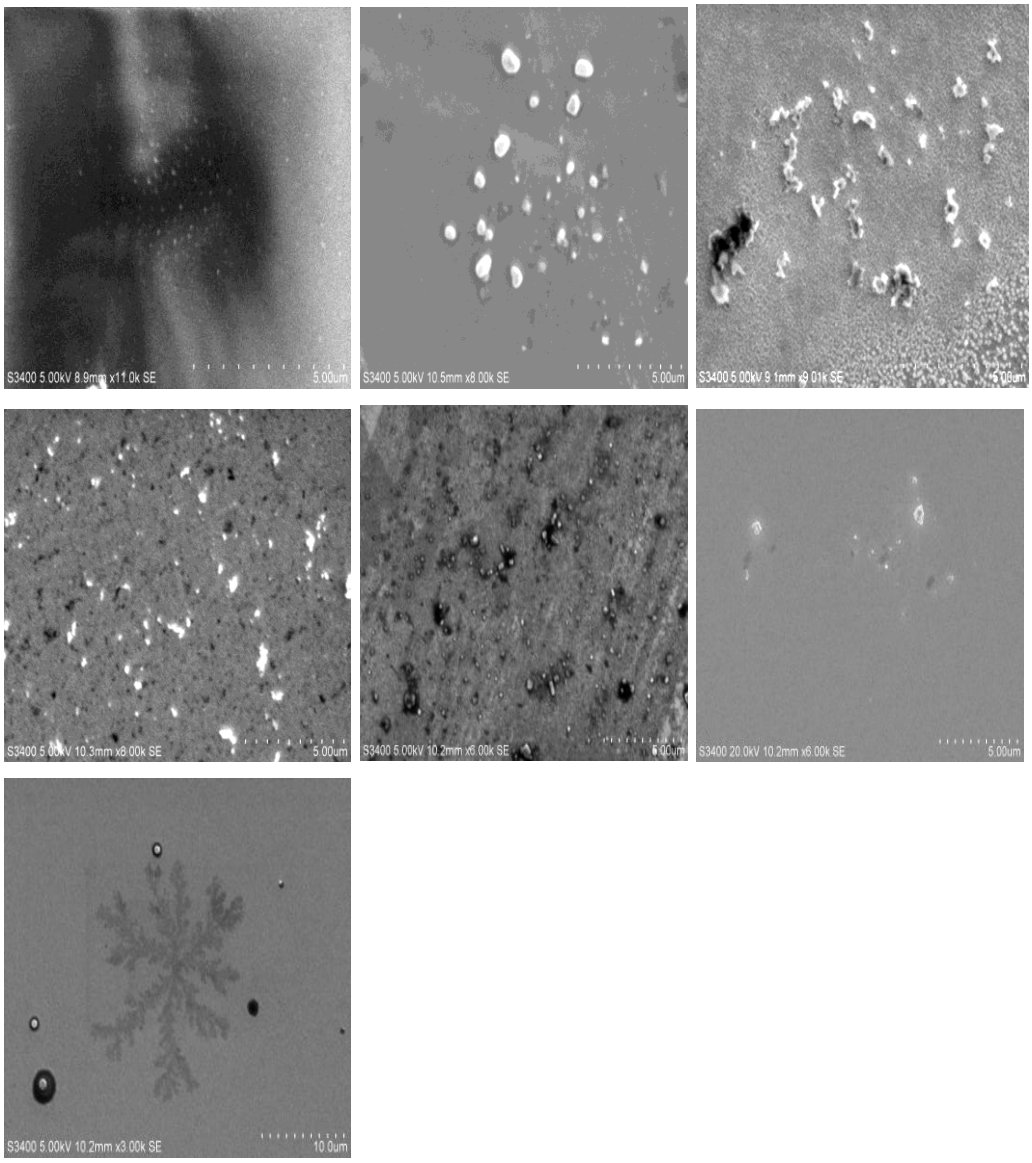

Scanning electron micrograph (SEM) images of a gold electrode after dropcasting the centrifuged desorbed platinum nanoparticles onto the surface.

Platinum had initially been deposited onto self-assembled monolayer modified evaporated gold on glass, with a nucleation potential of -1000 mV for 20 ms and a growth potential of 0 mV to -600 mV for 60 s.

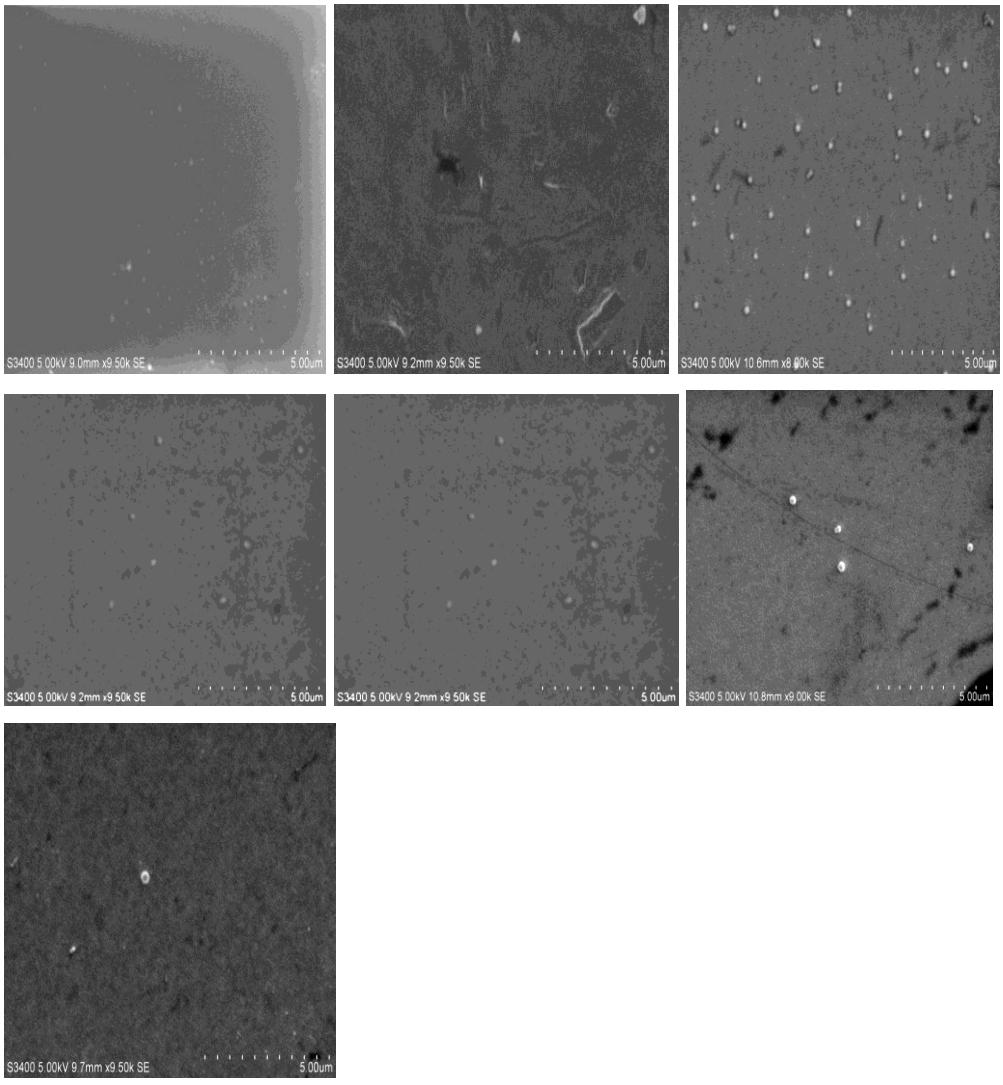

Platinum had initially been deposited onto ***self-assembled monolayer modified*** *evaporated gold on glass, with a nucleation potential of -1200 mV for 20 ms and a growth potential of* ***0 mV to -600 mV*** *for* ***60 s****.*

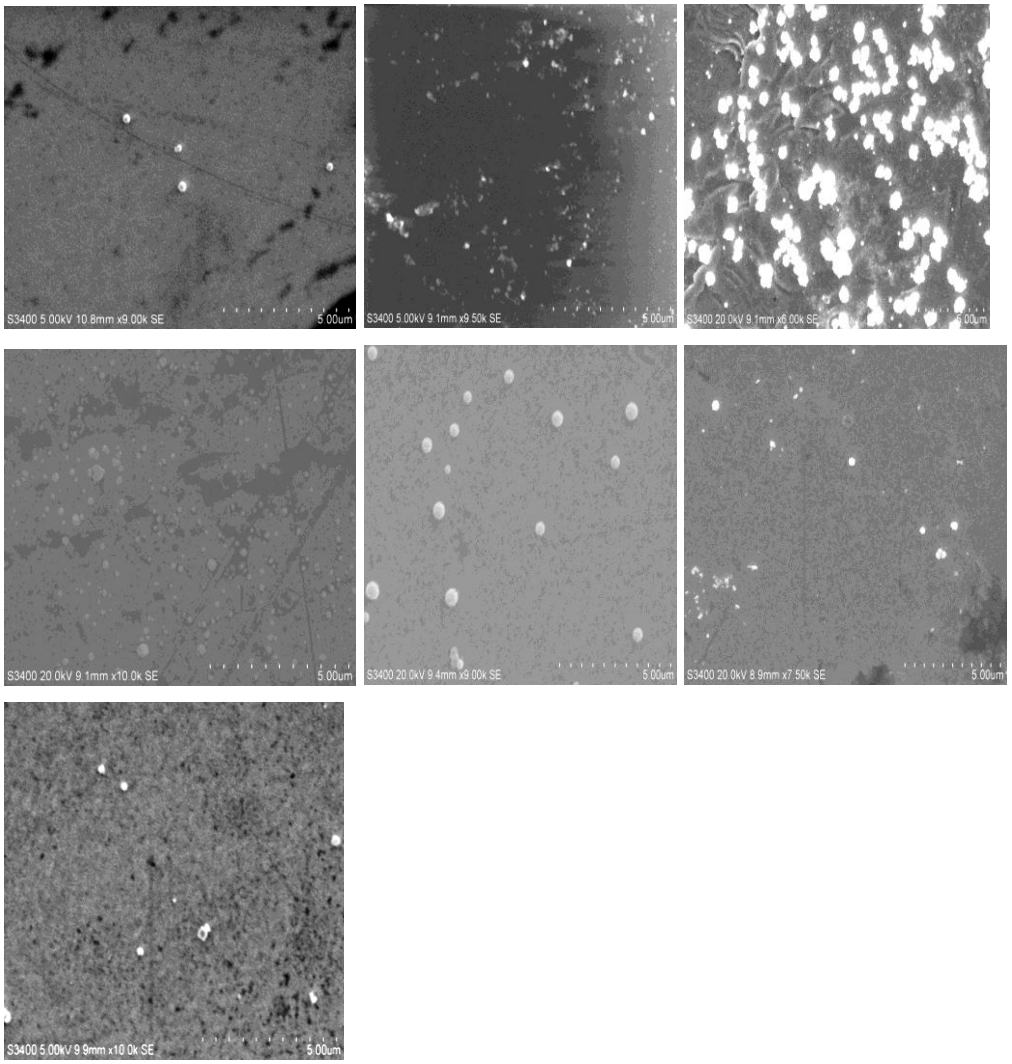

Platinum had initially been deposited onto ***self-assembled monolayer modified*** *evaporated gold on glass, with a nucleation potential of* ***-1400 mV*** *for* ***20 ms*** *and a growth potential of* ***0 mV to -600 mV*** *for* ***60 s****.*

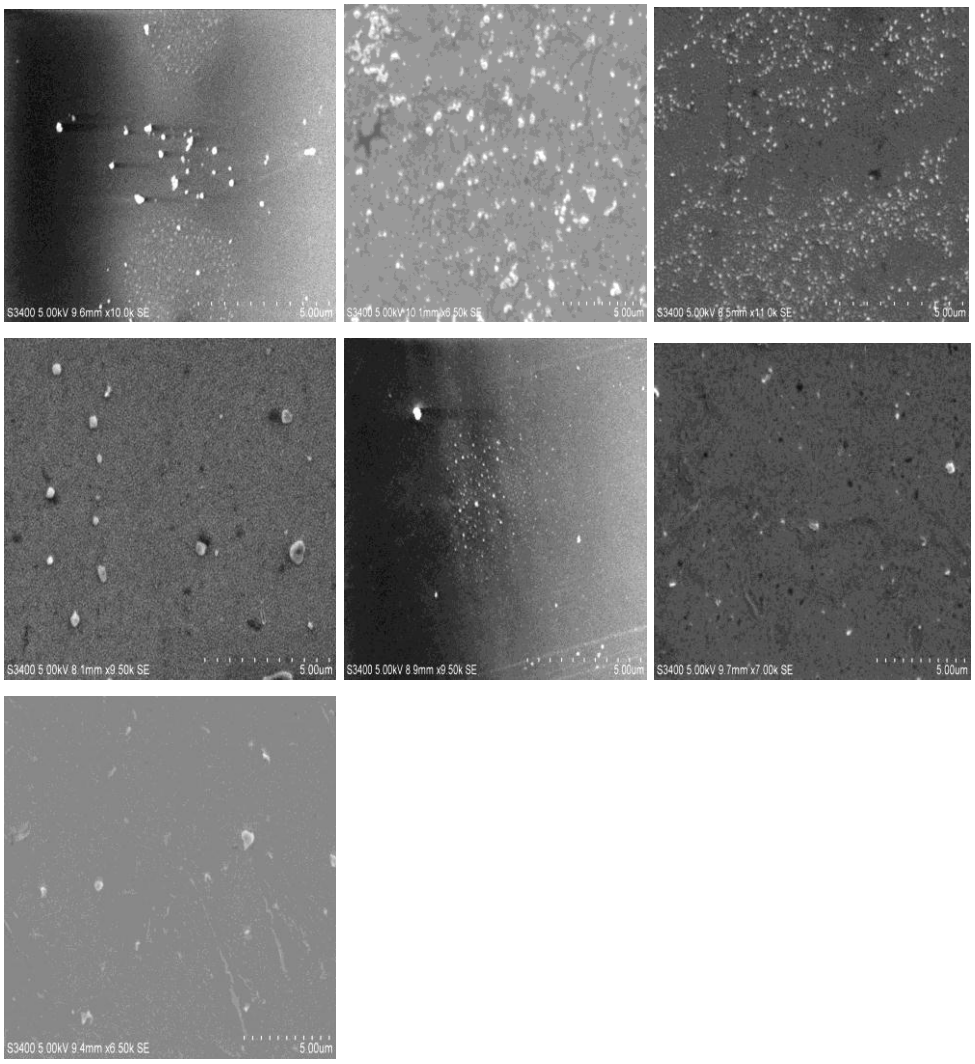

Platinum had initially been deposited onto ***self-assembled monolayer modified*** *evaporated gold on glass, with a nucleation potential of* ***-1600 mV*** *for* ***20 ms*** *and a growth potential of* ***0 mV to -600 mV*** *for* ***60 s****.*

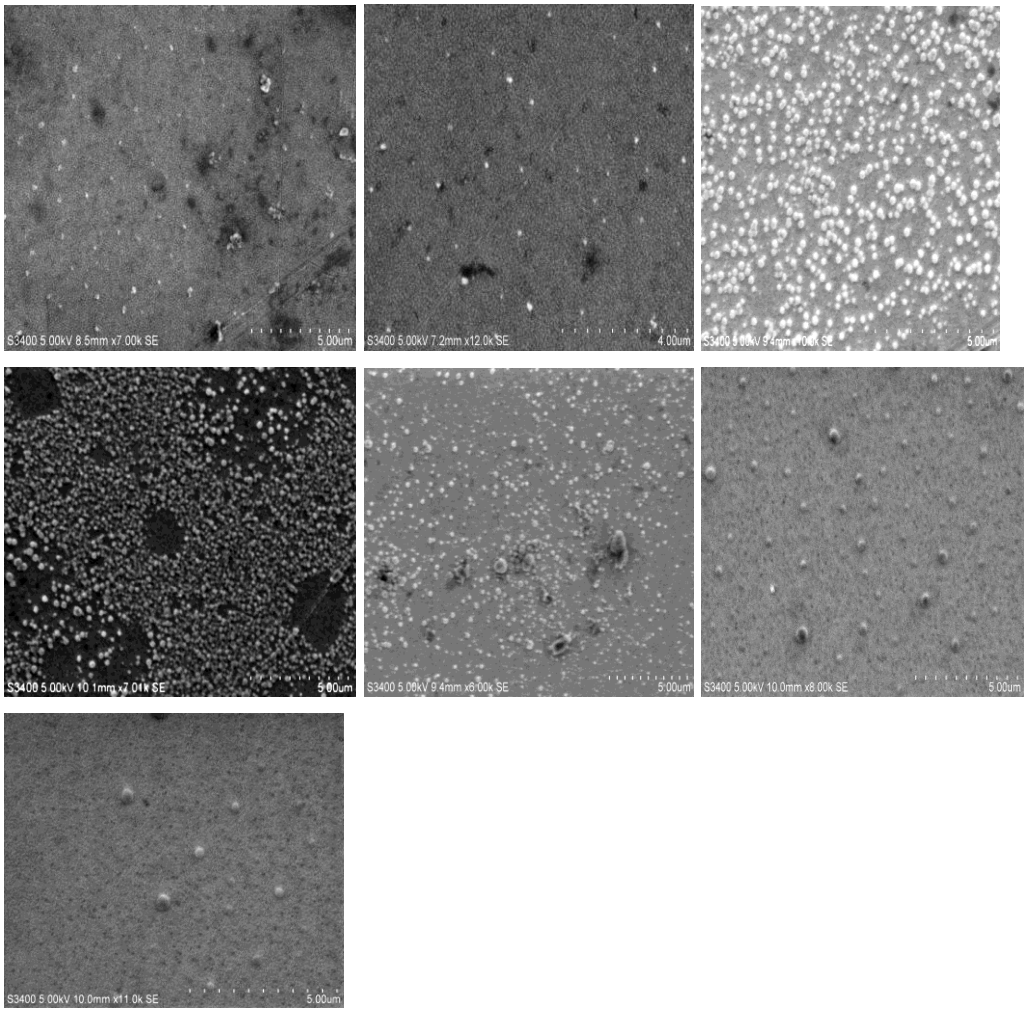

Platinum had initially been deposited onto ***self-assembled monolayer modified*** *evaporated gold on glass, with a nucleation potential of* ***-1800 mV*** *for* ***20 ms*** *and a growth potential of* ***0 mV to -600 mV*** *for* ***60 s****.*

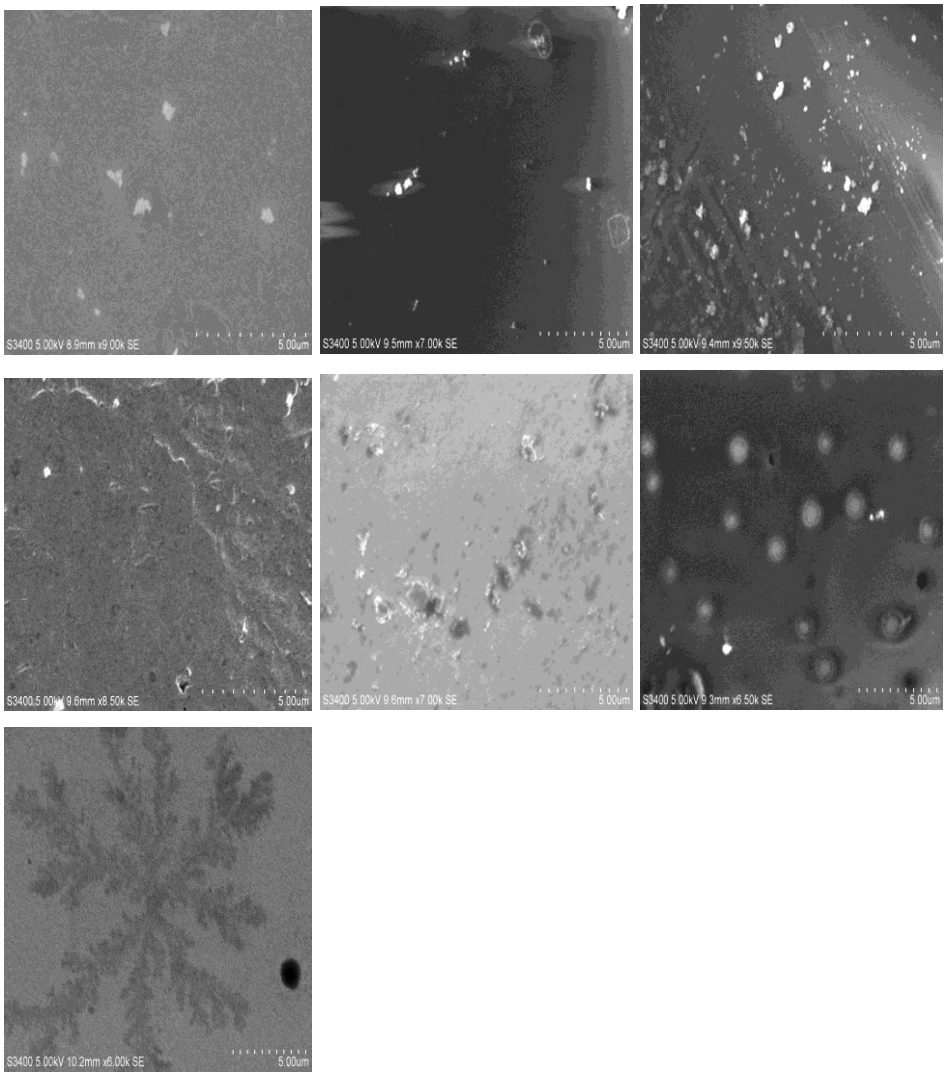

APPENDIX B

analytical chemistry

Article

pubs.acs.org/ac

High Sensitivity DNA Detection Based on Regioselectively Decorated Electrocatalytic Nanoparticles

Elaine Spain, Eoin Brennan, Hazel McArdle, Tia E. Keyes, and Robert J. Forster*

School of Chemical Sciences, National Centre for Sensor Research, Dublin City University, Dublin 9, Ireland

Supporting Information

ABSTRACT: Self-assembled monolayers (SAMs) of dodecanethiol have been formed on gold electrodes to produce nanoscale defects. These defects define nucleation sites for the electrodeposition of mushroom shaped platinum nanoparticles (PtNPs). The top surfaces of these PtNPs have been selectively functionalized with single stranded probe DNA. These regioselectively modified particles were desorbed by applying a current jump to yield nanoparticles capable of biorecognition on the top curved side and efficient electrocatalysis on the nonfunctionalized lower surface. A second electrode was functionalized with single stranded capture DNA that has a sequence that is complementary to the pathogen, *Staphylococcus aureus* but leaves a section of the target available to bind the probe strand immobilized on the PtNPs. Following hybridization of the target and capture strands, the surface was exposed to the probe DNA labeled electrocatalytic PtNPs. Target binding was detected by monitoring the current associated with the reduction of hydrogen peroxide in a solution of 0.01 M H_2SO_4. Calibration plots of the log[DNA] versus faradaic current were linear from 10 pM to 1 μM and picomolar concentrations could be detected without the need for amplification of the target, for example, using PCR or NASBA. As well as a wide dynamic range, this detection strategy has an excellent ability to discriminate DNA mismatches and a high analytical sensitivity.

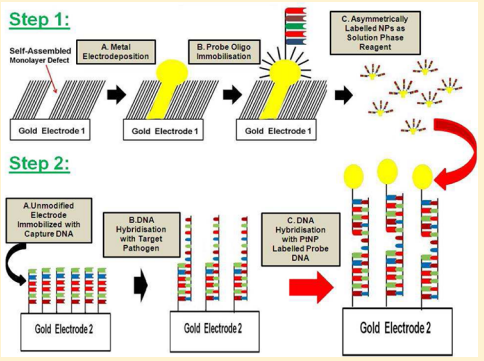

The ability to modify the size and structure of nanomaterials so as to control their properties has led to novel sensors and the enhanced performance of bioanalytical assays.[1−3] Extensive research[4−6] has been carried out on the catalytic properties of platinum nanoparticles (PtNPs) for many reactions including water and peroxide reduction. These reactions are of pivotal importance for fuel cells,[4,7−9] photoelectrochemical cells,[5] metal−air batteries,[10] water electrolysis and chemical sensors.[4] PtNPs have also been applied to medical applications, for example, the oxidation of glucose in blood sugar sensors and the construction of biological fuel cells.[4] Nanoparticles functionalized with nucleic acids represent a powerful approach to creating complex hierarchical nanostructures as well as proving useful for the highly sensitive detection of diseases biomarkers.[11] However, an ongoing challenge in this area is to create nanoparticles that are functionalized such that different binding chemistries, or functions, exist in different regions of the particles. Particles of this kind would allow complex, but well-defined, anisotropic structures to be created. Equally, for sensing applications, the very different demands of molecular recognition (e.g., DNA hybridization), and detection (e.g., electrocatalysis) can be optimized on a single particle. In this contribution, we demonstrate that electrodeposited nanoparticles can be regioselectively functionalized with probe strand DNA and desorbed from the electrode while retaining the functionality of the bound nucleic acid. This principle is demonstrated using the DNA sequence from the specific strain of *Staphylococcus aureus* that causes mastitis (mammary gland inflammation). Significantly, beyond the ability to create regioselective functionalized platinum nanoparticles, we demonstrate that these particles are capable of detecting DNA with high sensitivity and selectivity. This result is important since, due to the low concentrations of pathogen present before clinical symptoms become apparent, the target DNA must typically be amplified, for example, using PCR or NASBA. However, molecular amplification is costly, time-consuming, and labor intensive. Direct detection methodologies, for example, involving amplified electrochemical detection, avoid the need for target amplification.

As illustrated in Scheme 1, the approach is based on electrodepositing platinum nanoparticles using defects within a dodecanethiol monolayer as templates. The top surface of these PtNPs is functionalized with thiol terminated probe strand DNA. Then, a current step is applied to melt the nanowire connecting the hemispherical nanoparticle to the electrode causing rapid desorption of the DNA functionalized PtNPs. These DNA labeled electrocatalytic particles are then used in a hybridization assay to determine the concentration of the target by measuring the faradaic current associated with reduction of peroxide in solution. This approach can easily be extended to reduction of water, which, in the case of biological samples, can come from the sample itself.

Received: February 16, 2012
Accepted: June 11, 2012
Published: June 11, 2012

   dx.doi.org/10.1021/ac300458x | *Anal. Chem.* 2012, 84, 6471−6476

Scheme 1. Platinum Nanoparticle Formation and Regioselective DNA Functionalisation

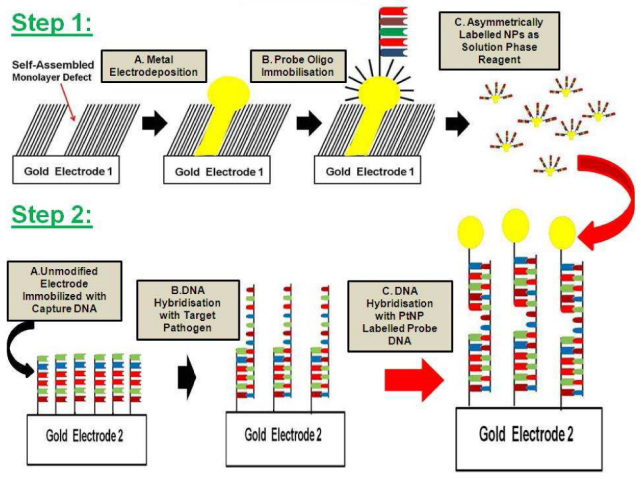

EXPERIMENTAL SECTION

Materials. Dodecanethiol was obtained from Sigma Aldrich. The buffer, denoted as 1 M NaCl-TE, contained 1.0 M NaCl, 10 mM Tris-HCl, and 1 mM ethylenediaminetetraacetic acid (adjusted to pH 7.0 by adding 1.0 M NaOH) and was used for DNA hybridization. Platinum nanoparticles (diameter 50−70 nm) for uniform functionalization with probe strand DNA were purchased from Particular GmbH. All aqueous solutions were prepared using Milli-Q water. The oligonucleotides were purchased from Eurogenec and their purity was >98%. The base sequences were as follows.

Capture: 5′- CGG-CAG-TCT-TTA-TCA-3′-SH

Target: 5′-TGA-TAA-ACA-CTG-CCG-TTT-GAA-GTC-TGT-TTA-GAA-GAA-ACT-TA-3′

Probe: SH-5′-AT-AGT-TTC-TTC-TAA-ACA-GAC-3′

1 Base Mismatch:5′-TGC-TAA-ACA-CTG-CCG-TTT-GAA-GTC-TGT-TTA-AAA-GAA-ACT-TA-3′

3 Base Mismatch:5′-TGC-TAA-ACA-CTG-CCG-CTT-GAA-GTC-TGT-TTA-GAT-GAA- ATA-TA-3′

Instrumentation. A three-electrode electrochemical cell was used at a temperature of 22 ± 2 °C. The working electrode was a 2 mm radius planar gold disc. It was polished with a nylon cloth with 1 μm diamond polish and thoroughly rinsed with Milli-Q water and ethanol before sonication in Milli-Q water for 5 min. Voltammetry in acid was used to determine the surface roughness factor by scanning the electrode between +1.500 and −0.300 V. The counter electrode was a large area coiled platinum wire and a silver/silver chloride (Ag/AgCl in 3 M KCl) acted as reference.

Monolayer Self-Assembly. The gold electrodes were cleaned by placing them in piranha solution (3:1 mixture of sulfuric acid and 30% hydrogen peroxide (*Caution, this mixture reacts violently with organic material!)* for 20 min, followed by thorough rinsing with ultra pure water. The electrode was then scanned between +1.500 and −0.300 V in 0.01 M H_2SO_4 to measure the surface roughness of the gold electrode and to ensure that the electrode is electrochemically clean. Afterward, the gold disc electrode was washed with ethanol and then placed in a 1 mM solution of dodecanethiol in ethanol and monolayer self-assembly was allowed to proceed for 7 h. After the formation of the monolayer, the substrate was rinsed 4 to 5 times with ethanol and dried under a N_2 stream.

DNA Probe Immobilization and Hybridization. *STEP 1: Fabrication of Regioselectively DNA Functionalized Platinum Nanoparticles.* Platinum nanoparticles, PtNPs, were electrodeposited from 1 mM hydrogen hexachlorideplatinate (IV) hydrate (H_2PtCl_6) in 0.5 M H_2SO_4 using the defects within the self-assembled monolayer as templates. Subsequently, in Step 1B, the PtNPs were functionalized with probe oligo (5′ thiolate) by immersing the nanoparticle functionalized electrode in a 10 μM solution of the probe DNA strand dissolved in 1 M NaCl-TE Buffer for 2 h. The modified electrodes were then washed with deionized water for 15 s to remove loosely bound oligo and immersed in 0.01 M H_2SO_4. The oligo functionalized platinum nanoparticles were then desorbed by applying a current of +0.01 A (reductive) for 120 s.

Step 2A: Monolayer of Capture Strand DNA. A monolayer of capture strand DNA was prepared on a freshly polished and electrochemically cleaned gold disc electrode by immersing it in a 10 μM solution of the capture strand DNA dissolved in 1 M NaCl-TE Buffer. After 5 h, the electrode was rinsed with deionized water for 15 s to remove loosely bound oligo.

Step 2B: Hybridization of Target Oligo to the Capture Surface. Hybridization of the target at concentrations between 10 pM and 1 μM to the immobilized capture strand was performed at 37 °C in 1 M NaCl-TE Buffer for 90 min. Following hybridization, the modified electrode was rinsed thoroughly with buffer.

Step 2C: Probe Hybridization. The nanoparticle labeled probe DNA was then hybridized to the complementary section of the target not used for binding to the capture strand for 2 h at 37 °C in 1 M NaCl-TE Buffer. Finally, before quantitation, it was thoroughly washed with deionized water.

Electrochemical Detection of *S. aureus* ss-DNA Target. Following assembly of the capture-target-nanoparticle labeled probe DNA sequence, the modified electrode was placed in an aqueous solution of 0.01 M H_2SO_4 and the current measured at −0.250 V after equilibration for 10 min. Then, sufficient hydrogen peroxide was added to give a final concentration of 200 μM and the reduction current associated with peroxide reduction at the bound PtNPs was measured at −0.250 V after 10 min. The analytical response was taken as the difference in current, Δi, measured before and after peroxide addition.

RESULTS AND DISCUSSION

Self-assembled monolayers of alkane thiols on gold provides one of the most elegant approaches to creating well-defined and organized surfaces for biosensor development.[12−16] Panels A and B of Figure 1 illustrate cyclic voltammograms for the 2 mm radius gold electrodes before and after deposition of the defective monolayer, respectively. STM reveals that a deposition time of 7 h produces an array of well separated defects that could be used as templates for nanoparticle deposition. The active surface area can be determined using voltammetry in 0.01 M H_2SO_4 as the supporting electrolyte by creating and subsequently reducing a gold oxide monolayer on the unmodified fraction of the electrode. By comparing the charge passed before and after monolayer deposition, the area available for PtNP electrodeposition can be determined. The area under the gold oxide peak reduction peak centered at approximately +0.8 V reveals that the electrode area decreased by approximately 50% following monolayer deposition for 7 h, that is, there are a substantial number of sites for metal deposition at the partially blocked surface Deposition of the

dx.doi.org/10.1021/ac300458x | *Anal. Chem.* 2012, 84, 6471−6476

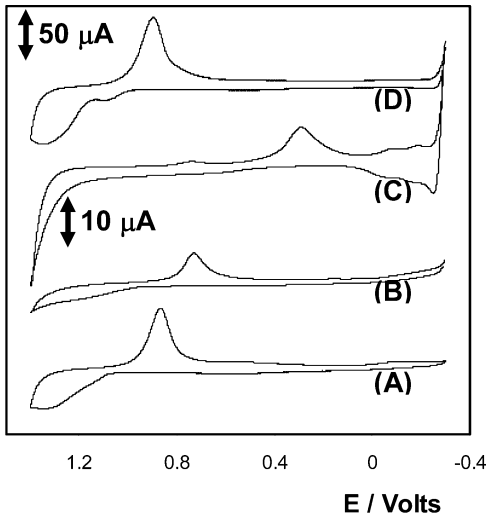

Figure 1. Cyclic voltammograms of (A) 2 mm unmodified gold electrode, (B) after deposition of a defective C_{12} monolayer, (C) following electrodeposition of platinum nanoparticles into the monolayer defects (D) after the platinum nanoparticles have been desorbed. The scale bar for panels A and B is 10 μA, while for panels C and D, it is 50 μA. In all cases, the supporting electrolyte is 0.01 M H_2SO_4 and the scan rate is 100 mV s^{-1}. The voltammograms have been displaced vertically for clarity of presentation.

thiol SAMs decreases the gold area from the value of 0.030 cm^2 found for the unmodified electrode (roughness factor of 1.09) to 0.018 cm^2. In addition to the decrease of the gold oxide peak, a potential shift in the negative potential direction by approximately 200 mV of both the gold oxide formation, and subsequent stripping, is observed. This observation indicates that deposition of the defective alkane thiol monolayer makes it thermodynamically more facile to deposit and remove gold oxide within the monolayer defects. This behavior is not typically observed for defect free monolayers[17] where mass transport to the gold surface is blocked and gold oxide/hydroxide formation is observed only after partial desorption of the monolayer occurs. The shift in a negative potential direction suggests that monolayer formation increases the electron density of the gold atoms within the defect.

Platinum nanoparticles were deposited into the defects within the monolayer from a 0.5 M sulfuric acid solution containing 1 mM hydrogen hexachlorideplatinate (IV) hydrate (H_2PtCl_6) at applied potentials ranging from +0.2 to −0.35 V for 180 s. As the applied potential became more negative, the specific active area of the platinum oxide peak increased. Concurrently, the gold oxide peak diminished as the PtNPs were electrochemically deposited. However, as the applied potential became more negative than −0.25 V, a decrease in specific active area as well as the catalytic activity was observed due to the formation of gas bubbles. Figure 1C illustrates the cyclic voltammogram following nanoparticle deposition at an applied potential of −0.250 V for 180 s. In the forward scan, the onset potential for the formation of gold oxide is 1.3 V. In the reverse scan, the reduction of gold oxide occurs at 0.8 V. After the electrodeposition of Pt, the peak associated with gold oxide formation and reduction disappears. The reduction of platinum oxide to metallic platinum is observed at around 0.3 V and the peak at approximately −0.25 V is attributed to hydrogen adsorption/desorption from the platinum nanoparticle surface.[6,18] Significantly, the microscopic area following deposition of the platinum nanoparticles is 0.232 cm^2, that is. nanoparticle deposition increases the area available for DNA deposition by a factor of approximately seven when compared to dodecanethiol templated electrode; that is, the PtNPs are definitely mushroom shaped. Following binding of the probe oligo, a short current pulse at a current density of approximately +100 mA cm^{-2} was applied to the nanoparticle modified electrode with the objective of melting the nanowire connecting the hemispherical nanoparticle to the electrode. These rather aggressive conditions were used to rapidly desorb the nanoparticles, which, once in solution, diffuse away from the electrode surface thus minimizing the opportunity for damage to the bound DNA. Figure 1D illustrates the apparent decrease in peak height in both the reduction and oxidation process for the platinum oxide peaks after desorption of the PtNPs. Significantly, the gold oxide peak is substantially larger than that found for the bare electrode suggesting that the current step removes not only the platinum nanoparticles, but also the templating alkane thiol monolayer and probably induces additional surface roughening. The interfacial capacitance can also provide a significant insight into nanoparticle formation. Formation of the templating monolayer decreases the interfacial capacitance by a factor of approximately 15 which increases to twice its initial value following platinum nanoparticle deposition. This behavior is consistent with the formation of a low dielectric constant monolayer and a subsequent increase in the electrochemically active electrode area following nanoparticle electrodeposition.

Scanning Electron Microscopy. Figure 2A shows a scanning electron microscope (SEM) image of the gold electrode following deposition of the defective alkane thiol template for 7 h and electrodeposition of the platinum nanoparticles using a deposition time of 30 s. The image reveals a relatively high surface coverage of nanoparticles with a radius of 80 ± 40 nm. Figure 2B shows an image for a gold substrate onto which a droplet of the suspended nanoparticles has been drop cast and allowed to dry. This image reveals that desorption does not change the average particle size significantly and a relatively high concentration of nanoparticles in the suspension can be achieved. Taking the nanoparticle radius of 80 nm in conjunction and the fact that the top hemispherical surface area, as obtained from voltammetry in acidic solution, is seven times larger than the underlying defect, the average defect diameter is estimated to be approximately 40 nm. This particle shape will result in approximately two-thirds of the total nanoparticle surface (hemisphere) being modified by probe strand DNA with at least one-third (disc) being unmodified and available for efficient electrocatalysis. Roughening of the unmodified surface during nanoparticle desorption

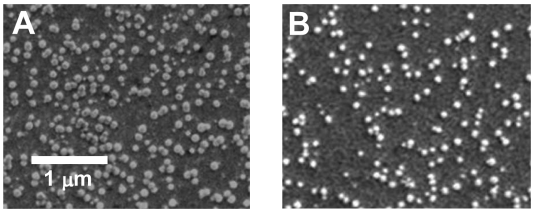

Figure 2. (A) SEM images of a gold electrode following deposition of the templating monolayer and electrodeposition of platinum nanoparticles for 30 s. (B) Drop cast film of desorbed nanoparticles from suspension. The acceleration voltage is 20 kV.

dx.doi.org/10.1021/ac300458x | Anal. Chem. 2012, 84, 6471−6476

is likely to increase the fractional surface area available for electrocatalysis. Surface diffusion of the thiolated probe strand DNA on the platinum nanoparticles, perhaps enabled by free surface area due to partial DNA stripping during nanoparticle desorption, may cause the modified and unmodified regions to become less well-defined over time. However, due to the slow rates of surface diffusion of thiols on metals,[19−21] this scrambling is likely to be significant only at long times, but may have implications for long-term storage of the regioselectively modified nanoparticles.

Binding of Regioselectively Decorated Nanoparticles. The electrodeposited PtNPs, functionalized only on their upper surface with capture oligos, were desorbed into aqueous solution using the current jump technique. It is essential to determine the electrocatalytic activity and DNA binding ability of these desorbed particles. As illustrated in Scheme 1, an electrode, modified with a DNA capture strand was first allowed to hybridize with the target strand, part of which is complementary to the capture strand. This electrode was then placed into the NP suspension for 90 min during which time the nonhybridized section of the target hybridizes with the oligo bound to the metal nanoparticle providing the DNA has not removed by the nanoparticle desorption process. Figure 3A

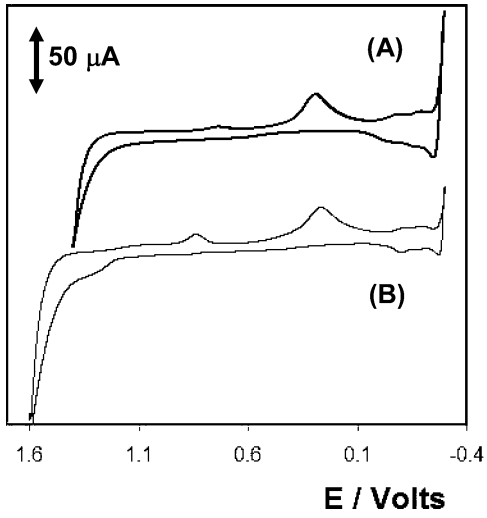

Figure 3. (A) Cyclic voltammogram of a 2 mm radius gold disc electrode after electrodeposition of the platinum nanoparticles and functionalization with probe DNA (image 3 of Scheme 1). (B) Cyclic voltammogram of a 2 mm radius gold disc electrode after modification with capture strand DNA and hybridization with the target and nanoparticle labeled probe sequence where the target strand concentration is 10 μM. The supporting electrolyte is 0.01 M H_2SO_4 and the scan rate is 100 mV s^{-1}.

illustrates the voltammogram obtained for an electrode in 0.01 M H_2SO_4 after electrodeposition of the platinum nanoparticles and functionalization with probe strand DNA. Figure 3B shows the response obtained for a pristine gold electrode modified with capture strand DNA after both the target and nanoparticle functionalized probe strand hybridization steps have occurred. Both of these figures show well-defined peaks at approximately +0.25 and −0.07/−0.20 V associated with the reduction of platinum oxide and hydrogen adsorption/desorption, respectively. These observations indicate successful binding of the nanoparticles suggesting that the DNA functionalized platinum nanoparticles can be put into suspension using the current jump approach. Significantly, control experiments in which platinum nanoparticles functionalized with probe strand DNA are exposed to freshly polished gold electrodes do not exhibit any measurable peaks associated with platinum oxide formation or reduction (Supporting Information). This result suggests that nonspecific binding of the platinum nanoparticles is not a significant issue and the probe labeled PtNPs will not bind significantly in the absence of a capture strand monolayer. Similarly, control experiments in which the target is not added or where the nanoparticles are either not functionalized with DNA, or are functionalized with entirely noncDNA, do not exhibit features associated with platinum oxide or hydrogen adsorption.

Electrochemical Detection of *S. aureus* DNA. Platinum nanoparticles are well-known to catalyze the reduction of hydrogen peroxide. As described in the Experimental Section, the probe-labeled PtNPs were hybridized with the section of the target sequence not used to hybridize to the capture strand immobilized on the electrode. Here, the catalytic activity of the platinum nanoparticles bound through DNA hybridization (Step 2-C in Scheme) was assessed by monitoring the difference in current associated with the reduction of hydrogen peroxide in a solution of 0.01 M H_2SO_4 before and after peroxide addition. Figure 4 shows the semi-log concentration versus Δi calibration curves. In each case, an acceptably linear response is observed for concentrations of sequence-specific DNA from *S. aureus* from 10 pM to 1 μM. The sensitivity of the bare electrode is 7.0 × 10^{-5} μA, reflecting the poor

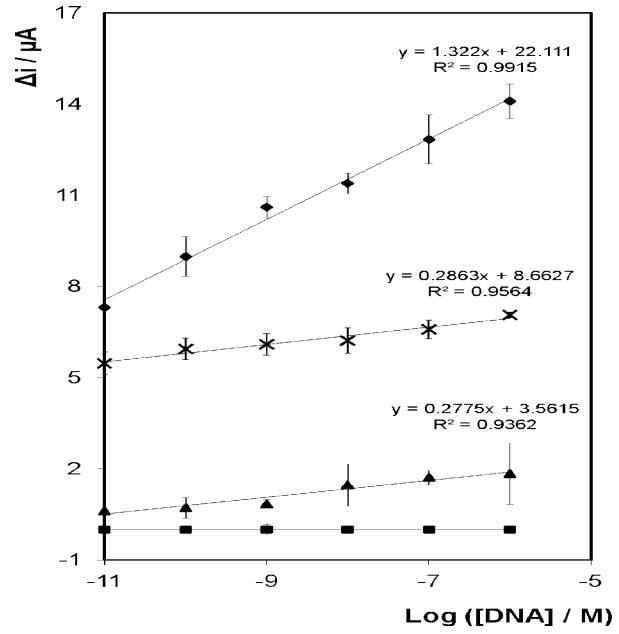

Figure 4. Calibration curves for the electrochemical detection of *S. aureus* mastitis DNA on a 2 mm diameter bare electrode following hybridization with probe DNA that is labeled with PtNPs (♦) and where the probe is unlabeled (■). The response of the electrode used to create the PtNPs after the nanoparticles have been desorbed is also shown (▲). A control experiment showing the dependence of Δi on the target strand DNA concentration using PtNPs that are uniformly functionalized with probe strand DNA (X). In all cases, the solution contains 200 μM H_2O_2 in aqueous 0.01 M H_2SO_4. Δi represents the difference in current before and after addition of the H_2O_2 at an applied potential of −0.250 V. Where error bars are not visible, they are smaller than, or comparable to, the size of the symbols.

dx.doi.org/10.1021/ac300458x | *Anal. Chem.* 2012, 84, 6471−6476

electrocatalytic properties of the DNA modified gold electrode. These low currents in the absence of PtNP labels indicate that the background current associated with direct reduction of hydrogen peroxide at the underlying electrode is low. This result is significant since the magnitude of this background current will directly influence the limit of detection. In sharp contrast, the sensitivity of the assay involving platinum nanoparticle labeled probe strands is approximately 20 000 times larger, 1.3 μA, than that found in the label free assay. This dramatically higher sensitivity and wide linear dynamic range indicates that the desorbed nanoparticles retain both their electrocatalytic and DNA binding capabilities. Also, the high current density observed suggests that heterogeneous electron transfer from the platinum nanoparticles, through the DNA linker, to the underlying electrode is relatively facile. The electrocatalytic current is also likely to be enhanced by efficient radial mass transfer of H_2O_2 to the metal nanoparticles. Figure 4 also shows the response when the DNA hybridization assay is performed using the electrode on which the regioselectively modified platinum nanoparticles were deposited and subsequently desorbed. If the PtNPs were completely removed using the current jump approach, then the behavior of this electrode ought to be indistinguishable from that observed for the bare electrode. The observation that the sensitivity is only approximately 5-fold lower than the assay based on PtNP labeled probe DNA indicates that a significant population of the nanoparticles are not desorbed by the current jump technique, that is, we anticipate further increases in the yield of the regioselectively functionalized nanoparticles by refining the desorption approach. Figure 4 also shows the dependence of Δi on the concentration of target strand DNA where the electrocatalytic platinum nanoparticles are uniformly functionalized with probe strand DNA. The electrocatalytic current observed at these homogeneously decorated nanoparticles is significantly lower than that found for the regioselectively decorated nanoparticles. Moreover, while the response is acceptably linear for target DNA concentrations from 10 pM to 1 μM, the sensitivity of the uniformly functionalized PtNP is almost 5-fold lower (0.29 μA) compared to the regioselectively functionalized particles (1.32 μA). The lower electrocatalytic currents and analytical sensitivity observed suggests that while the DNA layer is sufficiently porous to allow hydrogen peroxide access to the surface of the platinum nanoparticle, electrocatalysis is relatively less efficient. Thus, the physical separation of the molecular recognition and signal generation sites on each nanoparticle improves the overall analytical performance.

The selectivity of the sensor was also investigated using a target DNA sequence that contained a single mismatch. Significantly, the Δi observed for this one base mismatch DNA sequence was a factor of 4 smaller than that found for the fully complementary sequence suggesting a high discrimination ability. Moreover, *Staphylococcus epidermis*, which has 3 base mismatches, gives no measurable current response demonstrating the system is robust with respect to false positives. This result is particularly important since *S. epidermis* can often be mistaken for *S. aureus* and its presence incorrectly associated with mastitis. It also further confirms that the bound DNA has not been denatured as the particles are desorbed off the electrode surface.

CONCLUSIONS

Robust, low cost detection of low concentrations of infectious species and genetic mutation demands the development of novel high sensitivity detection strategies which can lead to a reliable diagnosis before any clinical symptoms of a disease appear. In addition, the development and expansion of novel therapeutics based on the regulation of gene expression can provide innovative new opportunities in the area of pharmaceutical science. Here, we demonstrate an approach that allows platinum nanoparticles to be regioselectively functionalized (upper surface only) with DNA while the remainder of the particles surface is unmodified allowing efficient electrocatalysis to occur. Significantly, the DNA remains bound and functional following desorption and the nanoparticles can selectively detect target strand DNA at picomolar concentrations. The assay is characterized by a wide dynamic range, high sensitivity, a low detection limit, and an excellent ability to discriminate against interferences.

ASSOCIATED CONTENT

Supporting Information

Additional information as noted in text. This material is available free of charge via the Internet at http://pubs.acs.org.

AUTHOR INFORMATION

Corresponding Author

*E -mail: Robert.Forster@dcu.ie.

Notes

The authors declare no competing financial interest.

ACKNOWLEDGMENTS

This material is based upon works supported by the Science Foundation Ireland under Grant No. 10/IN.1/B3021.

REFERENCES

(1) Burda, C.; Chen, X.; Narayanan, R.; El-Sayed, M. *Chem. Rev.* **2005**, *105*, 1025−1102.
(2) Tao, A. R.; Habas, S.; Yang, P. *Small* **2008**, *4*, 310−325.
(3) Tang, Z. Y.; Kotov, N. A. *Adv. Mater.* **2005**, *17*, 951−962.
(4) Kloke, A.; von Stetten, F.; Zengerle, R.; Kerzenmacher, S. *Adv. Mater.* **2011**, *23*, 4976−5008.
(5) Cho, S. J.; Ouyang, J. *J. Phys. Chem. C* **2011**, *115*, 8519−8526.
(6) El Roustom, B.; Sine, G.; Foti, G.; Comninellis, C. *J. Appl. Electrochem.* **2007**, *37*, 1227−1236.
(7) Steele, B. C. H.; Heinzel, A. *Nature* **2001**, *414*, 345−352.
(8) Zhang, X.; Lu, W.; Da, J.; Wang, H.; Zhao, D.; Webley, P. A. *Chem. Commun.* **2009**, 195−197.
(9) Luo, J.; Wang, L.; Mott, D.; Njoki, P. N.; Lin, Y.; He, T.; Xu, Z.; Wanjana, B. N.; Lim, I.-S.; Zhong, C. *Adv. Mater.* **2008**, *20*, 4342−4347.
(10) Suntivich, J.; Gasteiger, H. A.; Yabuuchi, N.; Nakanishi, H.; Goodenough, J. B.; Shao-Horn, Y. *Nat. Chem.* **2011**, *3*, 546−550.
(11) Mirkin, C. A.; Letsinger, R. L.; Mucic, R. C.; Storhoff, J. J. *Nature* **1996**, *382*, 607−609.
(12) Ulman, A. *Chem. Rev.* **1996**, *96*, 1533−1554.
(13) Love, J. C.; Estroff, L. A.; Kriebel, J. K.; Nuzzo, R. G.; Whitesides, G. M. *Chem. Rev.* **2005**, *105*, 1103−1169.
(14) Forster, R. J.; Keyes, T. E. *Coord. Chem. Rev.* **2009**, *253*, 1833−1853.
(15) Smith, R. K.; Lewis, P. A.; Weiss, P. S. *Prog. Surf. Sci.* **2004**, *75*, 1−68.
(16) Schwartz, D. *Annu. Rev. Phys. Chem.* **2001**, *52*, 107−137.
(17) Finklea, H. O.; Avery, S; Lynch, M; Furtsch, T. *Langmuir* **1997**, *3*, 409−413.
(18) Bartlett, P.; Marwan, J. *Phys. Chem. Chem. Phys.* **2004**, *6*, 2895−2898.
(19) Stranick, S. J.; Parikh, A. N.; Allara, D. L.; Weiss, P. S. *J. Phys. Chem.* **1994**, *98*, 11136−11142.

(20) McCarley, R. L.; Dunaway, D. J.; Willicut, R. J. *Langmuir* **1993**, *9*, 2775−2777.
(21) Petrovykh, D. Y.; Kimura-Suda, H.; Opdahl, A.; Richter, L. J.; Tarlov, M. J.; Whitman, L. J. *Langmuir* **2006**, *22*, 2578−2587.

Analyst

RSC Publishing

PAPER

View Article Online
View Journal | View Issue

Cite this: *Analyst*, 2013, **138**, 4340

Detection of sub-femtomolar DNA based on double potential electrodeposition of electrocatalytic platinum nanoparticles†

Elaine Spain, Hazel McArdle, Tia E. Keyes and Robert J. Forster*

Received 12th March 2013
Accepted 22nd May 2013

DOI: 10.1039/c3an00500c

www.rsc.org/analyst

Suspensions of electrocatalytic platinum nanoparticles with radii as small as 78.9 ± 3.5 nm that are functionalised with DNA only in one region have been created using templated electrodeposition. The integrity of the bound DNA following nanoparticle desorption from the electrode is demonstrated by detecting attomolar concentrations of DNA without the need for molecular, *e.g.*, PCR or NASBA, amplification. Double potential step approaches coupled with interface engineering *via* nucleation sites allows PtNPs to be created with controlled particle size and density in a facile and reproducible manner.

Introduction

The production of platinum nanoparticles (PtNPs) whose optical and electrochemical properties can be controlled by varying their size, has led to novel sensors and high performance bio-analytical assays.[1–3] Noble nanoparticles, such as platinum, can electrocatalytically reduce hydrogen peroxide (H_2O_2) and have been extensively used for sensing applications.[4–6] These reactions are of fundamental importance for fuel cells,[4,7–9] photoelectrochemical cells,[5] metal–air batteries,[10] water electrolysis and chemical sensors, *e.g.*, the determination of glucose in blood sugar.[4]

We previously described the regioselective functionalisation of metal nanoparticles that were functionalised on one side with DNA while the opposite side was electrocatalytically active.[11] The regioselective, hemi-spherical gold nanoparticles were obtained by laying a thiolated self-assembled monolayer onto the gold electrode surface before deposition. These particles were capable of detecting target DNA at picomolar concentrations in a DNA hybridisation assay. However, when the concentration of the target DNA is ultralow, very few electrocatalytic nanoparticles will be bound to the electrode surface. Under these circumstances, the nanoparticle size distribution will have a significant impact on the reproducibility of the current generated by the captured nanoparticles. Specifically, since the electrocatalytic current is proportional to the nanoparticle surface area, capturing a small number of randomly sized particles from within a size polydisperse population will lead to significant variation in the electrocatalytic current for a given target DNA concentration.

In this contribution, we report on the formation of PtNPs using a combination of defects within a self-assembled monolayer and the double potential step, *i.e.*, nucleation and growth, pioneered by Penner[12] so as to achieve a narrow particle size distribution. In order to achieve instantaneous nucleation without having a large driving force for growth, and to control the uniformity of the electrodeposited nanoparticles, it is necessary to separate the nucleation and growth steps. A nucleation pulse with a large overpotential is needed to achieve instantaneous nucleation which forms nuclei on the surface of the electrode. The potential is then changed to a lower potential so that these nuclei can be grown at the desired rate. This method was first proposed as a means of particle size distribution control[12] and has been used extensively.[13–17]

Here, we demonstrate that electrodeposited nanoparticles can be regio-selectively functionalized with probe strand DNA and desorbed from the electrode while retaining the functionality of the bound nucleic acid. Particles functionalized in a regio specific manner would allow for different linkers, *e.g.*, assorted DNA sequences or antibodies and nucleic acids, to be co-immobilized in distinct areas giving superior control over the direction of assembly and facilitating multianalyte detection using a single nanoparticle. This principle is demonstrated using the DNA sequence from the specific strain of *S. aureus* that causes mastitis (mammary gland inflammation). Significantly, beyond the ability to create regio selective functionalized platinum nanoparticles, we demonstrate that these particles are capable of detecting DNA with high sensitivity and selectivity. This result is important since, due to the low concentrations of pathogen present before clinical symptoms become apparent, the target DNA must typically be amplified, *e.g.*, using PCR or NASBA. Direct detection methodologies, *e.g.*, involving amplified electrochemical detection, avoid the need for target amplification that is costly, time consuming and labour intensive.

School of Chemical Sciences, Dublin City University, Dublin 9, Ireland. E-mail: Robert.Forster@dcu.ie; Tel: +00353 1 7005943

† Electronic supplementary information (ESI) available: Full experimental details. See DOI: 10.1039/c3an00500c

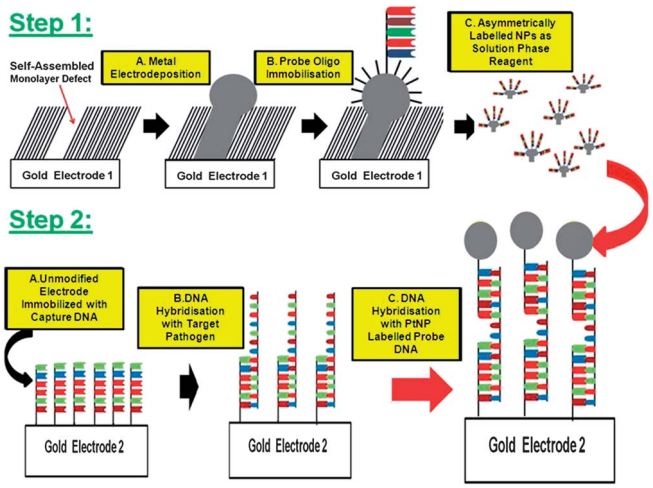

Scheme 1 Platinum nanoparticle formation and regio-selective DNA functionalization.

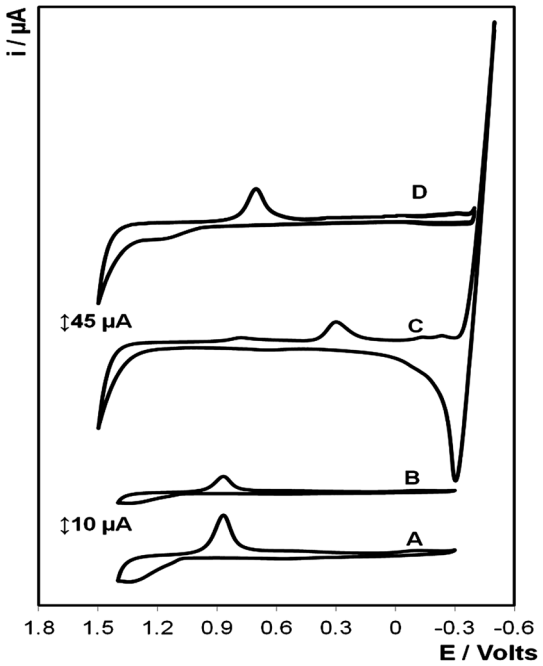

Fig. 1 Cyclic voltammograms in 0.1 M H_2SO_4 of: (A) 2 mm unmodified gold electrode, (B) after deposition of a defective C_{12} monolayer, (C) following electrodeposition of platinum nanoparticles into the monolayer defects (D) after the platinum nanoparticles have been desorbed. The scale bar for (A) and (B) are 10 μA while for (C) and (D) it is 20 μA. The counter electrode was a large area platinum wire and the reference electrode was a saturated Ag/AgCl (3 M KCl). The scan rate is 100 mV s^{-1}. The voltammograms have been displaced vertically for clarity.

As illustrated in Scheme 1, the approach is based on electrodepositing platinum nanoparticles using defects within a dodecanethiol monolayer as templates. The top surface of these PtNPs is functionalized with thiol terminated probe strand DNA. Then, a current step is applied to melt the nanowire connecting the hemispherical nanoparticle to the electrode causing rapid desorption of the DNA functionalized PtNPs. These DNA labelled electrocatalytic particles are then used in a hybridization assay to determine the concentration of the target by measuring the faradaic current associated with reduction of peroxide in solution. This approach can easily be extended to reduction of water, which, in the case of biological samples, can come from the sample itself.

Results and discussion

The formation of self assembled monolayers (SAMs) of alkane thiols on gold is well known to involve rapid adsorption to create films with a high defect density which slowly anneal to give a perfect monolayer. Fig. 1(A) and (B) illustrate cyclic voltammograms for the 2 mm radius gold electrodes before and after deposition of the defective monolayer, respectively. The active surface area can be determined using voltammetry in 0.01 M H_2SO_4 as the supporting electrolyte by creating and subsequently reducing a gold oxide monolayer on the unmodified fraction of the electrode. By comparing the charge passed before and after monolayer deposition, the area available for PtNP electrodeposition can be determined. The area under the gold oxide peak reduction peak centered at approximately +0.8 V reveals that the electrode area decreased from the value of 0.035 cm^2 found for the unmodified electrode (roughness factor of 1.1) to 0.028 cm^2 following monolayer deposition, *i.e.*, there are a substantial number of sites for metal deposition at the partially blocked surface. Platinum nanoparticles were deposited into the defects within the monolayer from a 0.5 M sulphuric acid solution containing 1 mM hydrogen hexachloroplatinate(IV) hydrate (H_2PtCl_6) with a nucleation pre-pulse of −1600 mV for 20 ms and growth potential of −200 mV. It was established that the greatest nucleation densities were attained at nucleation potentials (E_{nu}) negative of −1000 mV with nucleation density reducing significantly at potentials negative of −1600 mV presumably due to hydrogen evolution. The optimised growth conditions were −200 mV for 60 s. As the specific active area of the platinum oxide peak increased, the gold oxide peak diminished as the PtNPs were electrochemically deposited. Fig. 1(C) illustrates the cyclic voltammogram following nanoparticle deposition. In the forward scan, the onset potential for the formation of gold oxide is 1.5 V. In the reverse scan, the reduction of gold oxide occurs at +0.8 V. The reduction of platinum oxide to metallic platinum is observed at approximately +0.3 V and the peak at approximately −0.258 V is attributed to hydrogen adsorption/desorption from the platinum nanoparticle surface.[6,18] Significantly, the microscopic area following deposition of the platinum nanoparticles is 0.236 cm^2, *i.e.* nanoparticle deposition increases the area available for DNA deposition by a factor of approximately 8.4 when compared to the dodecanethiol templated electrode, *i.e.*, the PtNPs are definitely mushroom shaped. Following binding of the probe oligo, a short current pulse at a current density of approximately +100 mA cm^{-2} was applied to the nanoparticle modified electrode with the objective of melting the nanowire connecting the hemispherical nanoparticle to the electrode. These rather aggressive conditions were used to rapidly desorb the nanoparticles, which, once in solution, diffuse away from

the electrode surface thus minimizing the opportunity for damage to the bound DNA. Fig. 1(D) shows that the peak heights associated with both platinum oxide reduction and hydrogen adsorption/desorption are both dramatically lower after desorption of the PtNPs. Significantly, the gold oxide peak is substantially larger than that found for the dodecanethiol templated electrode suggesting that the current step not only removes the platinum nanoparticles but also the templating alkane thiol monolayer.

Fig. 2 shows an SEM image of the regioselectively modified nanoparticles as well as the particle size distribution. The mean particle size is 78.9 ± 3.5 nm indicating that the size distribution of the desorbed nanoparticles produced by the combination of a templating defect and double potential step electrodeposition is very narrow. This narrow distribution will improve the reproducibility of DNA detection when the concentration of the target is low. It is challenging to accurately determine the size distribution of the templating defects in the monolayer using SEM. However, it is clear that even with an electrodeposition time of 60 s that the radius of the nanoparticles typically exceeds the size of the defects by at least 50%, *i.e.*, the electrodeposited nanoparticles are mushroom shaped. This particle shape will result in approximately two thirds of the total nanoparticle surface (hemisphere) being modified by probe strand DNA with approximately one third (disk) being unmodified and available for electrocatalysis.

The electrocatalytic activity and DNA binding ability needs to be determined for the released PtNPs. As illustrated in Scheme 1, an electrode modified with DNA capture strands was first allowed to hybridize with the target strand, part of which is complementary to the capture strand. This electrode was then placed into the NP suspension for 90 minutes during which time the non-hybridized section of the target hybridizes with the oligo bound to the metal nanoparticle. Fig. 3(A) illustrates the voltammogram obtained for an electrode in 0.01 M H_2SO_4 after electrodeposition of the platinum nanoparticles and functionalisation with probe strand DNA. Fig. 3(B) shows the response obtained for a pristine gold electrode modified with capture strand DNA after both the target and nanoparticle functionalized probe strand hybridization steps have occurred. Both of these figures show well defined peaks for Pt oxide formation in the 0.6 to 1.2 V range, reduction of Pt oxide at approximately +0.3 V, as well as peaks in the range of −0.05 V to −0.3 V associated hydrogen adsorption/desorption, respectively. These observations indicate successful binding of the nanoparticles suggesting that the DNA functionalized platinum nanoparticles can be removed into suspension using the current jump approach. Control experiments in which the target is not added or where the nanoparticles are either not functionalized with DNA, or are functionalized with non-complementary DNA, do not exhibit features associated with platinum oxide or hydrogen adsorption.

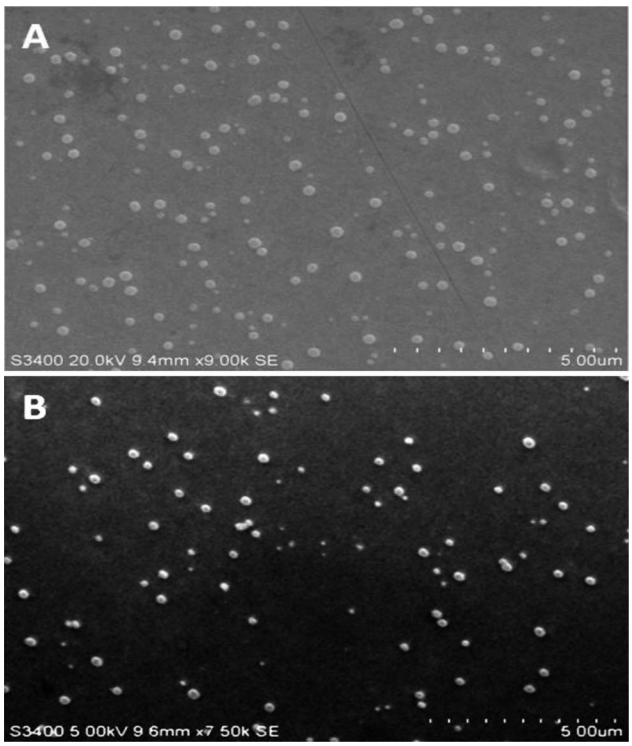

Fig. 2 SEM images of (A) a gold electrode following deposition of the templating monolayer and electrodeposition of platinum nanoparticles for 60 s. (B) Drop cast film of desorbed nanoparticles from suspension. The acceleration voltage is 5 kV.

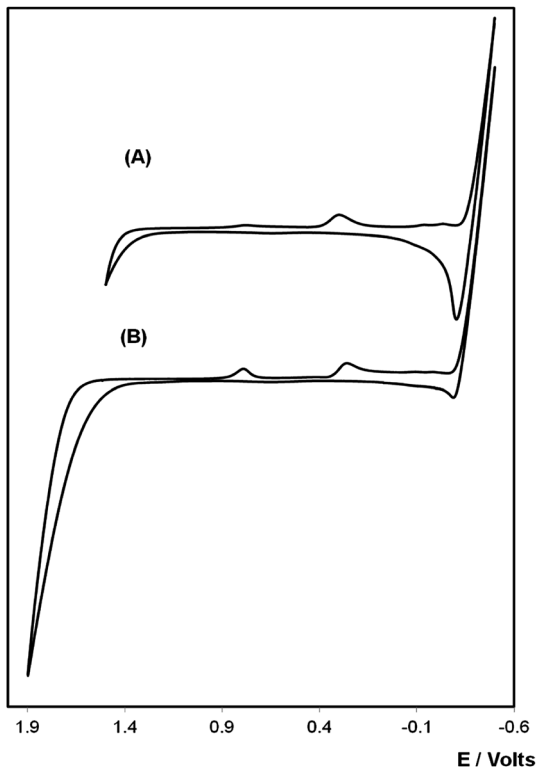

Fig. 3 (A) Cyclic voltammogram of a 2 mm radius gold disc electrode after electrodeposition of the platinum nanoparticles and functionalization with probe DNA (step 3 of Scheme 1). (B) Cyclic voltammogram of a 2 mm radius gold disc electrode after modification with capture strand DNA and hybridization with the target and nanoparticle labelled probe sequence where the target strand concentration is 1 μM. The supporting electrolyte is 0.01 M H_2SO_4 and the scan rate is 100 mV s^{-1}.

The analytical performance of the DNA sensor using the regio-selectively modified nanoparticles was investigated and compared with that observed for nanoparticles that are uniformly functionalized with probe DNA. Here, the catalytic activity of the platinum nanoparticles bound through DNA hybridization (step 2-C in Scheme 1) was assessed by applying fixed potential of −0.250 V to the working electrode and the difference in current associated with the reduction of hydrogen peroxide in a solution of 0.01 M H_2SO_4, Δi, between the initial current observed in the absence of any deliberately added peroxide and after the addition of H_2O_2, to the cell to give a final concentration of 200 μM, was measured. The system was allowed to equilibrate for ten minutes following peroxide addition. Fig. 4 shows the dependence of Δi on the log[DNA] for the two types of DNA functionalised nanoparticles. In both cases, an acceptably linear response is observed for concentrations of sequence-specific DNA from *S. aureus* from 1 aM to 1 μM. The high sensitivity as well as the wide linear dynamic range arises from efficient electrocatalysis as well as an increased mass transport rate to the nanostructured surface due to radial diffusion. However, the sensitivity of the response using regio-selectively modified nanoparticles is more than an order of magnitude better than the uniformly modified particles. This improvement arises because of more efficient electrocatalysis at the unmodified portion of the regio-selectively modified nanoparticles. This result clearly indicates that physically separating the two functions of the nanoparticles, *i.e.*, electrocatalysis and molecular recognition, leads to a significant improvement in assay performance. In order to probe the regioselective character of the DNA capture strand modification, these particles were suspended in a 5 mM ethanolic solution of dodecanethiol for 8 hours with the intention of passivating the electrocatalytic region of the particles. While recognising that the dodecanethiol could remove some of the probe strand DNA, the observation that the electrocatalytic current observed decreases to approximately 10% of that observed prior to alkane thiol deposition strongly suggests that the parent particles are regioselectively, rather than uniformly, modified with probe strands DNA. Moreover, when the probe strand is not labelled with a PtNP the current observed is less than 2% of that observed for the DNA labelled particles (Fig. S1, ESI†). This result indicates that non-specific adsorption is not a significant issue in this system.

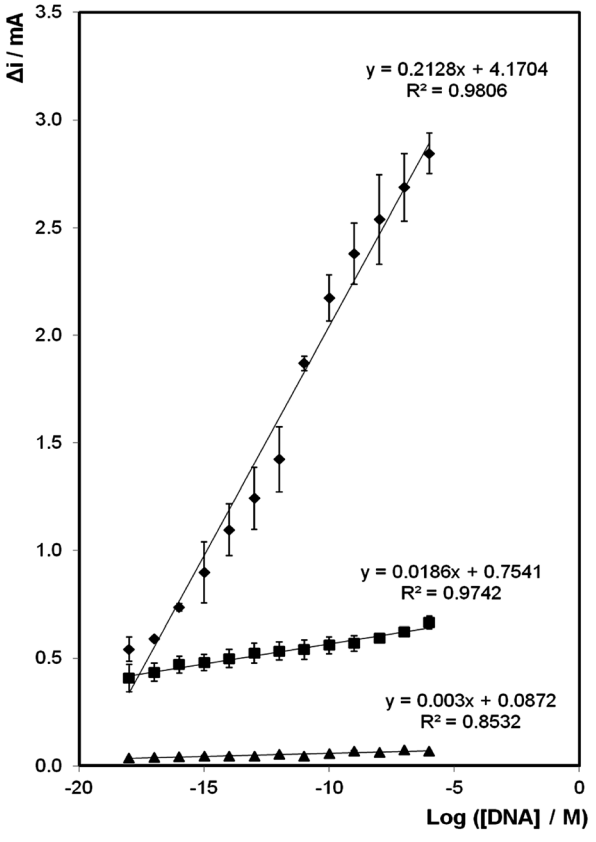

Fig. 4 Dependence of the difference in current before and after addition of H_2O_2 on log[DNA] for a 2 mm diameter bare electrode following hybridization with probe DNA immobilize regio selectively on PtNPs (◆),where the probe is unlabeled (▲) and where PtNPs are uniformly functionalized with probe strand DNA are used (■). In all cases, H_2O_2 in aqueous 0.01 M H_2SO_4 was added to give a concentration of 200 μM. Δi represents the difference in current before and after addition of the H_2O_2 at an applied potential of −0.250 V following approximately 10 min equilibration time. Where error bars are not visible, they are smaller than, or comparable to, the size of the symbols.

The selectivity of the sensor was also investigated using a target DNA sequence that contained a single mismatch (Fig. S1, ESI†). Significantly, the Δi observed for this one base mismatch DNA sequence was a factor of five smaller than that found for the fully complementary sequence suggesting a high discrimination ability. Moreover, *S. epidermis*, which has 3 base mismatches, gives no measurable current response demonstrating the system is robust with respect to false positives (Table S1, ESI†). This result is particularly important since *S. epidermis* can often be mistaken for *S. aureus* and its presence incorrectly associated with mastitis. It also further confirms that the bound DNA has not been denatured as the particles are desorbed off the electrode surface.

Conclusions

The affect of nucleation and growth modes for electrodeposition of platinum in monolayer templated gold disc electrodes was investigated. Here, we demonstrate a two pulse growth method where, instantaneous nucleation followed by negative growth potentials could be applied to achieve high density, low particle size nanoparticles. It was demonstrated that platinum nanoparticles could be regio-selectively functionalized (upper surface only) with DNA while the remainder of the particles surface is unmodified allowing efficient electrocatalysis to occur. The key advantage of desorbing these particles is that they can quickly sample the solution for target DNA by stirring rather than waiting for target strands to arrive at the electrode interface. This is particularly important for low, *i.e.*, aM concentrations, where diffusion is too slow to allow the surface coverage of the target to approach equilibrium on a meaningful timescale. The assay is characterized by a wide dynamic range, high sensitivity, a low detection limit and an excellent ability to discriminate against interferences.

Acknowledgements

This material is based upon works supported by the Science Foundation Ireland under Grant no. 10/IN.1/B3021.

Notes and references

1 C. Burda, X. Chen, R. Narayanan and M. El-Sayed, *Chem. Rev.*, 2005, **105**, 1025–1102, DOI: 10.1021/cr030063a.
2 A. R. Tao, S. Habas and P. Yang, *Small*, 2008, **4**, 310–325, DOI: 10.1002/smll.200701295.
3 Z. Y. Tang and N. A. Kotov, *Adv. Mater.*, 2005, **17**, 951–962, DOI: 10.1002/adma.200401593.
4 A. Kloke, F. von Stetten, R. Zengerle and S. Kerzenmacher, *Adv. Mater.*, 2011, **23**, 4976–5008, DOI: 10.1002/adma.201102182.
5 S. J. Cho and J. Ouyang, *J. Phys. Chem. C*, 2011, **115**, 8519–8526, DOI: 10.1021/jp2001699.
6 B. El Roustom, G. Sine, G. Foti and C. Comninellis, *J. Appl. Electrochem.*, 2007, **37**, 1227–1236, DOI: 10.1007/s10800-007-9359-4.
7 B. C. H. Steele and A. Heinzel, *Nature*, 2001, **414**, 345–352, DOI: 10.1038/35104620.
8 X. Zhang, W. Lu, J. Da, H. Wang, D. Zhao and P. A. Webley, *Chem. Commun.*, 2009, 195–197, DOI: 10.1039/b813830c.
9 J. Luo, L. Wang, D. Mott, P. N. Njoki, Y. Lin, T. He, Z. Xu, B. N. Wanjana, I.-S. Lim and C. Zhong, *Adv. Mater.*, 2008, **20**, 4342–4347, DOI: 10.1002/adma.200703009.
10 J. Suntivich, H. A. Gasteiger, N. Yabuuchi, H. Nakanishi, J. B. Goodenough and Y. Shao-Horn, *Nat. Chem.*, 2011, **3**, 546–550, DOI: 10.1038/nchem.1069.
11 E. Spain, B. Miner, T. E. Keyes and R. J. Forster, *Chem. Commun.*, 2012, **48**, 838–840, DOI: 10.1039/c1cc15115k.
12 R. M. Penner, *J. Phys. Chem. B*, 2002, **106**, 3339–3353, DOI: 10.1021/jp013219o.
13 E. Sheridan, J. Hjelm and R. J. Forster, *J. Electroanal. Chem.*, 2007, **608**, 1–7.
14 M. M. E. Duarte, A. S. Pilla, J. M. Sieben and C. E. Mayer, *Electrochem. Commun.*, 2006, **8**, 159–164, DOI: 10.1016/j.elecom.2005.11.003.
15 Z. Peng and H. Yang, *Nano Today*, 2009, **4**, 143–164, DOI: 10.1016/j.nantod.2008.10.010.
16 M. Ueda, H. Dietz, A. Anders, H. Kneppe, A. Meixner and W. Plieth, *Electrochim. Acta*, 2002, **48**, 377–386, DOI: 10.1016/S0013-4686(02)00683-7.
17 L. Niu, Q. H. Li, F. H. Wei, S. X. Wu, P. P. Liu and X. L. Cao, *J. Electroanal. Chem.*, 2005, **578**, 331–337, DOI: 10.1016/j.jelechem.2005.01.014.
18 P. Bartlett and J. Marwan, *Phys. Chem. Chem. Phys.*, 2004, **6**, 2895–2898, DOI: 10.1039/b404028g.

analytical chemistry

Article

pubs.acs.org/ac

A Label-Free, Sensitive, Real-Time, Semiquantitative Electrochemical Measurement Method for DNA Polymerase Amplification (ePCR)

Nihan Aydemir,[†,‡] Hazel McArdle,[†,§] Selina Patel,[▽] Whitney Whitford,[▽] Clive W. Evans,[▽] Jadranka Travas-Sejdic,*[,†,‡] and David E. Williams*[,†,‡]

[†]MacDiarmid Institute for Advanced Materials and Nanotechnology, [‡]Polymer Electronics Research Centre, School of Chemical Sciences, University of Auckland, Private Bag 92019, Auckland 1022, New Zealand

[▽]School of Biological Sciences, University of Auckland, Auckland 1022, New Zealand

Supporting Information

ABSTRACT: Oligonucleotide hybridization to a complementary sequence that is covalently attached to an electrochemically active conducting polymer (ECP) coating the working electrode of an electrochemical cell causes an increase in reaction impedance for the ferro-ferricyanide redox couple. We demonstrate the use of this effect to measure, in real time, the progress of DNA polymerase chain reaction (PCR) amplification of a minor component of a DNA extract. The forward primer is attached to the ECP. The solution contains other PCR components and the redox couple. Each cycle of amplification gives an easily measurable impedance increase. Target concentration can be estimated by cycle count to reach a threshold impedance. As proof of principle, we demonstrate an electrochemical real-time quantitative PCR (e-PCR) measurement in the total DNA extracted from chicken blood of an 844 base pair region of the mitochondrial Cytochrome c oxidase gene, present at ∼1 ppm of total DNA. We show that the detection and semiquantitation of as few as 2 copies/μL of target can be achieved within less than 10 PCR cycles.

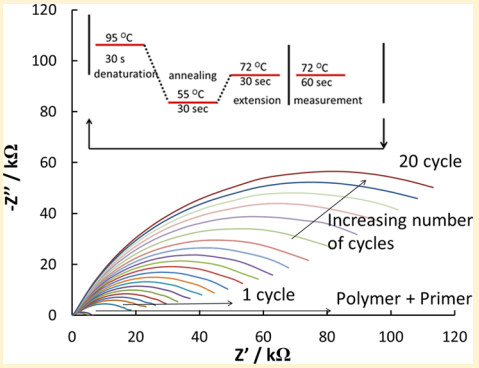

Amplification of nucleic acid sequences using the polymerase chain reaction (PCR) provides a powerful technology for both their detection and quantification.[1−5] Standard DNA PCR amplification is used primarily for the detection of particular sequences and is commonly assessed through the use of intercalation dyes, such as ethidium bromide, to detect the presence of specific products on electrophoretic gels. In quantitative PCR (qPCR), the amplification of specific sequences may be measured by using different intercalation dyes, such as SYBER Green, which fluoresce in the presence of double-stranded DNA. Alternatively, DNA amplification can be measured through the use of Taqman probes designed to bind to specific sequences between the amplifying primers.[6] As with intercalation dyes in qPCR, these probes also rely on the use of fluorescence methods for detection.[7] Electrochemical measurement in principle offers many advantages, in instrumentation, measurement system design, and cost of implementation, as exemplified by modern glucose measurement devices.[8] Hence, there has been significant interest in the electrochemical measurement of DNA[9−14] and several reports of coupling of electrochemical measurement with PCR or with various isothermal amplification methods.[15−17] These methods, again, have either used intercalation reagents for nonspecific measurement or electrochemical labels on the primers or nucleotides. The most sophisticated and now-commercialized methodology uses pH-sensitive field-effect transistors integrated into microwells[18] to detect the pH change caused by nucleotide incorporation.[19] The sensitivity (signal/noise or signal/background) of the measurement technique determines the number of cycles of amplification required to obtain a reliable signal, which, in turn, determines the time to result and also the influence of replication errors.

We and other researchers[11,20−28] have described oligonucleotide measurement based on the exclusion of a highly charged redox probe ($Fe(CN)_6^{3-/4-}$) from the electrode interface, as a result of the large negative surface charge introduced by the binding of oligonucleotides. Electrochemically active conducting polymers (ECP) can be used advantageously both as the active electrode and as the means of surface conjugation of a probe nucleotide.[29] The inhibition of the redox reaction of the polymer itself, through inhibition of the associated anion exchange with the solution, can also be used as the signal.[25−28] The presence in solution at concentrations in the low nanomolar (nM) to femtomolar (fM) range[13,20,22,30] or even lower concentrations[26] of purified nucleotide sequences that are complementary to a surface-attached probe can be measured relatively easily. The signal increases as the length of the target oligonucleotide sequence increases,[21] although with the caveat that the hybridization efficiency may decrease as the target length increases.[11,31] However, the measurement is based on

Received: January 7, 2015
Accepted: April 27, 2015
Published: May 6, 2015

DOI: 10.1021/acs.analchem.5b00079
Anal. Chem. 2015, 87, 5189−5197

the detection of global changes in the charge trapped at the reaction interface,[11,20,27] and so the measurement may be changed as a consequence of adsorption at the interface of any charged species, such as a protein or, indeed, from several other effects that alter the rate of reaction of the redox species. Thus, issues that are prominent include the need for calibration, repeatability of devices, nonspecific signals—effects of other species in the solution that may adsorb at the electrode surface and change surface charge and reaction rates as a consequence—and mismatched signals, where DNA that may not be completely complementary to the target can hybridize sufficiently with the surface-bound oligonucleotide to cause an alteration of the electrochemical reaction rate.

The combination of a high-sensitivity label-free electrochemical detection method with PCR (ePCR) offers specific attributes that overcome these problems, as well as the cost benefits generally associated with label-free electrochemistry. The particular advantage of PCR is that the composition of the solution steps in a defined way from one cycle to the next, the amplicon number ideally doubling. Therefore, any signal correlated precisely with each step in ePCR will be a signal that is derived specifically from the effect of the presence and amplification of the DNA target. The steps should be clear and distinct and progress in a well-defined way, and they should be clearly separable from any general, nonspecific drift in the electrochemical properties of the interface. A second feature of PCR is that it offers a digital encoding of target DNA concentration: the number of steps required to reach a threshold signal reflects the initial concentration of the target. The threshold can be chosen to be sufficiently large, with respect to any baseline drifts of the detector. Consequently, real-time ePCR should show correlated signal steps, which evolve with time and cycle number and are dependent only on the presence of the target. The number of steps to reach an appropriately chosen threshold should relate directly to the original target concentration. The very high sensitivity of a label-free electrochemical detector should allow specific detection and quantification of target DNA in a small number of cycles—that is, within a timeframe that could be significantly shorter than that required for detection and quantification using optical fluorescence methods. Whether the use of a redox probe, such as $Fe(CN)_6^{3-/4-}$, affects the efficiency of the polymerase enzyme is something that would have to be checked.

The electrochemical and mechanical stability of the electrochemical measurement interface upon cycling to the high temperatures necessary to implement PCR is clearly important. The stability of attachment of the primer to the surface could be an issue for methods using metal chelation,[25] or methods using thiolate adsorption to gold,[11] but should be less of an issue if the primer is conjugated to a polymer by a direct chemical bond.[20] However, for methods utilizing conducting polymers, irregular or otherwise large changes in adhesion of the polymer to the electrode substrate, or in polymer microstructure, or in the state of oxidation or doping of the polymer, would cause changes in electrochemical reaction rate at the polymer/solution interface that would militate against reliable and quantitative measurement. Temperature stability of the conducting polymer interface is not necessarily to be expected.[32] Previous studies have shown a time-varying collapse of microstructure in aqueous buffer that is dependent on the nature of the polymer, the nature of the dopant ions, and the solvent system used for synthesis, which also has a significant effect on the adhesion of the polymer to the electrode substrate.[24,33−35] These effects might be expected to become even more important with increasing temperature.

In the present work, we have explored the use of label-free electrochemistry using an electrode coated with an ECP, with a $Fe(CN)_6^{3-/4-}$ redox couple in solution as the detection methodology for real-time, quantitative PCR. We have chosen the surface-attached probe sequence to be one primer for the amplification, so extension of this surface-attached primer by the polymerase enzyme could occur.[36,37] We demonstrate that the ECP—in this case, electrochemically co-polymerized pyrrole and 3-pyrrolylacrylic acid, poly(Py-*co*-PAA)—is sufficiently temperature-stable, such that (i) the baseline does not significantly drift, (ii) the presence of $Fe(CN)_6^{3-/4-}$, although it does, to a degree, inhibit solution amplification, does not adversely affect the amplification measured electrochemically, and (iii) the sequence selectivity of a surface-bound primer is such that reliable detection and quantification of a specific sequence present in a minor amount in a mixed background of DNA can be obtained using either the surface-immobilized forward primer alone, or the surface forward primer with either the reverse primer alone in solution or with both forward and reverse primers in solution. We present a simple model, based on the "patch" model previously described,[20] that adequately describes the evolution of the electrochemical reaction impedance as the amplification proceeds.

EXPERIMENTAL SECTION

More detail is given in the Supporting Information (SI).

Electrode Preparation. A film nominally 6−12 nm thick of ECP, which is a co-polymer of pyrrole and pyrrolylacrylic acid, was electrochemically grown on a glassy carbon electrode (GCE, see the SI). Electrodes having films that were relatively uniform and adherent were selected based on impedance measurement (see the SI). Figure 1C shows a typical scanning electron microscopy (SEM) image of the resultant polymer layer. The ECP-coated GC showed polymer nodules with a size scale up to 200 nm scattered across a thin underlying layer, which had a discernible microstructure that was distinct from any structure of the underlying glassy carbon, which was itself very smooth (Figure 1B). The layer was probably significantly thicker than the nominal 6−12 nm, and thus was significantly porous.

Electrochemical Measurement and Impedance Data Extraction. A two-terminal electrochemical cell was assembled in a 100 μL Eppendorf tube, suitable for insertion into a PCR temperature cycler. The working electrode was the polymer-functionalized GC and the counter/reference electrode was a Pt wire. Since the solution contained the ferri-ferrocyanide redox couple, the Pt electrode (to a reasonable approximation dependent on the current flowing) would adopt the redox potential for this couple. The base electrolyte (40 μL) was the PCR buffer (20 mM Tris-HCl, pH 8.4, 50 mM KCl) containing 2.5 mM $MgCl_2$ and 5 mM of each of $Fe(CN)_6^{3-/4-}$. Electrodes were checked by cyclic voltammetry and impedance measurement at 72 °C before and after surface attachment of the primer. All electrochemical impedance measurements in this work were obtained at a cell potential difference of +0.23 V over a frequency range from 100 kHz to 1 Hz. Figure 1A shows the diminution in reversibility of the redox couple caused by the coating of the surface by the polymer. The electrochemical impedance (Figure 1D) was characteristic of a microscopically rough interface, namely, a semicircle with the center depressed

DOI: 10.1021/acs.analchem.5b00079
Anal. Chem. 2015, 87, 5189−5197

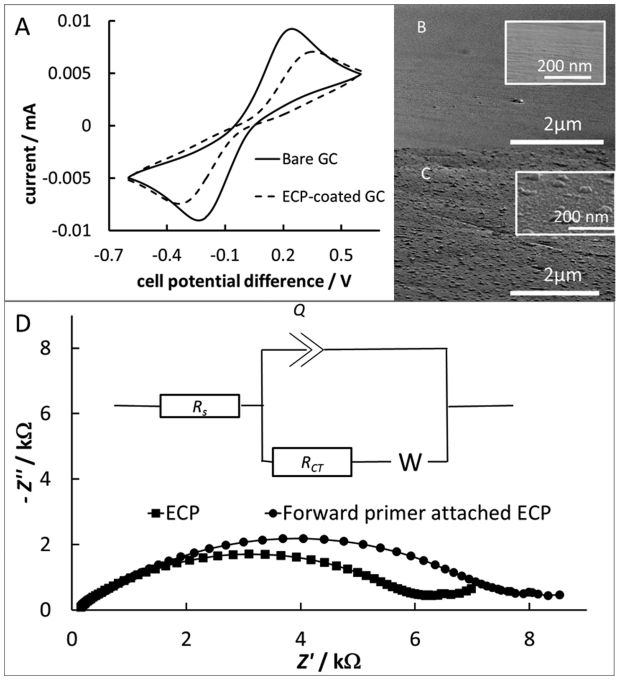

Figure 1. (A) Cyclic voltammetry (0.1 V/s) at 72 °C in the two-terminal electrochemical cell, of 5 mM $Fe(CN)_6^{3-/4-}$ in base electrolyte, comparing the bare glassy carbon electrode (GCE) with an electrode modified with a thin film of ECP. (B) SEM image of the bare GCE surface. (C) SEM of the ECP-coated GCE. (D) Electrochemical impedance (72 °C, +0.23 V cell potential difference) in base electrolyte containing 5 mM $Fe(CN)_6^{3-/4-}$, confirming successful attachment of the probe sequence from the resultant increase in impedance. The inset for panel D shows the approximate equivalent circuit: R_s, solution resistance between the working electrode and the counter/reference electrode; Q, constant phase element describing the capacitive behavior of the ECP-coated electrode; R_{CT}, charge transfer resistance for the reaction of the redox couple; and W, impedance contributed by diffusion of the redox couple to the electrode.

an angle $n\pi/2$ below the real impedance axis. The maximum value of the imaginary component of impedance, $(-Z'')_{max}$, for the approximate equivalent circuit over the frequency range where the diffusional impedance does not affect the data, is given as

$$(-Z'')_{max} = \frac{R_{CT}}{2}\left\{1 - \sin\left(\frac{n\pi}{2}\right)\right\} \quad (1)$$

Hence, provided n, which is dependent on the roughness of the interface,[38] does not greatly vary, $(-Z'')_{max}$, which we call the reaction impedance, is an easily obtained measure of the variation of the resistance due to the charge-transfer reaction of the redox couple (R_{CT}). We define the reaction conductance (σ) as

$$\sigma = \frac{1}{(-Z'')_{max}}$$

We have used this measure because it is pragmatic and practical, directly reflecting the raw experimental data; it is not dependent on arbitrary details of a specified equivalent circuit.

Materials. DNA was extracted from whole chicken blood by a standard proteinase K digestion and a modified version of the phenol/chloroform method.[39,40] Forward and reverse primers designed for amplification of a 844 base pair region of the mitochondrial Cytochrome c oxidase (CO1 or cox1) gene[39] were 26 bases long (see the SI). A thymidine 10-mer extension, amino-terminated, was used for covalent attachment of the forward primer to the ECP surface by standard EDC-NHS chemistry (see the SI). Successful primer attachment was verified by the increase in electrochemical impedance (Figure 1D).

PCR Protocol. The PCR solution, in addition to the base electrolyte, contained dNTPs (0.2 mM each), Taq polymerase (7×10^{-3} unit/μL), and the extracted DNA sample (1.2 ng/μL of chicken blood cell DNA for 1× dilution to 1.2 pg/μL for 1000× dilution). Solution primers were added at 0.5 μM. Experiments in the absence of Taq polymerase controlled for nonspecific impedance effects during cycling. The electrodes were open-circuit until the electrochemical impedance measurement was made, which, unless otherwise stated, was at 72 °C, following the extension time, and required 60 s to complete.

Quantification of the Target Concentration. Following solution amplification of the Cox1 template present in the chicken blood extract with the same forward and reverse primers used for ePCR, the amplified product was separated by gel electrophoresis, extracted, purified, and sequenced. The gel electrophoresis (Figure 2) confirmed clean amplification. The

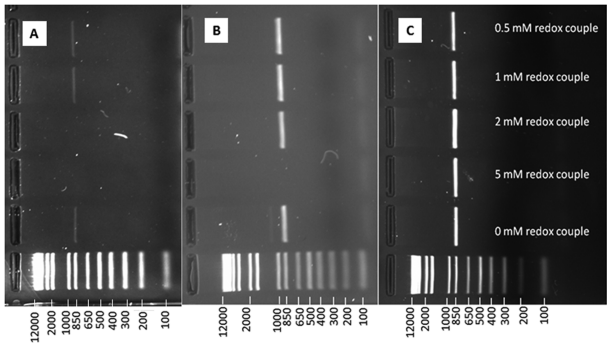

Figure 2. Gel electrophoresis of PCR solution amplification product (both forward and reverse primer present in solution) showing the effect of redox couple and Taq polymerase concentration. The first lane (lowest) is the scale in base pairs. Taq polymerase concentrations (unit/μL, cycle): (A) 7×10^{-3} unit/μL, 20 cycles; (B) 2.5×10^{-2} unit/μL, 25 cycles; and (C) 0.4 unit/μL, 25 cycles.

sequence of the amplified product was identical to part of a known chicken Cox1 DNA sequence (GenBank database AP003317.1). A standard curve was obtained using the purified, diluted product, and the mass of Cox1 template in the total chicken blood DNA extract was determined by standard q-PCR (details are given in the SI). The Cox1 template comprised 1 ppm of the total chicken blood DNA present. The 1× dilution of total DNA (1.2 ng/μL) contained 1.3 fg/μL or 1450 copies/μL of the Cox1 template.

RESULTS

Effect of the Redox Couple on Amplification of the Target Sequence. In the presence of the redox couple, the efficiency of the amplification in solution, as judged by gel electrophoresis (see Figure 2) decreased as the redox couple concentration increased, ameliorated by increases in enzyme concentration.

Temperature Stability of Electrochemical Behavior of ECP Electrodes. Temperature stability of the electrochemical impedance of the ECP-coated electrodes is critical to the

DOI: 10.1021/acs.analchem.5b00079
Anal. Chem. 2015, 87, 5189−5197

reliability of the method. Initial explorations established that cyclic voltammetry on the ECP was reasonably stable at temperatures up to 95 °C, provided that the potential range was restricted to avoid irreversible oxidation or reduction of the polymer. The thermal stability of the ECP electrodes under the PCR measurement regime described above was then evaluated first by impedance measurement in the PCR/redox couple mixture in the absence of target DNA. This measurement also explores the stability of attachment of the primer to the electrode surface. The electrode impedance changed by <20% after 20 temperature cycles. In addition, cyclic voltammetry and impedance measurement of the electrode without attached primer in the absence of the redox couple, measured at 72 °C during the temperature cycling with the electrode otherwise at open circuit, showed a change of <20% in either the apparent capacitance of the electrode or the current due to the redox process of ion injection and removal.

Single-Primer PCR: Amplification from the Surface-Attached Forward Primer Alone. DNA polymerase is active on surface-bound templates.[36,37] In the absence of the reverse primer in the solution, the surface-bound primer would be extended to a length determined by the extension time. A statistical distribution of length of surface-bound single-stranded DNA is expected to result. Figure 3 illustrates that, with the surface-bound primer alone, in the presence of the chicken blood DNA containing the mitochondrial DNA target, 5 mM redox couple, and the low concentration of enzyme (Taq polymerase, 7×10^{-3} unit/μL), the impedance signal increased progressively with each temperature cycle. Figure 3A shows the evolution of the impedance diagram with cycle number (cycle 0 labels the impedance with the primer attached to the surface, measured in the absence of Taq polymerase). Figure 3B shows the evolution of the reaction impedance as defined in the Experimental Section ($(-Z'')_{max}$). Figure 3C shows the evolution of the relative change in reaction conductance after each cycle.

$$\frac{\Delta\sigma}{\sigma_0} = \frac{(-Z'')_{\text{max,cycle } n} - (-Z'')_{\text{max,cycle 0}}}{(-Z'')_{\text{max,cycle } n}} \quad (2)$$

The result is consistent with our previous observation that reaction impedance for the ferro-ferricyanide redox couple increases with increasing length of DNA coupled to the surface, and with our deduction that the mechanism is exclusion of the redox couple due to increase of surface charge on the electrode.[20,21] The result shows that there has been extension of the oligonucleotide on the surface, despite the initial studies in solution indicating a decrease in the efficiency of the amplification for this combination of redox couple and Taq polymerase concentration.

Electrochemical Measurement of PCR Amplification with Both Primers in Solution, Together with Surface-Bound Forward Primer. In this configuration (three-primer system), the target 844 bp sequence is amplified in solution as a double-stranded DNA, as expected in standard solution PCR. In addition, the surface-bound primer may also be extended, as in the case treated above. Following the dissociation step at 95 °C, during the annealing step at 55 °C, single-stranded DNA from the solution can be hybridized onto both the surface-bound extended primer and to any nonextended, surface-bound primer. Impedance diagrams had the same form as Figure 3. The reaction impedance evolved systematically with cycle number (see the SI) but was variable between repetitions. In

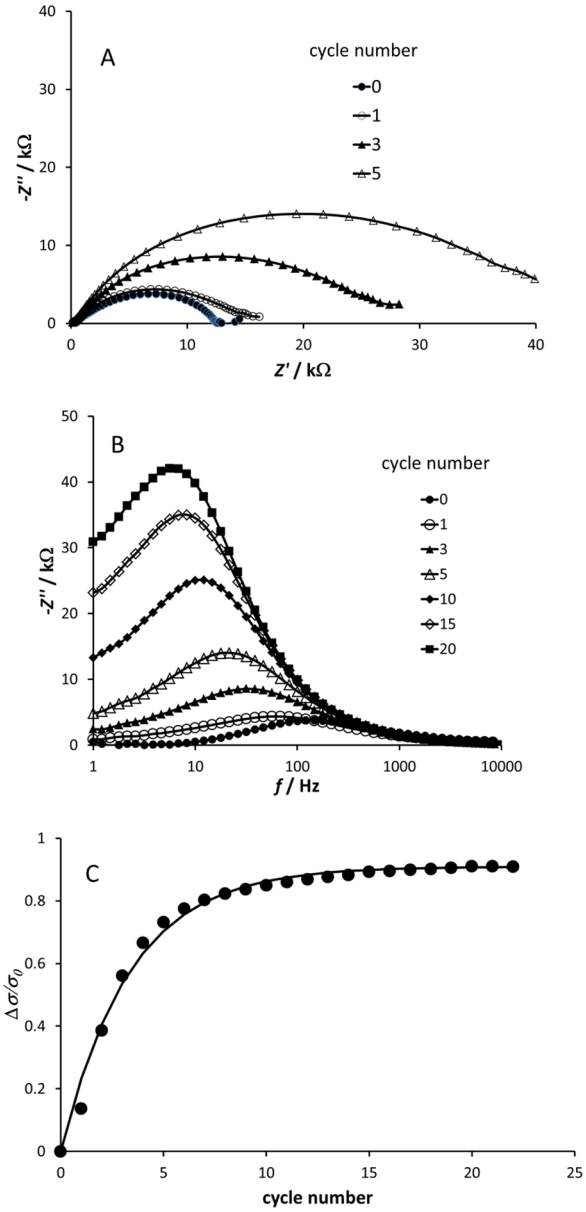

Figure 3. Amplification with surface-attached forward primer only. Measurements at 72 °C following extension, in the presence of 5 mM redox couple, +0.23 V cell pd (chicken blood DNA, 1.2 ng/μL, 7×10^{-3} unit/μL Taq): (A) evolution of impedance diagram with cycle number; (B) imaginary impedance component, $-Z''$, against measurement frequency, f and evolution with cycle number; and (C) evolution of relative reaction conductance (eq 2) with cycle number, where the line is fitted to a simple two-state model (see the Discussion section).

Figure 4A, the evolution, with cycle number, of the relative reaction conductance is shown. Figure 4A illustrates, by comparison with Figure 3C, that an additional amplification had indeed been obtained as a consequence of the presence of both primers in the solution, although, for this combination of redox couple and enzyme, concentration amplification in the solution had been inhibited, to some degree, by the presence of the redox couple (see Figure 2). Good reproducibility between different electrode preparations, and very high sensitivity for the method is demonstrated. Figure 4A shows a comparison of the signal (relative reaction conductance) evolution at 1000× dilution (1.2 pg/μL total DNA; 1.3 ag or ~2 copies/μL of the mitochondrial DNA target based on the quantification

DOI: 10.1021/acs.analchem.5b00079
Anal. Chem. 2015, 87, 5189−5197

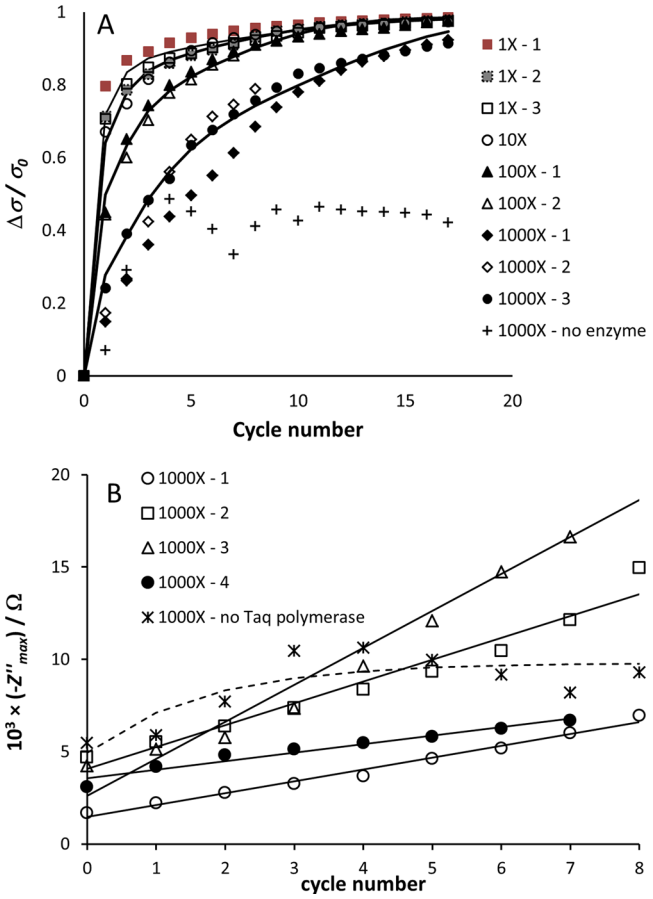

Figure 4. Evolution of (A) relative reaction conductance (eq 2) and (B) reaction impedance for the first cycles for the 1000× dilution including the initial measurement of the template-modified electrode and the Taq polymerase-free blank, for the three-primer system. Measurements at 72 °C following extension, 5 mM redox couple, and 7×10^{-3} unit/μL Taq polymerase at +0.23 V cell pd. The effect of dilution of the original chicken blood DNA sample is shown: from 1.2 ng/μL (1× dilution) to 1.2 pg/μL (1000× dilution). The lines in panel A are a fit to a four-state model (see the Discussion section) and those in panel B are empirical linear (Taq polymerase present) and exponential (Taq polymerase absent) fits. The repeat measurements shown are for independent electrode preparations.

described in the SI) in the presence and absence of the Taq polymerase. The signal for the Taq polymerase-free blank reached a plateau within the first three cycles. That, for the case with Taq polymerase present, exceeded the blank within <10 cycles and increased to the same level as that found for the higher concentrations of DNA target. Figure 4B shows the variation of the raw data (the reaction impedance) at 1000× dilution over the first few cycles, including the Taq polymerase-free blank (see the SI (Figure S4 shows the full dataset)). This illustrates the significant variation in reaction impedance for the primer-modified electrode (cycle 0: between 1−6 kΩ), which is the cause of the variability in evolution of reaction impedance. Figure 4B also shows the rapid approach to a plateau of reaction impedance in the absence of Taq polymerase, contrasting with the regular increase with cycle number in the presence of Taq polymerase. Detection of the presence of the target can be achieved just by observing the regular increase of reaction impedance with cycle number for a sufficient number of cycles to discriminate against any blank effects.

Quantification requires the use of the relative reaction conductance change and can be achieved by counting cycles to reach a threshold (see Figure 5). Such quantification requires the determination of the impedance of the primer-modified electrode before any amplification: $(-Z'')_{\max,\text{cycle }0}$ in eq 2.

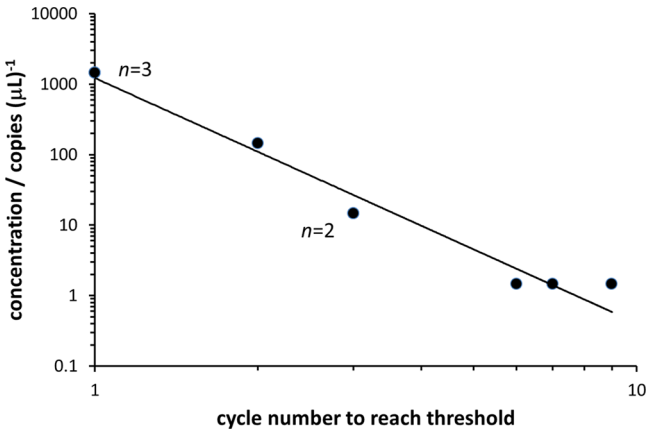

Figure 5. Cycle number to reach $\Delta\sigma/\sigma_0 > 0.7$, vs concentration of target in the diluted chicken blood DNA. Three-primer system: both primers in solution and forward primer on electrode. Repeat measurements on independent electrodes at dilutions from 1× to 1000× of 1.2 ng/μL total DNA shown; where these overlap, the number of independent determinations is shown.

Electrochemical Measurement of PCR Amplification with Reverse Primer Only in Solution, Together with Surface-Bound Forward Primer. In this configuration, the surface-bound primer may be extended, as described above. However, in the solution, single-stranded DNA will be formed by reaction from the single primer present, to a length defined by the extension time. This single-stranded DNA can be captured onto the surface-bound oligonucleotide (i.e., extended or nonextended primer) during the annealing step at 55 °C. Impedance diagrams had the same form as illustrated in Figure 3, and reaction impedance evolved with cycle number in a similar way to that shown in Figures 3 and 4. However, the results were not as reproducible.

Effects of Changing Measurement Temperature and Time Delay before Measurement. It is to be expected that the measurement signal would be altered as a consequence of the effects of the kinetics of the polymerase reaction both in the solution and on the electrode surface, as well as the effects of the diffusion of single-stranded DNA to the electrode surface, the kinetics of hybridization to the surface-bound oligonucleotide, and the competition for dissociated single-stranded DNA between solution hybridization and surface hybridization. The measurement could also just as conveniently be made at the end of the annealing step at 55 °C as at the end of the extension step at 72 °C. Figure 6 shows the effect of changing the annealing time, with measurements made for three successive temperature cycles between 95 °C and 55 °C. In this experiment, Taq polymerase was absent; the forward primer was present on the electrode surface. In the presence of the mixed DNA, the temperature was increased stepwise to 95 °C to dissociate surface-hybridized DNA. The temperature then was stepped back to 55 °C and successive impedance measurements were made at that temperature as the annealing proceeded. Figure 6 shows that the relative reaction conductance change approached a limit with a time constant

DOI: 10.1021/acs.analchem.5b00079
Anal. Chem. 2015, 87, 5189−5197

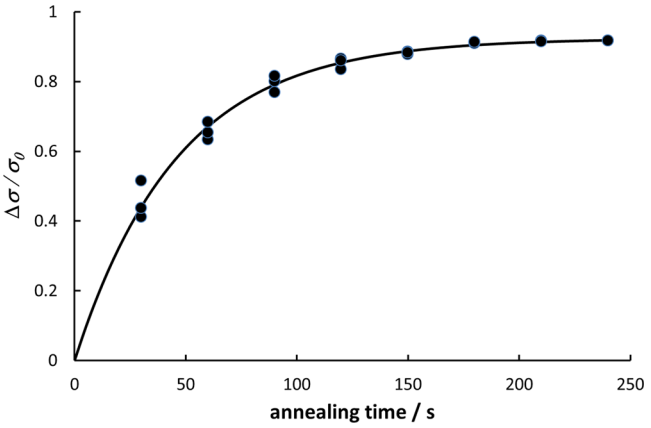

Figure 6. Relative reaction conductance change (eq 2) at 55 °C versus annealing time, following a step from 95 °C. Impedance measured in the absence of Taq polymerase. Total chicken blood DNA concentration = 1.2 ng/μL. The line is the fit to a simple exponential approach to a limit (see the Discussion section). Reaction conductance (σ_0) of the forward primer-modified electrode measured in the absence of DNA, 1600 Ω; projected reaction conductance from fit: 1100 Ω.

of ~84 s. Similarly, an increase in the extension time at 72 °C in the presence of the Taq polymerase gave an increase of reaction impedance. The choice of extension and annealing time represents a compromise between signal development at each cycle, stability of the electrochemical impedance during the time that the measurement is made, and the number of cycles that can be completed within a given analysis time. The reaction conductance (σ_0) of the forward-primer-modified electrode measured in the absence of DNA could be obtained by fitting the annealing time dependence of the relative reaction conductance to a simple exponential evolution with time, although not with great accuracy, given the time resolution of the measurements in the present work.

DISCUSSION

The hypothesis formulated earlier in this paper, that a label-free electrochemical method utilizing exclusion of a redox couple from the surface of an electrochemically active conducting polymer could be used as a high-sensitivity real-time measurement of the progress of PCR amplification of a minor component from total cellular DNA, has been demonstrated to be correct. Figure 5 illustrates that quantitation can be achieved by counting cycles to reach a threshold, and that the method has extremely high sensitivity that is obtainable within a small number of PCR cycles. The time scale for quantification at the highest dilution, with a target concentration in the ~2 copies/μL or ag/μL range was 25 min (7 cycles). A significant part of these times was that for temperature stabilization, which can be mitigated by appropriate design of the cell and cycler, and for measurement of the full impedance spectrum, which is clearly unnecessary. Figure 4 illustrates that the blank signal, in the absence of Taq polymerase, increased over the first two or three cycles and then stabilized. Although there may be some nonspecific binding of nontarget DNA (likely to occur in most complex PCR amplifications), the primer design and tuning of PCR conditions should minimize any such effect. Then, we can interpret the signal in the absence of Taq polymerase as being indeed due to binding of the target, the extent of which would depend on the concentration of target in the boundary layer near the electrode and increase over the first few cycles, as a consequence of dissociation from the surface of previously bound DNA, during the 95 °C part of the cycle.

Despite pre-existing caveats concerning the stability of the ECP, the present work has shown an adequate temperature stability in aqueous buffer for the system employed here. We presume that there were three factors that were important: (i) the conducting polymer layer was very thin; (ii) the synthesis used a solvent that was predominantly water, with just a small addition of organic solvent; and (iii) the ions doped into the polymer during synthesis were the same as those predominantly present in the measurement solution. In the following, we discuss the results using the simple patch model for the electrochemical kinetics previously presented:[20] the total current through the interface is the sum of that through different patches carrying different surface charge.

Figure 6 illustrates the simplest case: the annealing of the target sequence onto the surface primer, which is the first step of the first cycle. In this case, the surface-bound primer captures onto the interface the entire single DNA strand within which the complementary sequence is embedded. A two-patch model applies, with one patch being the hybridized fraction of the surface and the other being the unhybridized fraction. The conductance (σ) that is due to the interface reaction is the sum of the conductance through the unhybridized patches (σ_0) and that through the hybridized patches (σ_1):

$$\sigma = \theta_0\sigma_0 + (1 - \theta_0)\sigma_1 \tag{3}$$

where θ_0 denotes the fraction of the surface that is not hybridized. The variation with time t of the relative change in reaction conductance during the annealing step, where the reaction conductance for the state with unhybridized surface-attached primer only is σ_0, shows the progressive coverage of the surface by hybridized DNA. Figure 6 indicates that, in accord with our previous work,[20] this is a simple first-order kinetic process with a time constant τ:

$$\frac{\Delta\sigma}{\sigma_0} = (1 - \theta_0)\left[1 - \left(\frac{\sigma_1}{\sigma_0}\right)\right] = \left(1 - \frac{\sigma_1}{\sigma_0}\right)\left[1 - \exp\left(-\frac{t}{\tau}\right)\right] \tag{4}$$

The significance is that extrapolation back to the reaction impedance at t = 0 during annealing at 55 °C, following the initialization of the sequence at 95 °C, would give σ_0, the reaction conductance for the state with unhybridized surface-attached primer only, obviating the need for prior measurement of this number, which varies from one electrode to another (Figure 4B) but is also key to reducing the data onto the repeatable curve of relative reaction conductance against cycle number (Figure 4A). A better time resolution of the impedance changes than has been obtained in the present work would be needed for an accurate determination (see Figure 6).

The simplest measurement system of those studied here is that where the only primer present is that bound to the surface: the results are shown in Figure 3. We interpret the increase in reaction impedance (decrease in reaction conductance) on each cycle, shown in Figure 3, as being due to the progressive extension of surface-bound primer.[36] After dissociation then annealing, complementary single-strand DNA from the solution is annealed to the surface-bound primer. In the extension step, the hybridized, surface-bound primer is extended to an extent that is dependent on the extension time and the length of the hybridized complementary sequence, which is limited only by

DOI: 10.1021/acs.analchem.5b00079
Anal. Chem. 2015, 87, 5189−5197

the length of the original DNA, since there is no second primer present in the solution. The cycle then repeats, upon which complementary DNA can be captured both onto the extended and unextended surface-bound primers. The theoretical curve for the evolution of relative reaction conductance with cycle number, shown in Figure 3C, was derived by approximating the heterogeneous collection of extended primer and extended, hybridized primer states as a single low-conductance state. The model is thus a simple two-state model. The progression from state 0 (unreacted primer) to state 1 (reacted primer) is presumed to occur via a simple first-order process during both annealing and extension. To simplify further, just one of these steps is assumed to be rate-limiting and, in view of the result shown in Figure 6, we assume that this is the annealing step. Thus, following step n, where t denotes the annealing time for each step,

$$\theta_{1,n} = \theta_{0,n-1} \exp\left(-\frac{t}{\tau}\right) \tag{5}$$

The reaction conductance at each step is the sum of that due to state 1 and that due to state 0 (see eq 3). The data can then be fitted with the two parameters t/τ and σ_1/σ_0, as shown in Figure 3C. For both the data in Figure 3 and the data in Figure 6, $\sigma_1/\sigma_0 \approx 0.09$. The redox couple is relatively strongly excluded from the interface, as a consequence of the surface charge due to the surface-bound primer and DNA. This effect might explain why the electrochemical surface extension proceeded satisfactorily, despite the effect of the redox couple on the solution extension (recall Figure 2).

In the three-primer system (results shown in Figures 4 and 5), amplification should occur in the solution, as well as extension on the surface. In the solution, the system would evolve rapidly to a multiplication of the fixed-length target DNA segment, whose concentration increases in each cycle: $c_{\text{target},n} = \alpha^n c_{\text{target},0}$, where the multiplication factor, $\alpha \approx 2$, is expected for the ideal case. Amplification of the target DNA sequence in the solution should lead to an increase of sensitivity above that obtained when the only effect is extension of the primer on the surface: indeed, this effect was observed. In this case, to take into account both the effect of extension of the primer on the surface and the effect of capture onto the surface of amplicons from the solution, the surface can be represented by a four-state model, as indicated in Figure 7: state 0 is the unextended, unhybridized surface-attached primer; state 1 is extended, unhybridized surface-attached primer; state 2 is unextended surface-attached primer hybridized to complementary target from the solution; and state 3 is extended, surface-attached primer hybridized to complementary target from the solution. Following an amplification cycle, after the denaturation step at 95 °C, only states 0 and 1 are present on the surface; states 2 and 3 are formed at 55 °C by annealing from the solution remaining from the previous extension step. In the subsequent extension step at 72 °C, conversion of state 2 to state 3 by the Taq polymerase occurs, as well as multiplication in the solution.

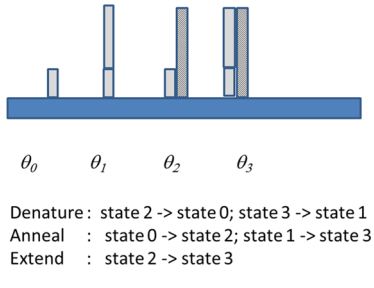

Figure 7. Schematic representation of the states for the surface-bound DNA, and the transitions during the PCR cycle; θ_j denotes the fraction of the surface covered by state j.

To take account of the effect of increase of solution amplicon concentration with cycle number, we assume that, during the annealing and extension phases, for the states $j = 0, 1$ where target DNA is captured onto the surface from the solution:

$$\left(\frac{d\theta_j}{dt}\right)_{\text{cycle } n} \approx -\frac{\alpha^n c_{\text{target},0}}{\tau} = -\frac{\alpha^n}{\tau'} \tag{6}$$

with time constant τ', which is independent of cycle number. For each cycle, the system is reset to a condition with no captured DNA—i.e., just states 0 and 1—at the end of the denaturing phase at 95 °C. Hence, using the subscript "d" to denote the relative surface coverages of states $j = 0$ at the end of the denaturing phase, in view of eq 6, we write

$$(\theta_{0,\text{d}})_{\text{cycle } n} = (\theta_{0,\text{d}})_{\text{cycle } n-1} \exp\left(-\frac{\alpha^{n-1}}{\tau'}\right) \tag{7}$$

$$(\theta_{1,\text{d}})_{\text{cycle } n} = 1 - (\theta_{0,\text{d}})_{\text{cycle } n} \tag{8}$$

Then, using the subscript "e" to denote the state of the system at the end of the extension phase at 72 °C, for states $j = 0, 1$:

$$(\theta_{j,\text{e}})_{\text{cycle } n} = (\theta_{j,\text{d}})_{\text{cycle } n} \exp\left(-\frac{\alpha^n}{\tau'}\right) \tag{9}$$

The relative coverage of the other states, $j = 2, 3$, is then easily obtained, because they are derived by conversion of states 0 and 1 during annealing and extension:

$$(\theta_{2,\text{e}})_{\text{cycle } n} = (\theta_{0,\text{d}})_{\text{cycle } n} - (\theta_{0,\text{e}})_{\text{cycle } n} \tag{10}$$

$$(\theta_{3,\text{e}})_{\text{cycle } n} = (\theta_{1,\text{d}})_{\text{cycle } n} - (\theta_{1,\text{e}})_{\text{cycle } n} \tag{11}$$

The reaction conductance is expressed as the sum of that from each of the individual states. Figure 4B shows the result of a least-squares fit to the experimental data of the relative reaction conductance thus predicted. The derived parameters are given in Table 1. Figure 8 shows the derived variation of the relative coverage of the four different states as the PCR cycling proceeds, for a sample where the total chicken blood DNA was diluted 1000×. Although the model is clearly oversimplified (e.g., τ' does not increase as expected with decreasing target concentration), the derived parameters allow some discussion of features of the results. First, the multiplication factor α is significantly less than 2, which is consistent with the effect of the redox couple on the solution amplification. This effect

Table 1. Fitting Parameters for Simple Four-State Model for the System with Both Primers in Solution and Forward Primer Surface-Attached

relative concentration	τ' /cycle	α	state	relative conductance
1	0.75	1.08	0	1
0.1	0.93	1.1	1	0.6
0.01	1.4	1.15	2	0.6
0.001	2.9	1.14	3	0.02

DOI: 10.1021/acs.analchem.5b00079
Anal. Chem. 2015, 87, 5189−5197

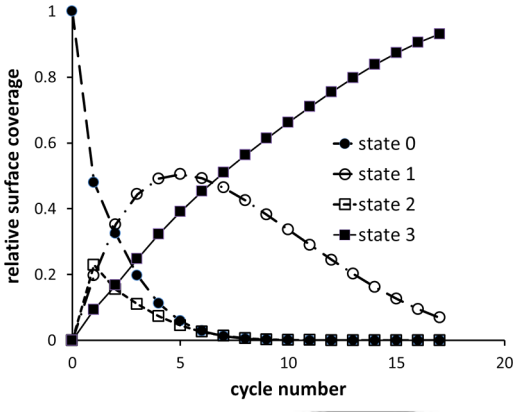

Figure 8. Evolution of relative surface coverages for the simple four-state model at a dilution of 1000× of total chicken blood DNA (data taken from Figure 4).

could be mitigated, as implied by Figure 2, by either increasing the concentration of the Taq polymerase or decreasing the concentration of the redox couple. However, such alterations involve compromises of cost (of Taq polymerase) and signal/noise (in the impedance measurement). Second, the signal development is dominated in the early cycles by the effect of extension of the surface primer and then in the later stages of the amplification by the capture of amplicons from solution. This is reasonable and accounts for much of the difference between the results of Figures 3 and 4. Third, the relative conductances due to states 1 and 2 are much greater than those suggested by the fitting of the two-state model to the data of Figures 3 and 6. This reflects both deficiencies of the model and subtleties in the evolution of the system that differs according to whether primers are present in the solution or not. In theory, the length to which the polymerase can extend the surface-attached primer is determined by the accessible length of the complementary strand hybridized to it. With no solution primers, this can proceed, in principle, to as much as the total length of the DNA sequence within which the target is embedded. However, with both primers present in solution, the target sequence itself will become the dominant complementary strand after a few cycles, resulting in the surface primer being extended only to the length of the target.

The discussion highlights that the high-temperature stage, at 95 °C, dissociates the untethered complementary DNA strand from the surface (i.e., the surface is "reset"). Thus, immediately after this step, the surface is in a defined reset condition of unhybridized primer, both extended and unextended, in proportion depending on the number of prior amplification cycles. Although we have not explored the possibility other than the results shown in Figure 6, clearly evolution of the signal from this "reset" state, and a systematic change from one cycle to the next, should provide another specific indicator of the presence of the target DNA.

CONCLUSION

Label-free, highly sensitive, real-time electrochemical detection of polymerase chain reaction amplification (ePCR) can be accomplished simply, using an electrochemically active conducting polymer as the electrode with one primer surface-bound, and the highly negatively charged redox couple $Fe(CN)_6^{3-/4-}$ in the solution as the signal species. Electrostatic exclusion of the redox couple from the electrode surface as the surface charge increases in each successive step of the PCR causes a successively stepping increase in the reaction impedance signaling the target-specific extension of surface-attached primers and amplification in the solution. We have shown, in proof of principle, that the ePCR method works successfully, despite some inhibition of the solution amplification by the redox couple. Once the detection system is in place, the technique is simple, rapid, and straightforward to apply. It needs only the addition of a redox couple to the standard PCR mix, and it does not require any fluorophores such as a Cy dye or a Taqman probe. It can be used both as a straightforward detection system and as a qPCR system, and has potential application wherever nucleic acid detection or quantitation is required.

ASSOCIATED CONTENT

Supporting Information

Materials, electrode preparation, electrode selection criteria, forward primer attachment procedure, measurement setup, ePCR protocol, complete data of reaction impedance evolution with cycle number for a three-primer system, quantitative PCR (qPCR) procedures, and results. The Supporting Information is available free of charge on the ACS Publications website at DOI: 10.1021/acs.analchem.5b00079.

AUTHOR INFORMATION

Corresponding Authors

*E-mail: j.travas-sejdic@auckland.ac.nz (J. Travas-Sejdic).
*E-mail: david.williams@auckland.ac.nz (D. E. Williams).

Present Address

[§]Dept. of Chemical Sciences, Dublin City University, Glasnevin, Dublin, 9, Ireland.

Author Contributions

All authors contributed to this manuscript and have given approval to its final version.

Notes

The authors declare no competing financial interest.

ACKNOWLEDGMENTS

This work was funded by the Tertiary Education Commission, New Zealand through the MacDiarmid Institute, by the NZ Ministry of Business, Innovation and Employment, through Contract No. C08X0806 (scholarship to N.A.), and by a Science Foundation Ireland Travel Scholarship to H.McA. (under Grant No. 10/IN.1/B3021).

REFERENCES

(1) Schmittgen, T. D.; Livak, K. J. *Nat. Protocols* **2008**, *3*, 1101−1108.
(2) Heid, C. A.; Stevens, J.; Livak, K. J.; Williams, P. M. *Genome Res.* **1996**, *6*, 986−994.
(3) Fraga, D.; Meulia, T.; Fenster, S. In *Current Protocols Essential Laboratory Techniques*; John Wiley & Sons: Hoboken, NJ, 2008.
(4) Bustin, S. A.; Mueller, R. *Clin. Sci.* **2005**, *109*, 365−379.
(5) Bartlett, J. M. S.; Stirling, D. In *PCR Protocols*; Bartlett, J. S., Stirling, D., Eds.; Humana Press: Totowa, NJ, 2003; pp 3−6.
(6) Van Guilder, H. D.; Vrana, K. E.; Freeman, W. M. *BioTechniques* **2008**, *44*, 619−626.
(7) Cao, H.; Shockey, J. M. *J. Agric. Food Chem.* **2012**, *60*, 12296−12303.
(8) Gubala, V.; Harris, L. F.; Ricco, A. J.; Tan, M. X.; Williams, D. E. *Anal. Chem.* **2012**, *84*, 487−515.
(9) Palecek, E.; Bartosik, M. *Chem. Rev.* **2012**, *112*, 3427−3481.

DOI: 10.1021/acs.analchem.5b00079
Anal. Chem. 2015, 87, 5189−5197

(10) Kukol, A.; Li, P.; Estrela, P.; Ko-Ferrigno, P.; Migliorato, P. *Anal. Biochem.* **2008**, *374*, 143−153.
(11) Riedel, M.; Kartchemnik, J.; Schoning, M. J.; Lisdat, F. *Anal. Chem.* **2014**, *86*, 7867−7874.
(12) Travas-Sejdic, J.; Aydemir, N.; Kannan, B.; Williams, D. E.; Malmstrom, J. *J. Mater. Chem. B* **2014**, *2*, 4593−4609.
(13) Lazerges, M.; Bedioui, F. *Anal. Bioanal. Chem.* **2013**, *405*, 3705−3714.
(14) Dulgerbaki, C.; Oksuz, A. U.; Ahmad, S. *Electrochim. Acta* **2014**, *122*, 87−92.
(15) Lee, D. C.; Yip, S. P.; Lee, T. M. H. *Electroanalysis* **2013**, *25*, 1310−1315.
(16) Lusi, E. A.; Passamano, M.; Guarascio, P.; Scarpa, A.; Schiavo, L. *Anal. Chem.* **2009**, *81*, 2819−2822.
(17) Ren, Y.; Deng, H.; Shen, W.; Gao, Z. *Anal. Chem.* **2013**, *85*, 4784−4789.
(18) Toumazou, C.; Shepherd, L. M.; Reed, S. C.; Chen, G. I.; Patel, A.; Garner, D. M.; Wang, C.-J. A.; Ou, C.-P.; Amin-Desai, K.; Athanasiou, P.; Bai, H.; Brizido, I. M. Q.; Caldwell, B.; Coomber-Alford, D.; Georgiou, P.; Jordan, K. S.; Joyce, J. C.; La Mura, M.; Morley, D.; Sathyavruthan, S.; Temelso, S.; Thomas, R. E.; Zhang, L. *Nat. Methods* **2013**, *10*, 641−646.
(19) Zhang, F.; Wu, J.; Wang, R.; Wang, L.; Ying, Y. *Chem. Commun.* **2014**, *50*, 8416−8419.
(20) Kannan, B.; Williams, D. E.; Booth, M. A.; Travas-Sejdic, J. *Anal. Chem.* **2011**, *83*, 3415−3421.
(21) Booth, M. A.; Harbison, S.; Travas-Sejdic, J. *Biosens. Bioelectron.* **2011**, *28*, 362−367.
(22) Kannan, B.; Williams, D. E.; Laslau, C.; Travas-Sejdic, J. *Biosens. Bioelectron.* **2012**, *35*, 258−264.
(23) Peng, H.; Soeller, C.; Travas-Sejdic, J. *Macromolecules* **2007**, *40*, 909−914.
(24) Spires, J. B.; Peng, H.; Williams, D.; Travas-Sejdic, J. *Electrochim. Acta* **2011**, *58*, 134−141.
(25) Thompson, L. A.; Kowalik, J.; Josowicz, M.; Janata, J. *J. Am. Chem. Soc.* **2003**, *125*, 324−325.
(26) dos Santos Riccardi, C.; Kranz, C.; Kowalik, J.; Yamanaka, H.; Mizaikoff, B.; Josowicz, M. *Anal. Chem.* **2008**, *80*, 237−245.
(27) Kalantari, R.; Cantor, R.; Chen, H.; Yu, G.; Janata, J.; Josowicz, M. *Anal. Chem.* **2010**, *82*, 9028−9033.
(28) Riccardi, C. D.; Yamanaka, H.; Josowicz, M.; Kowalik, J.; Mizaikoff, B.; Kranz, C. *Anal. Chem.* **2006**, *78*, 1139−1145.
(29) Lassalle, N.; Mailley, P.; Vieil, E.; Livache, T.; Roget, A.; Correia, J. P.; Abrantes, L. M. *J. Electroanal. Chem.* **2001**, *509*, 48−57.
(30) Nie, G.; Bai, Z.; Chen, J.; Yu, W. *ACS Macro Lett.* **2012**, *1*, 1304−1307.
(31) Corrigan, D. K.; Schulze, H.; McDermott, R. A.; Schmuser, I.; Henihan, G.; Henry, J. B.; Bachmann, T. T.; Mount, A. R. *J. Electroanal. Chem.* **2014**, *732*, 25−29.
(32) Malhotra, B. D.; Kumar, N.; Chandra, S. *Prog. Polym. Sci.* **1986**, *12*, 179−218.
(33) Spires, J. B.; Peng, H.; Williams, D.; Travas-Sejdic, J. *J. Electroanal. Chem.* **2011**, *658*, 1−9.
(34) Spires, J. B.; Peng, H.; Williams, D. E.; Soeller, C.; Travas-Sejdic, J. *Electrochim. Acta* **2010**, *55*, 3061−3067.
(35) Serra Moreno, J.; Panero, S. *Electrochim. Acta* **2012**, *68*, 1−8.
(36) Braslavsky, I.; Hebert, B.; Kartalov, E.; Quake, S. R. *Proc. Natl. Acad. Sci. U.S.A.* **2003**, *100*, 3960−3964.
(37) Palanisamy, R.; Connolly, A. R.; Trau, M. *Bioconjugate Chem.* **2010**, *21*, 690−695.
(38) Ball, R.; Blunt, M. *J. Phys. A: Math. Gen.* **1988**, *21*, 197.
(39) Lawrence, H.; Taylor, G.; Millar, C.; Lambert, D. *Conserv. Genet.* **2008**, *9*, 1293−1301.
(40) Sambrook, J., Fritsch, E. F., Maniatis, T. *Molecular Cloning: A Laboratory Manual*; Cold Spring Harbor Laboratory Press: Cold Spring Harbor, NY, 1989.

DOI: 10.1021/acs.analchem.5b00079
Anal. Chem. 2015, 87, 5189−5197